[redacted]

UNCLASSIFIED

UCRL-6726
Nuclear Ramjet
Engines, C-90
M-3679 (25th Ed.)
This document contains 283 pages,
including pp. i-vi.
This is copy 143 of 187 Series A .

UNIVERSITY OF CALIFORNIA
Lawrence Radiation Laboratory
Livermore, California

Contract No. W-7405-eng-48

CLASSIFICATION CANCELLED
Date 11-26-73
R. B. Martin, USAEC ORO
Research & Technical Support Div.

Exempt from CCRP Re-review Requirements
(per 7/22/82 Duff/Caudle memorandum)
NK 7-3-14

PLUTO QUARTERLY REPORT NO. 10*

(October-December 1961)
(Title: Unclassified)

by

The Nuclear Propulsion Division Staff

January 5, 1962

---

*Previous Quarterly Reports

No. 1, UCRL-5699
No. 2, UCRL-5829
No. 3, UCRL-5925
No. 4, UCRL-6036
No. 5, UCRL-6143
No. 6, UCRL-6258
No. 7, UCRL-6376
No. 8, UCRL-6516
No. 9, UCRL-6625

UNCLASSIFIED

~~RESTRICTED DATA~~

~~This document contains restricted data as defined in the Atomic Energy Act of 1954. Its transmittal or the disclosure of its contents in any manner to an unauthorized person is prohibited.~~

[redacted]

DIST

IS UNLIMITED

DISTRIBUTION

Series A

	Copy No.
LRL Livermore,	
Information Division	1 - 15
John S. Foster	16
Forrest Fairbrother	17
C.M. Van Atta	18
Roger E. Batzel	19 - 20
Theodore C. Merkle	21 - 25
Harry L. Reynolds	26
Richard P. Connell	27
James W. Bell	28
Robert W. Westbrook	29
Albert J. Kirschbaum	30
Henry C. McDonald	31
W. Blake Myers	32 - 36
Albert J. Rothman	37
Monte P. Hickenlooper	38
James S. Kane	39
W. E. Humphrey	40
William C. Grayson, Jr.	41
DASA Livermore Liaison Office,	
Norman G. Hunt	42
LRL Berkeley,	
R.K. Wakerling	43
Hayden S. Gordon	44
LRL Mercury, Nevada,	
James L. Olsen	45
Division of Military Application, Washington,	
Brig. Gen. A.W. Betts	46
U.S. Atomic Energy Commission, Washington,	
Irving Hoffman	47 - 48
U.S. Naval Radiological Defense Laboratory, San Francisco	49
Advanced Research Projects Agency	50
Air Force Special Weapons Center	51

DISCLAIMER

DISTRIBUTION (Continued)

Series A

	Copy No.
Air Technical Intelligence Center	52
Air University Library	53
Albuquerque Operations Office	54
Allegany Ballistics Laboratory	55
Argonne National Laboratory	56
Army Ballistic Missile Agency	57 - 58
Atomic Energy Commission, Washington	59 - 62
Atomics International	63
Battelle Memorial Institute	64
Brookhaven National Laboratory	65
Bureau of Naval Weapons	66 - 69
Bureau of Naval Weapons (SPO)	70
Bureau of Ships	71
Canoga Park Area Office	72
Chance-Vought Aircraft, Inc., Dallas (BUWEPS)	73
Chicago Operations Office	74
Chicago Patent Group	75
Convair Division, San Diego	76
Convair Division, San Diego (BUWEPS)	77
Defense Atomic Support Agency, Sandia	78
Defense Atomic Support Agency, Washington	79
Director of Defense Research and Engineering (OSD)	80
duPont Company, Aiken	81
General Electric Company (ANPD)	82 - 87
General Electric Company, Richland	88 - 89
Jet Propulsion Laboratory	90
Lockheed Aircraft Corporation, Burbank	91
Los Alamos Scientific Laboratory	92 - 93
Marquardt Corporation	94 - 97
NASA Ames Research Center	98
NASA Flight Research Center	99
NASA George C. Marshall Space Flight Center	100
NASA Langley Research Center	101

DISTRIBUTION (Continued)

Series A

	Copy No.
NASA Lewis Research Center	102 - 106
National Aeronautics and Space Administration, Washington	107 - 108
Naval Air Development Center	109
Naval Ordnance Test Station	110
North American Aviation, Inc., Downey	111
United Nuclear Corporation (NDA)	112 - 113
Oak Ridge Operations Office	114
Office of the Chief of Naval Operations	115
Patent Branch, Washington	116
Phillips Petroleum Company (NRTS)	117
Pratt and Whitney Aircraft Division	118
RAND Corporation	119 - 120
San Francisco Operations Office	121
Sandia Corporation	122
School of Aviation Medicine	123
Strategic Air Command	124
Union Carbide Nuclear Company (ORNL)	125 - 134
USAF Headquarters	135
USAF Headquarters (OVCS)	136
Aeronautical Systems Division	137 - 142
Division of Technical Information Extension	143 - 187

PLUTO QUARTERLY REPORT NO. 10

TABLE OF CONTENTS

Page No.

CHAPTER I – Tory II-A-1 . . . 1

- Section I – Operations 1
- Section II – Neutronics 5
- Section III – Instrumentation 12
- Section IV – Controls 26

CHAPTER II – Materials Development and Pilot Plant Activities . . . 28

- Section I – Process and Materials Development . . 28
- Section II – General Chemistry 92

CHAPTER III – Hot Box . . . 118

CHAPTER IV – Tory II-C . . . 122

- Section I – Neutronics 122
- Section II – Aerothermodynamics 152
- Section III – Controls 180
- Section IV – Engineering 195

CHAPTER V – Tory III . . . 250

- Section I – Engineering 250

TABLE OF CONVERSIONS

°C	°F	°C	°F	°C	°F
0	32	650	1202	1250	2282
50	122	700	1292	1300	2372
100	212	750	1382	1350	2402
150	302	800	1472	1400	2552
200	392	850	1562	1450	2642
250	482	900	1652	1500	2732
300	572	950	1742	1550	2822
350	662	1000	1832	1600	2912
400	752	1050	1922	1650	3002
450	842	1100	2012	1700	3092
500	932	1150	2102	1750	3182
550	1022	1200	2192	1800	3272
600	1112				

Btu/second-in^3 = 1.82 megawatts/foot^3

Btu/second = 1.0548 kilowatts

Btu/hour-ft^2-°F = 5.676×10^{-4} watt/cm^2-°C

Btu/lb-°F = 1.0 calorie/g-°C

calorie = 4.186 joules or watt-seconds

pound = 454 grams

inch = 2.54 centimeters

cubic foot = 1728 cubic inches

cubic inch = 16.387 cubic centimeters

megawatt-day = 1.05 gram U^{235} fissioned (200 Mev per fission)

pound/ft^2 = 0.4882 gram/centimeter^2

pound/in^2 = 70.30 grams/centimeter^2

barn = 10^{-24} centimeter^2

gravity (g) = 980.7 cm/sec^2 = 32.17 ft/sec^2

MUL-14122

PLUTO QUARTERLY REPORT NO. 10
(October-December, 1961)

Lawrence Radiation Laboratory, University of California
Livermore, California

CHAPTER I. TORY II-A-1

SECTION I. OPERATIONS

All data from reactor operation have now been reduced, and analysis is continuing. The high-power test series on the Tory II-A-1 reactor consisted of three runs designated as follows:

High-Power Test 1	September 28, 1961
High-Power Test 2	October 5, 1961
High-Power Test 3	October 6, 1961

The variation of five important system parameters with time is shown for each of these runs in Figs. I-1, I-2, and I-3. The curves shown are:

A) Percent ion chamber current (chamber C1; not directly proportional to reactor power at high air-flow rates).

B) Air flow rate in pounds per second, computed from measurements at the flowmeter used for each run.

C) Average core temperature in degrees F, taken from traces produced by the six-core-thermocouple averaging network at x/L = 0.723, described in Sec. III. The actual traces from which these temperature curves are taken are reproduced in Figs. I-11, I-12, and I-13.

D) Exit gas temperature in degrees F, measured by a total temperature rake 27 in. downstream from the reactor baseplate.

E) Inlet air temperature in degrees F, measured by a total temperature rake upstream from the diffuser.

The power-range-compensated ion chambers (the output of one of these is used in curve A) were located so that the inlet air ducting was between them and the reactor. It was noted during the high-power runs, at high flow rates, that density and temperature changes in the air "plug" between the chambers and the reactor scattered neutrons sufficiently to produce a noticeable decrease in chamber sensitivity. While these detectors gave period information that was valid enough for safety and control purposes, their output could no longer be used to indicate relative power level at high air-flow rates.

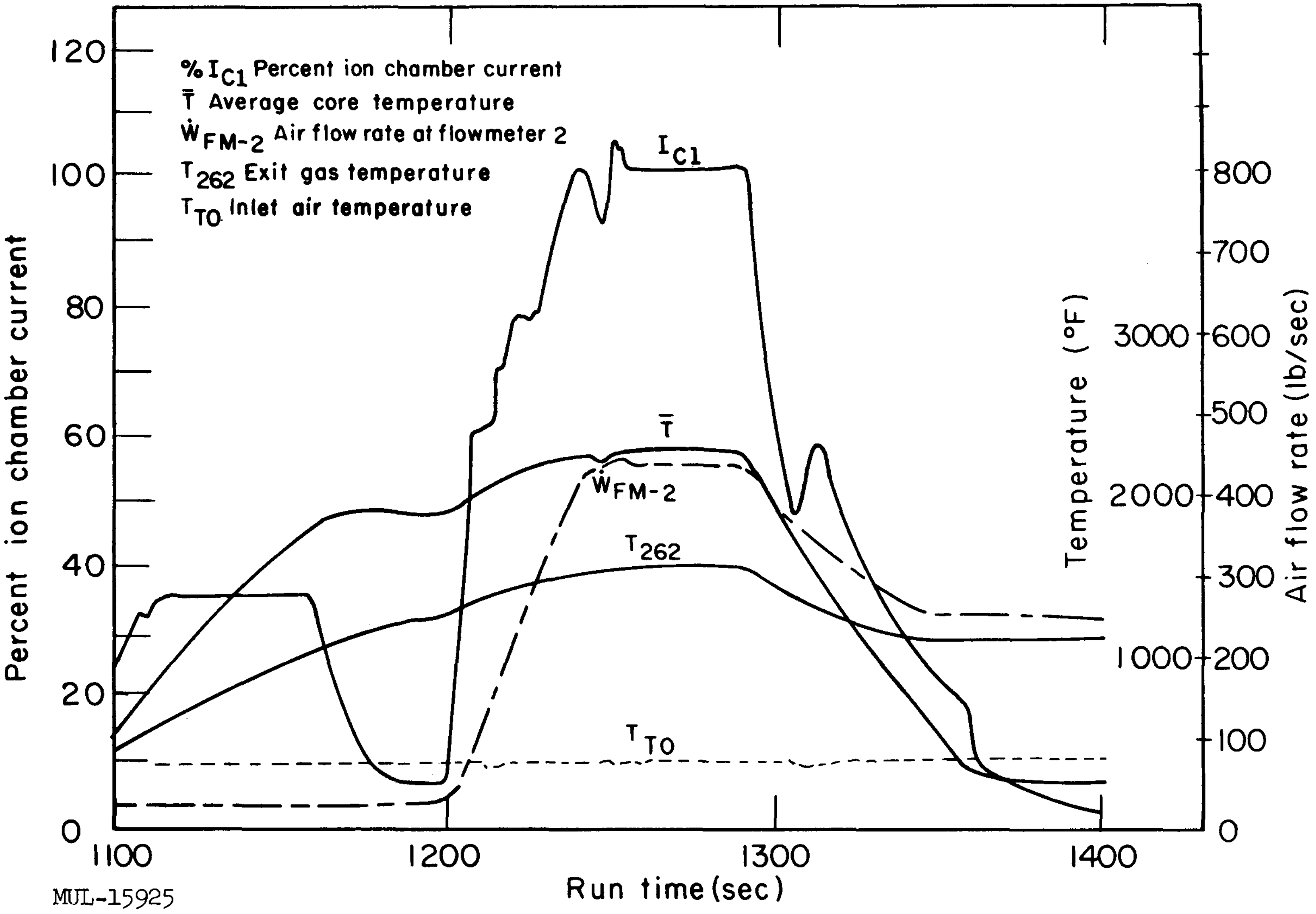

Fig. I-1. High-power test 1: variation of system parameters with time.

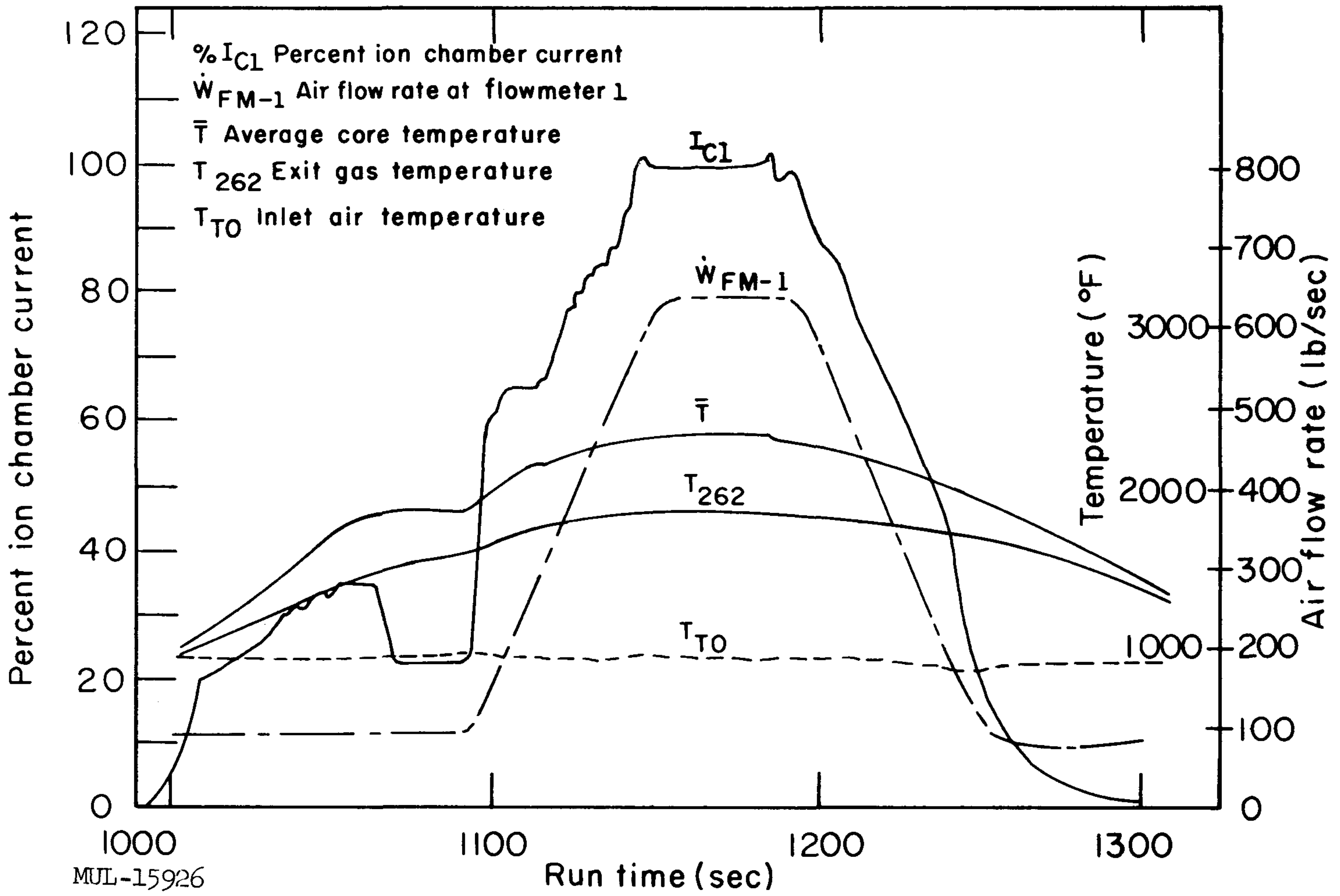

Fig. I-2. High-power test 2: variation of system parameters with time.

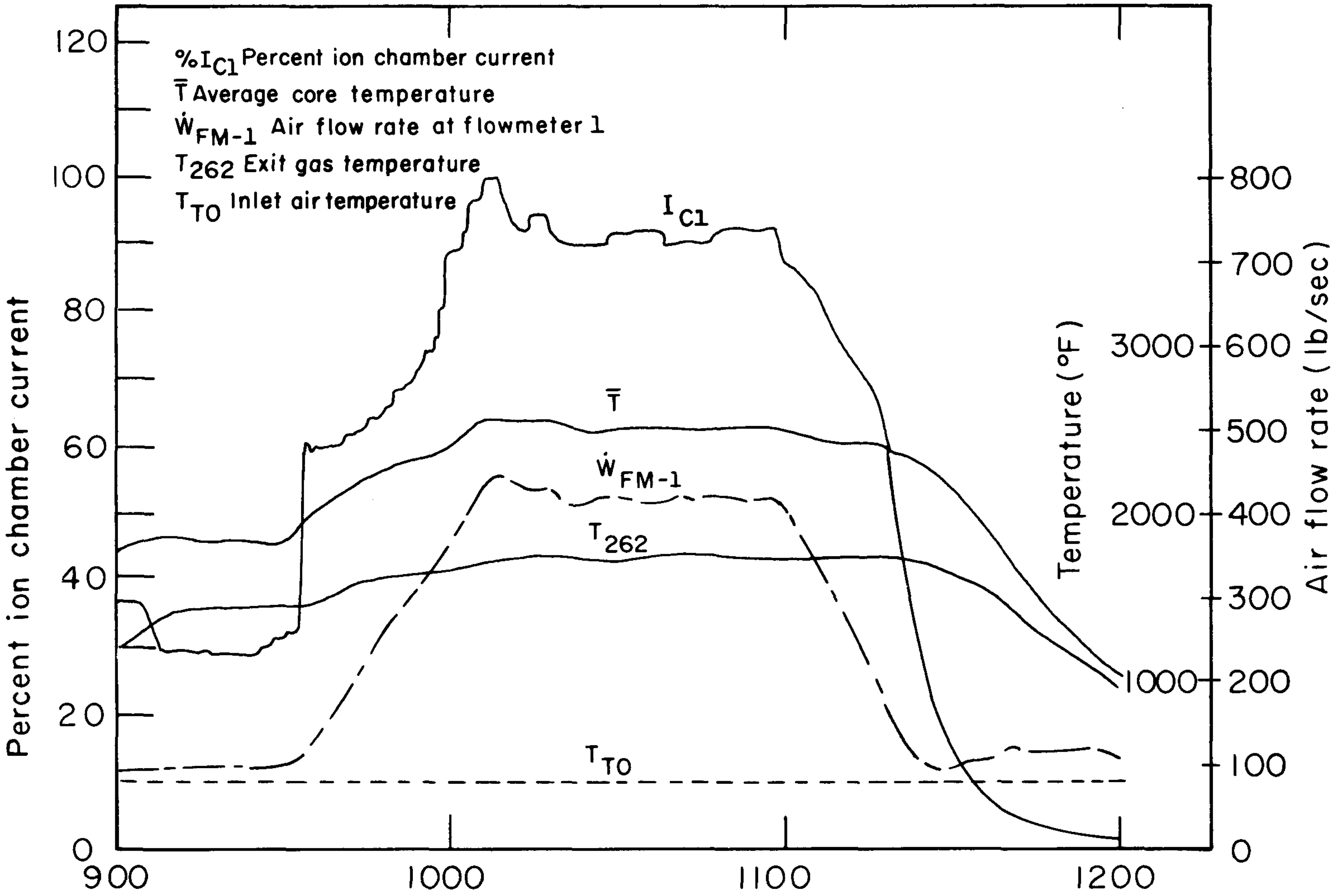

MUL-15927

Fig. I-3. High-power test 3: variation of system parameters with time.

SECTION II. NEUTRONICS

The Tory II-A-1 performance during the series of high-power tests has been studied on the basis of the data now available. A preliminary analysis shows satisfactory agreement between calculated and observed reactivity effects.

Values of critical vane angle, corrected to an average core temperature of 320°F, are shown in Table I-1 together with critical vane angles at indicated values of average core temperature. Values of corresponding Δk_{eff} are given, with predicted values for comparison. Experimental uncertainties in temperature are of the order of 50°F.

Note that the overall variation in critical vane angle at 320° is no greater than 2°, corresponding to about 0.2% in Δk_{eff} or 1.3% possible change in core fuel content, giving an upper limit on loss of fuel during the first three runs. Visual observation of digital voltmeter readings of vane angle during the final run showed no variation in vane angle of as much as 0.1°, giving additional evidence that essentially no fuel loss took place.

Table I-1. Tory II-A-1 Vane-Angle Data for Four High-Power Tests.

	May 14, 1961	Sept. 28, 1961	Oct. 5, 1961	Oct. 6, 1961
Bulk average core temp	2005°F	1950°F	2030°F	2150°F
Vane angle	101.3°	100.2°	98.5°	104.5°
Critical vane angle at 320°F	71.9°	71.8°	74.3°	73.7°
Actual Δk_{eff}	-0.0301 abs	-0.0292 abs	-0.0250 abs	-0.0308 abs
Predicted Δk_{eff}	-0.0244 abs	-0.0233 abs	-0.0268 abs	-0.0260 abs

FISSION FRAGMENT ESCAPE IN TORY II-A-1

Estimates

Theoretical estimates of the loss fraction of fission products were given in pp. 2-6 of the previous quarterly report (UCRL-6625, Oct. 10, 1961). These fractions were attributed to fragment recoil into the airstream only. Diffusion and erosion losses were shown to be negligible.

The theoretical estimates appropriate to the actual reactor runs are shown in Table I-2. The maximum possible escape fraction is 0.0015. Values below this are due to the fact that some fragments will leave an inner wall, traverse the air hole, and become imbedded in the opposite wall.

The axial variations in air density and power density were taken into account in the determination of the escape fractions.

Table I-2. Fission Fragment Escape Fractions

Date of run	Peak power (Mw)	Recoil escape fraction
May 14, 1961	50	0.0004
Sept. 28, 1961	150	0.0011
Oct. 5, 1961	185	0.0014
Oct. 6, 1961	175	0.0011

Field Observations

Considerable effort was expended during operation of Tory II-A-1 to provide radiological safety information and to obtain effluent cloud and fallout data. The following items represent part of this support effort:

A) Fixed detector net at 1.2 and 1.3 miles for gamma dose-rate measurements.

B) Roving teams using portable radiation detection instruments at approximate distances of 5 and 8 miles from the reactor.

C) Aerial monitoring and cloud tracking with an L-20-type aircraft employing portable monitoring instruments.

D) Personnel, experimental, and shielding effectiveness dosimetry.

E) Fallout trays for determination of gross alpha and beta activity from airborne particulate emitters.

F) High-volume air samplers at various distances from the reactor.

G) Effluent air-monitoring system which sampled the reactor exhaust for gross beta activity, and a filter system to permit chemical or radiochemical analysis.

The results presented here are based largely upon the gamma dose rates measured at the fixed detector net. Detector locations are shown in Fig. I-4. The recorded dose rates for the three runs considered are presented in Figs. I-5, I-6, and I-7.

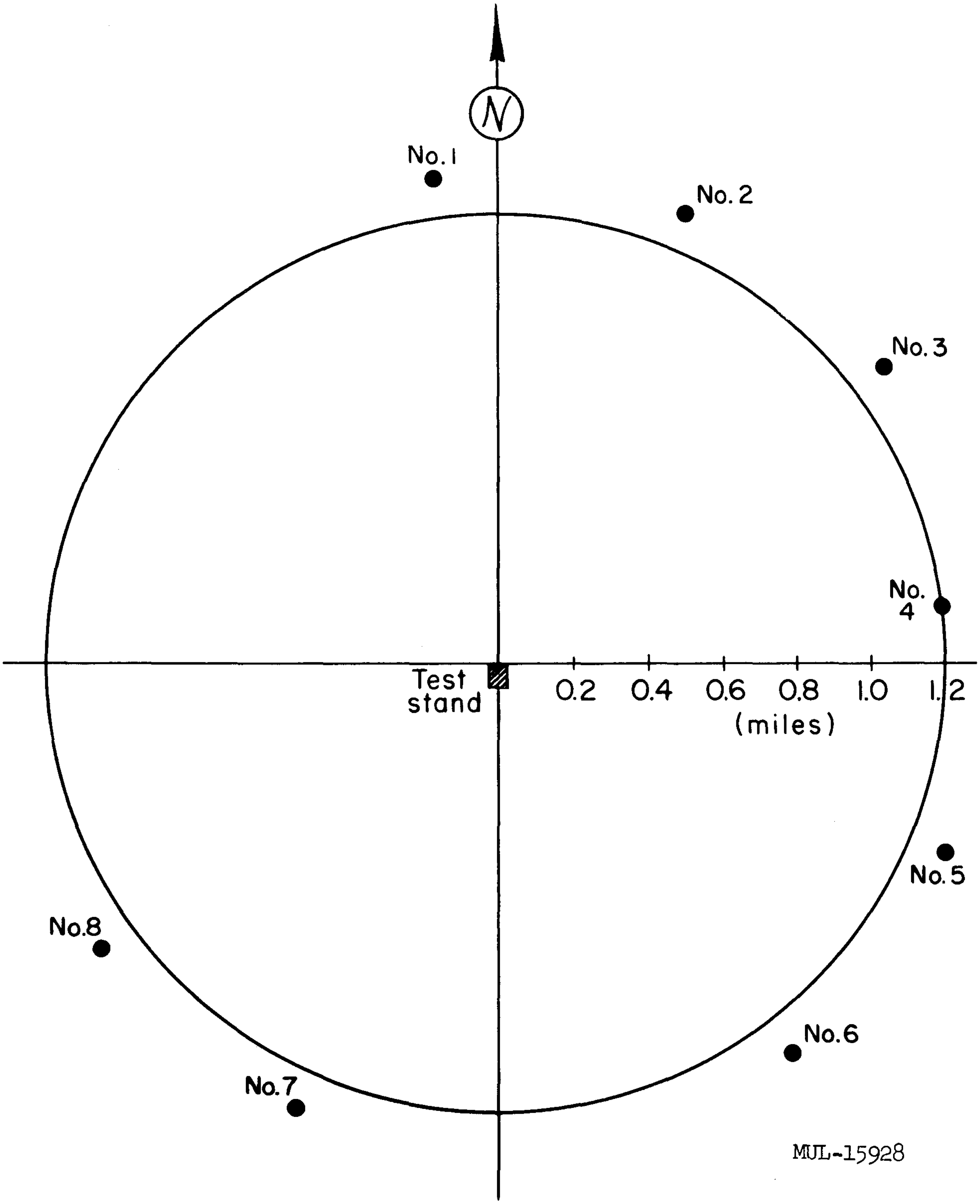

Fig. I-4. Perimeter monitoring system. Location of detector units No. 1 through No. 8.

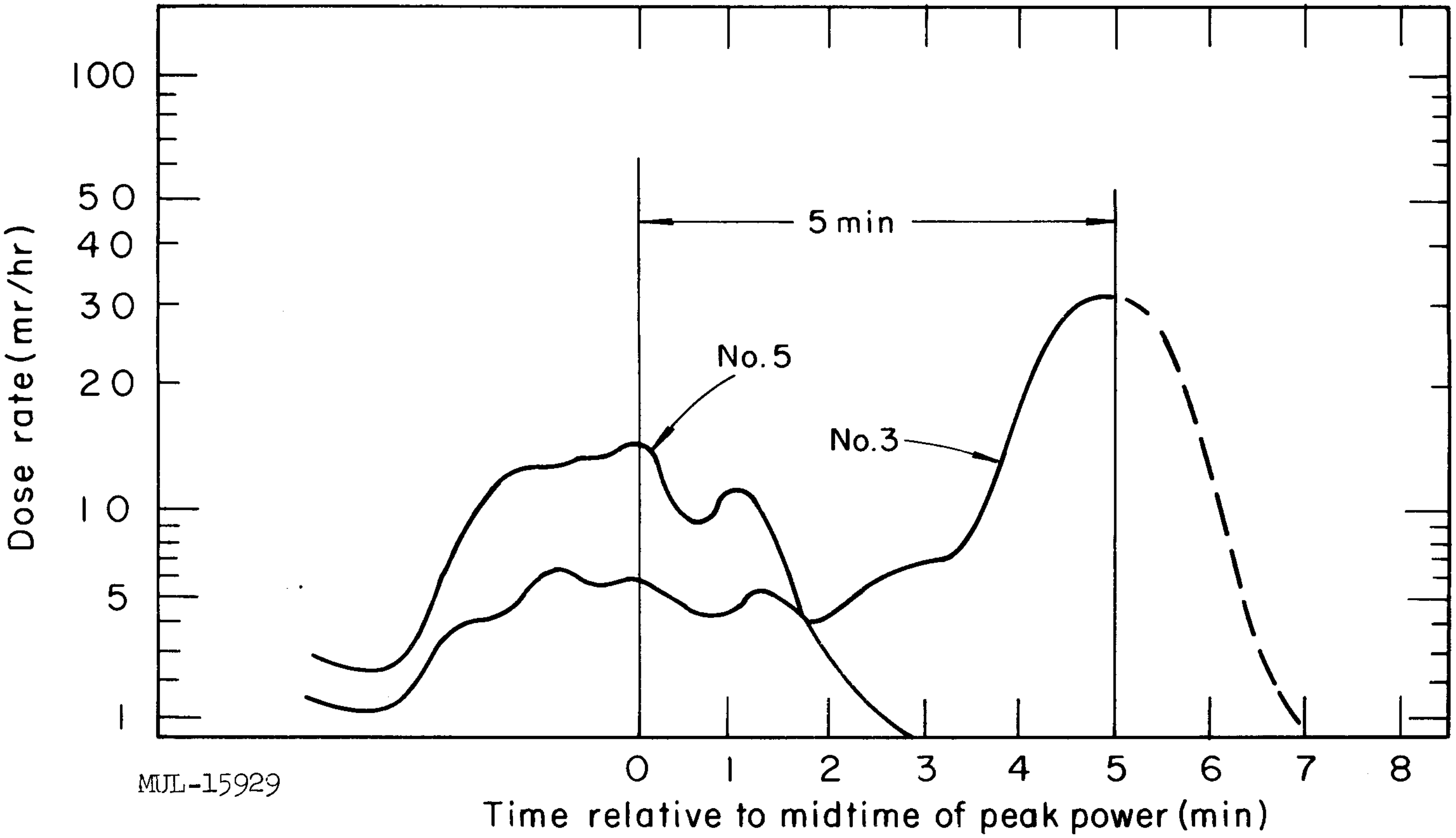

MUL-15929

Fig. I-5. Recorded radiation dose rates at detectors 3 and 5 of perimeter monitor net on May 14, 1961.

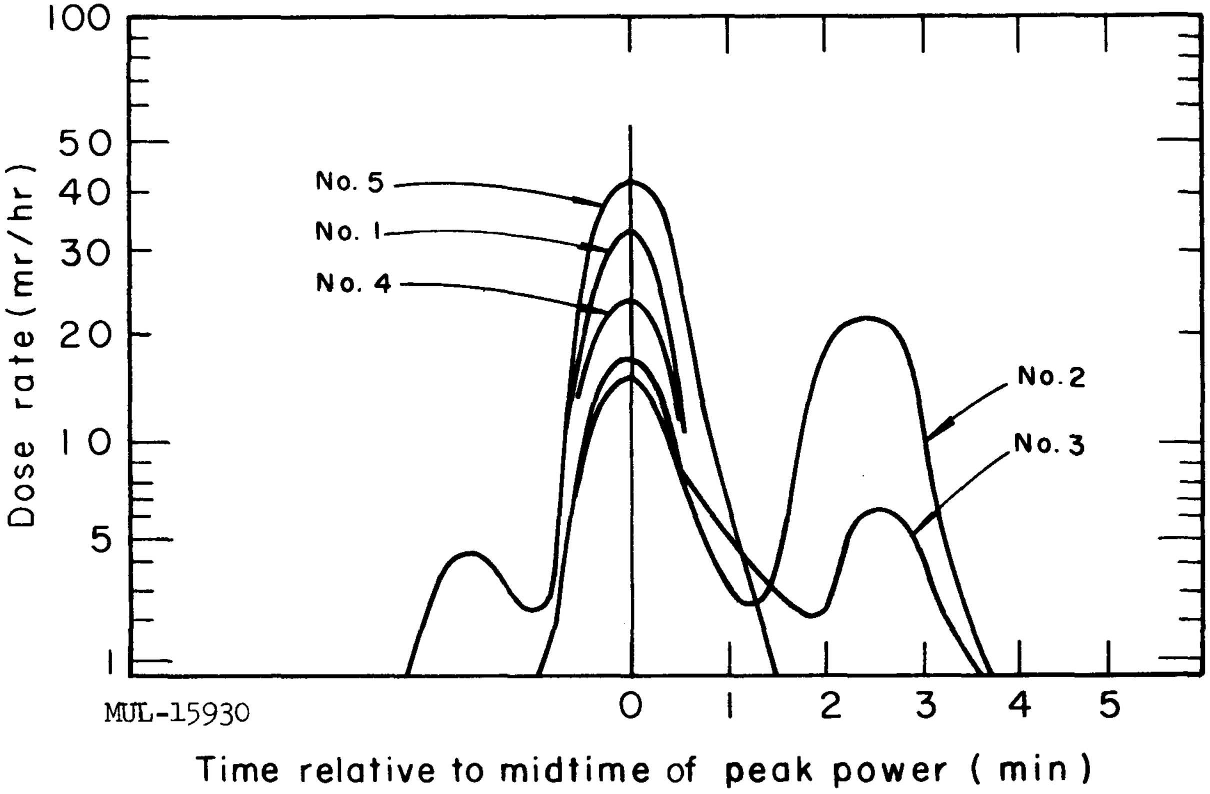

Fig. I-6. Recorded radiation dose rates at detectors 1-5 of perimeter monitor net on Sept. 28, 1961.

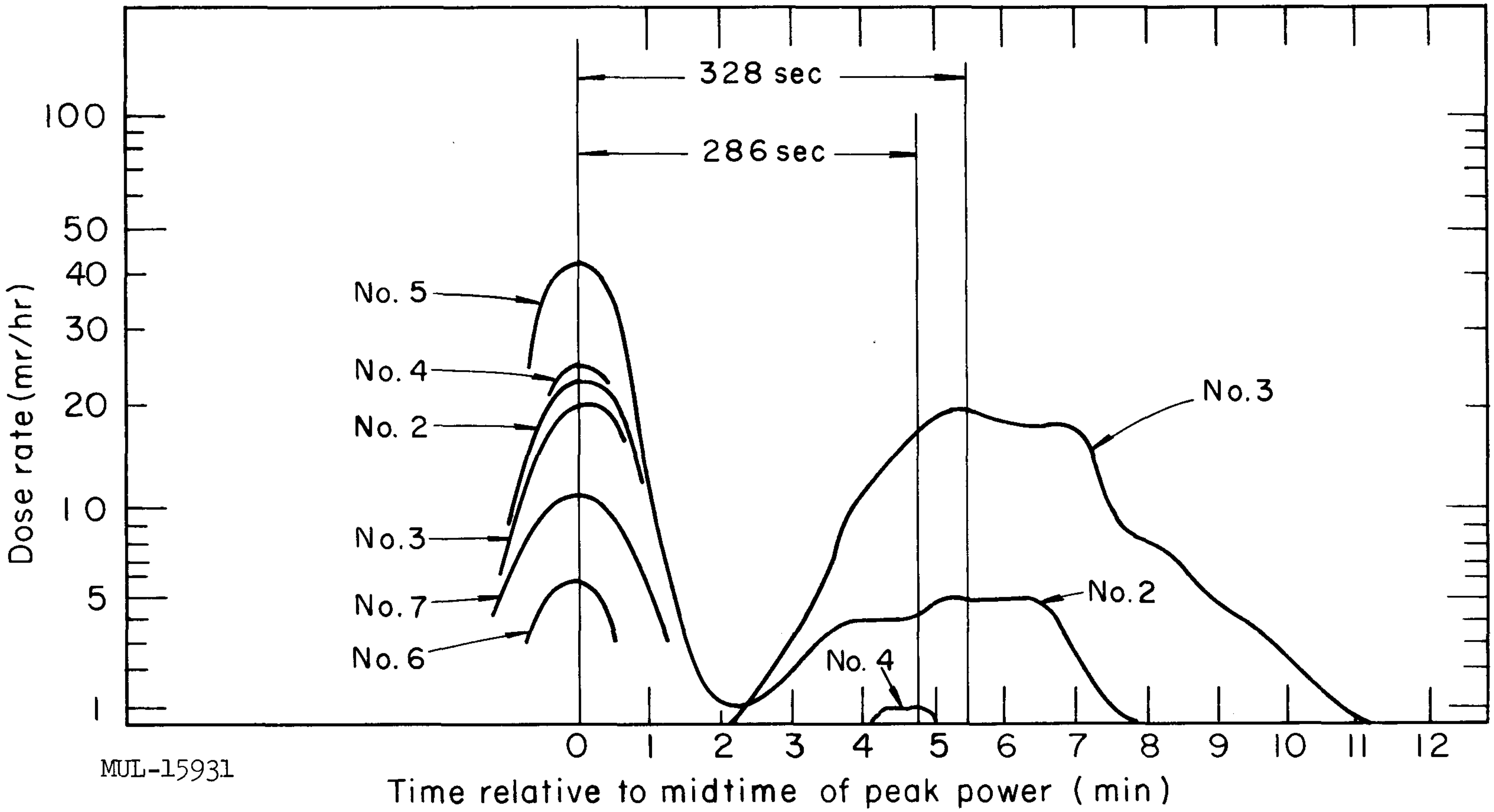

MUL-15931

Fig. I-7. Recorded radiation dose rates at detectors 2-7 of perimeter monitor net on October 5, 1961.

Cloud height. The dose rate at the detector net for the Tory II-A-1 runs depends strongly upon the position of the radioactive cloud. Field information of cloud height and position was very sparse and hence considerable uncertainty still exists. In order to have some estimate of cloud height, Holland's equation (see AECU-3066) for the effective stack height Δh has been utilized:

$$\Delta h = \frac{1.5 v_s d + 3 \times 10^{-4} Q_H}{u} \quad (\mathrm{ft}),$$

where d is the stack orifice diameter in feet, v_s and u are stack and wind velocity respectively in miles per hour, and Q_H is the emission rate in calories per second. While Tory II-A-1 operates outside the range of conditions considered by Holland, we assume that his equation will give reasonable values if the proper approach is used.

While the exit velocity of the effluent is ~5300 ft/sec, it becomes subsonic after traveling about 85 feet. If we assume that the diameter has not changed during this supersonic period, then we can apply Holland's equation at this point (85 ft from exit) to get the additional rise $\approx \frac{1.5 \times 750\ (\mathrm{mi/hr}) \times 2.74\ (\mathrm{ft})}{\bar{u}\ (\mathrm{mi/hr})} = \frac{3080}{\bar{u}}$ (ft) where $\bar{u}$ is the wind component normal to the effluent exit direction. In the runs to date $\bar{u} \approx u$, so one obtains for the rise due to velocity alone (if the effluent were directed vertically upward):

$$\Delta h_{v_s\ \mathrm{vert}} = \frac{3080}{u} + 85\ \mathrm{ft}.$$

Since the Tory II-A-1 exhaust was directed at a 30° angle to the horizontal, only half of this value is realized:

$$(\Delta h)_{v_s} = \frac{1540}{u} + 43\ \mathrm{ft}, \quad \text{and}$$

$$\Delta h = \frac{1540 + 3 \times 10^{-4} Q_H}{u} + 43\ \mathrm{ft}.$$

It is felt that the main objection in applying Holland's equation is the possibility that more turbulent mixing occurs for Tory II-A-1 during its stack velocity rise phase than for the conditions encountered by Holland. If this is true, one would expect the effective stack height calculated from the foregoing equations to be too large, which would lead to an overestimate of the escape fraction. But there is evidence that our calculated effective stack heights are not too large: During the October 5 run (see below), the calculated effective stack height would have been 1915 ft with a 13.4-mi/hr wind. This compares favorably with the 1965-ft effective stack height found for the Kiwi-A reactor under very similar conditions.

Below are listed the calculated effective stack heights for three Tory II-A-1 runs.

Date	u(mi/hr)	Q_H(cal/sec)	Effective stack height (ft)
May 14, 1961	15	1.6×10^7	465
Sept. 28, 1961	26.5	5.34×10^7	705
Oct. 5, 1961	13.7	7.84×10^7	1875

Model. The effluent cloud was considered as a point source in the present analysis. Because the cloud was examined only 1.3 miles downwind, it was felt that transverse diffusion had not spread the cloud by more than 200 meters in radius. As long as this radius is less than an absorption mean free path for gamma rays (~300 m), the point source model is reliable. In the present geometry, the simplified model is felt to contribute much less than a factor-of-two error in the results. Comparison with calculations involving a distributed model tends to confirm this error estimate.

Also, calculations were simplified by determining an "effective energy-absorption mean free path" consistent with the gamma energy spectrum at the time of interest. The attenuation was therefore given in the following form:

$$\frac{e^{-r/\lambda_a}}{r^2} ,$$

where $\lambda \approx 360$ meters ($\rho_{air} = 0.00109$ g/cc).

Test results. For each of the Tory II-A-1 runs, dose rates were simultaneously recorded at two (or more) detector locations during cloud passage. The locus of positions of an equivalent point source is then a curved surface such that a source at any point on it would produce the observed ratio of dose rates at the two detectors. The intersection of this surface with a plane at the assumed point-source height gives the path of the point source. Since the distance between detectors is known, the detector-to-source distances can be calculated. These distances are then used with the point source model to calculate the expected dose rate based upon the calculated fission fragment escape corrected for decay time. For each run these calculations have been made using the effective stack height as the height of source. In some cases the calculations were repeated for source heights which seemed to represent a reasonable upper or lower limit. These results are given in Table I-3.

Table I-3. Comparison of Observed and Calculated Dose Rates.

Date	Source height, h (ft)	D_{obs}/D_{calc} [a]	Comments
May 14	465	0.7	h = effective stack height
	1000	1.8	estimated upper limit on h
Sept. 28	705	1.3	h = effective stack height
	0	1.0	lower limit of h
Oct. 5	1875	2.7	h = effective stack height
	0	0.7	lower limit of h

[a] D_{obs} and D_{calc} are the observed and calculated dose rates, respectively.

The data of the Oct. 6 run were unsatisfactory. The run on Oct. 5 is worthy of comment, for readings were obtained simultaneously on three detectors. At 286 sec after midtime of peak power, No. 4 detector peaked at 1mr/hr, at which time No. 2 read 4 mr/hr and No. 3 read 16 mr/hr. If one triangulates using this information, one obtains a cloud height of 1720 feet. Not much reliance can be placed in this figure for several reasons: a) The three detectors concerned are viewing the cloud from different aspects and the equivalent point source differs for each detector; b) The height is very sensitive to small errors in the distance from No. 4 detector to its equivalent point source in the cloud; c) The reading of No. 4 detector was of very short duration, indicating some unexplained condition at that time such as an exaggerated meandering of the cloud (this is indicated by the fallout pattern); d) The accuracy of the detectors falls off at the lower dose rates. However, from the ratio of dose rates at No. 2 and No. 3 detectors at various times, coupled with a knowledge of wind speed, one can locate the ground position of the cloud within close limits. Since No. 4 detector is a considerable distance away, the distance from it to the cloud is not so sensitive to the cloud height. Using this distance to calculate the expected dose rate at No. 4 detector (based on the expected escape fraction), we then obtain a quite firm upper limit on the ratio of observed to calculated dose rates for a point source. This gives an upper limit of 2.6 for D_{obs}/D_{calc}, the value being as reliable as the reading of the No. 4 detector.

From the May 14 run, another opportunity exists to compare dose rates. At 17 minutes after the run, a portable detector 4.7 miles from the test pad had a reading of 0.8 mr/hr during cloud passage. About 4 minutes later the aerial monitor was in the cloud and estimated the center at 1500 ft. This sounds reasonable in view of the unstable conditions below 1600 ft and the stable layer above 1600 ft which existed at that time. Taking 1500 ft as the cloud height and using the effective mean free path of 330 meters for 17 minutes decay time, the ratio is now $D_{obs}/D_{calc} \approx 0.6$. This tends to confirm the value 0.7 which resulted from a cloud height of 465 feet at 1.3 miles from the test pad.

If there were no uncertainties or errors involved, the ratio of actual to calculated escape fraction would be given by the ratio of observed to calculated dose rate. It is estimated that, for the particular runs considered, the error introduced by our simplified model is probably no more than a factor of two or three. After combining this with the errors due to uncertainty in cloud height, etc., one is led to the conviction that the calculated escape fractions are easily within a factor of 10 of being correct.

If the effluent cloud position were more accurately determined (warranting use of a more accurate model), it is believed that the escape fraction could be verified within a factor of three.

Analysis of the Tory II-A-1 runs is still progressing. Since control vane angle is related, among other things, to the loss of BeO and UO_2, it is theoretically possible to calculate the extent of erosion during the runs. Careful observations reveal no vane motion during the period of high-power operation that could be attributed to loss of reactivity by erosion. Less than 0.1% of the core was lost due to erosion.

SECTION III. INSTRUMENTATION

CORE THERMOCOUPLE MORTALITY

The overall survival of all platinum/platinum-10%-rhodium core thermocouples, from time of start of installation through the final high-power test, was 53%. Table I-4 is a breakdown of failure rates by group according to location within the core.

Considering power operation only, 76% of the thermocouples survived: Out of 115 thermocouples which were operational prior to the intermediate power test, 87 remained. For fuel element thermocouples only, 29 out of 43 (or 64%) survived.

A large number of the thermocouples (49) were lost during installation.

AUTOMATIC DATA REDUCTION

The Tory II-A-1 intermediate power test of May 14, 1961, was the occasion of the first integrated operation of the complete data acquisition system. Generally the system's performance was satisfactory; however, the sheer bulk of run data obtained from that test suggested that automatic data reduction techniques were necessary if a systematic and rapid reduction of data from this and future runs was to be attempted.

In the four-month period between the intermediate power test and the first high-power run an effort was made to evaluate various automatic and semiautomatic techniques. The most promising method was judged to be conversion of our PDM (pulse duration modulation) magnetic tapes to digital form compatible with one of the high-speed Livermore computers.

The data acquisition system is described in detail in other reports (UCRL-5484, UCRL-5906). The ASCOP subsystem lends itself most readily to automatic reduction techniques; also, it records all reactor component temperatures and important duct pressures. ASCOP consists of three 90-channel PDM units. Data signals from temperature and pressure transducers are brought into three multicoders in the test bunker. Each unit mechanically commutates 86 data channels, amplifies and converts signal amplitude to pulse width, and transmits this train of pulses over 11,000 feet of coaxial cable to the control point. The commutator samples each of 90 input signals at a rate of 10 times per second. The 90 channels constitute a frame of data so that 10 frames are transmitted per second from each of the 3 units to the control point.

Table I-4. Tory II-A-1 Thermocouple Performance Record

Thermocouple location (x/L)	Original number	OK before IPT 5/14	Failed in IPT 5/14	Failed in HP-1 9/28	Failed in HP-2 10/5	Failed in HP-3 10/6	OK after HP-3 10/6
Fuel at 0.175 (0.239)[a]	10	8	0	1	0	1	6
" 0.300 (0.354)	2	1	0	0	0	0	1
" 0.540 (0.576)	2	0	-	-	-	-	0
" 0.700 (0.723)	42	29	3	4	3	1	18
" 0.910 (0.916)	6	5	0	1	0	0	4
Total fuel	62	43	3	6	3	2	29
Dummy tubes	2	1	0	0	0	0	1
Outer links @ 0.175	2	2	0	0	0	0	2
" " 0.700	14	12	0	0	2	2	8
" " 0.910	8	8	2	0	0	1	5
Total links	24	22	2	0	2	3	15
Slats @ 0.175	4	1	0	0	0	0	1
" 0.700	18	6	0	0	0	1	5
" 0.910	6	1	0	0	0	0	1
Total slats	28	8	0	0	0	1	7
Tie rods @ 0.700	6	6	0	0	1	0	5
" " 0.910	6	5	0	0	0	0	5
Total rods	12	11	0	0	1	0	10
Wiper seals @ 0.700	4	4	0	0	0	1	3
" " 0.910	4	4	0	0	0	0	4
Total seals	8	8	0	0	0	1	7

Shroud @ 0.700	4	4	1	0	0	0	3
" 0.910	4	3	0	0	0	0	3
Total shroud	8	7	1	0	0	0	6
Front support struct.	8	5	0	0	0	0	5
Base plate	4	4	2	0	0	0	2
Base plate springs	4	2	0	0	0	0	2
Total in core	160	111	8	6	6	7	84
PT-4 rake	4	4	1	0	0	0	3

IPT: intermediate power test, 5/14/61

HP-1: high-power test 1, 9/28/61

HP-2: " " " 2, 10/5/61

HP-3: " " " 3, 10/6/61

[a] Number in parenthesis refers to x/L for lengthened core; x = axial distance from forward face of forward reflector; L = distance from x = 0 station to aft face of aft reflector.

At the control room the PDM data is permanently recorded via a 14-track magnetic tape recorder. Three of the tracks are utilized to record PDM data from the ASCOP units.

After some investigation it was found that the Air Force Flight Test Center (AFFTC) at Edwards AFB had developed equipment to perform PDM-to-digital conversion in a manner precisely suited to our purpose. A code was written for the IBM 7090 computer to handle the digital tapes produced at AFFTC, and by the time the high power tests were under way, all of the PDM data from the May 14 run had been reduced.

The flow chart for the reduction process is shown in Fig. I-8. Briefly the process consists of the following five steps:

1) PDM data recorded during run on magnetic tape.

2) Pulse-duration converted to binary bits on IBM-compatible magnetic tape at AFFTC.

3) Digital tapes edited and one data sample per second selected.

4) Edited data sorted out by track.

5) Data bits converted to temperature and pressure by means of thermocouple and pressure tables in the code.

The end product of this process is a computer-produced tabulation of temperature versus time and a CRT (cathode-ray-tube) plot for each data channel. Within a week of the final high power test (Oct. 6) all of the PDM data from the three runs was converted to digital form. Approximately a month was required to completely reduce all the data in this manner. A typical temperature trace from a fuel element thermocouple is shown in Fig. I-9.

CORE THERMOCOUPLE AVERAGING SYSTEM

The control philosophy which finally evolved for the Tory II-A-1 reactor consisted of having the air flow operator bring the air flow rate up to a preset level with the nuclear operator adjusting power level to hold a desired core temperature during the flow-rate plateau. For the intermediate power test of May 14, 1961, the signals from six selected core thermocouples were displayed on individual meters before the nuclear operator. These meters each had a range of 32-2650°F on a face about 4 inches long. One signal was also displayed on a strip chart recorder.

It was found that the operator gave most of his attention to one meter, thus relying rather heavily on a single thermocouple signal for control.

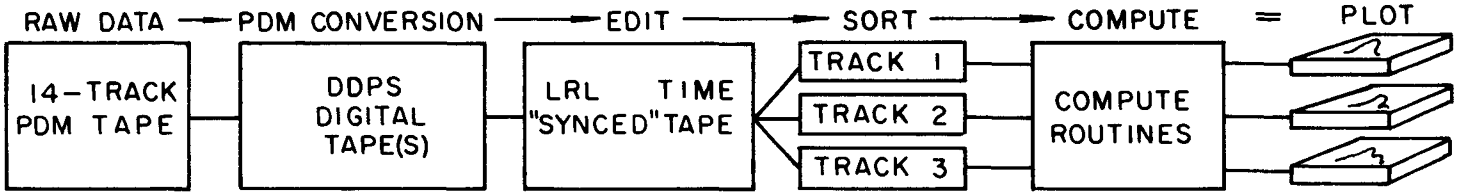

MUL-15932

Fig. I-8(a). Tory II-A-1 PDM-to-digital data reduction process.

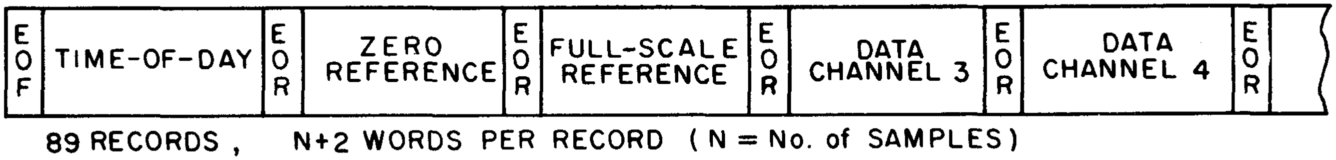

MUL-15933

Fig. I-8(b). LRL working data tape format.

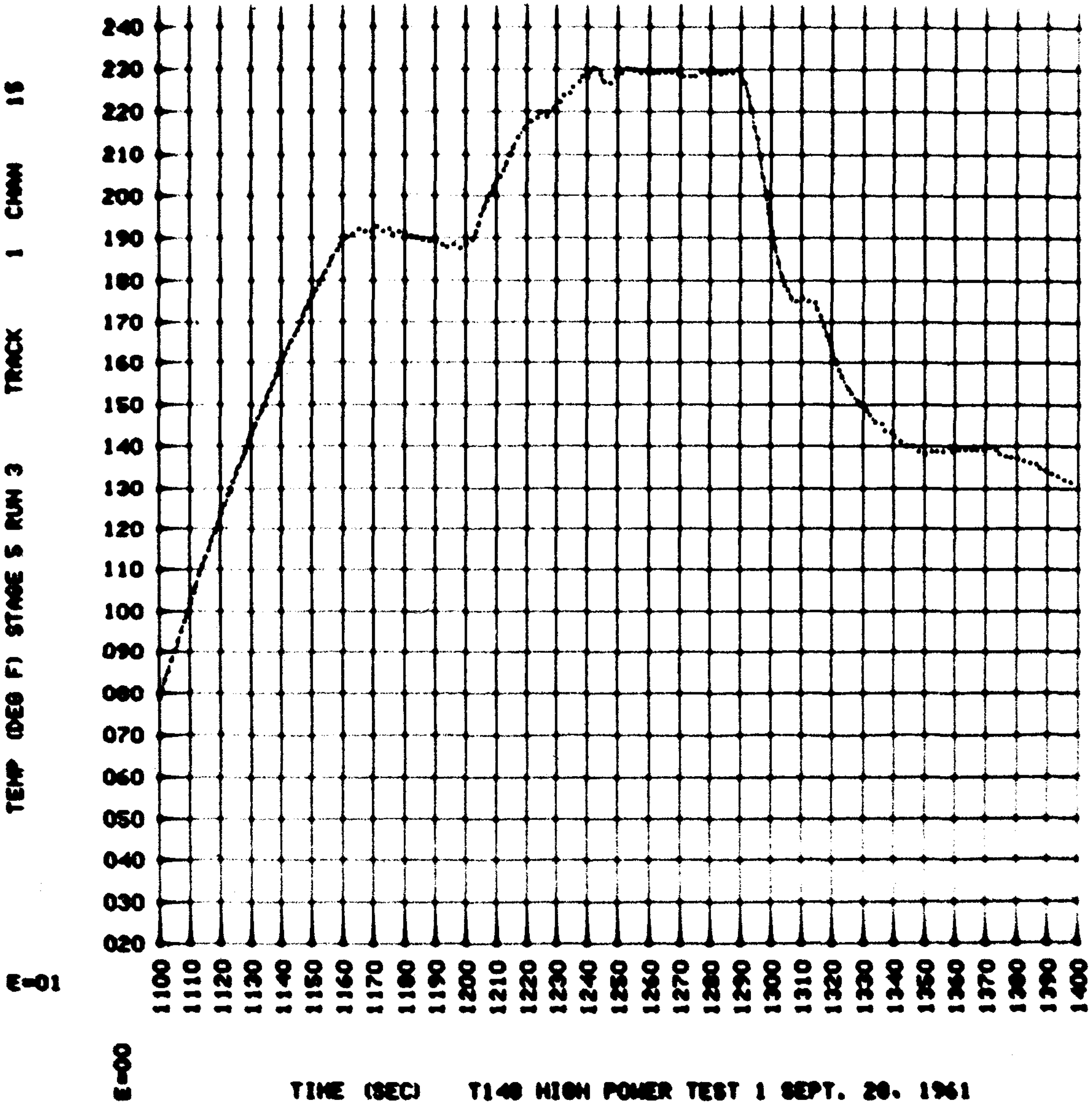

MUL-15474

Fig. I-9. Typical temperature trace from a fuel element thermocouple in high-power test 1.

This situation showed the need for a system that would compute the average of the outputs of six core thermocouples and display it on a recorder. Also desirable was the capability of switching questionable signals out of the network.

Such a system was built and operated successfully during the three high-power reactor tests. The important features of the system are shown in the block diagram in Fig. I-10. The three ASCOP pulse-width modulation systems served as input-signal-conditioning networks, converting thermocouple signals to high level signals capable of driving the electronic averaging amplifier. The outputs of 30 translators (10 from each system) were sent to patch panels on ASCOP systems 1 and 3. The signals selected for averaging were sent first to their appropriate translators and from there to the patch panels.

From the patch panel on system 1, 10 selected signals went to the translator meters on system 1 and the meters on the nuclear operator's console. From the patch panel on system 3, six selected signals went to the averaging amplifier which averaged its inputs and conditioned the resulting voltage to a level capable of driving the 10-in. [Brown] strip chart recorder. Questionable signals could be switched out at the translator meters by an ASCOP observer during a run. The meters on the nuclear operator's console were retained as a backup in the event of a recorder failure. In addition to the six core temperatures, two exit gas temperatures were also displayed on the meters as a further backup in case of complete failure of all core thermocouples.

The average temperatures recorded during high-power tests 1, 2, and 3 are shown in Figs. I-11, I-12, and I-13. During the last two runs, three of the six thermocouples in the averaging network failed and had to be switched out. The trace, however, maintained a reasonable level throughout these maneuvers. The following table compares the temperatures recorded by the averaging system with the average of the individual component temperatures obtained by digital data reduction methods. The temperatures are taken over a 5-second interval on the high-power plateau of each run.

Source	H.P. Test 1	H.P Test 2	H.P. Test 3
Averaging network	2290°F	2310°F	2505°F
Digital reduction	2305°F	2306°F	2490°F

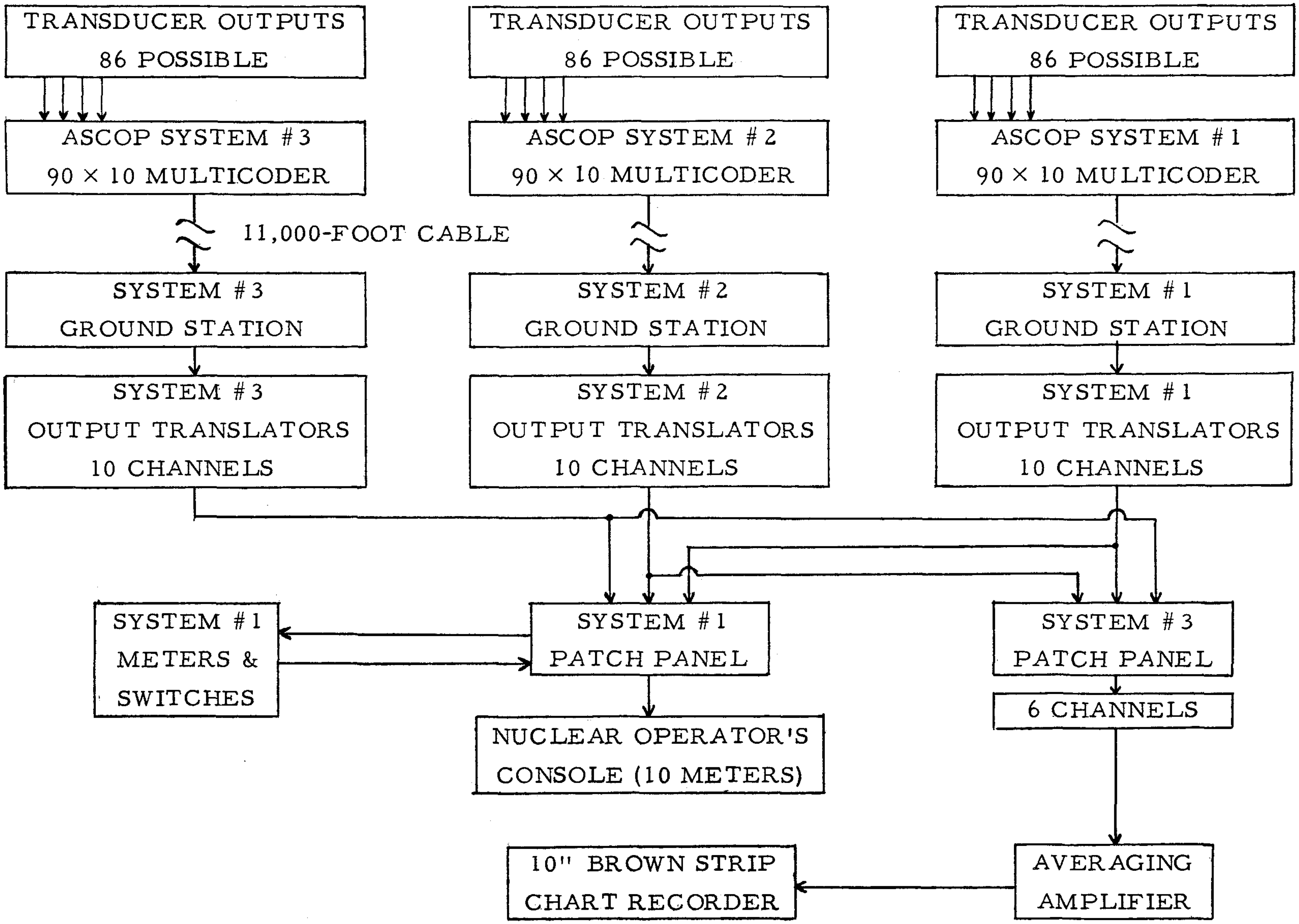

Fig. I-10. Tory II-A-1 temperature averaging system.

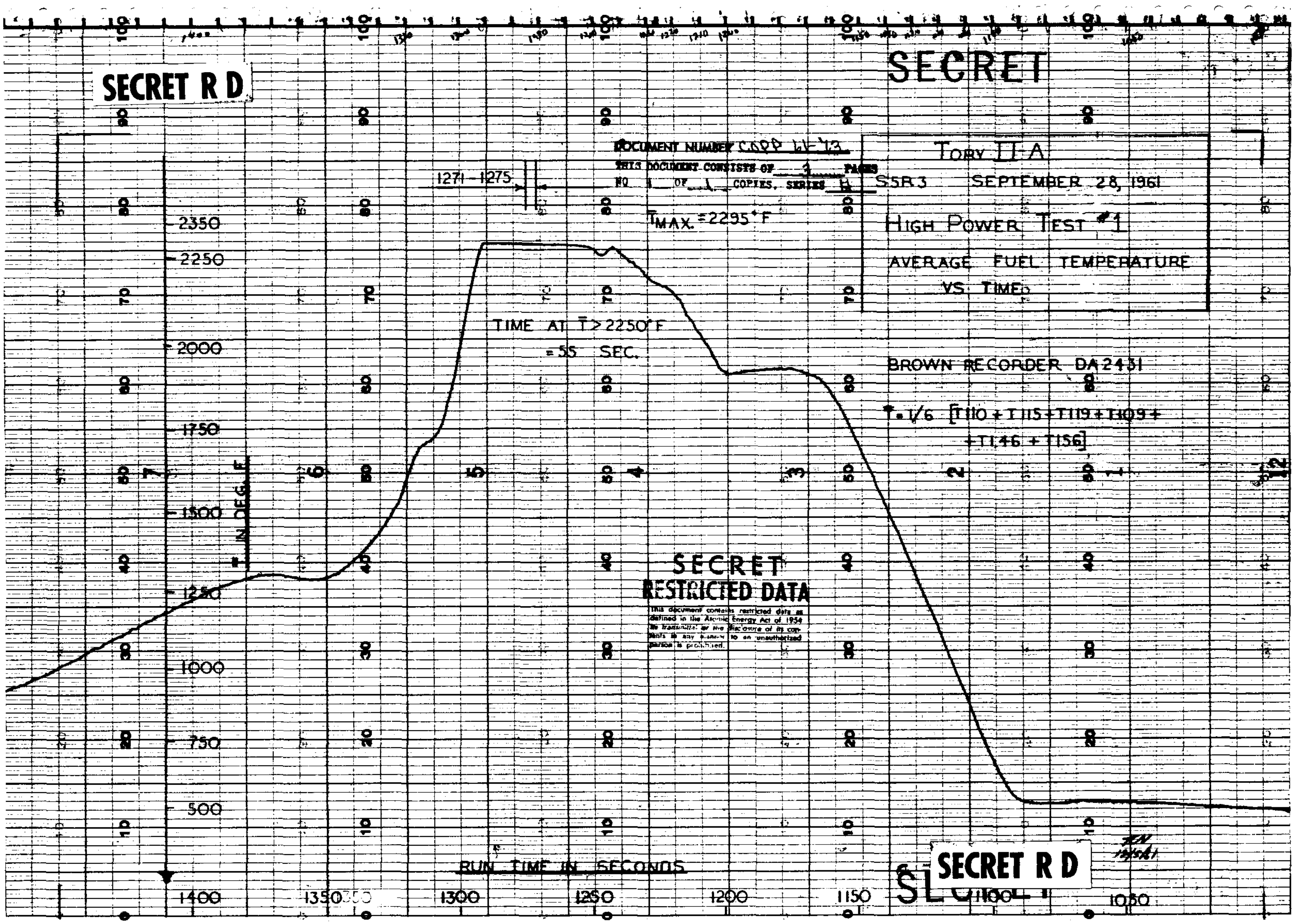

MUL-15365

Fig. I-11. Average fuel temperature during high-power test 1.

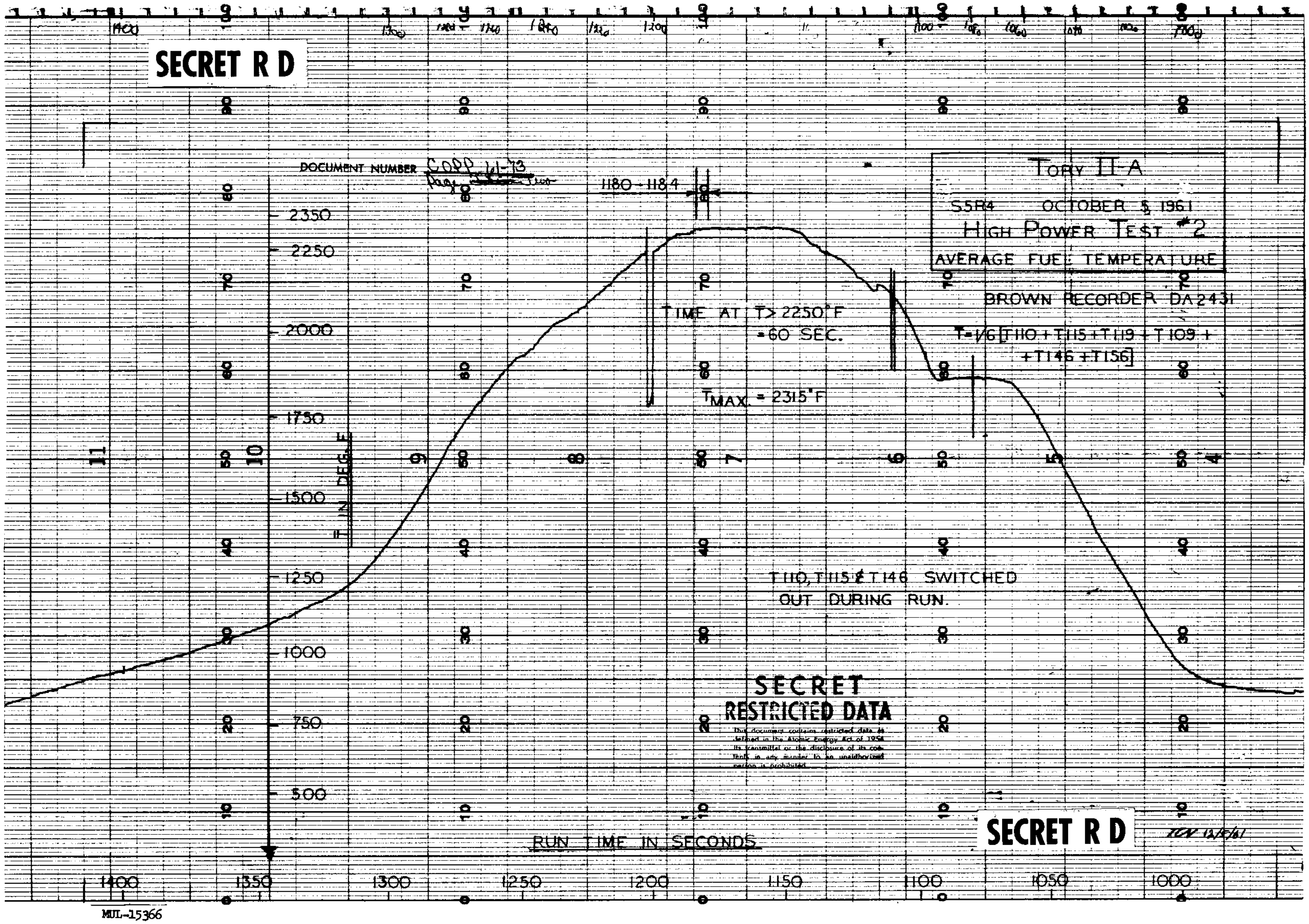

Fig. I-12. Average fuel temperature during high-power test 2.

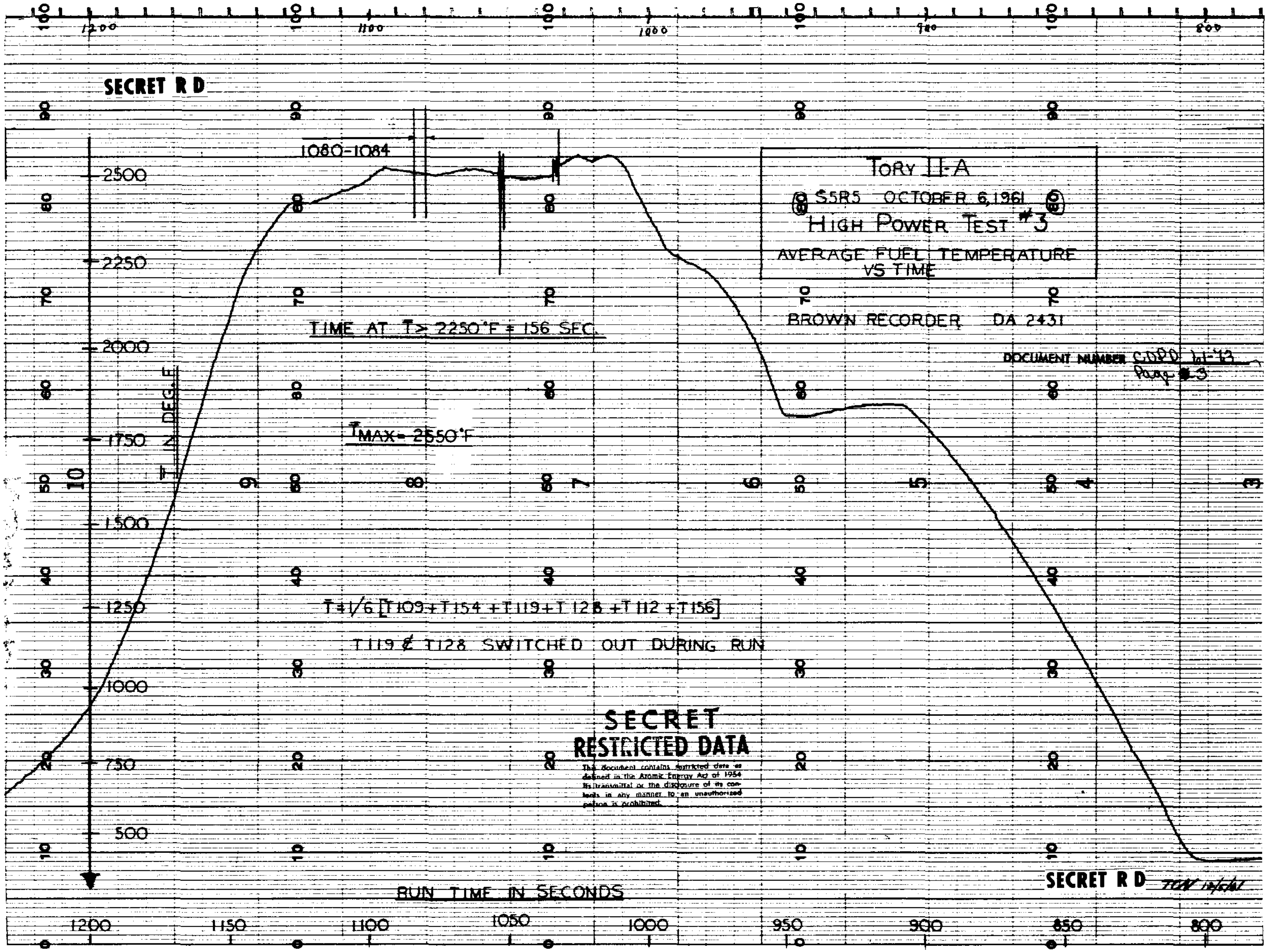

DOCUMENT NUMBER CDPD 61-43
Page #3

SECRET
RESTRICTED DATA
This document contains restricted data as defined in the Atomic Energy Act of 1954. Its transmittal or the disclosure of its contents in any manner to an unauthorized person is prohibited.

MUL-15367
Rev. 12/16/61

Fig. I-13. Average fuel temperature during high-power test 3.

SECTION IV. CONTROLS

Summary

Since the last report, all full-power runs have been successfully accomplished at the Nevada Test Site. All Tory II-A-1 control systems operated completely satisfactorily during the full-power runs on Sept. 28 and Oct. 5 and 6. Following completion of the test series, the control systems were disassembled and will be returned to Livermore for inspection of the components.

Test Results

The control system aspects of the high-power tests are next briefly described.

High-power test No. 1 (Sept. 28). During this test, the reactor power level was brought to 100 kw under manual control. Here the nuclear control system was switched to the automatic log-power mode in order to program power level to its full design value. Following a short period at full power, the nuclear control system was switched to the manual mode for reactor shutdown. All transfers were made without any measureable perturbation of the reactor power or period, and operation was precisely as planned. The air flow rate to the reactor was controlled using AV-4 (small flow control valve) in the manual servo mode. The air flow operator maintained the desired flow rate by visual means using the P_{to} measurement at the choked upstream venturi. During this run both level and period fast-reset channels were bypassed. Reactor temperature control was accomplished by the nuclear operator, who observed selected thermocouple readings and programmed power demand accordingly.

High-power test No. 2 (Oct. 5). During this run the nuclear control system was used exactly as in the Sept. 28 run. The period fast-reset system was used with the variable set point at approximately 2 seconds. The level fast-reset system was again bypassed because of the uncertainty of the detector output signal at full power. Actually, the three log-power detectors read slightly different values throughout most of the high-power region, making it difficult to fix the level set points. The air flow rate to the reactor was controlled using AV-3 (large flow control valve). The manual control mode was used below 50 lb/sec, the automatic control mode above. Programming to full flow was done using the preprogrammed vernistat for flow rate demand variations. All systems performed satisfactorily throughout the run. Again, the nuclear operator controlled the core temperature.

High-power test No. 3 (Oct. 6). This run was identical to the Sept. 28 run as regards nuclear and air-supply control. The period fast-reset system was again used with the variable set point at 2 seconds. Again, all control systems worked as planned.

It is notable that during the entire test series in Nevada (prenuclear and nuclear) there were no control system malfunctions or deviations during actual test operations. The testing period for the control system encompassed approximately 650 hours of "on" time for the hydraulic control systems and over 2000 hours of "on" time for the system electronics. This good record is attributable to several factors:

1) Complete detailed component and systems checkout at Livermore. Considerable redesign was done during this phase with many components (such as potentiometers and servo valves) replaced by superior versions. A series of significant tests were conducted and recorded to serve as a control for future system testing in Nevada.

2) Continuous maintenance and upgrading at the test site. Those components or subsystems which gave trouble (such as the servo amplifiers) were replaced with improved versions built by LRL.

3) Sufficient debugging time in the field. The control systems reached NTS during the summer of 1960, which allowed a number of weeks and months for integration, checkout, and upgrading.

CHAPTER II. MATERIALS DEVELOPMENT AND PILOT PLANT ACTIVITIES

SECTION I. PROCESS AND MATERIALS DEVELOPMENT

MATERIAL STUDIES

Basic Studies

1. Growth of BeO single crystals. Beryllium oxide single crystals are being grown for a variety of high-temperature physical and chemical property measurements. Crystals having a tabular habit were successfully grown for the first time. Measurements were made of the hardness and optical properties of these crystals as well as crystals having an acicular habit.

Crystals exhibiting a tabular habit were successfully grown from a lithium polymolybdate($Li_2Mo_2O_7$) flux by deposition on polycrystalline disks of BeO in a temperature gradient at 1300°C. The crystals were hexagonal platelets 4 mm across the flats and 1 mm in thickness. The crystals are bounded by $(10\bar{1}0)$ faces, capped by $(10\bar{1}1)$ faces, and have the (0001) face in the plane of the plate.

2. BeO-water phase equilibria. Phase equilibrium relations in the beryllium oxide-water system are being studied to provide basic information necessary for the successful growth of BeO crystals by hydrothermal synthesis. The approximate location of the univariant pressure-temperature curve along which beryllium hydroxide and beryllium oxide and water coexist was determined using static hydrothermal methods and quenching techniques.

The curve is reasonably close to a straight line with positive slope and passes through points at 225°C and 60,000 psi, 220°C and 30,000 psi, 215°C and 16,000 psi, and 195°C and 5500 psi.

The data demonstrate that during the hydrothermal synthesis of BeO crystals (400°C and 30,000 psi) BeO will be the stable phase, and they suggest that if the required supersaturation conditions can be achieved, growth of BeO crystals should occur.

3. Optical properties of BeO. The first peak of the ultraviolet absorption spectrum lies at a wavelength of 800 ± 50Å or an energy of 15.5 ev (band gap calculated = 14.32 ev). This value, previously undetermined, is the largest optical band gap measured for any oxide material. It suggests that the bonding in BeO has a very high degree of ionic character, possibly greater than the

calculated value of 64% based on the difference in electronegativity of the ions. The ionic character of the bonding is reflected in the material's high melting point, hardness, and ionic electrical conductivity.

The crystals were transparent in the range 50,000 cm^{-1} (0.19 micron) to 5000 cm^{-1} (2.0 microns).

The infrared spectra for crystals having a tabular habit show absorption peaks at 2060 cm^{-1} (4.8 microns), 1560 cm^{-1} (6.4 microns), and 1380 cm^{-1} (7.3 microns). Crystals having an acicular habit show absorption peaks at 2030 cm^{-1} (4.9 microns), a broad peak in the range 1300 to 1500 cm^{-1} (7.7 to 6.7 microns), a peak at 680 cm^{-1} (14.7 microns), and increasing transparency from 667 cm^{-1} (15 microns) to 200 cm^{-1} (50 microns). No specific assignment of vibrational modes to the absorption peaks has been made although the 1380-cm^{-1} (7.3-micron) peak corresponds to an energy value that one would calculate for a combination mode in BeO.

4. Hardness of BeO. Table II-1 gives hardness values measured for BeO; they correspond to a hardness of 8 (topaz) on Mohs' scale, in contrast to the reported literature value of 9 for BeO.

The dependence of hardness upon crystallographic direction on the 100 plane is expected, since BeO exhibits cleavage parallel to the c axis. However, the observed equality in hardness on the basal plane remains unexplained.

Table II-1. Hardness of BeO Obtained Using Leitz Durimet Tester with Knoop Diamond and 100-g Load.

	HK_{100} (kg/min^2)
Single Crystal	
Basal Plane	
Across corners	1300
Across flats	1300
100 Plane	
Parallel to c axis	860
Normal to c axis	1161
Polycrystalline	
Parallel to c axis	Not determined
Normal to c axis	1145

5. BeO inversion. High-temperature x-ray patterns of BeO above 2050°C have been obtained using rhenium heaters in the x-ray furnace. The patterns verify the existence of a high-temperature polymorph previously suggested by optical observations as well as by decrepitation of fabricated BeO bodies heated above 2050°C. Figure II-1 shows a portion of the x-ray patterns obtained both above and below the 2050°C transformation temperature from a platelet with the c axis normal to the sample plane. Of particular interest are the disappearance of the hexagonal 002 reflection and the increase in intensity of the cubic 200 reflection when the sample is heated above 2050°C, and the reversibility of these relations on cooling. The other significant differences at the transformation temperature are the disappearance of the hexagonal 102 and the appearance of the cubic 110 and 220.

Table II-2 lists a composite x-ray pattern obtained from 12 samples. Because of the preferred orientation present in the samples, no one pattern showed all the reflections. It is also possible that other peaks have been missed for the same reason. All samples used for the composite were heated on rhenium, and the rhenium lines are included in the table because of possible overlap. The pattern can be indexed, using a cubic cell with $a_0 = 4.76$ Å where lattice is primitive. The only systematic absence which appears substantiated is $\underline{h}00$ when $\underline{h} = 2\underline{n} + 1$, although $\underline{hhh}$ when $\underline{h} = 2\underline{n} + 1$ may also be extinct. Intensity values may not be real because of the strong preferred orientation of most of the starting materials. If the above extinction is considered valid, the only possible space groups are $\underline{P}2_13$, $\underline{P}4_232$, and $\underline{Pm}3\underline{n}$.

Single crystals of several sources have been heated above 2050°C and cooled. Examples of the observations under a polarizing microscope are shown in Figs. II-2, 3, and 4. All the crystals heated above the inversion temperature showed a domain structure on cooling. Many domains were present in a given crystal in which the c axis was no longer parallel to the original c direction in the starting crystal. Universal stage measurements were made on several crystals to determine if any pattern of resultant c-axis directions was present, but the results were negative. Although the crystals rarely fragmented, practically all showed marked fracturing. Fractures commonly conformed to the domain boundaries where the c axis were highly inclined to each other. Figure II-2 shows the domain structure resulting after one heat treatment.

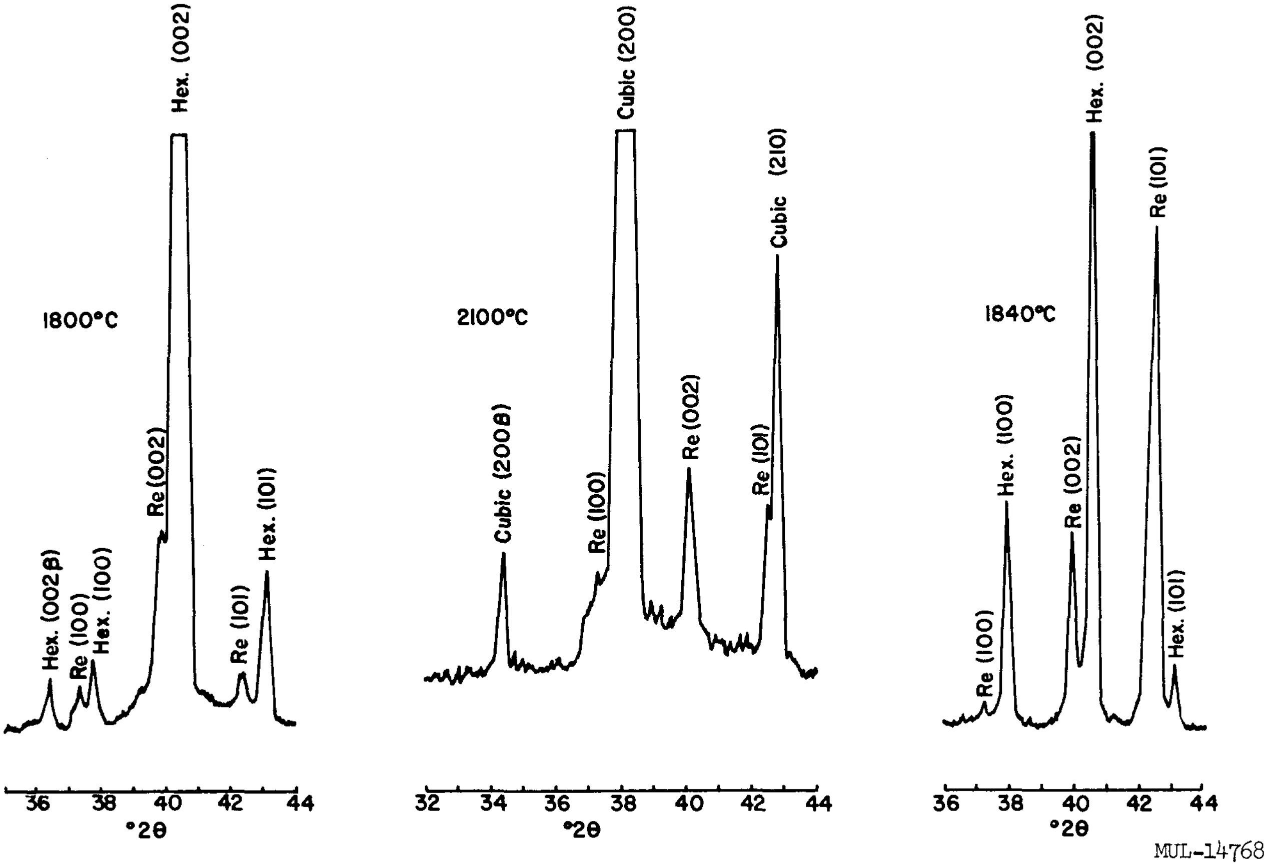

Fig. II-1. A portion of the high-temperature x-ray pattern of BeO. The first pattern was obtained before the sample was heated above the critical temperature, the second obtained above the critical temperature, and the third obtained after cooling from 2100°C. The peaks labeled hexagonal are due to the low-temperature form of BeO. The peaks labeled cubic are from the high-temperature form.

Table II-2. High-Temperature X-Ray Pattern of BeO Obtained in Nitrogen Atmospheres Using Rhenium Heaters.

					Cubic[a]			Rhenium[b]	
2θ(°)	I	d(Å)	Sin^2 θ	Sin^2 θ	hkℓ	d(Å)	Sin^2 θ	hkℓ	d(Å)
26.60	w	3.348	0.0529	0.0526	110	3.358			
34.48	w	2.606	.0874	.0859	200β				
37.10	w	2.421	.1012				0.1006	100	2.416
37.80	s+	2.375	.1049	.1052	200	2.374			
40.00	m	2.252	.1170				.1170	002	2.252
42.50	m	2.125	.1314	.1315	210	2.124			
42.85	m	2.063	.1335				.1308	101	2.130
54.60	w+	1.679	.2104	.2104	220	1.679			
55.75	w	1.647	.2186				.2184	102	1.648
61.50	w	1.529	.2614	.2630	310	1.502			
66.85	w	1.417	.3033				.3040	110	1.397
68.10	m	1.376	.3135	.3156	222	1.371			
71.60	w	1.317	.3422	.3419	320	1.314			
73.80	m	1.283	.3605				.3639	103	1.277
80.85	w	1.187	.4204	.4208	400	1.187	.4211	112	1.187
82.10	w	1.173	.4213				.4349	201	1.168
84.00	w	1.151	.4477	.4471	410,322	1.152			
85.80	w	1.132	.4634				0.4662	004	1.128
87.10	w	1.118	0.4747	0.4734	411,330	1.119			

[a] Cubic cell based on a_0 = 4.756 Å.

[b] Cell based on a_0 = 2.760 Å, c_0 = 4.458 Å, $\alpha = 6 \times 10^{-6}/°C$, calculated for T = 2050°C assuming expansion isotropic.

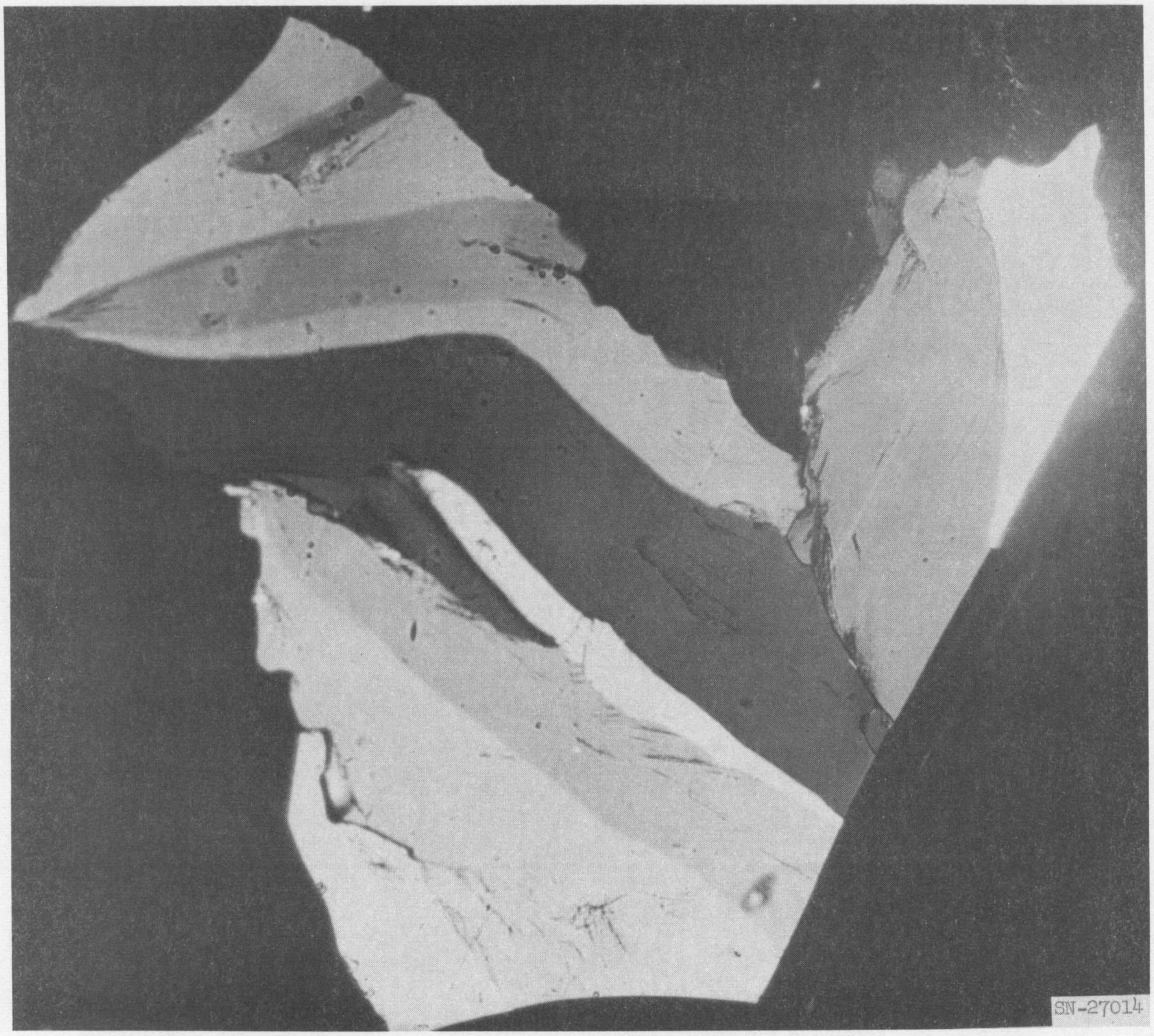

Fig. II-2. Photomicrograph of a BeO single crystal after heating to 2100 °C. The original c axis was parallel to the straight edge of the crystal. The new c axis of the domain at extinction is parallel to one edge of the photograph. Polarized light, 152×.

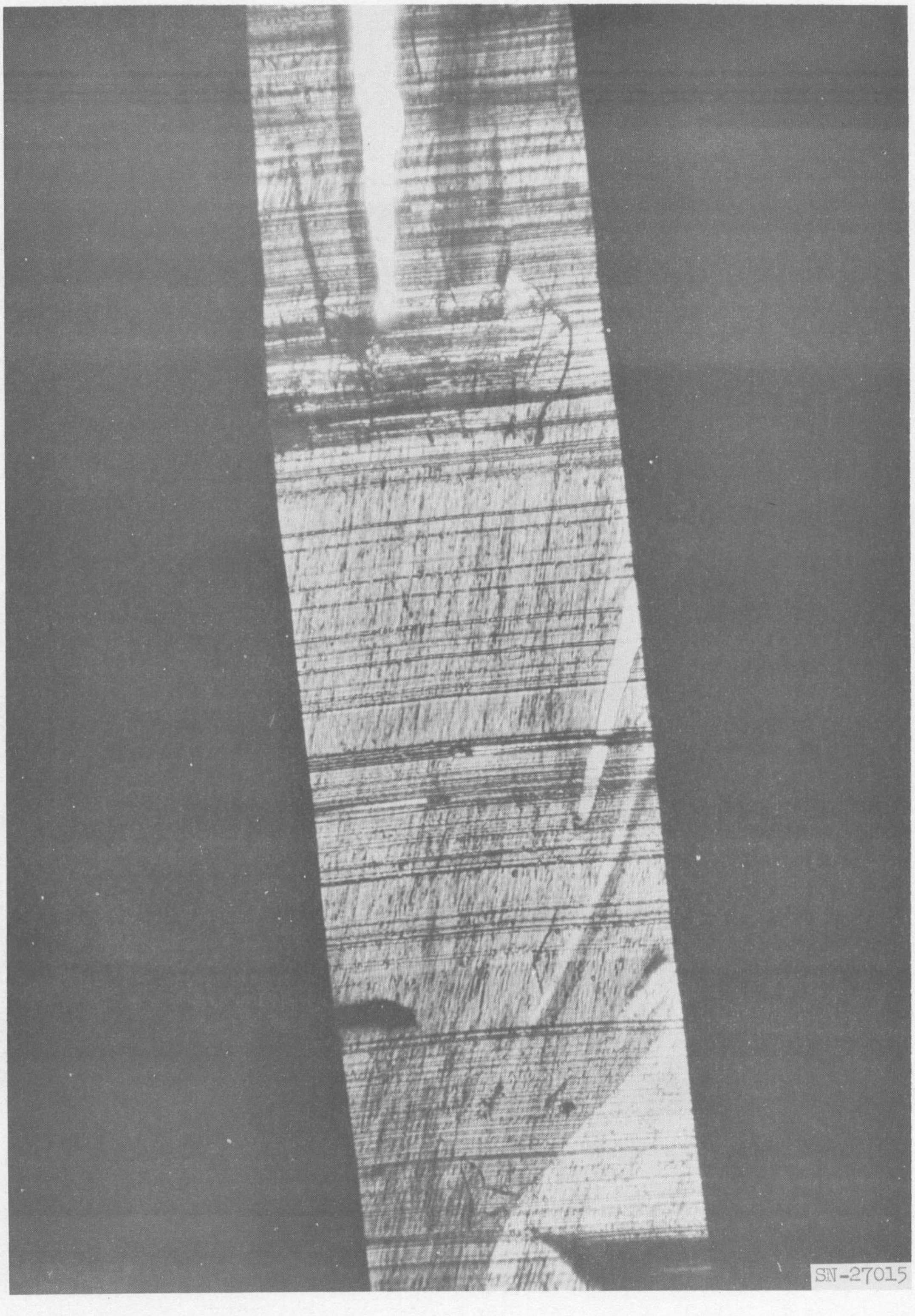

Fig. II-3. Photomicrograph of a BeO single crystal after heating to 2100 °C. The original c axis was parallel to the elongation of the crystal. The coarse striae are normal to the original c axis. The fine striae are normal to the new c axis. Polarized light, 50 ×.

Fig. II-4. Photomicrograph of a portion of the crystal in Fig. II-3 showing both sets of striae. Polarized light, 152×.

Also observed on crystals obtained from vapor deposition are sets of very fine striae. These striae seem to be normal to the c axis. Figures II-3 and II-4 show one set of striae over most of the crystal face which are perpendicular to the original c axis. A second superimposed set is normal to the new c-axis direction of the domain with which the striae are associated.

Rhenium has been investigated up to 2300°C by LaPlaca at Brookhaven National Laboratory. No anomalies were found which would cause additional peaks to appear in patterns in this study. Thus, all the newly observed reflections are due to the high-temperature BeO polymorph.

Thermal cycling of the samples through the critical temperature more than once usually resulted in a disintegrated sample. The phase transition is rapid as evidenced by the completeness of the change indicated in the x-ray patterns taken after short time intervals. Single crystals used in the optical study were usually kept at temperature less than 1 minute, and their appearance also indicated complete transition. In addition, the high-temperature phase appears unquenchable.

The existence of a high-temperature polymorph explains the spalling and decrepitation observed in ceramic bodies treated above 2050°C. It also explains the development of the domain structures during the treatment of single crystals. There is no evidence that single crystals behave any differently than crystals in a polycrystalline body, as was reported by Austerman [S. Austerman, Atomics International USA Report NAA-SR-6428 (1961)]. No special transformation mechanism is necessary, therefore, to explain the observations.

Figure II-1 indicates that the cycling through the transformation tends to randomize the orientation. This tendency toward randomization is also observed in the single crystals as indicated by the universal stage measurements. The fact that the crystals commonly remain in one piece, even though internally fractured, suggests that the crystal structure of the high-temperature form retains similarities to the low-temperature structure. The relatively large size of the domains also indicates a similarity in the crystal structures. This idea is also supported by the striae shown in Figs. II-3 and II-4 which suggest that gliding occurs during the transformation both on heating and cooling.

Assuming the extinction of $\underline{h}00$ when $\underline{h} = 2\underline{n} + 1$ is valid, the possible space groups are $\underline{P}2_13$, $\underline{P}4_232$, and $\underline{Pm}3\underline{n}$. These space groups have 12-, 8-, 6-, and 4-fold special positions. Assuming the structure is cubic the calculated specific gravities for 12, 8, 6, and 4 molecules of BeO per unit cell give 4.63, 3.09, 2.32, and 1.59 respectively. Using the thermal expansion values of Taylor, the specific gravity of hexagonal BeO at 2000°C is 2.80. By comparison the 2.32 value for six molecules seems the most logical although 3.09 for eight molecules is not impossible.

The only structure allowed by the six-fold positions, which are identical in $\underline{P}4_232$ and $\underline{Pm}3\underline{n}$, results in oxygen-oxygen distances of 2.38 Å which are unacceptably close. This structure corresponds to Wells' 4 connected net [A. F. Wells, Acta. Cryst. 7, 545 (1954) (see Fig. 18)]. The interesting feature of this structure is that it leads to a Be-O distance of 1.68 Å, which is reasonable, and the bonds are parallel to the face diagonals of the unit cube (note the spacing at 220).

Evidently the high-temperature structure is not simple. The lack of good intensity data and the limited amount of any data do not allow the structure to be determined readily.

6. Sintering of BeO. In a previous report it was noted that, for several sintering runs, a plot of log $\Delta L/L_0$ versus log time could be resolved into two straight lines with different slopes. The initial slope was close to the predicted 2/5 for volume diffusion, while the second slope was 1/4.

A careful check of the physical system indicated that creep in the platinum sample holder could be the only possible defect that would cause such a divergence. To eliminate this possibility an alumina holder was installed in place of the platinum one.

Runs were made at three different temperatures in a helium atmosphere. At 994°C a log-log plot was not linear. The 1120 and 1180°C runs again showed the distinct change in slope.

All samples were held at a presintering temperature of approximately 800°C and then moved to the sintering temperature. A thermocouple directly under the sample indicated that they reached the sintering temperature only after 10-11 minutes. The change in slope on the log-log plots also came at that time. Further consideration will be given to the time necessary for the sample to reach temperature equilibrium.

The isothermal runs were reproducible in values of the two slopes, but the intercepts were displaced. Although all samples were supposedly pressed at 20,000 psi, a slight difference in the pressing pressure may have occurred and contributed to this discrepancy.

Attention will be given to the significance of the 1/4 slope at longer periods of time. This slope is actually the true representation of the isothermal shrinkage curve. The 1/4 slope may be associated with grain boundary diffusion rather than volume diffusion. The aspects of this interesting possibility will be considered further.

7. Effect of minor additions on the sintering of BeO. Cation additions of Ca^{++}, Mg^{++}, and Zr^{++++} have been made to UOX grade BeO powder to determine their effects on fired density and shrinkage. The cations were added as the oxide on a dry basis in successive quantities of 0.1, 0.3, 0.5, and 1.0 w/o. The dry-pressed pellets were fired under the following conditions: 1550°C in H_2, 1550°C in air, 1700°C in H_2, 1700°C in air. A 2-hour soak at maximum temperature was maintained for all samples. Control samples of unadulterated BeO were sintered with the samples containing additives. Duplicate runs were made for each of the firing conditions. Table II-3 lists the averaged densities of the duplicate pellets. The theoretical densities have been corrected to include the nominal weight of the additive as incorporated in the BeO powder, assuming additive volumes.

The batch of UOX grade BeO used for this study was a highly sinterable powder giving fired densities of 96.8% to 98.3% of theoretical after sintering. The effects of the additives appear to have been somewhat masked by the high degree of sinterability of the parent powder. The sharp improvement in density for particular additions as reported by other experimenters was not observed [E. J. Felton, J. Am. Ceram. Soc. 44, 251 (1961); E. A. Aitken, G. E. Research Lab. Rept. 60-6C-81 (Feb., 1960)]. It must be kept in mind that the results obtained are valid only for this particular batch of sulfate-derived UOX powder and the observed effects of the cations are not necessarily representative for all BeO powders.

The data show that the 1550°C-H_2 firings generally resulted in a higher density pellet than the 1700°C-H_2 firings. The only notable exception occurred with the addition of CaO at all concentrations studied. Firings in air at 1700°C generally led to a denser pellet than firings at 1550°C in air. However, this was reversed at higher concentrations (>0.3%) of CaO and MgO. H_2 firings at 1550°C generally led to the greatest density with the exception of all CaO additions. The densities for 1700°C firings in air were generally a little lower

Table II-3. Densities (% of Theoretical) of Sintered BeO Containing Small Amounts of Various Additives.

	Additive w/o			
Additive	0.1	0.3	0.5	1.0
Sintered at 1550°C in H_2				
None	98.0	98.0	98.0	98.0
Ca	94.0	94.0	93.3	95.3
Mg	97.7	98.4	98.2	97.8
Zr	97.6	97.6	97.4	96.7
Sintered at 1550°C in Air				
None	96.8	96.8	96.8	96.8
Ca	95.1	95.6	95.0	85.0
Mg	96.7	97.5	97.7	97.5
Zr	96.3	97.2	96.6	94.6
Sintered at 1700°C in H_2				
None	97.7	97.7	97.7	97.7
Ca	96.6	94.4	93.3	96.1
Mg	97.4	96.8	96.5	95.2
Zr	97.7	97.5	96.9	96.4
Sintered at 1700°C in Air				
None	97.4	97.4	97.4	97.4
Ca	95.0	93.6	94.6	94.7
Mg	97.8	97.5	97.0	93.0
Zr	97.3	97.3	97.1	96.7

than those observed for 1700°C-H_2 when the additive concentration was less than 0.5%. As the concentrations increased the densities for the 1700°C firings decreased, with the firings in H_2 exhibiting the greatest drop. The densities of pellets fired in air at 1550°C showed the smallest reduction, with the exception of the 1.0% CaO addition. The drop in density observed for 1.0% CaO was very marked.

The addition of MgO (above 0.1%) resulted in an increase in density for firings made at 1550°C in air. A small increase in density was observed for 0.3% to 0.5% MgO concentrations fired at 1550°C-H_2. A deleterious effect was noticed for concentrations exceeding 0.3% when fired at 1700°C-air and for all concentrations when fired at 1700°C-H_2. For these conditions the density decreased as the concentration of MgO was increased.

The addition of CaO proved to be deleterious for all concentrations studied, with the 1550°C-H_2 firings exhibiting the greatest decrease in density. The 1550°C air firings exhibited the smallest decrease in density. Densities for all firing conditions reached a minimum at intermediate concentrations (0.3%-0.5%) and subsequently increased with larger concentrations, though remaining below the density of the pure BeO control sample.

Additions of ZrO_2 at concentrations of 0.3% led to a slightly denser body when fired in air at 1550°C. The overall effect for other conditions appeared to be deleterious, with density decreasing as concentration increased.

The linear shrinkage of the pellets fluctuated around 16.5% for the ZrO_2 and MgO additions and around 15.5% for the CaO. For the ZrO_2 and MgO additions there was little marked variation in shrinkage; the trends were about the same as for the densities.

For MgO the shrinkage of the 1550°C-air samples increased with increasing concentrations, corresponding to the observed increase in density, whereas the 1700°C firings resulted in a decrease in shrinkage with increased concentrations, corresponding to the decrease in density.

ZrO_2 additions caused little variation in shrinkage, with the exception of firings at 1550°C in air which gave increased shrinkage, roughly corresponding to the increase in density.

The shrinkage for CaO additions fluctuated widely. Shrinkage of firings at 1550°C in H_2 and in air increased while the density of the pellets decreased in an inverse relation. Firings at 1700°C in H_2 and in air tended to exhibit a decrease in shrinkage as additive concentration increased, corresponding to the observed density decrease at this temperature. Maximum shrinkages at intermediate concentrations (0.3% to 0.5%) were observed for the 1550°C firings and minimum shrinkages for the 0.3% to 0.5% range for the 1700°C firings.

The results obtained contradict usual literature expectations in that:

1. Unusually high densities of the undoped UOX were obtained at 1550°C.
2. Additives which have been shown by others to assist densification actually decreased densities (especially Ca); Mg and Zr, however, had little effect except at 1550°C in air.

It is conceivable that the particular lot of BeO was exceptionally sinterable, so as to reverse usual expectations.

8. Oxidation of uranium monocarbide. Investigation of the oxidation of uranium monocarbide was continued in two different areas.

First, efforts were made to identify the unknown amorphous phase. One method used was to heat the oxidation products to higher temperatures at a linear rate. Decomposition of the amorphous phase to U_3O_8 should be complete at 800°C. The thermogram constructed from the results of this heating showed three distinct peaks indicating the following reactions:

$$\text{Unknown phase} \rightarrow UO_3 \rightarrow UO_{2.9} \rightarrow U_3O_8 .$$

Further evidence for these reactions is supplied by observation of color changes and by x-ray and infrared analysis of the $UO_{2.9}$ and U_3O_8 phases. Hoekstra and Siegel have found amorphous UO_3 to decompose to the intermediate $UO_{2.9}$ and then to U_3O_8, which substantiates our findings.

The unknown phase was also found to react very readily with water at room temperature. The reaction product was a bright-yellow crystalline solid, identified as $UO_3 \cdot 2H_2O$ by x ray. Further information is necessary before definite conclusions as to the identity of the amorphous oxidation phase can be made.

Second, consideration was given to the kinetic models of oxidation. Samples of two widely different particle size were oxidized. The coarse sample ranged in size from -20 to +35 mesh, while the finer one passed through a 200 mesh screen. The oxidation results showed no difference in rate between the two samples. Data so far indicate that the oxidation is a bulk phenomenon represented by the $\ln(1/1 - R) = kt$ rate equation.

Fuel Retention and Stability

1. Summary. Work has continued on various binaries and ternaries of urania with stabilizing components. Zirconia-urania in BeO was shown to have satisfactory properties (fuel loss and mechanical stability) for Tory II-C. However,

its fuel loss is high and erratic at 100 to 150°C above the Tory II-C design peak interior temperature of 1400°C at 75 psia oxygen. This high loss is consistent with our observation that powdered reaction mixtures of ZrO_2 and UO_2 decompose to U_3O_8 upon oxidation, which has an appreciable vapor pressure of UO_3 in oxygen.

The ternary ZrO_2-UO_2-Y_2O_3 in BeO has shown good fuel retention even at 1650°C, as well as no indication of breaking down to U_3O_8 in oxygen. Consequently, efforts now are directed toward determining the processing and properties of this fueled material. Some work on other binaries is also reported.

2. UO_2-ZrO_2-Y_2O_3

a. Preparation and properties. Another organization has published work on a urania-zirconia-yttria composition which had low fuel losses when subjected to 1525°C for over 500 hours in a moving air stream. It appeared desirable to investigate this system (ZrO_2-UO_2-Y_2O_3 in BeO) as a possible stable system in high pressure oxygen.

A mix (450X230) was made using the published procedure (report XDC 61-5-48), i. e., reaction of powdered compounds at 1800 to 1900°C in air. X-ray patterns of material heated in air and helium to 1800°C/2 hours were measured and had the same lattice parameter (FCC $a_0 = 5.27_4$ Å) found in the above-mentioned work. The same material heated in hydrogen had two phases, FCC $a_0 = 5.28_1$ Å and FCC $a_0 = 5.31_2$ Å.

Another mix (254X233 Hy) containing beryllia was made by coprecipitating Zr, U, and Y with NH_4OH from the nitrates, and then stirring this slurry with BeO. Material from this mix was sintered to 1800°C/2 hours in a hydrogen atmosphere. X-ray data indicated a single FCC phase $a_0 = 5.31_3$ Å. When this powder was subjected to 75 psia oxygen pressure and 1250°C/10 hours, the phase was still FCC but the lattice parameter had shifted to $a_0 = 5.26_1$ Å. Also, no U_3O_8 phase was observed under these conditions. For x-ray results of mixes containing UO_2-ZrO_2 and UO_2-ZrO_2-Y_2O_3, see Table II-4.

Several interesting observations have been made on the ternary compositions with and without BeO.

1. X-ray diffraction of the coprecipitated ternary heated to 350°C for 3 hours indicated that the reaction is starting to take place at this low temperature.

Table II-4. Ternary Fuel Properties.

Sample No.	ZrO_2/Y_2O_3	Fuel composition mole %			Contains BeO	Mixing method	Phases before sintering; temp in °C, a_0 in Å	Sintering conditions			Phases after sintering (excludes BeO)	Phases after testing 1250°C/10 hours/ 75-psia O_2 (excludes BeO)
		UO_2	ZrO_2	Y_2O_3				°C	hr	atm		
80X200	1:0.12	80.81	17.09	2.10	Yes	Coppt slurry	Not tested	1725	6	H_2	FCC $a_0 = 5.41_8$	U_3O_8 hex plus several lines
80X202	1:0.06	76.54	22.04	1.42	Yes	"	" "	"	"	"	FCC $a_0 = 5.31_7$	" " " " "
80X200A	1:0.13	46.34	47.52	6.14	Yes	"	" "	1625	6	H_2	FCC $a_0 = 5.32_6$	U_3O_8 hex + FCC $a_0 = 5.25_1$
								1750	4	H_2	FCC $a_0 = 5.32_6$	" " " "
								1850	2	H_2	FCC $a_0 = 5.32_6$	" " " "
450X230	1:0.98	34.37	33.13	32.50	No	Powder	Not tested	1800	2	Air	FCC $a_0 = 5.27_4$	FCC $a_0 = 5.26_2$
								1800	2	He	" "	FCC $a_0 = 5.26_2$
								1400	3	Air	" "	FCC $a_0 = 5.26_2$
								1800	2	H_2	FCC $a_0 = 5.28_1$ FCC $a_0 = 5.31_4$	FCC $a_0 = 5.26_2$
450X232Y	1:1.53	40.13	23.68	36.18	No	Ppt UO_2 on ZrO_2 & Y_2O_3 powders	Not tested	1800	2	H_2	FCC $a_0 = 5.30_7$	FCC $a_0 = 5.27_0$
254X233Y	1:1	34.58	32.92	32.50	Yes	Coppt, add to BeO slurry	Not tested	1500	2	H_2	[a]FCC $a_0 = 5.30_9$ FCC $a_0 = 5.47_1$ FCC $a_0 = 5.25_1$	[b]FCC $a_0 = 5.27_9$ FCC $a_0 = 5.32_1$
								1600	2	H_2	FCC $a_0 = 5.30_9$	[b]FCC $a_0 = 5.27_9$ FCC $a_0 = 5.32_1$
								1700	2	H_2	FCC $a_0 = 5.31_8$	FCC $a_0 = 5.26_1$
								1750	2	H_2	FCC $a_0 = 5.31_8$	FCC $a_0 = 5.26_1$
								1800	2	H_2	FCC $a_0 = 5.31_8$	FCC $a_0 = 5.26_1$
								1850	2	H_2	FCC $a_0 = 5.31_3$	FCC $a_0 = 5.27_3$
80X239Y	1:1.31	34.54	28.36	37.10	Yes	Coppt, add to BeO slurry	[c]FCC $a_0 = 5.26_1$ 800°/air	1700	5	He	FCC $a_0 = 5.31_0$	Not tested
							FCC $a_0 = 5.26_1$ FCC $a_0 = 5.31_1$ 1000°/air	1700	5	Air	FCC $a_0 = 5.26_1$	
							FCC $a_0 = 5.26_2$ FCC $a_0 = 5.31_1$ 1150°/air	1700	5	H_2	FCC $a_0 = 5.32_8$	
80X230D	1:1	34.37	33.13	32.50	Yes	Powder	[d]Fuel FCC $a_0 = 5.27_4$	1700	5	He	FCC $a_0 = 5.31_1$	Not tested
80X230D-1	1:1	34.37	33.13	32.50	Yes	Powder	[d]Fuel FCC $a_0 = 5.27_4$	1700	5	H_2	FCC $a_0 = 5.33_1$	Not tested
450X249	1:1	34.37	33.13	32.50	No	Coppt	[e]FCC $a_0 = 5.2$ or 5.3 350°/air	--	-	--	Not sintered	Not tested

[a] Can fit FC tetragonal.

[b] FCC lines all very broad, could fit FC tetragonal.

[c] FCC lines very broad, could be two FCC.

[d] The fuel for these tubes was mix 450X230 sintered in air at 1800°C/2hr, then ground to -325 mesh and added to BeO and sintered in hydrogen.

[e] Practically amorphous; four weak lines present, FCC $a_0 = 5.2$ or 5.3 Å.

MUL-15963

2. Material sintered in air at 1800°C (FCC $a_0 = 5.27_4$ Å) then resintered in hydrogen to 1700°C/5 hours has a lattice parameter of FCC $a_0 = 5.31_3$ Å. The hydrogen-sintered material will revert back to the FCC $a_0 = 5.27_4$ Å parameter when subjected to 1250°C/10 hours and 75 psia oxygen pressure.
3. Temperature alone is not the criterion for one or two FCC phases when sintering powders in a hydrogen atmosphere. Two face-centered cubic phases have been observed at 1500°C, 1600°C, and 1800°C. Air-sintered samples at 1700°C and higher have shown only one phase, FCC $a_0 = 5.26_1$ Å. However, coprecipitated materials show single-phase FCC in hydrogen-sintering above 1500°C.
4. The powder mix showed the same phase and lattice parameter at a low reaction temperature (1400°C) as at the higher reaction temperature (1800°C). However, the ternary reacted at 1800°C in air was oxygen-richer than that reacted at 1400°C. See below.

(-325 mesh) Sample No.	Calcining Temp (°C)	Time (hours)	Atmosphere	1250°C/10 hr, 75 psia O_2 % wt change
450X230 A	1400	3	Air	+1.20
450X230 B	1800	2	He	+0.90
450X230 C	1800	2	H_2	+0.74
450X230 D	1800	2	Air	+0.39

5. Compositions of the ternary other than 1:1:1 mole also showed similar phases and stability toward conversion to U_3O_8. However, at very low Y:Zr ratios (about 0.1) conversion to U_3O_8 occurred in oxygen at 1250°C.

b. Fuel loss. In Table II-5 results are listed for testing at 1650°C for 10 and 20 hours in 75 psia O_2. These results are preliminary and more detailed investigations are in process. The following observations are evident:

1. Fuel loss at 1650°C for 10 hours is about 2% or less. For comparison, losses in BeO-ZrO_2-UO_2 are this low only at 1400°C to 1450°C.
2. Strength after test for three-point loading on 1-1/2-inch span was approximately 33,000 psi.

Table II-5. Fuel Loss and Strength Data for 80X239Y Tubes (BeO-UO_2-ZrO_2-Y_2O_3) Tested in 75 psia Oxygen; All Samples Fired 5 Hours at 700°C.

Sample No.	Firing atm	w/o After firing			Test		% Wt change	% Fuel loss[a]	Mod. rupt.[b] (psi)
		UO_2	Y_2O_3	ZrO_2	Temp (°C)	Time (hr)			
147-4	H_2	8.22	7.10	3.08	1625-50	20	+0.1	2.4	32,900
-4A	H_2	"	"	"	"	"	+0.2	1.5	30,600
150-11	He	8.24	6.99	3.08	1650-75	"	-0.4	4.0	24,800
-12	He	"	"	"	"	"	-0.4	4.5	25,900
-16	Air	7.18	7.08	3.05	"	"	0	0.9	37,800
-17	Air	"	"	"	"	"	0	1.1	34,900
157-10	H_2	8.22	7.10	3.08	1650	10	+0.2	0.7	33,900
-10A	H_2	"	"	"	"	"	+0.2	0.9	32,000
-18	Air	7.18	7.08	3.05	"	"	-0.1	1.4	34,300
-19	Air	"	"	"	"	"	0	0.6	40,200

[a] By gamma count.

[b] Three-point loading, 1-1/2-inch centers.

3. Little can be said from these tests about the effects of firing atmosphere on the fuel loss, but they appear to be small for the test conditions.
4. Approximately 1% UO_2 has been lost in the air-firing operation. The starting compositions were the same in each case, and a chemical analysis after firing indicates about 1% loss.

c. High-temperature x-ray diffraction. Phase relations are being studied in the ternary system Y_2O_3-UO_2-ZrO_2-O_2 in the region around the compound $3Y_2O_3 \cdot UO_3$. The ternary mixtures will be prepared by coprecipitation as hydroxides from nitrate solutions. The samples will be fired in various atmospheres and then tested for phase content and phase stability by x-ray diffraction and fuel loss tests.

High-temperature x-ray studies have been made on two previously prepared ternary mixtures, both in powder form, prepared by coprecipitation, subsequently hydrogen-fired at 1800°C and reground. One mixture (450X230Y) contained 44.9 w/o UO_2, 35.9 w/o Y_2O_3, and 19.2 w/o ZrO_2; the second sample (254X233Y) contained the same ratio of oxides with 43.8 w/o BeO added by slurrying BeO powder with the coprecipitate. Both samples were heated on platinum heaters in an x-ray furnace under 5 atmospheres oxygen.

The sample containing BeO was heated successively for extended time intervals at 200, 400, 600, 800, 1000, 1200, and 1400°C. The time at temperature for 400, 800, and 1200°C was more than 16 hours. One 800°C run was left for 100 hours. Samples without BeO were heated to 1400°C and were at temperature approximately 10 hours.

All samples followed much the same pattern. At 800°C after 100 hours the UO_2 was not fully oxidized, as evidenced by the cell constant of the solid solution being $a_0 = 5.27_9$ Å. The unoxidized sample had $a_0 = 5.31_0$ Å. Samples heated above 1000°C showed an $a_0 = 5.27_4$ Å. This value is the smallest observed and appears to represent the "stable" phase in oxygen.

Samples heated above 1200°C show the development of an orange-colored phase. Powder patterns of cooled samples using carefully isolated grains of the orange material show the phase to be dominantly FCC with additional weak lines. The new lines correspond to no reported phase in the BeO-UO_2-Y_2O_3-ZrO_2-O_2 system. It has not yet been determined whether the pattern represents one phase or an orange phase mixed with a fuel phase. The new phase may represent a urania-deficient zirconia-yttria solid solution. It does not involve BeO, and it is doubtful if a reaction with platinum is involved.

3. CeO_2-UO_2

a. High-urania compositions. The objective of this work was to first prepare stoichiometric solid solutions ($U_xCe_{1-x}O_{2.00}$ where x is greater than 0.5) and then to equilibrate these solid solutions at an optimum "U_3O_8-forming" temperature in 75-psia O_2. Solid solutions high in uranium were chosen by analogy to the UO_2-ThO_2-O_2, of which an oxidized solid solution with up to 70 m/o UO_2 will retain the cubic fluorite structure in air.

Three solid solutions were carefully homogenized in vacuum at 1400°C for 2 hours in a platinum crucible. The weight losses during heating were small (~0.5%) and a chemical analysis after heating confirmed the original composition. The solid solutions were x-rayed after vacuum treatment and after heating powdered material in 75-psia O_2 at 1250°C for about 4 hours.

The results of this work are shown in Table II-6. Conclusions to date are as follows:

1. Complete solid solution is achieved in vacuum at 1400°C for 2 hours without significant changes in composition.
2. The cubic cell size shows a positive deviation from Vegard's law. Magneli and Kihlborg's work [Acta. Chem. Scand. 5, 578 (1951)] in evacuated SiO_2 tubes at 1000°C for several days shows a negative deviation from Vegard's law. If all of the weight loss (0.5%) were ascribed to oxygen and the oxygen loss attributed to reduction of $CeO_{2.00}$, the oxygen deficiency would result in $CeO_{1.92}$. This could explain the positive shift from Vegard's law.
3. All three solid solutions are unstable in 75-psia O_2, breaking down to U_3O_8 and a stable cubic phase.
4. Prior work at this laboratory shows that the lattice parameter $a_0 = 5.420_4$ Å represents an oxidized (75-psia O_2) 60 m/o CeO_2-40 m/o UO_2 solid solution. We can say then that such solid solutions containing more than 40 m/o UO_2 are not stable in 75-psia O_2.

Future objectives are to measure the vapor pressure in 1 atmosphere O_2 of $UO_{3(g)}$ over the compositions richer in CeO_2 than 60 m/o CeO_2-40 m/o UO_2 solid solution. In view of the present performance in vacuum it is conceivable, but not yet proven, that CeO_2 will volatilize in 75-psia O_2 faster

Table II-6. X-Ray Results of CeO_2-UO_2-O_2 System.

Sample No.	CeO_2/UO_2 w/o before vac. treat.[a]		CeO_2/UO_2 w/o after vac. treat.[b]		CeO_2/UO_2 m/o after vac. treat.		Theoret. cell size using Vegard's law[c] a_0 (Å)	Cubic cell size after vac. treat.	Phases present after 75-psia O_2 at 1250°C	Cubic cell size after 75-psia O_2 at 1250°C
1	21.5	78.5	21.2	78.8	30	70	5.4510	5.462_7	U_3O_8 + Cubic	5.420_4
2	29.8	70.2	30.0	70.0	40	60	5.4453	5.454_1	U_3O_8 + Cubic	5.420_4
3	38.9	61.1	37.9	62.1	49	51	5.4402	5.446_3	U_3O_8 + Cubic	5.420_4

[a] By calculations.

[b] By chemical analysis.

[c] CeO_2: a_0 = 5.4110 Å
UO_2 : a_0 = 5.4682 Å } NBS values, confirmed in present tests.

than UO_3, thereby increasing the mole fraction UO_2 to the point that the solid solution becomes unstable.

b. Preparations of CeO_2-UO_2. Studies in this system have been concerned primarily with high-ceria powder compositions. The following table lists the range of compositions studied, their code identifications, and the x-ray analysis of the reacted powders.

Fuel powder code number	Nominal composition				Phases identified
	w/o CeO_2	w/o UO_2	m/o CeO_2	m/o UO_2	
F-7	30	70	40.2	59.8	FCC $a_0 = 5.43_7$
F-8	40	60	51.1	48.9	FCC $a_0 = 5.43_0$
F-9	50	50	61.1	38.9	FCC $a_0 = 5.42_4$
F-10	60	40	70.2	29.8	FCC $a_0 = 5.42_7$
F-16	70	30	78.6	21.4	FCC $a_0 = 5.40_5$
F-18	70	30[a]	78.6	21.4[a]	FCC $a_0 = 5.42_0$

[a] Reacted as U_3O_8 with the CeO_2 powder.

The fuels were prepared by solid state reaction of the blended powders. The reaction products were crushed and screened through a 325 mesh sieve prior to being used in the foregoing studies.

Powdered samples of the CeO_2-UO_2 compositions listed above were subjected to heating treatments at various temperatures, in different oxidizing atmospheres and for varying periods of time.

Testing at 1250°C. Fuels F-7, F-8, F-9, and F-10 were heat-treated at 1250°C for 10 hours in 5 atmospheres of oxygen. The treated powders were then examined by x-ray diffraction to determine their phase stabilities. A single cubic phase was present in all the treated powders. In addition, a hexagonal U_3O_8 phase was also present in the F-7 (40 m/o CeO_2-60 m/o UO_2) sample. These results indicate that no phase changes occur in fuel powders of this system containing more than 50 m/o CeO_2 when exposed to 1250°C for 10 hours in 5 atmospheres of oxygen. The changes in lattice constants of the fuel powders because of the test conditions were found to be notably small in general. The following table lists the results obtained.

X-Ray Analysis of As-Reacted and Heat-Treated CeO_2-UO_2 Powders; 1250°C for 10 Hours in 5 Atm of Oxygen.

Fuel number	Nominal Comp. m/o CeO_2	Nominal Comp. m/o UO_2	Phases identified by x-ray analysis: Initial powder	Phases identified by x-ray analysis: Heat-treated powder
F-7	40.2	59.8	FCC $a_0 = 5.43_7$	FCC $a_0 = 5.43_1$; Hex. U_3O_8
F-8			FCC $a_0 = 5.43_0$	FCC $a_0 = 5.42_0$
F-9			FCC $a_0 = 5.42_4$	FCC $a_0 = 5.42_3$
F-10			FCC $a_0 = 5.42_7$	FCC $a_0 = 5.41_7$

Testing at 1400°C. Since no phase changes were experienced for fuel powder F-8, F-9, and F-10 in the experiment, a sample of F-10 powder was heated in a thermal balance at 1400°C for 2 hours in 1 atmosphere of oxygen. The experimental data indicated no weight or phase change during the experiment. Another sample of the F-10 powder was then heated to approximately 1425°C for 3 hours in 5 atmospheres of oxygen in the x-ray diffraction furnace. The lattice constant change found for the F-10 sample was from $a_0 = 5.42_7$ to $a_0 = 5.42_3$. These results indicate that F-10 powder does not undergo phase change when exposed to about 1425°C for 3 hours in 5 atmospheres of oxygen.

Testing at 1370°C for extended time periods. F-8, F-9, and F-10 powders were tested at 1370°C in a flowing oxygen atmosphere (5 liters/min) for extended time periods to determine what weight and phase changes these fuels would undergo with time. Weighed samples of each of the powders in tared rhodium boats were placed in tube furnaces and heated at 1370°C in 5-liter/min flowing oxygen. There was intermittent removal of boats and sampling of powders for x-ray diffraction. The total heating time of these powders was 114 hours at 1370°C. The results of these tests are summarized in Table II-7. The weight changes found for the different heating periods are also shown graphically in Fig. II-5.

Table II-7. Changes in Weight, Phase and Chemistry of Fuel Powders Resulting from Heating at 1370°C for Extended Times in 5-liter/min Flowing Oxygen.

Fuel No.	Nominal m/o CeO_2	Nominal m/o UO_2	Heating time, hr	Weight loss, %[a]	X-ray phases identified	Chemical analysis w/o UO_2	Chemical analysis w/o CeO_2	Chemical analysis w/o ZrO_2
F-8	51.1	48.9	0	0	FCC $a_0 = 5.43_0$	59.3	37.3	--
			114	9.2	FCC $a_0 = 5.42_5$	56.3	41.9	--
F-9	61.1	38.9	0	0	FCC $a_0 = 5.42_4$	48.0	48.6	--
			114	5.8	FCC $a_0 = 5.43_8$	45.3	51.0	--
F-10	70.2	29.8	0	0	FCC $a_0 = 5.42_7$	41.7	54.9	--
			114	2.1	FCC $a_0 = 5.44_8$ + Extra lines	37.6	59.9	--
F-12	40 m/o ZrO_2 20 m/o CeO_2 40 m/o UO_2		0	0	FCC $a_0 = 5.32_3$ + Trace ZrO_2(m)	54.8	15.3	23.4
			114	15.4	FCC $a_0 = 5.34_3$	48.6	20.5	28.1

[a] Based on cumulative weight losses.

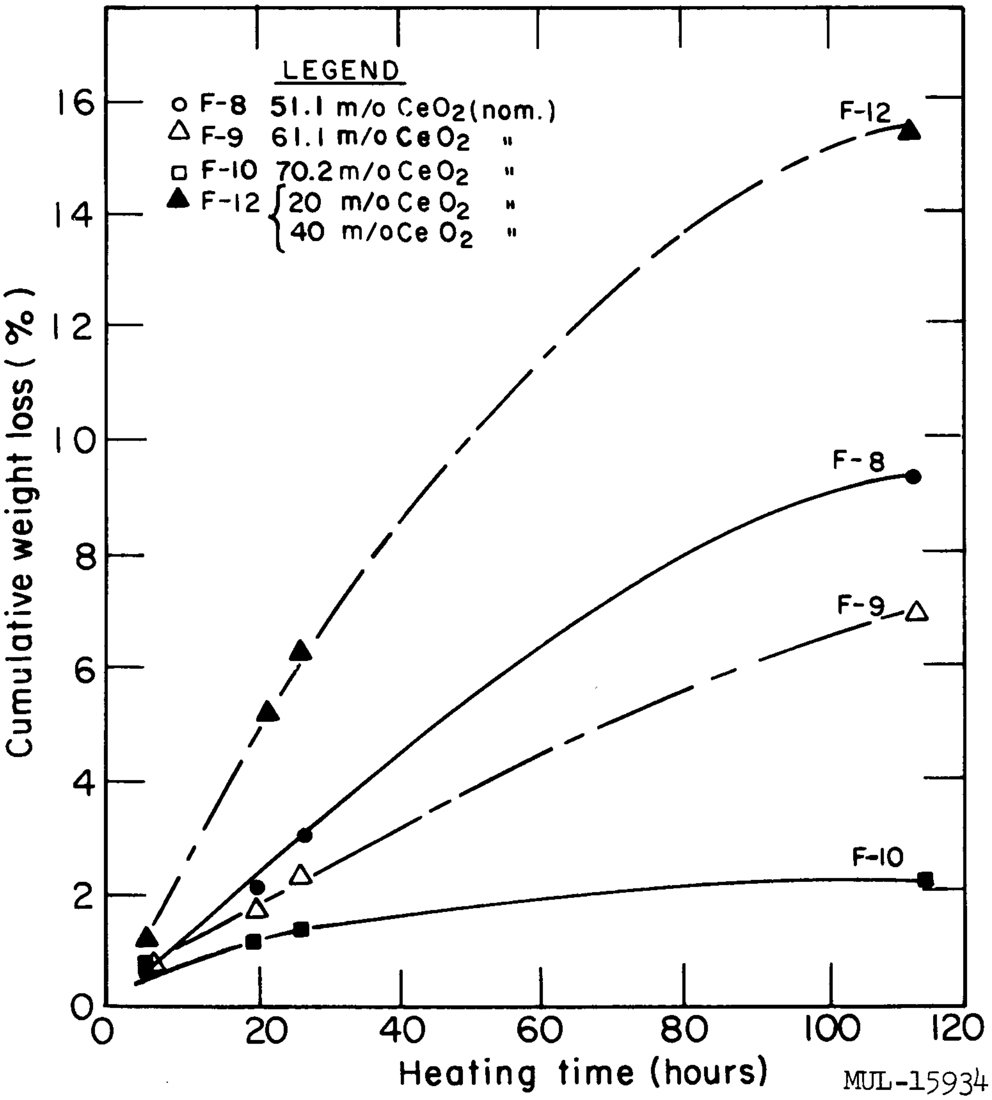

Fig. II-5. Cumulative weight loss as a function of heating time, for various reacted fuel powders heated at 1370 °C in flowing oxygen. Powder size, -325 mesh; oxygen flow rate, 5 liters/min.

The results of these studies show that the initial single phase of the reacted fuel powders is maintained for the test conditions as evidenced by x-ray diffraction analysis. The F-10 fuel powder (70.2 m/o CeO_2-29.8 m/o UO_2) appears to be the most promising, based upon the total weight losses of the fuel powders tested. It must be noted that the total weight losses measured included loss in weight of any absorbed moisture that may have been present in the initial powder. This may account for the relatively large percentages of weight loss exhibited by the powders during the initial heatings. In addition some of the weight loss may also be attributed to rhodium vaporization from the boats used during the tests. Although the fuel powders' single phase was found to be stable for the test conditions, some changes in the lattice cell constants of the powders were found. These changes are anomalous, for they did not occur in the same direction for the different compositions. The lattice constant for F-8 decreased toward that of CeO_2, due presumably to loss of UO_2. The reverse is found for the F-9 and F-10 powders.

<u>Testing at 1650°C for extended time periods</u>. The previous extended heating tests indicated that the F-10 composition most closely approached the desired fuel criteria. To further ascertain whether the F-10 composition was the optimum one for this system, fuel powders F-16 and F-18 were prepared. Both powders were composed of 78.6 m/o CeO_2 and 21.4 m/o UO_2. The difference between the fuels was the uranium oxide powder that was blended with the ceria powder and reacted. F-16 was prepared by reacting UO_2 powder with CeO_2 powder; F-18 was prepared by reacting U_3O_8 with CeO_2 powder. These reacted powders were crushed, screened, and oxidation-tested at 1650°C in a flowing oxygen atmosphere (2.5 liters/min) for extended time periods. The results of these studies are listed in Table II-8.

The data show that the initial single FCC phase persists at 1650°C for a period up to 89 hours in 2.5-liter/min flowing oxygen. Another point of interest is the fact that when UO_2 was used as a reactant, the lattice constant changed from $a_0 = 5.40_5$ Å to 5.39_2 after heating for a period of 60 hours. The lattice constant change was not direct, however, because during the intermediate heatings it initially increased to a value of 5.42_6 and then decreased to 5.39_2. These changes may be due to additional oxidation of the solid solution powder to form a more highly oxidized UO_2-CeO_2 solid solution in the early stages of the heat treatment. This was then followed by loss of fuel from the

Table II-8. Changes in Weight and Phase of Fuel Powders Resulting from Heating at 1650°C for Extended Times in 2.5-liter/min Flowing Oxygen.

Fuel No.	Nominal comp. m/o CeO_2	Nominal comp. m/o UO_2	Heating time, hr	Weight loss, %[a]	Phases identified by x-ray diffraction
F-16	78.6	21.4	0	--	FCC $a_0 = 5.40_5$, Broad lines[b] from 25°θ on
			5	0.6	FCC $a_0 = 5.42_6$
			7-1/2	1.2	FCC $a_0 = 5.42_6$
			16	1.7	FCC $a_0 = 5.42_6$
			21-1/2	2.8	FCC $a_0 = 5.41_8$
			37-1/2	3.5	FCC $a_0 = 5.41_8$
			60	5.7	FCC $a_0 = 5.39_2$
			82-1/2	7.5	--- ---
			89	8.9	FCC $a_0 = 5.39_2$
F-18	78.6	21.4[c]	0	--	FCC $a_0 = 5.42_0$
			20-1/2	3.6	FCC $a_0 = 5.42_0$
			26	4.5	FCC $a_0 = 5.42_0$
			42	7.5	FCC $a_0 = 5.42_0$
			65	11.3	FCC $a_0 = 5.42_0$

[a] Corrected for Rh vaporization loss.

[b] As-reacted fuel powder.

[c] Blended as U_3O_8 powder prior to reaction for solid solution formation.

solid solution on continued heating with the concurrent decrease in the lattice constant. The weight loss results from these studies are shown graphically in Fig. II-6.

c. BeO-CeO_2-UO_2 mixtures. Fuel powders F-8 (40 w/o CeO_2-60 w/o UO_2) and F-10 (60 w/o CeO_2-40 w/o UO_2) were incorporated in BeO by powder-blending and extrusion mixtures were prepared. Hexagonal tubes containing nominal 8 w/o UO_2 were extruded and tested to determine their sinterability in air. In addition, air-sintered tubes of BF-10 composition (8 w/o UO_2) were heat-treated in 2.5-liter/min flowing oxygen at 1650°C for varying times to determine if any phase changes occurred because of the incorporation of the fuel powder in BeO. BF-16 powder, consisting of F-16 (70 w/o CeO_2-30 w/o UO_2 nominal) and BeO in equal weights, was treated similarly. The results from these studies are listed in Table II-9.

The results indicate the following:

1. BeO tubes containing CeO_2-UO_2 powders in 8 w/o UO_2 concentrations are reasonably sinterable in air under the conditions studied.
2. The stability of the FCC phase in the presence of BeO under the sintering and heat-treating conditions has been demonstrated for the fuel compositions studied.

Table II-10 summarizes the results of the weight loss tests performed during the quarter. The results of these 1650°C treatments are also shown graphically in Fig. II-6.

d. CeO_2-UO_2-ZrO_2 mixtures. A single stable phase has been shown to exist in the CeO_2-UO_2 system. Similarly, it has been shown that the ZrO_2 can be stabilized by CeO_2 [O. Ruff and F. Ebert, Z. anorg. u. allgem. Chem. 180, 19 (1929); Duwez and Odell, J. Am. Ceram. Soc. 33, 274 (1950); Weber, Garrett, Mauer, and Schwartz, J. Am. Ceram. Soc. 39, 197 (1956)]. From the neutronic and ceramic standpoints (volatility, absence of low-m.p. eutectics), it would be preferable to obtain a zirconia-rich stabilized fuel rather than a ceria-rich one. However, attempts to prepare an air-stable zirconia-rich fuel were apparently not successful.

Based upon the literature concerning the stabilizing effect of CeO_2 on ZrO_2, a powder blend (F-12) composed of 40 m/o UO_2, 40 m/o ZrO_2, and 20 m/o CeO_2 was prepared. Portions of this blend were reacted under different conditions. The products were analyzed chemically for resultant compositions and by

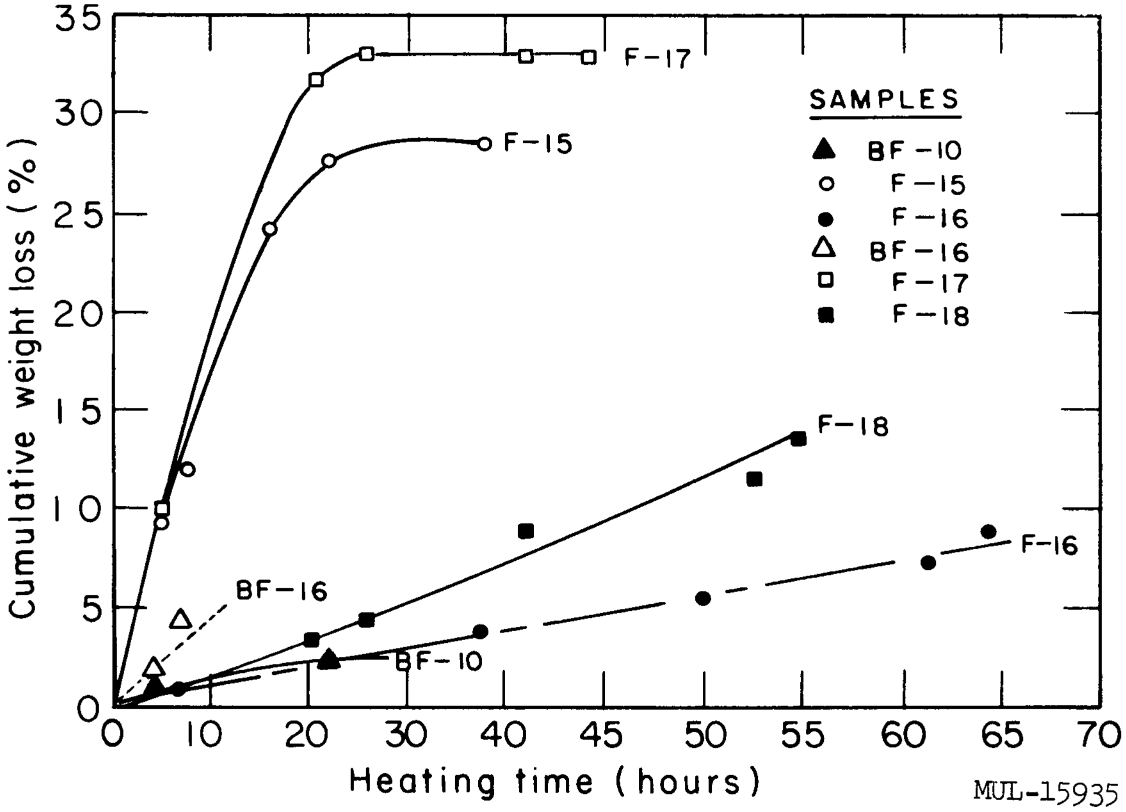

Fig. II-6. Cumulative weight loss as a function of heating time, for various fuel powders and sintered pieces heated in flowing oxygen (2.5-liter/min) at 1650 °C.

√

Table II-9. Sinterability and Heat-Treating Results for BeO-CeO_2-UO_2 Compositions.

Comp. No.	Sintering conditions	Average density % theoret.	Average shrinkage (%)	Heat treatment[a] Time (hr)	Heat treatment[a] Cum. wt loss (%)	X-ray diffraction phases identified
BF-8C Tube	1600°C, Air, 6 hr	97.4[b]	22.5			BeO, FCC $a_0 = 5.42_3$
BF-8C Tube	1650°C, Air, 3 hr	96.5[b]	21.5			BeO, FCC $a_0 = 5.42_3$
BF-10B Tube	1650°C, Air, 5 min	97[c]	22	0	0	
				5	1.3	
				20-1/2	2.3	BeO, FCC $a_0 = 5.42_0$
				26	2.5	BeO, FCC $a_0 = 5.42_0$
BF-16 Powder blend, by weight	50-50	94.1[c]	22	5	1.7[d]	
				21	4.2	BeO, FCC $a_0 = 5.42_0$

[a] Annealed at 1650°C in 2.5-liter/min flowing O_2.

[b] Based on chemical analysis of sintered tube.

[c] Based on chemical analysis of starch-burned tube.

[d] Corrected for Rh vaporization loss only.

Table II-10. Cumulative % Weight Loss from Heated Powders and Sintered Pieces in Flowing Oxygen at Elevated Temperatures for Various Times.

Heating time (hr)	Fuel powder and sintered piece compositions									
	F-8[a]	F-9[a]	F-10[a]	BF-10[b,c]	F-12[a]	F-15[b]	F-16[b]	BF-16[b,d]	F-17[b]	F-18[b]
5				1.28		9.5	0.63	1.66	9.78	1.43
6	0.74	0.85	0.78		1.06					
7.5						12.0	1.17	4.16		
16						24.3	1.68			
20.5				2.34					32.01	3.55
21.5						27.76	2.80			
22	2.14	1.83	1.27		5.05					
26				2.54					33.05	4.54
28	3.14	2.39	1.50		6.21					
37.5						28.66	3.48			
42									33.05	7.50
48									32.86[e]	
60							5.66			
65										11.25
82.5							7.54			
89							8.90			
114	9.27	6.76	2.09		15.44					

[a] Heated in 5-liter/min flowing oxygen at 1370°C; Rh weight loss not considered.

[b] Heated in 2.5-liter/min flowing oxygen at 1650°C; values corrected for Rh vaporization; correction for BeO vaporization not included.

[c] Air-sintered tube, 1650°C, 5 minutes. Nominal 8 w/o UO_2 added as F-10 powder.

[d] 50-50 BeO-F-16 powder blend by weight.

[e] Indicates weight gain.

x-ray diffraction to identify the phases present. A summary of the reactions performed and the results obtained from the reaction products is given in Table II-11. The reaction containers used included alumina and beryllia crucibles. In no instance was there any notable reaction between the crucibles and the reactants. The reacting powders sintered and shrank away from the walls of the crucibles for all reaction conditions used. The products were crystalline in appearance. They varied in friability with reaction temperature. The most friable product was the powder that had been reacted at the lowest temperature, while the least friable one had been reacted at the highest temperature.

The x-ray results show that a single phase product is formed at 1650°C and above. Since the UO_2 content after reaction agreed reasonably well with the nominal starting content, a fair retention may be expected. This fuel powder was heat-treated at 1370°C in 5-liter/min flowing oxygen. The results of these tests are listed in Table II-12 and shown graphically in Fig. II-5. The material appears inferior to CeO_2-UO_2, but the data are preliminary.

4. UO_2-ZrO_2-BeO

a. Fuel loss. In retrospect (see last report, UCRL-6625) the fuel loss testing from the standpoint of reproducibility is only satisfactory in the temperature range 1400 to 1450°C, where the fuel loss in 10 hours averaged 2%, with a range of 0.2 to 2.5%. Above 1500°C the fuel loss was strongly temperature-dependent, with losses ranging from 6% to 46% at 1525°C.

In an effort to better define the specimen temperature, all samples tested were shortened from 4 to 2 inches. The temperatures reported are accurate to ± 10°C. Results are reported in Tables II-12 and II-13, the mean values of fuel loss are shown in Fig. II-7. The results are self-explanatory. From the standpoint of Tory II-C requirements (moderate loss in 10 hours at 1400°C) this material is acceptable. However, losses become erratic and high above 1500°C.

b. Hot bend testing. High fuel losses and relatively low fracture strengths (~15,000 psi) have been encountered in thermal stress-oxidation tests at apparent temperatures of 1100-1250°C. The temperatures in these tests were somewhat uncertain. The losses could not be explained on the basis of fuel loss data obtained in the absence of stress, and the failure stresses seemed low compared with previous modulus-of-rupture measurements at high temperatures in air.

Table II-11. Reactions of 0.4 UO_2 - 0.4 ZrO_2 - 0.2 CeO_2 Powder Blends (F-12) and Results Obtained from Reaction Products.

Reaction conditions	Observations	X-ray phases present	Chemical analysis of prod.		
				w/o	m/o
1550°C, air, 4-1/2 hr, Al_2O_3 crucible	a) No reaction with crucible	1) FCC a = $5.32'_3$	ZrO_2	23.4	39.6
		2) ZrO_2, monoclinic	UO_2	54.8	41.7
	b) Crystalline sintered prod.		CeO_2	15.3	18.7
1650°C, air, 3 hr, BeO crucible	a) No reaction with crucible	1) FCC a = 5.32_3	ZrO_2	21.2	36.2
		2) One extra line	UO_2	54.7	42.5
	b) Crystalline sintered prod.		CeO_2	17.4	21.3
1750°C, H_2, 3-1/2 hr, BeO crucible	a) No reaction with crucible	1) FCC a = 5.33_8	ZrO_2	25.1	40.0
			UO_2	54.5	40.0
	b) Crystalline sintered prod.		CeO_2	17.4	20.0

Consequently we attempted to simulate thermal stress conditions in high pressure oxygen (75-psia) by hot bend tests on both 60 m/o ZrO_2 - 40 m/o UO_2 and 70-30 m/o ZrO_2-UO_2 in BeO. Two hours was chosen as the test time to simulate the thermal stress-oxidation tests. The objective was to determine whether hot strength degraded as a consequence of oxidation in high pressure oxygen. Another objective was to compare hot modulus of rupture at high oxygen pressures with that obtained in air (to be reported later). The data are listed in Table II-14.

Samples were loaded in air and at temperature (1150°C and 1250°C). The furnace was flushed once with 35-psia oxygen. Next the furnace was pressurized with dry oxygen to 75 psia. If after 2 hours the sample had not broken, the furnace was opened and the sample withdrawn (all at test temperature).

Creep was encountered at these temperatures. Consequently, the initial stress applied is the listed stress. The final stresses in the tubes cannot be specified because of the change in stress distribution. The final strains in most tubes after 2 hours were 0.03 to 0.2%, although one was 0.6%. The low

Table II-12. Fuel Loss Testing, BeO-UO_2-ZrO_2, 7.5-psia O_2.

Sample No.	Tube description	Nominal % UO_2	Nominal mole ratio UO_2/ZrO_2	Text conditions °C/hr	Wt Loss (%)	UO_2 Loss (by γ count) (%)	Mean UO_2 Loss (%)	Mod. rupt. after test[a] (psi)	Mean Mod. rupt. (psi)
109-91B	10X210Y, surface ground	1.0	60/40	1525/9	0.50	31	31	18,500	21,400
109-81B	"	"	"	"	0.49	31		24,900	
109-79B	"	"	"	"	0.52	31		19,100	
109-88B	"	"	"	"	0.48	31		19,900	
112-91A	10X210Y, unground	"	"	"	0.32	29		24,700	
112-81A	"	"	"	"	0.36	33		8,700	
112-79A	"	"	"	"	0.32	29		24,100	
112-88A	"	"	"	"	0.36	30		24,300	
112-78A	"	"	"	"	0.34	31		28,000	
122-44A	10X210Y, surface ground	1.0	60/40	1500/5	0.17	17	10	2,300	18,600
122-47A	"	"	"	"	0.06	5		25,300	
123-49A	"	"	"	"	0.09	15		6,700	
123-57A	"	"	"	"	0.07	6		22,400	
122-42	10X210Y, unground	"	"	"	0.09	7		28,900	
123-42A	"	"	"	"	0.09	8		28,600	
124-44	"	"	"	"	0.09	8		7,500	
124-45	"	"	"	"	0.11	10		22,700	
124-45A	"	"	"	"	0.14	10		28,100	
125-47	"	"	"	"	0.09	7		25,100	
125-49	"	"	"	"	0.13	13		6,900	
109-7B	249-800-201-22, surface ground	8.0	70/30	1525/9	2.58	29	36	6,000	6,300
109-53	"	"	"	"	4.53	55		8,800	
109-53B	"	"	"	"	2.83	32		5,700	
109-55	"	"	"	"	2.45	28		8,200	
109-55B	"	"	"	"	4.36	52		9,300	
112-4	249-800-201-22, unground	"	"	"	3.70	47		1,800	
112-7	"	"	"	"	2.10	25		6,300	
112-8	"	"	"	"	1.88	23		4,800	
112-19	"	"	"	"	2.76	33		6,000	
122-13	249-800-201-22, surface ground	8.0	70/30	1500/5	0.97	15	7	4,700	
122-13A	"	"	"	"	0.43	7		No Test	5,800
123-14	"	"	"	"	0.56	9		4,600	
123-14A	"	"	"	"	0.24	6		4,600	
122-9	249-800-201-22, unground	8.0	70/30	"	0.40	8		5,800	
122-9A	"	"	"	"	0.30	6		6,900	
123-10	"	"	"	"	0.16	5		5,100	
124-10A	"	"	"	"	0.04	4		7,400	
124-12	"	"	"	"	0.08	4		5,300	
124-12A	"	"	"	"	0.07	4		5,600	
125-17	"	"	"	"	0.29	6		5,700	
125-17A	"	"	"	"	0.26	6		7,700	

[a] Three-point loading, 1-1/2-inch span.

MUL-16048

Table II-13. Results of Fuel Loss Testing, $BeO-UO_2-ZrO_2$, 75-psia Oxygen.

Sample No.	Batch No.	Firing °C/hr	Surface condit.[a]	Test temp (°C)	Nominal % UO_2	Nominal mole ratio ZrO_2/UO_2	Density (g/cc)	Cumulative fuel loss by γ-count								Mod. rupt.[b] (psi)
								2 hr		7 hr		17 hr		37 hr		
								% Loss	Mean loss	% Loss	Mean loss	% Loss	Mean loss	% Loss	Mean loss	
137-43	276-800-241-53	1700/4	U	1400	8.0	60/40	3.28	1.6	1.4	1.6	1.5	2.0	1.8	2.6	2.3	16,300
-43A	"	"	"		"	"	3.28	1.6		2.0		2.4		2.9		15,700
-42	"	"	S		"	"	3.28	1.0		1.0		1.0		1.2		11,000
-42A	"	"	"		"	"	3.27	1.3		1.5		1.6		2.4		14,500
-66	272-200-237-53	"	U		2.0	"	3.04	1.7	1.3	2.7	2.2	3.5	3.1	4.7	4.4	28,000
-66A	"	"	"		"	"	3.04	0.8		1.7		2.6		4.0		28,300
138-45	276-800-241-53	1700/4	U	1450	8.0	60/40	3.28	2.7	2.2	5.1	4.0	8.4	6.6	No test	No test	20,400
-45A	"	"	"		"	"	3.28	2.3		4.1		4.7				19,700
-35	"	"	S		"	"	3.27	1.4		2.6		6.3				12,600
-35A	"	"	"		"	"	3.27	2.7		4.6		7.7				12,100
-64	272-200-237-53	"	U		2.0	"	3.04	2.6		4.5		7.2				27,000
-64A	"	"	"		"	"	3.04	1.3		3.3		5.5				27,600
142-39	276-800-241-53	1700/4	U	1500	8.0	60/40	3.28	2.3	2.2	4.2	4.4	6.4	6.3	"	"	31,800
-39A	"	"	"		"	"	3.28	1.9		4.3		6.4				27,200
-18	249-800-201-22	1700/5	S		"	70/30	3.34	2.8		5.2		8.0				11,800
-18A	"	"	S		"	"	3.34	2.9		5.0		8.0				9,200
-63	272-200-237-53	1700/4	U		2.0	60/40	3.05	2.0		3.4		4.3				27,700
-63A	"	"	"		"	"	3.05	1.5		3.2		4.6				26,000
144-86	276-800-243-51	1700/5	U	1400	8.0	60/40	3.28	No test	No test	No test	No test	2.1	1.9	"	"	38,500
-86A	"	"	"		"	"	3.28					2.0				36,100
-31	272-200-236-52	1700/5	"		2.0	"	3.05					1.6				26,500
-31A	"	"	"		"	"	3.05					1.5				26,200
145-79	276-800-243-51	1700/5	U	1450	8.0	60/40	3.28	"	"	"	"	2.2	3.0	"	"	36,600
-20	249-800-201-22	1700/5	S		8.0	70/30	3.34					3.9				14,800
-65	272-200-273-53	1700/4	U		2.0	60/40	3.05					3.3				28,300
-65A	"	"	U		2.0	"	3.05					2.7				29,000
146-40	276-800-241-53	1700/4	U	1500	8.0	60/40	3.28	"	"	"	"	6.2	8.2	"	"	37,400
-40A	"	"	U		8.0	"	3.28					5.8				32,400
-20A	249-800-201-22	1700/5	S		8.0	70/30	3.34					14.6				8,400
-67	272-200-273-53	1700/4	U		2.0	60/40	3.05					6.9				26,900
-67A	"	"	U		"	"	3.04					7.5				27,400

[a] S = surface ground, U = unground.

[b] Three-point loading, 1-1/2-inch span.

MUL-15964

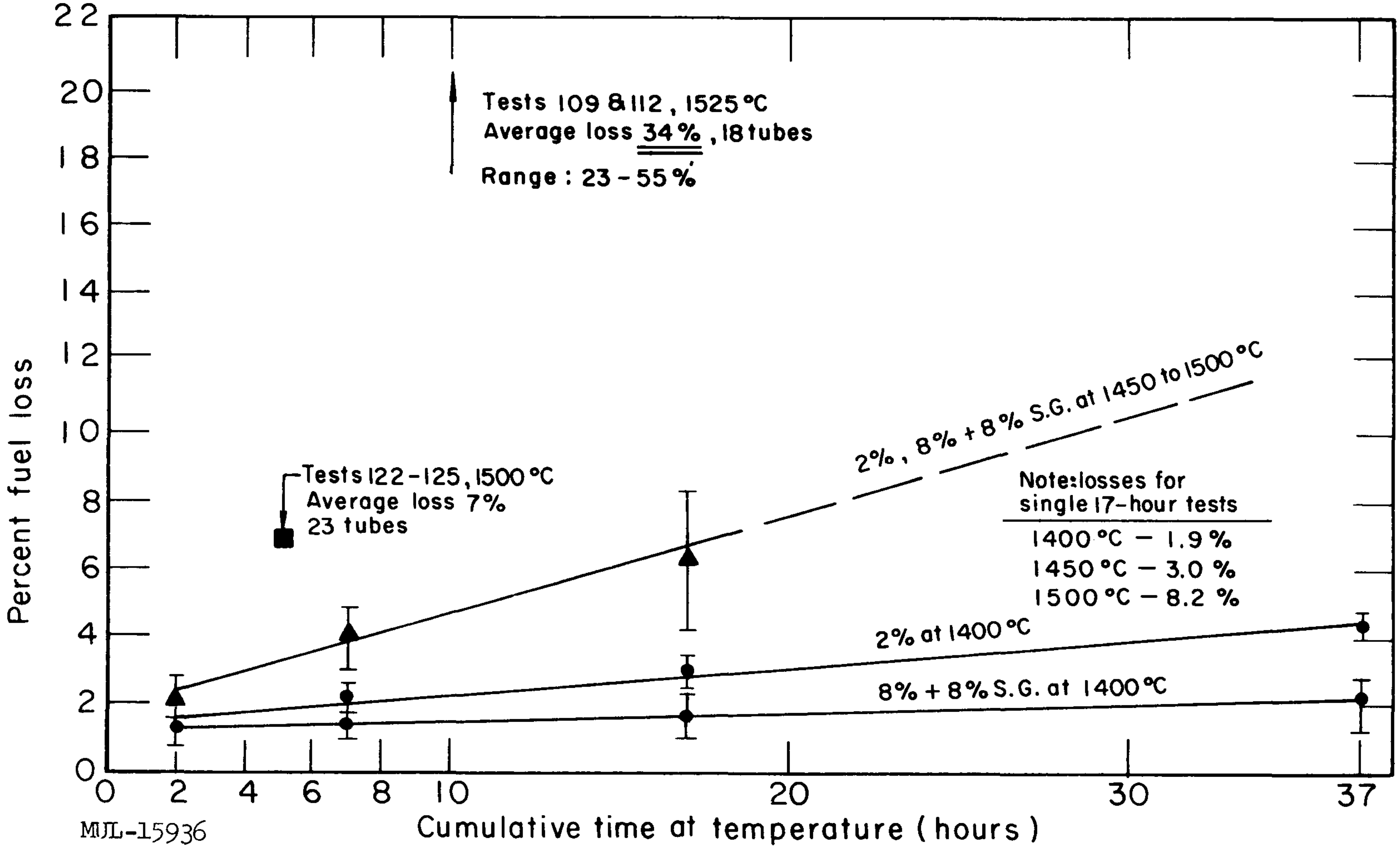

Fig. II-7. Fuel loss as a function of heating time, for UO_2-ZrO_2-BeO heated to various temperatures in oxygen at 75 psia.

Table II-14. Results of Hot Bend Testing BeO-UO_2-ZrO_2 Tubes in 75-psia O_2 for 2 Hours. All Specimens Fired 1700 °C/5 hr, Fast Cycle, Before Testing.

Spec. No.	Specimen	m/o ZrO_2 / m/o UO_2	w/o UO_2 / w/o ZrO_2	Density (g/cc)	Test temp (°C)	Initial hot bend load[a] (psi)	Hot bend performance[b]	% wt change	Change in chamber (in.)	Mod. rupt. after testing (psi)
113-76	80X1260	60/40	7.53/6.21	3.40	1250	24,600	1 min Broken	No test	No test	No test
114-79		60/40	7.53/6.21	3.40	1250	24,600	1 hr 17 min Broken	No test	No test	No test
115-49		60/40	7.53/6.21	3.40	1250	24,600	41 min Broken	No test	No test	No test
116-1		60/40	7.53/6.21	3.40	1250	21,400	1 hr 53 min Broken	No test	No test	No test
117-121		60/40	7.53/6.21	3.40	1250	21,400	1 hr 48 min Broken	No test	No test	No test
118-92		60/40	7.53/6.21	3.40	1250	21,400	1 min Broken	No test	No test	No test
119-53		60/40	7.53/6.21	3.40	1150	24,600	2 hr Unbroken	+0.02	-0.003	31,100
120-13		60/40	7.53/6.21	3.40	1150	24,600	2 hr	+0.03	-0.004	31,400
121-113		60/40	7.53/6.21	3.40	1150	24,600	-5 min Broken	No test	No test	No test
87-125	80X218	70/30	7.32/9.14	3.34	1250	13,500[c]	10 hr Unbroken, 0.9% strain	+0.11	-0.113	No test
102-118		70/30	7.32/9.14	3.34	1250	24,600	20 min Broken	No test	No test	No test
104-125		70/30	7.32/9.14	3.34	1250	24,600	55 min Broken	No test	No test	No test
105-119		70/30	7.32/9.14	3.34	1250	24,600	1 hr Broken	No test	No test	No test
93-52		70/30	7.32/9.14	3.30	1250	21,400	2 hr Unbroken	+0.02	-0.074	42,500
100-117		70/30	7.32/9.14	3.34	1250	21,400	2 hr Unbroken, 0.2% strain	+0.05	-0.031	22,800
101-57		70/30	7.32/9.14	3.34	1250	21,400	2 hr Unbroken, 0.2% strain	+0.04	-0.022	32,700
91-17		70/30	7.32/9.14	3.34	1250	18,500	2 hr Unbroken, 0.2% strain	+0.04	-0.026	26,200
92-19		70/30	7.32/9.14	3.34	1250	18,500	2 hr Unbroken, 0.2% strain	+0.05	-0.023	19,700
93-113		70/30	7.32/9.14	3.34	1250	18,500	2 hr Unbroken, 0.2% strain	+0.05	-0.021	45,200
95-21		70/30	7.32/9.14	3.34	1150	24,600	7 min Broken	No test	No test	No test
106-136		70/30	7.32/9.14	3.34	1150	24,600	2 hr Unbroken, 0.03% strain	+0.03	-0.005	42,700
107-170		70/30	7.32/9.14	3.34	1150	24,600	2 hr Unbroken, 0.03% strain	+0.03	-0.004	32,400
108-200		70/30	7.32/9.14	3.32	1150	24,600	2 hr Unbroken, 0.08% strain	+0.01	-0.010	40,200
96-89		70/30	7.32/9.14	3.34	1150	21,400	2 hr Unbroken, 0.03% strain	+0.02	-0.004	42,200
97-56		70/30	7.32/9.14	3.32	1150	21,400	2 hr Unbroken, 0.03% strain	+0.02	-0.006	33,700
98-124		70/30	7.32/9.14	3.34	1150	21,400	2 hr Unbroken, 0.03% strain	+0.02	-0.005	39,800
88-116		70/30	7.32/9.14	3.34	1150	18,500	2 hr Unbroken, 0.03% strain	+0.03	-0.004	49,300
89-58		70/30	7.32/9.14	3.34	1150	18,500	2 hr Unbroken, 0.03% strain	+0.02	-0.002	43,500
90-84		70/30	7.32/9.14	3.34	1150	18,500	2 hr Unbroken, 0.03% strain	+0.03	-0.003	47,700
94-1	BeO Tube	0	0	2.76[d]	1150	24,600	1-1/2 hr Broken	No test	No test	No test
87-190	80X218	70/30	7.32/9.14	3.34	1250	No load	No test	+0.12	No test	44,000
91-115		70/30	7.32/9.14	3.34	1250	No load	No test	+0.03	No test	40,500
92-114		70/30	7.32/9.14	3.34	1250	No load	No test	+0.04	No test	40,000
88-121		70/30	7.32/9.14	3.34	1150	No load	No test	+0.02	No test	47,200
89-86		70/30	7.32/9.14	3.34	1150	No load	No test	+0.02	No change	46,800

[a] Three-point loading, 3-in. support.

[b] Time given is time at test temperature. Heating and cooling rates are similar in all tests.

[c] Four-point loading, 1-in. downcomer, 3-in. support.

[d] BeO tube 92% of theoretical density.

MUL-15965

strains imply that the stresses probably were not greatly reduced in the 2 hours, but we cannot place bounds on the stresses without more extensive creep data than are now available.

The 70/30 tubes appeared somewhat better than the 60/40 tubes in hot bend performance. The 70/30 tubes under an initial load of 21,400 psi did not break in 2 hours, and all 60/40 tubes did break. Two 60/40 tubes did hold for almost 2 hours, however, and their performance under 24,600 psi initial stress was comparable to that of the 70/30 tubes.

The strengths after hot bend testing for the 70/30 tubes were high. Six tubes tested at 1250°C under initial loads of 18,500 and 21,400 psi had a mean modulus of rupture after test of 31,500 psi (range 20,000 to 45,000 psi). Nine tubes tested at 1150°C under initial loads of 18,500, 21,400, and 24,600 psi had a mean modulus of rupture after test of 41,300 psi (range 33,000 to 49,000 psi). This compares favorably with virgin strengths of 80X218 tubes which are reported below. Tubes that experienced the same temperature and furnace atmosphere without load performed like those under load.

In conclusion:

1. The existence of creep did not permit a test of hot strength as a function of temperature, although the tubes did withstand initial stresses close to 24,600 psi.
2. The fuel losses encountered in this test were negligible as evidenced by the extremely small weight gains. In thermal stress-oxidation tests, the high fuel losses experienced up to 1250°C were apparently not due merely to the stresses applied. Note that in thermal stress tests as well as in these tests, some stress relaxation occurred during the interval of test (2 hours), so that the initial stresses listed in both cases did not apply throughout the test. The conclusion is that the high fuel losses in the thermal stress tests were more likely a result of higher temperatures than actually recorded in those tests.
3. There was virtually no degradation in room-temperature strength after these hot bend tests. This confirms that little or no structural degradation or oxidation occurred in the tests.
4. The BeO unfueled tube at 1150°C did not behave as well (broke) at 24,600 psi as the fueled tubes. Because the density of the BeO tube was lower (92%), this does not prove, but helps confirm, that the oxidation effect on the stressed fueled tubes was small.

5. The 70/30 tubes had a slight edge over the 60/40 tubes in the tests, but the differences are not profound enough to favor the 70/30 tubes over the 60/40 ones without other tests.

c. Additional preparations

1) ZrO_2-UO_2. Studies in this system have been concerned with powder compositions in the range summarized in the following table:

Fuel powder code number	Nominal composition			
	w/o ZrO_2	w/o UO_2	m/o ZrO_2	m/o UO_2
F-1	20	80	35.4	64.6
F-2	30	70	48.4	51.6
F-3	40	60	59.4	40.6
F-4	50	50	68.6	31.4
F-5	60	40	76.7	23.3
F-13	40	60[a]	59.4	40.6
F-14	40[a]	60	59.4	40.6
F-15	70	30	83.5	16.5
F-17	70	30[b]	83.5	16.5

[a] Added as the phosphate prior to reaction.

[b] UO_2 added as U_3O_8 prior to reaction.

Fuel powders F-1, F-2, and F-3 were prepared by reaction of blended oxide powders and by coprecipitation of the hydroxides from mixed salt solutions followed by calcination to mixed oxides. The latter products were then reacted to form the fuels under the same conditions as the blended oxide powders. Since comparable reaction products were obtained from both types of oxide blends according to x-ray diffraction analysis, the later fuel compositions were prepared by solid state reactions of the blended powders only.

The different ZrO_2-UO_2 compositions were reacted under different temperature conditions and analyzed for phases present by x-ray diffraction analysis. With few exceptions, all oxide powders up to 50/50 w/o ZrO_2-UO_2 (68.6 m/o ZrO_2 - 31.4 m/o UO_2) reacted in air below 1700°C showed the formation of $UO_{2.6}$ (U_3O_8). In the 76.7 m/o ZrO_2 - 23.3 m/o UO_2 mixtures, an orthorhombic "ZU" phase (possibly a compound) appeared under these conditions. Decomposition to U_3O_8, however, occurred at 1250°C in oxygen.

2) Oxidation testing. Samples of F-3 reacted powders (59.4 m/o ZrO_2 - 40.6 m/o UO_2) were oxidation-tested for 10 hours in 5 atmospheres of oxygen at 900 °C and at 1200 °C. Weight gains of the order of 1.5% to 2.5% were found for hydrogen-reacted samples at the lower heating temperature. No weight gains were found for samples prepared by reaction in air. At 1200 °C, however, all samples exhibited weight gains ranging from 0.5% to ~2.5%. The highest weight gains were also found to be related to the hydrogen-reacted samples. All the powders exposed to the 1200 °C treatment reverted completely to hexagonal U_3O_8 and monoclinic zirconia. The same conversion occurred at 900 °C, although less completely in several cases.

Air heatings were also performed with F-5 powders (76.7 m/o ZrO_2 - 23.7 m/o UO_2) which had been reacted in air at ~1525 °C for a 3-hour period. The following table summarizes the experiments performed and the results obtained.

Specimen	Treatment	Phases identified
F-5	None	Ortho. ZU[a] + mono. ZrO_2
F-5	Reheated to 1000 °C overnight in air	ZU + U_3O_8 + ZrO_2
F-5	Heated to 1200 °C, 24 hours, air	ZU + ZrO_2

[a] ZU signified ZrO_2-UO_2 solid solution or compound.

Thus, at higher temperatures in air the orthorhombic ZU phase seems to be stable, although it breaks down to U_3O_8 in the region of 900 °C to 1200 °C.

3) Effect of cycling in H_2 and O_2. Fuel powders F-4 (50 w/o ZrO_2) and F-5 (60 w/o ZrO_2) were reacted in H_2 at 1800 °C for 3 hours. Fueled BeO mixtures (8% UO_2) were prepared from these powders and extruded and sintered to provide samples for further evaluation.

Samples of the crushed F-4 reaction mix were oxidized at 1200 °C in flowing oxygen for 3 hours. Samples of the crushed F-5 powder were similarly oxidized at 1370 °C in flowing oxygen for 2 hours. The F-5 powders were then heated in a hydrogen atmosphere at 1200 °C for 2 hours and finally at 1370 °C for an additional 2 hours. Since air-reacted fuel powders blended with

BeO are sintered in a hydrogen atmosphere, the latter experiments were performed to determine the degree of conversion of the air-oxidized fuel phase to the reduced phase. In each case the oxidized powders showed U_3O_8 (trigonal or hexagonal) and monoclinic ZrO_2. During subsequent reduction FCT and FCC zirconia-urania solid solutions appeared.

4) High-zirconia mixes. Fuel powders F-15 and F-17 (78.6 m/o ZrO_2 and 21.4 m/o UO_2) were prepared and oxidation-tested at 1650°C in 2.5-liter/min flowing oxygen. The difference between the two samples was the fact that U_3O_8 was the uranium oxide powder reacted with the zirconia in the F-17 samples. The initial phases in both cases were found to break down under the test conditions to give predominantly a monoclinic ZrO_2 phase. Weight loss results indicate that further studies in this system are not warranted because of the poor performance of these fuels in meeting the established evaluation criteria.

5) $BeO-ZrO_2-UO_2$. Fuel powders F-1 through F-5 were incorporated in BeO by powder blending or "slurpitation" of the -325 mesh fuel powder from beryllium sulfate solutions and converting the precipitated mixtures to the mixed oxides. The mixtures were cold-pressed at 20,000 to 30,000 psi, presintered in air, and finally sintered under various conditions. The BeO bodies contained 6 or 8 w/o UO_2 added as the stabilized ZrO_2-UO_2 reacted powders. The sintering conditions studied included the temperature range of 1600 to 1750°C in hydrogen or air for a maximum soak period of 3 hours.

The results of these sintering studies indicated that the desired densification of the bodies could be obtained when sintering conditions of 1600 and 1650°C in hydrogen for a 2- to 3-hour soak period were used. This was found to be the case for powder blended mixtures and coprecipitated oxide mixtures. The compacts sintered in air under the same temperature and time conditions rarely attained the desired minimum degree of densification (97% theoretical).

Extruded samples of F-4 powder incorporated in BeO to contain 8 w/o UO_2 were prepared and used to study the effects on density of (1) prefiring temperature and time in air and (2) sintering temperature and time in hydrogen. The results of these studies showed that about 1% higher density was obtained at 1650°C for 3-hour heatings than at 1550°C for 4-hour heatings, irrespective of the prefiring conditions used (1-hour prefiring at 900°C or 2-hour prefiring at 815°C). Solid bodies composed of $BeO-ZrO_2-UO_2$ were exposed to 1150°C and 5 atmospheres of oxygen for 10 hours. These were examined by x-ray diffraction analysis. Hexagonal U_3O_8 appeared generally.

6) ZrO_2-UO_2 systems containing phosphate. The use of phosphates for forming a stabilized single-phase fuel was based upon the facts that these compounds have high melting points and cubic crystalline forms.

Powder blends of uranyl phosphate-zirconia (F-13) and zirconyl phosphate-urania (F-14) were prepared. The nominal mole % composition of these mixtures, on an oxide bases, was 40 m/o UO_2 and 60 m/o ZrO_2. The difference between the "F" powders was the cation-phosphate combination. The composition was selected for comparison with results from earlier ZrO_2-UO_2 reacted powders. Table II-15 lists a summary of the reactions carried out and data obtained from the investigations.

Since a single-phase product was not formed in the reactions performed, as evidenced by x-ray diffraction analysis, it was concluded that these compound compositions were not worthy of further study. The x-ray results for the compositions studied were similar to those for comparable ZrO_2-UO_2 reacted powder mixtures.

5. Thermal stress-oxidation testing

a. Errors. Data from 33 thermal stress tests were examined for possible systematic errors in the test. A heat balance was approximated to compare with the calculated heat transfer rate. Several important assumptions were:

1. That a heater with a closely spaced coils acts like a solid cylindrical heater, and has a uniform temperature.
2. That the power radiated by a very hot heater is relatively independent of the temperature gradient in a much colder sample.
3. That convection heat transfer from the heater to the sample can be neglected.
4. That the air stream receives all its heat energy from the sample.

It was found that in the average test about twice as much power was transferred through the sample as was required to produce the desired stresses. The standard deviation of this ratio was about ±10%.

Part of this high heat transfer rate was believed to be due to true sample temperatures being consistently higher than those recorded optically. To determine sample temperatures independently, a thermocouple was glued to the outside of a sample, and temperature readings were taken at a variety of

Table II-15. Reaction Conditions and Results Obtained with Reacted Phosphate-Containing Powder Blends F-13 and F-14, Nominal Compositions 60 m/o ZrO_2 - 40 m/o UO_2, on an Oxide Basis.

Fuel	Reaction conditions	Observations	X-ray phases present
F-13[a]	1550 °C, air, 4-1/2 hr Al_2O_3 crucible	a) Reaction with crucible b) Reaction product glassy	1) ZrO_2, monoclinic[b] 2) ? (very, very weak lines)
F-13[a]	1650 °C, air, 3 hr BeO crucible	a) Reaction with crucible b) Reaction product glassy	
F-13[a]	1450 °C, air, 6 hr Pt. crucible	a) No reaction with crucible b) Reaction product glassy	
F-13[a]	1750 °C, H_2, 3-1/2 hr BeO crucible	a) Reaction with crucible b) Reaction product well sintered, crystalline	1) FCT, a = 5.18, c = 5.25 2) FCT, a = 5.26, c = 5.47_9 3) ? (weak)
F-14[c]	1550 °C, air, 4-1/2 hr Al_2O_3 crucible	a) Reaction with crucible b) Reaction product glassy	1) ZrO_2, monoclinic[b] 2) ? (very, very weak)
F-14[c]	1650 °C, air, 3 hr BeO crucible	a) Reaction with crucible b) Reaction product glassy	
F-14[c]	1450 °C, air, 6 hr Pt. crucible	a) No reaction with crucible b) Reaction product glassy	
F-14[c]	1750 °C, H_2, 3-1/2 hr BeO crucible	a) Reaction with crucible b) Reaction product well sintered, crystalline	1) FCC, a = 5.34 2) FCT, a = 5.18, c = 5.25

---

[a] Uranyl phosphate reactant.

[b] a = 5.21, b = 5.26, c = 5.37, $\beta = 80° 32'$.

[c] Zirconyl phosphate reactant.

conditions. The data indicated that a turbulent flow in the bore caused optical readings of the sample to be 200 to 300 °C lower than actually existed. Attempts to verify this with temperature-indicating paints have not been successful. Work with thermocoupled samples is continuing.

The test temperatures reported here, and in earlier reports, have not been corrected for the above error in optical readings. The reader should bear in mind that the actual sample temperatures were higher than the nominal test temperatures shown in Table II-16.

b. Test results for UO_2-ZrO_2-fueled tubes. Samples containing a UO_2-ZrO_2 fuel in BeO (mix 80X206) were fired at four temperatures. It was hoped that samples with the highest room-temperature strengths (lowest firing temperature) would show more resistance to cracking. There was slightly less cracking in samples fired to 1600 and 1650°C, but no trend was seen in fuel losses as a function of the firing temperature. Complete test results are shown in Table II-16. Sample 22 differed markedly from the others; after testing, the bore was coated with a "bubbled" layer of nearly pure ZrO_2, while the tube contained massive crystals of nearly pure BeO. Because the inner ZrO_2 bore of the tube was maintained at the test temperature, its low thermal conductivity permitted the tube interior to reach much higher temperatures. For each group of samples fired at the same temperature (and having similar densities), higher test temperatures always resulted in higher fuel losses regardless of the range of stresses covered here. Several of the tests shown in Table II-16 were reported in the previous quarterly progress report (UCRL-6625, September, 1961); stress levels for these tests have been corrected for a minor error in the calibration of air flow rates.

Plans were made to run several samples at each of several temperatures and stress levels to show the effects of increasing stress at temperature. The samples were 5% UO_2 stabilized with ZrO_2 (mix 266-500-227-51). This series was stopped after five tests because of the unusual behavior of sample 26 at 1370°C. After testing, the sample had lost 59% of the fuel, and resembled sample 80X206-22 described above. Again, this could happen only at temperatures much higher than those recorded. The four samples reported at 1150°C do not show any increase in fuel loss as the thermal stresses were increased.

c. UO_2-ZrO_2-Y_2O_3-fueled tubes. Samples containing both ZrO_2 and Y_2O_3 to stabilize the fuel (mix 80X239 Y) were tested for fuel loss. These were extruded to Tory II-C size (0.230-in. i.d.), requiring high power levels for

Table II-16. Thermal Stress-Oxidation Test Results; All Tests Made in Air at 275 psia for 2 Hours, Except Where Noted.

Sample	UO_2 (w/o)	Additive (w/o)	Firing temp (°C)	Density (g/cc)	Special conditions	Nominal test temp[a] (°C)	σ_θ, σ_z (psi tension)	$\frac{\sigma K}{E \alpha}$ (watts/in.)	ΔUO_2 % by (analysis)	ΔUO_2 % by (γ-count)	Modulus of rupt. (psi)	Cracks	Appearance
Lot 80X206													
126	7.84	3.8 ZrO_2	1600	3.02		1150	15,300	16.9	+1		0	L	Black throughout
142	7.84	3.8 ZrO_2	1600	3.04		1260	11,600	12.8	-6		20,300	None	Black throughout
137	7.84	3.8 ZrO_2	1600	3.03		1370	11,600	12.8	-14		14,800	L	White along bore, then black
87	7.99	3.8 ZrO_2	1650	3.10		1150	15,000	16.6	-2		15,300	None	Black, few brown areas
96	7.99	3.8 ZrO_2	1650	3.12		1370	11,700	12.9	-13		20,900	None	White along bore, then black
170	8.00	3.8 ZrO_2	1700	3.24		980	15,000	16.6	-1		24,100[b]	None	Black bore, brown outside
179	8.00	3.8 ZrO_2	1700	3.23		1150	15,000	16.6	-7		24,700[b]	L, T	Black throughout
7	8.03	3.8 ZrO_2	1750	3.24		1150	15,500	17.1	-1		0	L, T[c]	Black bore, brown outside
17	8.03	3.8 ZrO_2	1750	3.26		1260	11,600	12.8	-2		18,500	None	Black bore, brown outside
22	8.03	3.8 ZrO_2	1750	3.24		1370	11,600	12.8	-96		0	L, T	White; ZrO_2 coat on bore
Lot BF-7B													
6	8.15	3.1 CeO_2	1550	3.10		1150	15,500	17.1	-4		2,600	L, T	Black throughout
13	8.15	3.1 CeO_2	1550	3.11	Air-anneal @ 1000°C	1150	15,500	17.1	-7		2,200	L, T	Black throughout
Lot 50X162													
14	5.20	0	1750	3.09		1150	15,700	17.3	-2		5,200	L, T	Black bore, brown outside
32	5.20	0	1750	3.09		1150	15,000	16.6	-2		3,100	L, T	Black throughout, some crazing
Lot 266-500-227-51													
4	5.14	4.71 ZrO_2	1700	3.20		1150	5,000	5.5	-6	-2		None	Black bore, brown outside
10	5.14	4.71 ZrO_2	1700	3.20		1150	10,000	11.1	-10	-3		None	Black throughout
--	5.14	4.71 ZrO_2	1700	3.20		1150	11,600	12.3	-3	-1		L[c]	Black bore, brown outside
30	5.14	4.71 ZrO_2	1700	3.20		1150	15,000	16.6	-2	0		None	Black bore, brown outside
26	5.14	4.71 ZrO_2	1700	3.20		1370	5,000	5.5	-59	-90		L	Gray; ZrO_2 coat on bore
Lot 80X239 Y													
59	8.14	All tubes 3.03 ZrO_2 7.38 Y_2O_3	1700	3.35		1150	15,000	16.6	0	-3		L, T	Black throughout
72	8.13		1700	3.35		1150	15,000	16.6	0	-3		L, T	Black throughout
58	8.07		1700	3.35	Tested only 1/3 hour	1370	15,000	16.6	-1	-3		L, T	Black throughout

[a] True temperature is higher than this; see text.

[b] Three-point loading; all others four-point loading.

[c] Sample cracked after it was removed from test furnace.

MUL-15966

thermal stress testing. Sample 58 tested at 1370°C was interrupted after only 20 minutes when the heater burned out. Chemical analyses showed no fuel loss after 2 hours at "1150°C," and a 1% loss after 20 minutes at "1370°C." Gamma counting showed 3% losses for all samples. (Chemical analyses are believed to be more reliable for fuel losses in thermal stress tests.) Examination under a binocular microscope showed no apparent damage other than typical thermal stress cracking. This fuel appeared to be more stable than any other fuel tested.

d. Miscellaneous fueled tubes. Samples of mix BF-7B contained CeO_2 in place of ZrO_2 to stabilize the fuel. Fuel losses were not decreased by the addition of CeO_2.

Samples of mix 50X162 had no additives to stabilize the UO_2, and were run for background information. Fuel losses were comparable with those in ZrO_2-stabilized samples at the same test conditions, and the 50X162 samples tended to craze, as observed in tests earlier this year.

e. Conclusions. A large error was found in measuring temperatures in thermal stress tests. Actual test temperatures are believed to be 200 to 300°C higher than those reported.

A UO_2-ZrO_2-Y_2O_3 fuel in BeO was the most stable mix tested to date.

Protective Coatings

1. Vapor phase Al_2O_3 coatings. The object of this study was to vapor-deposit Al_2O_3 coatings on BeO and fueled tubes and evaluate their effectiveness in preventing water attack at high temperature in moving moist air.

Vapor deposition of Al_2O_3 on hexagonal tubes is accomplished as follows: $AlCl_3$ is volatilized at about 135°C in a gas stream of CO_2, H_2, and CO. When this gas mixture passes over the surface of a hot tube, the Al_2O_3 is deposited out. CO is present to suppress the reaction so that Al_2O_3 is deposited as a uniform thick layer over the entire tube surface. Separate runs are required for the inside and outside.

In these experiments, BeO hexagonal tubes 4 inches long were completely coated by vapor deposition of Al_2O_3 and tested for water attack along with uncoated BeO tubes. One fueled tube was coated and included in these tests. Coating thickness ranged between 0.9 and 3.3 mils, figured by weight gain, after deposition for 30 minutes on the inside and 60 minutes on the outside.

The test conditions and results are listed in Table II-17. Six specimens were vapor-deposited with Al_2O_3 for testing in the chemistry blowpipe and thermal stress apparatus.

It was found that the alumina coating reduced the water attack on the BeO tube by a factor of about 20 in both the 1525 and 1550°C tests.

The 1550°C test was stopped after 4 hours to weigh the specimens (test 6). It was then continued for an additional 17 hours (test 7). The coated tube showed a weight loss of 0.04% in the first 4 hours and only 0.02% loss in the additional 17 hours.

Since the coated BeO tubes in all the individual tests above showed consistently low loss, it appears that the process is reproducible with sufficient control of the variables involved. This pertains to an experimental setup to do one side of one tube at a time.

Satisfactory coatings were obtained at coating temperatures between 1250 and 1350°C. The salt temperature for these runs varied from 130 to 140°C, which represents volatilization rate of about 100 to 400 mg/min. The deposition rate of Al_2O_3 varied between about 3 and 20 mg/min for these conditions. At the higher temperature (1350°C) the outside coating became roughened. A nominal 1-mil coating would vary between about 0.5 and 1.5 mils when viewed under a microscope. To obtain a smooth and dense-appearing coat, tube temperatures of 1250°C and salt volatilization temperatures of about 140°C appear most suitable.

2. Coating materials. The objective here is to find a coating material to protect BeO from high-temperature water attack. A review of the literature showed the oxides of the following materials to be stable in a humid, oxidizing atmosphere:

aluminum
cerium
chromium
cobalt
hafnium
magnesium
tantalum
thorium
titanium
zirconium
yttrium

The procedure is to press the coating material into pellets, sinter it and then subject it to the standard water-attack conditions; namely, 1550°C for 4 hours, 0.217-cfm air at a dew point of at least 90°F. If the weight loss of the material is sufficiently low during this phase of the study, the material is

Table II-17. Test Conditions and Results of Vapor-Depositing Al_2O_3 Coatings on BeO and Fueled Tubes.

Test Number	4	4	4	5	5	6	6	7	7
Material	BeO	BeO	8.36% UO_2-BeO Oralloy	BeO	BeO	BeO	BeO	BeO	BeO
Coated	No	Yes	Yes	No	Yes	No	Yes	No	Yes
Inside coating thickness, mils	--	1.0	1.5	--	1.0	--	1.7	--	1.7
Outside coating thickness, mils	--	1.7	0.9	--	3.3	--	1.8	--	1.8
Test Conditions[a]									
Air flow, fpm	15.6	15.6	15.6	15.6	15.6	24.0	24.0	24.0	24.0
Temperature, °C	1525	1525	1525	1525	1525	1550	1550	1550	1550
Time, hours	4	4	4	4	4	4	4	17	17
Dew point, °F	91	91	91	85	85	91	91	86	86
Test Results									
Uncoated wt, g	8.847	8.823	9.054	8.828	8.216	8.809	8.225	8.809	8.225
Pretest wt, g	8.847	9.478	9.558	8.828	9.262	8.809	9.016	8.782	9.013
After test wt, g	8.828	9.477	9.555	8.808	9.261	8.782	9.013	8.715	9.011
Weight loss, g	0.019	0.001	0.003	0.020	0.001	0.027	0.003	0.067	0.002
Percent loss	0.21	0.01	0.03	0.23	0.01	0.31	0.04	0.76	0.02

[a] Calculated average values.

applied to unfueled BeO tubes which are then tested to see if the coating effectively protects the BeO. If so, fueled tubes are then coated. At each coating step a check is made to see if the coating material is adversely reacting with the tube.

The materials which have been, or are in the process of being, evaluated are:

1. ZAT 1600 40 w/o ZrO_2 20 w/o Al_2O_3 40 w/o TiO_2
2. ZAT 1650 40 w/o ZrO_2 40 w/1 Al_2O_3 20 w/o TiO_2
3. ZAT 1700 40 w/o ZrO_2 50 w/o Al_2O_3 10 w/o TiO_2
4. 85 w/o ZrO_2 - 15 w/o Y_2O_3
5. 95 w/o ZrO_2 - 5 w/o CaO
6. CeO_2
7. MgO
8. CoO

Results are summarized in Table II-18. A microscopic examination of ZAT-coated BeO tubes revealed a reaction between the ZAT and the BeO, as evidenced by a great increase in grain size (at least 10 times) with very distinct grain boundaries and no coating layer. The tubes had a water-attack weight loss of 0.24%, the same as the uncoated tubes. These facts caused the ZAT materials to be dropped from consideration as coating materials for BeO.

The following conclusions can be drawn from the results:

1. ZAT and CoO cannot be used as coatings for BeO: ZAT reacts with BeO, while CoO shows too high weight loss.
2. ZrO_2-Y_2O_3, ZrO_2-CaO, CeO_2, and MgO show little or no weight loss when tested by themselves, and therefore might be useful as coating materials.

Mechanical Properties

1. Thermal stress. The previous work on thermal stress was concerned with unfueled BeO. The current period was devoted to experiments with short sections of tubes ("washers") of BeO + 5 w/o UO_2, 3/8 in. long except for one 3/4-in. specimen. The data are listed in Table II-19. The fueled samples have an outer-to-inner radius ratio of 3.39; hence

$$\frac{\sigma K}{E \alpha} = 0.0612\ Q.$$

Table II-18. Results of Water-Attack Tests on Various Coating Materials. Test Temperature, 1550°C; Duration, 4 hr; Water Carrier, Dry Compressed Air at 0.217 cfm.

Material	Sintering temp (for 1 hr in air) (°C)	Dew point (°F)	Water attack wt loss[a] (%)
ZAT 1600	1550	107	0.09
	1600	106	0.25
ZAT 1650	1550	115	0.08
	1600	115	0.03
	1650	93	0.13
ZAT 1700	1650	93	0.10
	1700	100	0.12
	1750	102	0.12
85 w/o ZrO_2 - 15 w/o Y_2O_3	1700	95	0.00
95 w/o ZrO_2 - 5 w/o CaO	1600	108	0.00
CeO_2	1600	100	0.10
CoO	1600	103	0.80
MgO	1600	95	0.00

[a] As a comparison, a group of BeO tubes of 99.2% theoretical density lost from 0.20 to 0.28 w/o under the same testing conditions.

Table II-19. Steady-State Thermal Stress Resistance of BeO + 5 w/o UO_2

Sample No.	Mean temp (°F)	Q (watts/in.)	$\frac{\sigma K}{E \alpha}$	$\frac{\text{No. fractured}}{\text{No. tested}}$	σ_f^a (psi)	Sample length (in.)
9	2345	168	10.3	2/4	11,590	3/8
8	2365	182	11.1	2/4	12,600	3/8
6	2500	163	10.0	4/4	12,000	3/8
8	2495	156	9.5	3/4	11,350	3/4
3	2530	128	7.8	0/4	9,480	3/8

[a] Calculated from $E\alpha/K$ data.

The data indicate that the BeO + 5 w/o UO_2 has a thermal stress resistance similar to unfueled BeO. (See previous quarterly report, UCRL-6625, Sept. 1961, p. 61.)

2. Compressive creep. Fuel stability problems in the $BeO-UO_2$ system have led to current efforts to find additive components that will improve stability. Of recent interest is the $BeO-UO_2-Y_2O_3$ ceramic. It has mechanical properties that apparently are suitable for present design conditions, but some uncertainty has been raised concerning its adaptability to higher temperatures [G. E. ACT Ceramic Materials Status Rept. XDC 60-12-17 (1961), Vol. I]. Olds and Perkins ["Phase Diagram Study of Oxide Systems," Progr. Rept. No. 4, Denver Research Inst., XDC 59-8-120 (1959); "Study of Ceramics and Intermetallic Materials," Progr. Rept. No. 9, Denver Research Inst., XDC 60-8-106 (1960)] observed a eutectic reaction between Y_2O_3 and BeO near 2900°F. In many structural materials, formation of small quantities of liquid phase can cause gross reductions in strength. (A good example is the effect of hot shortness in steel.) Because of this consideration, a limited study was undertaken to evaluate the compressive creep properties of $BeO-UO_2-Y_2O_3$ below and above the eutectic temperature.

Samples 1/2 inch high were obtained from one randomly selected supplier's hexagonal fuel element of composition BeO-6 w/o UO_2-7.3 w/o Y_2O_3. During production, this tube was (presumably) sintered at 2950°F in hydrogen for 2 hours. No macroscopic defects were revealed by radiograph and Zyglo techniques, and therefore it is assumed that specimen-to-specimen variations have been minimized by these quality controls.

Test results are given below:

Specimen No.	Stress (psi)	Temp (°F)	Time (hr)	Strain (%)	Predicted strain[a] (%)	Density (percent theoret.)	Grain size (microns)
1	3000	2700	6	0.8	0.5	99.5	30
2	500	3000	1	0.2	0.18	99.5	30

[a] Strain predicted for similar stress, temperature, and time, based on theoretical considerations [F. R. N. Nabarro, "Deformation of Crystals by the Motion of Single Ions," Report of a Conference on Strength of Solids, The Physical Society (London) (1948); C. Herring, "Diffusional Viscosity of a Polycrystalline Solid," J. Appl. Phys. 21 (1950)] and other experimental results [R. Chang, "Creep and Anelastic Studies in Polycrystalline Ceramics," J. Nuclear Materials 1 (1959); S. Austerman, "Diffusion of Beryllium in Beryllium Oxide," Atomics International NAA-SR-3170 (1958)].

Since it was believed that eutectic melting had not been attained in tests 1 and 2, similar tests were conducted at 3100°F and 500 psi stress. The load was applied before the samples were brought to temperature. At 3050°F and 3030°F, respectively, the samples abruptly failed. The results of these tests are as follows:

Specimen No.	Stress (psi)	Temp at failure (°F)	Time to failure above 3000°F (hr)	Predicted time[a] to failure (hr)	Density (percent theoret.)	Grain size (microns)
3	500	3050	0.02	50	99.5	30
4	500	3030	0.03	50	99.5	30

[a] Based on 5% strain and extrapolation of data taken at 2500-2800°F.

In this material, the major portions of the dispersed phases are located in the grain boundaries. Consequently, the eutectic reaction would most likely predominate in the grain boundaries. Formation of a liquid phase between the grains seems to have produced disastrous effects in this substance.

The normal "cordwood"-like fracture seen in BeO-UO_2 specimens (analogous to the cracking of ice) was not produced. Instead, a granular agglomerate was formed at failure, similar to the disintegration of a sugar cube in the presence of a small amount of water.

These results raise serious doubt whether fuel elements utilizing a combination of BeO and Y_2O_3 would be structurally reliable above 3000°F.

3. Hot bend creep (BeO-UO_2-ZrO_2). In the past (see previous report, UCRL-6625, Sept., 1961) tubes have displayed considerable creep under low hot-bend loads (6000 psi) at 1400 to 1450°C in 75-psia O_2. The objective of test 110 was to conduct a hot bend test in a nonoxidizing atmosphere to better assess the effect of oxidation on hot bend behavior.

The test was performed in a mildly reducing atmosphere. After loading a specimen (80X218, 7.32% UO_2, 70 ZrO_2/30 UO_2) to 21,400 psi the pressure vessel was evacuated to 10^{-2} mm Hg overnight at room temperature, pressurized to 25 psia H_2, and then pressurized further with argon to 75 psia total. The specimen was heated to 600°C and the temperature held constant for 3 hours to get rid of any oxygen in the system. The vessel was depressurized through a bubbler to one atmosphere, purged once with 35-psia argon and finally repressurized with 75-psia argon to start the test. The total time at 600°C was about 5 hours.

Figure II-8 gives the time-temperature plot for test 110 starting from 600°C. The major portion of creep occurred during approximately 38 minutes at 1400°C.

Table II-20 summarizes test 110 as well as tests 76 (in oxygen) and 86, which have been reported in the September Quarterly (UCRL-6625). Test 86 was conducted in argon which was contaminated with traces of oxygen, as evidenced by darkening of the tube.

In conclusion, it appears that oxidation reduces the strain attainable prior to failure.

FABRICATION DEVELOPMENT

Fuel Element Fabrication Facility

1. Summary. The ceramic quality of LRL tubes has been substantially improved. Recognition of the importance of a rough surface finish in the die to the quality of the extrusions resulted in a major reduction in transverse cracking.

With the switch to Tory II-C tube dimensions the problems of dimensional control were accentuated. Thin-walled tubes tend to slump out of round in the production process. Several approaches to the alleviation of this problem are underway. Questions raised about dimensional variations in production have resulted in a more careful consideration of the uncertainties in the production process, a consideration of the gaging methods and techniques being used, and a consideration of the interpretation of the dimensional data.

2. Extrusion. The problem of transverse cracking of tubes which has long plagued the extruder operations appears to be solved. The answer to the riddle of the "magic die" seems to lie in the internal surface finish of the die. The "K" style die has an 80- to 100-micro-inch finish, comparable to the "magic die" finish, and is a straight-through hexagonal with no radius or chamfer. To date, out of 16 different extrusions examined in the pre-starch burn Partek examination, 729 tubes out of 756 have shown crack-free surfaces. This is a 96% recovery, which is certainly comparable to the "magic die" recovery of 94%. The rough surface of the "K" style die consistently produces crack-free tubes.

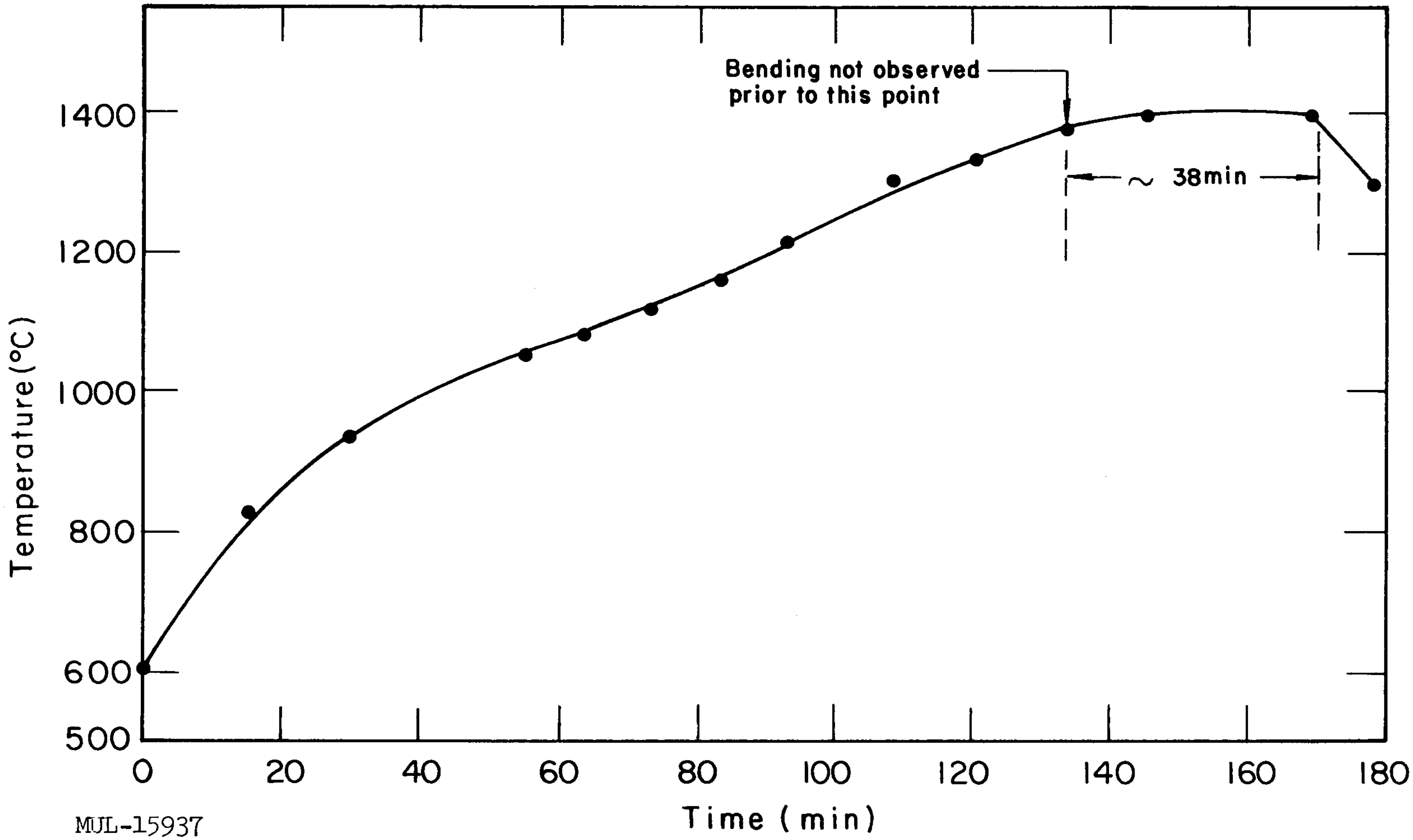

Fig. II-8. Time vs temperature for hot bend test No. 110 in oxygen-free atmosphere at 75 psia.

Table II-20. Results of Hot Bend Tests at 1400°C in Oxidizing and Nonoxidizing Atmospheres at 75 psia. All Samples Presintered at 1700°C/5 hr.

	Sample No.		
	110-146	76-14	86-22
Tube description	80X218	244-800-192-21	249-800-201
Nominal % UO_2/% ZrO_2	7.3/9.1	7.8/8.7	8.0/5.0
Test atmosphere	Argon	Oxygen	Argon[a]
Initial hot bend load[b] (psi)	21,400	6,000	15,000
Performance	No failure.	Failure.	Failure.
	4.0% strain in 38 min	0.8% strain in 116 min	1.5% strain in 120 min

[a] Contained traces of oxygen.

[b] Three-point loading, 3-in. span.

Although the cracking problem seems to be solved, tube curvature on the belt still exists. This curvature, though not severe enough to prevent the insertion of mandrels in the tubes, seems to be affected by the temperature in the dryer, and possibly the depth of cut. Die and mandrel misalignment can be ruled out as a cause of curvature for two reasons: (1) The tubes are coming off the end of the mandrel straight, and (2) the orientation of the curvature (left, right, up or down) varies during a given extrusion. If the mandrel were not aligned with the die then the tubes would be curving as they come off the mandrel, and always curving in the same direction.

A nose piece has been added to the cam which reduces the size of the extruder plug from about 700 to about 400 grams.

Recent cross-flats measurements of starch-burned tubes show that they are being squashed out of hexagonal shape at some point in the operation before they are sintered. The results of the measurements are summarized in Tables II-21 and II-22. They show that most of the squashing occurs between the flats that are at top and bottom of the tube as it comes out of the extruder and down the belt, with a lesser amount of distortion occurring between the other two sets of cross-flats. Measurments on extrusion 1312 which were made before the tubes were starch-burned indicate that the tubes are already squashed before they enter the starch burner. Measurements on extrusion 1315, which

Table II-21. Average Cross-Flats Measurements on Starch-Burned, Thin-Walled BeO Tubes.[a]

Extrusion No.	C.F. 1[b] (mils)	C.F. 2[c] (mils)	Difference, 2 - 1	C.F. 3[d] (mils)	Difference, 3 - 1	Remarks
1303	368.2	371.4	3.2	372.2	4.0	
1305	369.9	372.5	2.6	373.6	3.7	
1307	370.2	371.6	1.4	372.8	2.6	
1309	369.4	370.9	1.5	372.3	2.9	
1310	369.0	371.3	2.3	372.8	3.8	
1311	369.1	372.4	3.3	373.3	4.2	
1312	367.7	371.9	4.2	373.0	5.3	Air-dried
1313	367.8	371.1	3.3	371.8	4.0	

[a] Ten tubes per extrusion were measured with nine cross-flats measurements per tube.

[b] C.F. 1 is the pair of cross-flats that are top and bottom as the tube is riding down the belt in the conveyor.

[c] C.F. 2 is the average of the pair of cross-flats that is nearest in size to C.F. 1.

[d] C.F. 3 is the average of the third pair of cross-flats on each tube.

Table II-22. Average Cross-Flats Measurements on BeO and Fueled Tubes.

Extrusion No.	C.F. 1[a] (mils)	C.F. 2[b] (mils)	Difference, 2 - 1	C.F. 3[b] (mils)	Difference, 3 - 1	Remarks
1271	385.1	388.4	3.3	386.7	1.6	2% - Thick wall
1273	386.6	386.9	0.3	386.9	0.3	8% - Thick wall
1284	392.1	392.2	0.1	391.7	-0.4	2% - Thin wall
1292	392.2	393.3	1.1	392.4	0.2	8% - Thin wall
1315	369.0	372.3	3.3	372.4	3.4	BeO - No heat on conveyor, air-dried on snoeshoe
1315	367.7	371.3	3.6	371.3	3.6	No heat on conveyor, air-dried on belt.

[a] C.F. 1 is the cross-flats pair that are top and bottom as the tube is riding down the belt in the conveyor.

[b] C.F. 2 is always chosen to have the same orientation with respect to C.F. 1; similarly for C.F. 3.

was extruded without heat in the conveyor system, indicate that the slumping is not due to a thermoplastic effect.

It should be pointed out that the results in Tables II-21 and II-22 are averages and do not necessarily present an accurate picture of a given tube. Extrusions which have close cross-flats averages do not necessarily have small spreads between the maximum and minimum readings on each tube.

3. Starch burn-out cycle. A new starch burn-out cycle was determined for the methyl cellulose, polyvinyl alcohol, and water binder now used in extruding fuel elements.

Unfueled and extruded beryllia tubes having 26.2% total combustible were air-dried over night and then starch-burned on two cycles as shown in Fig. II-9. No visual damage, such as spalling or longitudinal cracking, was observed for either cycle. Tubes sintered from these tests showed no loss in density. Conclusion: Extruded fuel elements can be starch-burned using either cycle without harming the quality of the tube.

4. Sintering. The sintering operation in the small batch kilns has become routine. Batch size is limited to 40 tubes (5 plates out of 8) because of poor vertical temperature distribution in the kilns. Additional heating elements are being designed for the bottom of the kilns to bring the temperature of the bottom plates up to that of the upper plates.

Data are being accumulated on a number of variables affecting tube straightening. These are:

1. Starch-burned tube camber.
2. Sintered tube camber.
3. Groove straightness in kiln furniture.
4. Straightness of sintering mandrel.
5. Orientation of tube in kiln furniture.

No firm conclusions can be drawn as yet.

The Huppert kiln remains in standby condition.

5. Evaluation of tubes containing flaws by modulus of rupture. The objective was to compare the modulus of rupture before and after oxidation of fuel elements which are "flaw-free" with those showing defects according to Zyglo and radiographic inspection tests. Currently tubes are accepted or rejected based on low and high density inclusions (radiograph) and on "cracks" (Zyglo).

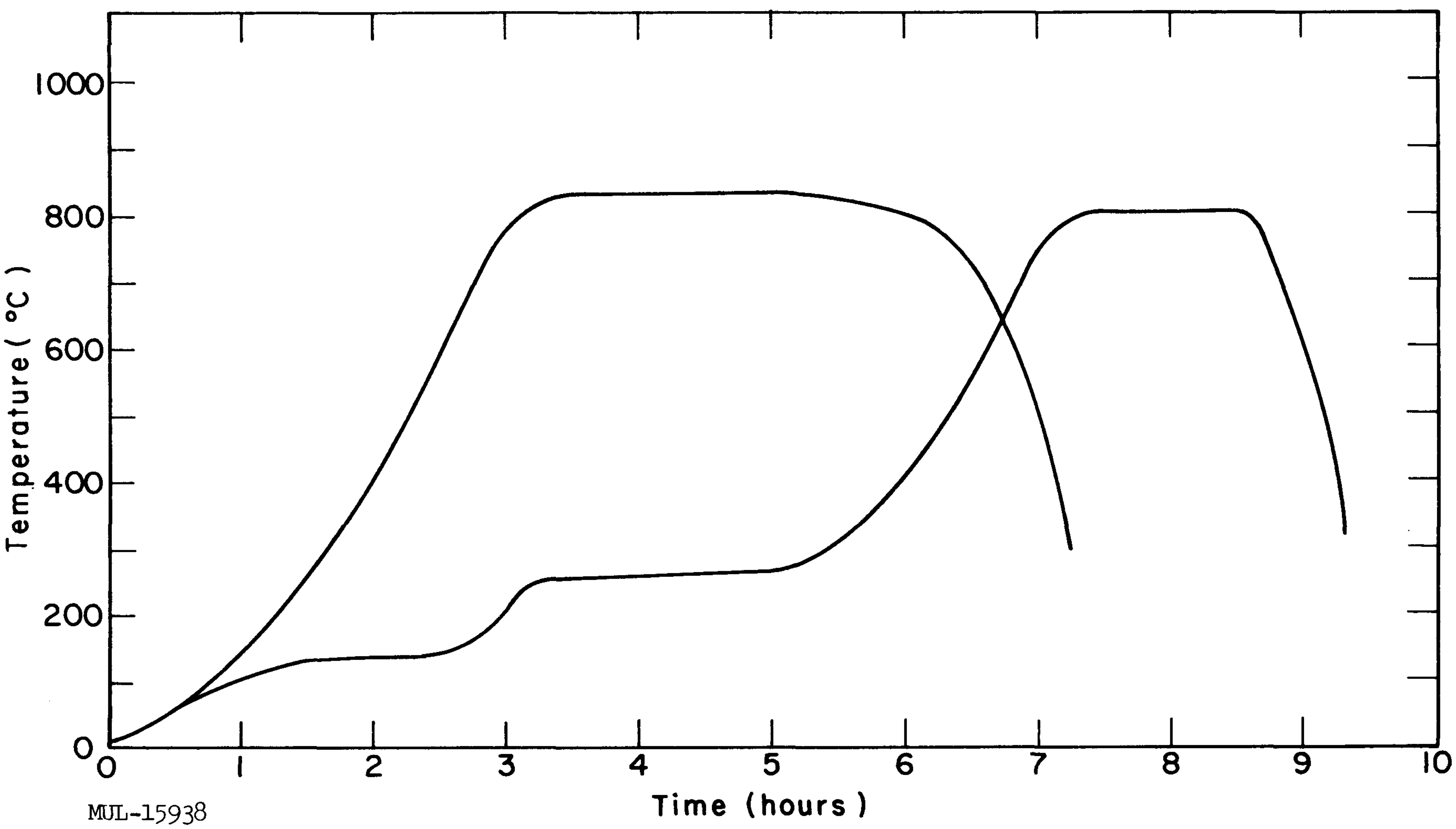

Fig. II-9. Starch burn-out cycles used to test effect of starch burning on extruded beryllia tubes.

There is a question as to what effect these flaws have on actual usable properties of the tubes such as strength, oxidation resistance, etc. In many cases, "cracks" determined by Zyglo may be only surface marks.

The modulus-of-rupture values were grouped into segments of 5000 psi and their distribution values are shown on Figs. II-10, II-11, and II-12.

A group of tubes (80X206) with a 60/40 m/o ZrO_2-UO_2 ratio were sintered at 1700 °C for 5 hours and then oxidation-tested (Table II-23). Fourteen tubes with no defects were broken without oxidation testing to establish a base strength of these tubes. The average modulus of rupture was 34,700 psi, with a range of 26,600 to 43,300 psi. Nine tubes (no defects by radiograph and Zyglo inspection) were then tested in 75-psia oxygen at 1400 °C for 10 hours. Their average strength was 34,300 psi, with a range of 31,500 to 37,000 psi. Eight tubes with a multitude of defects were also tested in high pressure oxygen. The average strength was 30,700 psi, with a range of 26,600 to 37,000 psi.

The forms of the frequency distribution curves in Figs. II-10, II-11, and II-12 suggest a strong similarity between the strengths of the transversely cracked tubes and the flaw-free tubes. The means, variances, and standard deviations of these tubes are summarized in Table II-24.

A comparison of the variances, which are a measure of the heterogeneity of the material to the strength tests, indicates no significant difference in the variability in strength between transversely cracked tubes and flaw-free tubes in batches 80X219 and 80X218 (1700 °C). The variances were barely significant for batch 80X218 (1750 °C).

The average strengths of the transversely cracked tubes and the flaw-free tubes in batches 80X219 and 80X218 (1700 °C) were compared. In batch 80X219, the flaw-free tubes were, statistically, significantly stronger than the transversely cracked tubes, although only by 3880 psi. In batch 80X218 (1700 °C) the strengths were not significantly different.

It appears that transverse cracks observed by Zyglo are not a good enough criterion for rejection of a tube, based on strength data alone. If we use an arbitrary lower limit of 20,000 psi, for example, then of the transversely cracked tubes we are presently rejecting 80% (80X219), 85% 80X218 (1750 °C), and 90% 80X218 (1700 °C) of the "good" ones. Furthermore, within the flaw-free tubes we are accepting 8% (80X219), 6% (80X218-1750 °C), and 6% (80X218-1700 °C) which test less than 20,000 psi.

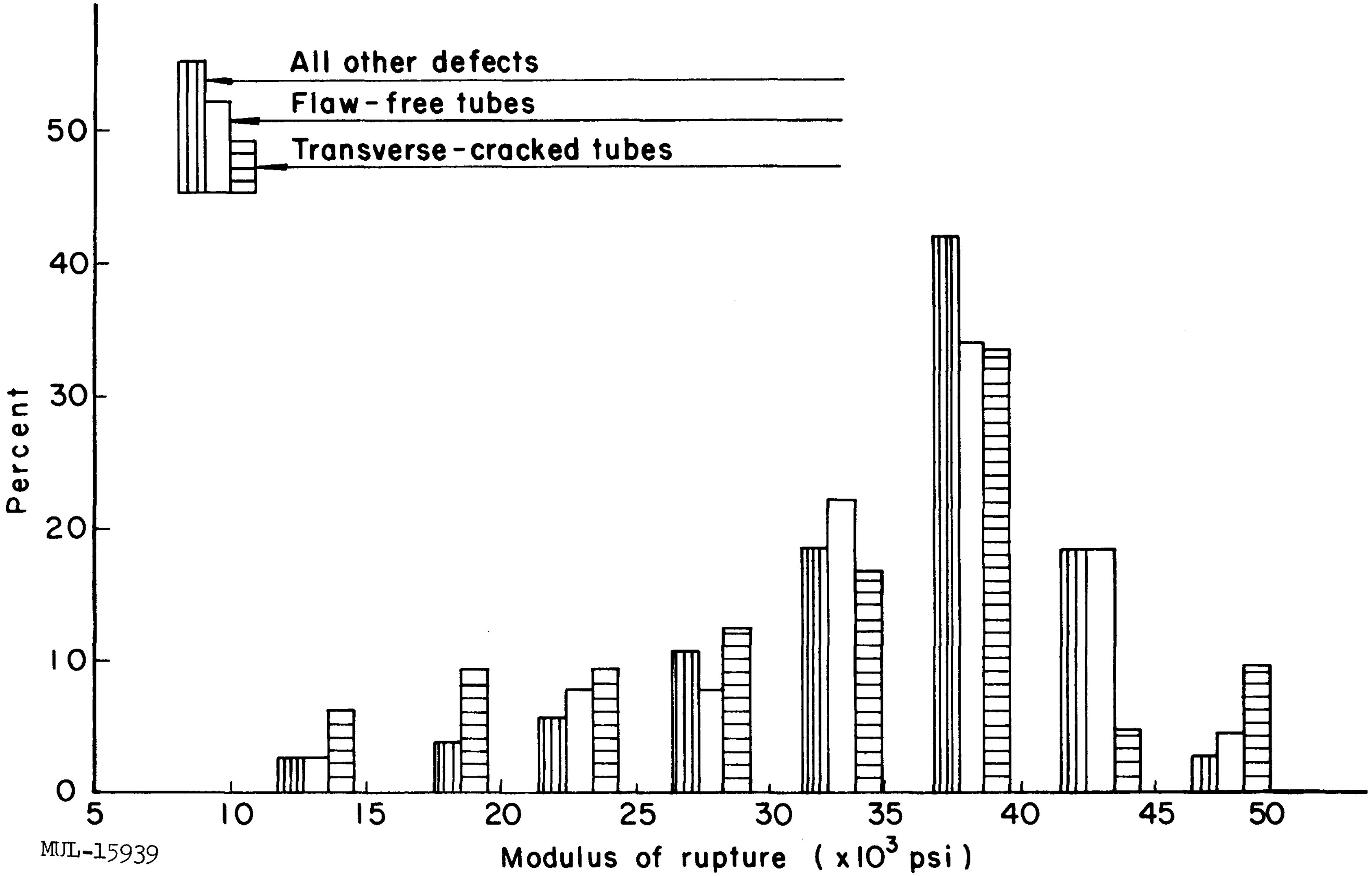

MUL-15939

Fig. II-10. Modulus-of-rupture comparison of flaw-free, transverse-cracked, and otherwise defective fuel tubes (mix 80X218, 70/30 m/o ZrO_2-UO_2, sintered 5 hours at 1750°C).

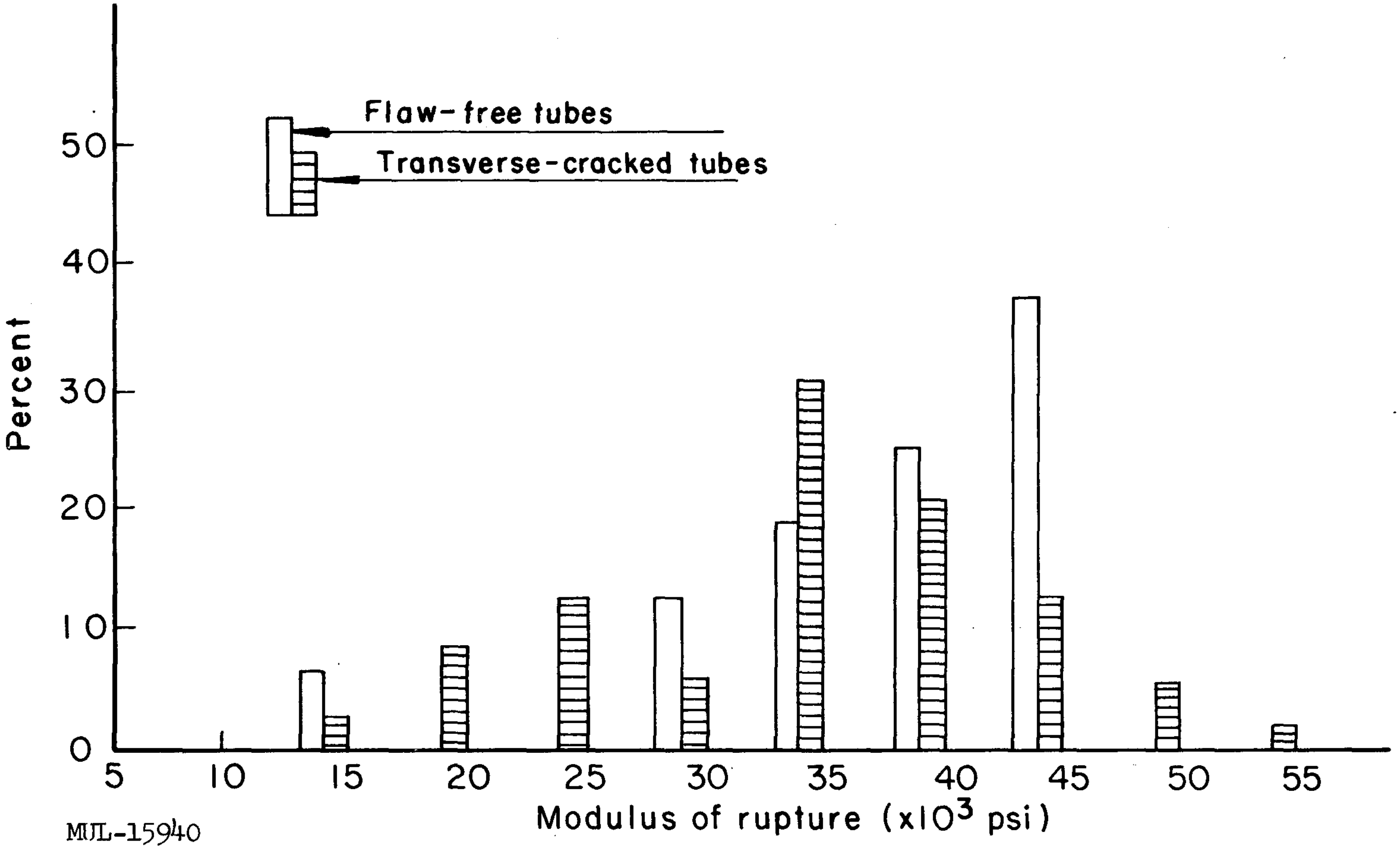

Fig. II-11. Modulus-of-rupture comparison of flaw-free and transverse-cracked fuel tubes (mix 80X218, 70/30 m/o ZrO_2-UO_2, sintered 5 hours at 1700°C).

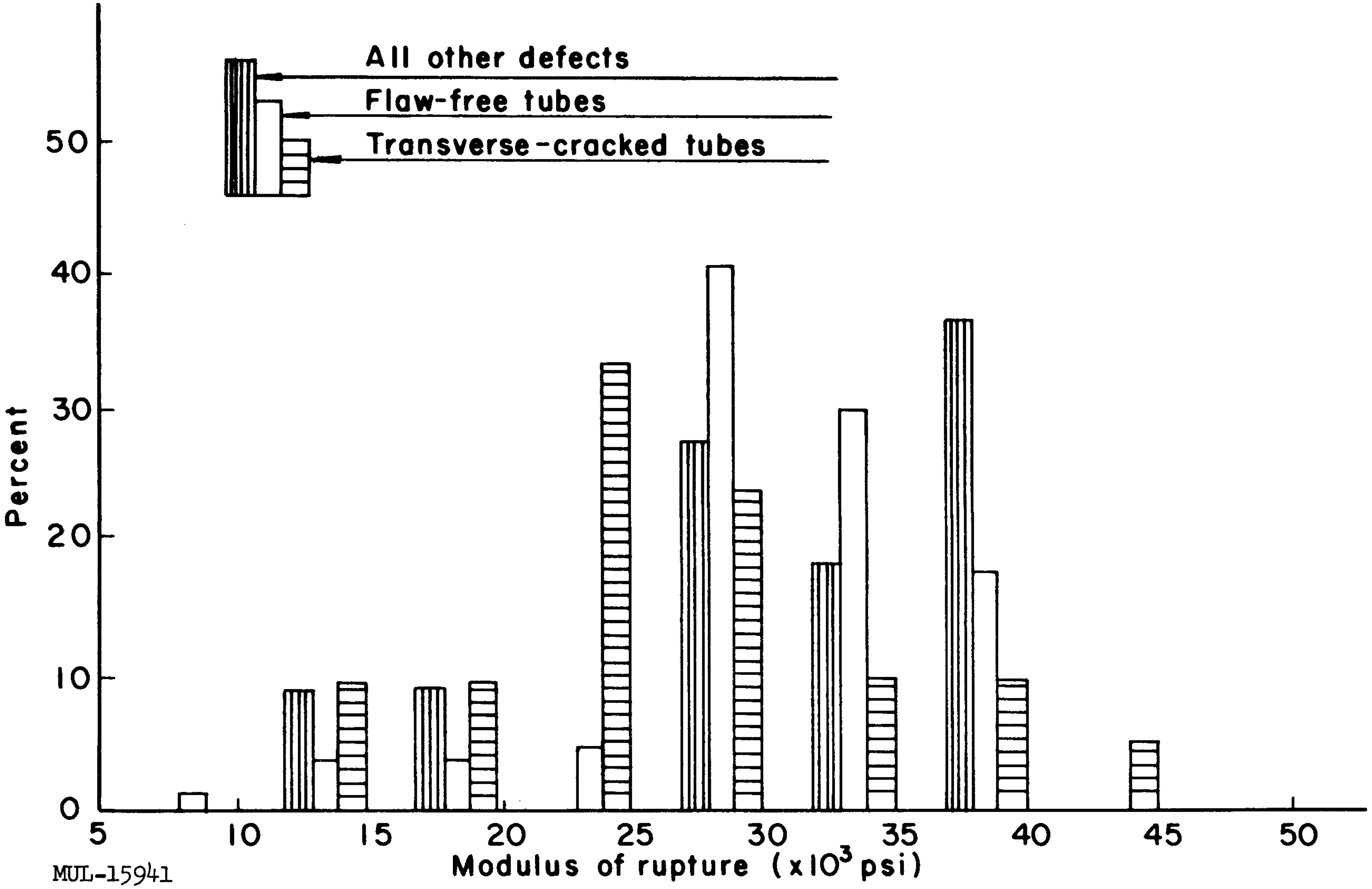

Fig. II-12. Modulus-of-rupture comparison of flaw-free, transverse-cracked, and otherwise defective fuel tubes (mix 80X219, 60/40 m/o ZrO_2-UO_2, sintered 5 hours at 1700°C).

Table II-23. Results of Modulus-or-Rupture Tests on BeO-ZrO_2-UO_2 Tubes. Both "Flaw-Free" and "Defective" Tubes Tested, With and Without Oxidation (75-psia O_2).

Specimen No.[a]	Oxidation test conditions (°C/hr)	Mod. rupt.[b] (psi)	Defects before test
38	No test	32,000	No defect
40	"	26,600	"
41	"	41,200	"
42	"	35,100	"
44	"	34,100	"
45	"	33,300	"
49	"	33,100	"
50	"	33,900	"
52	"	35,200	"
57	"	34,600	"
58	"	43,270	"
59	"	37,900	"
62	"	31,200	"
73	"	37,200	"
55	"	38,500	Transverse crack
67	"	33,800	Low density inclusions
		(34,700 avg)	
33	1400/10	35,000	No defect
39	"	31,500	"
47	"	37,000	"
48	"	33,200	"
51	"	34,100	"
63	"	35,200	"
64	"	34,700	"
69	"	35,900	"
72	"	32,200	"
		(34,300 avg)	
46	1400/10	27,500	Longitudinal crack
54	"	30,000	Low dens. incl.
60	"	34,100	"
61	"	37,000	Long. and transv. cracks
65	"	26,600	Low dens. incl. and long. crack
70	"	25,900	" "
71	"	32,600	Transverse crack
43	"	32,200	Longitudinal crack
		(30,700 avg)	

[a] All tubes 80X206 (nom. comp. 7.90 w/o UO_2 - 3.77 w/o ZrO_2), presintered 5 hours at 1700°C.

[b] Four-point loading, 3-in. support, 2-in. downcomer.

Table II-24. Means ($\overline{x}$), Variances (σ^2), and Standard Deviations (σ) of Modulus-of-Rupture Results for Flaw-Free, Transversely Cracked, and Otherwise Defective Tubes.

	Flaw-free	Transversely cracked	Other flaws
Batch 80X219 (1700°C/5 hr)			
n	87	21	11
$\overline{x}$	29,580	25,699	29,848
σ^2	36.9×10^6	55.71×10^6	59.8×10^6
σ	6075	7463	7733
Variance test[a]	$F^{86}_{20} = 1.5$, not significant		--
Mean test[a]	$t = 2.5$, sign. at 95% level		--
Batch 80X218 (1750°C/5 hr)			
n	118	66	38
$\overline{x}$	34,504	31,698	35,202
σ^2	58.1×10^6	90.3×10^6	44.4×10^6
σ	7622	9502	6663
Variance test[a]	$F^{65}_{117} = 1.55$, just sign. at 95% level		--
Mean test[a]	Not appropriate		--
Batch 80X218 (1700°C/5 hr)			
n	16	73	--
$\overline{x}$	35,359	32,603	--
σ^2	62.5×10^6	76.4×10^6	--
σ	7906	8741	--
Variance test[a]	$F^{72}_{15} = 1.22$, not significant		--
Mean test[a]	$t < 1.0$, not significant		--

[a] Variance test and mean test are between flaw-free and transversely cracked specimens.

Does the criterion "transverse cracks" separate one group of tubes from another? Generally speaking, tubes without transverse cracks (i.e., accepted by Zyglo) are slightly stronger and slightly more homogeneous to modulus of rupture. However, too many tubes are rejected by Zyglo which, based on strength alone, would be adequate for our purposes. It is now suggested that the group of transversely cracked tubes be examined to see which of them are the weakest. Perhaps one type of transverse crack is "worse" than another. After this has been done a re-evaluation of the transverse-crack criterion for accepting or rejecting is in order.

It is also apparent that the presence of various "defects" has only a small effect on strength after oxidation testing at 1400°C for 10 hours.

SECTION II. GENERAL CHEMISTRY

ANALYTICAL AND SUPPORT ACTIVITIES

Determination of Yttrium and Zirconium in Fueled BeO

Two new procedures for determining yttrium and zirconium in fueled BeO have been developed. The procedures allow determination of Y and Zr without prior separations.

The samples are dissolved in the usual manner and diluted to volume, then aliquots are taken for U, Zr, and Y. The final solution should be 10% in H_2SO_4. An aliquot containing 0.5 mg Zr is taken and diluted to 50 ml. An approximately twofold excess of EDTA (ethylenediaminetetraacetic acid) is added and the solution is heated but not boiled. It is then allowed to cool and the excess EDTA is back-titrated photometrically at 2815Å with standard bismuth solution, using a recording spectrophotometer.

For the Y determination, EDTA exceeding the combined Y and Zr is added to an aliquot containing 5 mg Y. After the pH is adjusted to 2, the solution is heated just short of boiling and allowed to cool. The pH is adjusted to 5.5 and the Y determined by back titrating the excess EDTA with standard zinc solution using dithizone in chloroform as an extractive end point. The zirconium is subtracted from the results.

Electron Microscopy

A study of BeO powders which had been sorted according to mesh size has been completed. It was found that the size of the individual particles is generally the same for 20 mesh as for 200 mesh; the gross size of the material is determied by the degree of agglomeration.

Several BeO powders from commercial vendors were examined using the electron microscope. It was found that the size, shape, and agglomerate state of the BeO particles are directly related to the method by which the powder was prepared. The methods by which these specimens were prepared can therefore be inferred, at least in part, by electron microscopic examination.

Surface examination experiments have been performed on BeO tubes fired at 1500, 1600, 1700, and 1800°C for 1/2, 2, 4, and 8 hr. A method of obtaining direct positive replicas from the BeO tubes was found and used for the 1700 and 1800°C specimens. The resolution of detail was better in these replicas than in the previously used cellulose acetate film replicas, so some of the 1500 and 1600°C specimens are being redone.

MATERIALS DEVELOPMENT

Oxidation Tests on F-48 Alloy

Specimens of F-48 alloy were heated isothermally at temperatures ranging from 1100 to 1300°C, and at pressures from 1 to 10 atm oxygen. In the previous quarterly report (UCRL-6625, Sept., 1961) the results of heatings in 1 atm oxygen at temperatures to 1000°C were given.

Since no spalling of the oxidation layer was observed, the weight change data were considered a measure of the extent of oxidation. No correction was made for the volatility of MoO_3 and WO_3. The results are given in Figs. II-13 and II-14.

The surface recession of the sample was calculated from the observed weight change, assuming formation of Nb_2O_5, WO_3, MoO_3, and ZrO_2. No measurement was made of oxygen penetration into the metal. The data are given in Tables II-25 and II-26.

Oxidation Tests on Commercially Coated F-48 Alloy

In the previous quarterly report, the oxidation behavior of some refractory coatings (Supplier #1) on F-48 alloy was described. During this quarter, the work was continued and oxidation studies were begun on coatings prepared by Supplier #2. Table II-27 gives the data on two Supplier #1 specimens, and Table II-28 gives the results for a group of Supplier #2 specimens. Isothermal weight change data are included in Fig. II-15 for the latter group. The data presented are characteristic of 2-mil-thick Supplier #2 coats, and 5- to 7-mil-thick Supplier #1 coats.

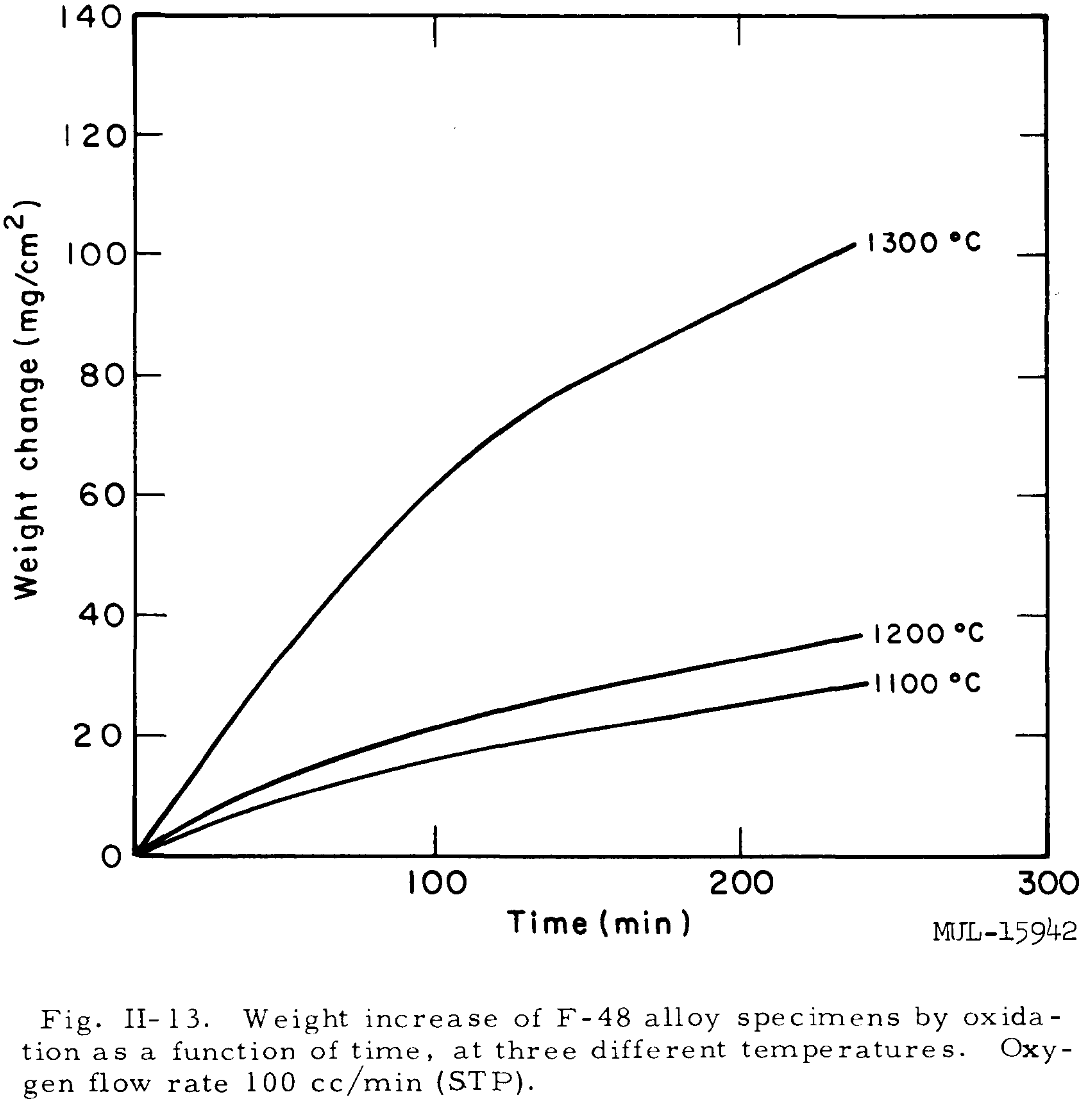

Fig. II-13. Weight increase of F-48 alloy specimens by oxidation as a function of time, at three different temperatures. Oxygen flow rate 100 cc/min (STP).

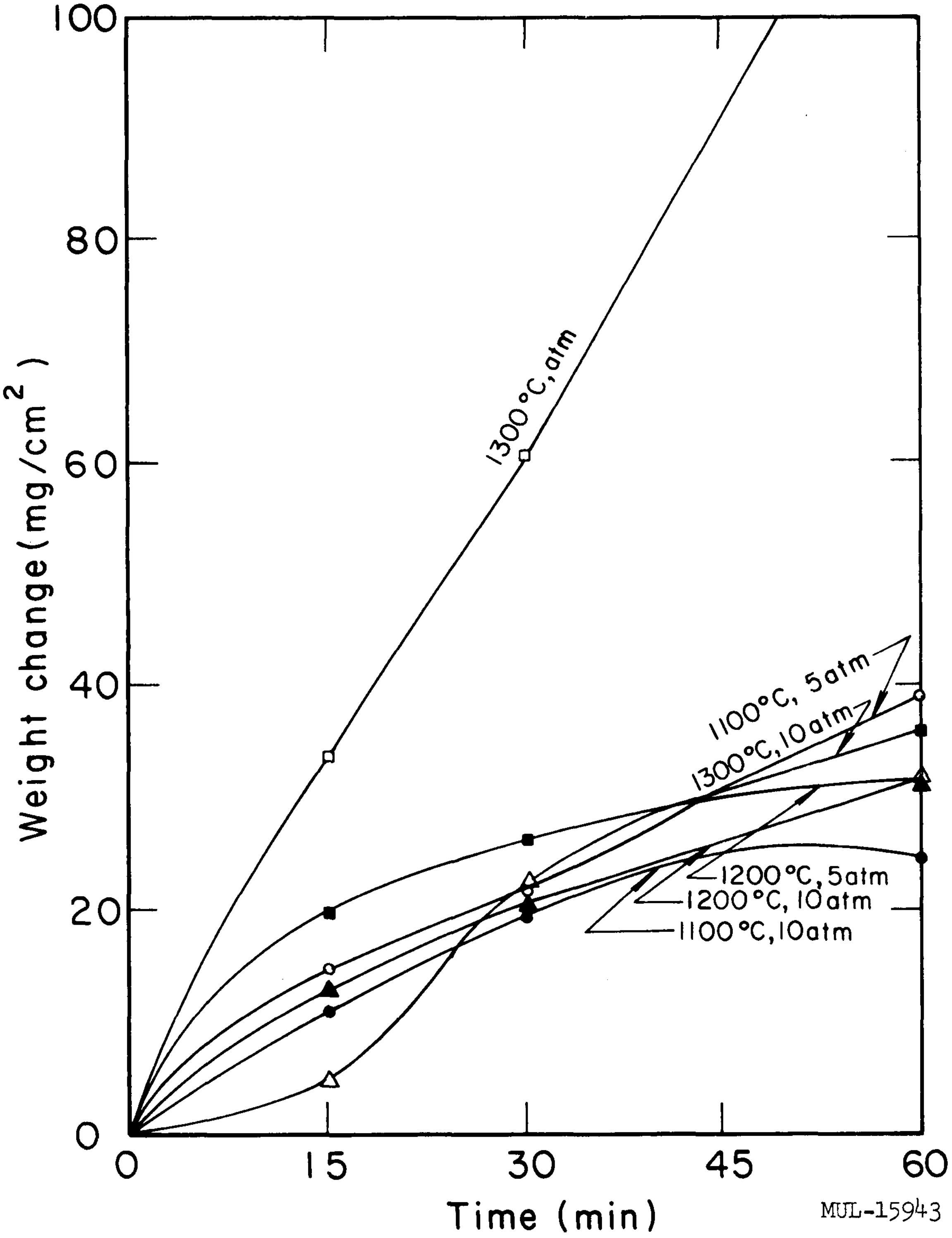

MUL-15943

Fig. II-14. Weight increase of F-48 alloy specimens by oxidation as a function of time, at three different temperatures and two pressures. Oxygen flow rate 700 cc/min at 25°C.

Table II-25. Surface Recession Upon Oxidation of F-48 Alloy Under 1 Atmosphere Oxygen.[a]

Temperature (°C)	Surface Recession In 120 min (mils)	 In 240 min (mils)
1100	1.8	2.7
1100	1.6	2.5
1170	2.5	3.5
1200	2.3	3.4
1270	4.3	6.6
1300	6.6	9.7

[a] Flow rate was 100 cc/min of oxygen (STP).

Table II-26. Surface Recession Upon Oxidation of F-48 Alloy Under 5 and 10 Atmospheres Oxygen.[a]

Temperature (°C)	Pressure (atm)	Surface Recession In 15 min (mils)	 In 30 min (mils)	 In 60 min (mils)
1100	5	1.4	2.1	3.7
1200	5	0.5	2.2	3.1
1300	5	3.2	5.9	12.5
1100	10	1.1	1.9	2.4
1200	10	1.2	1.9	3.1
1300	10	1.9	2.5	3.4

[a] Flow rate was 700 cc/min of oxygen (1 atmosphere, 25°C).

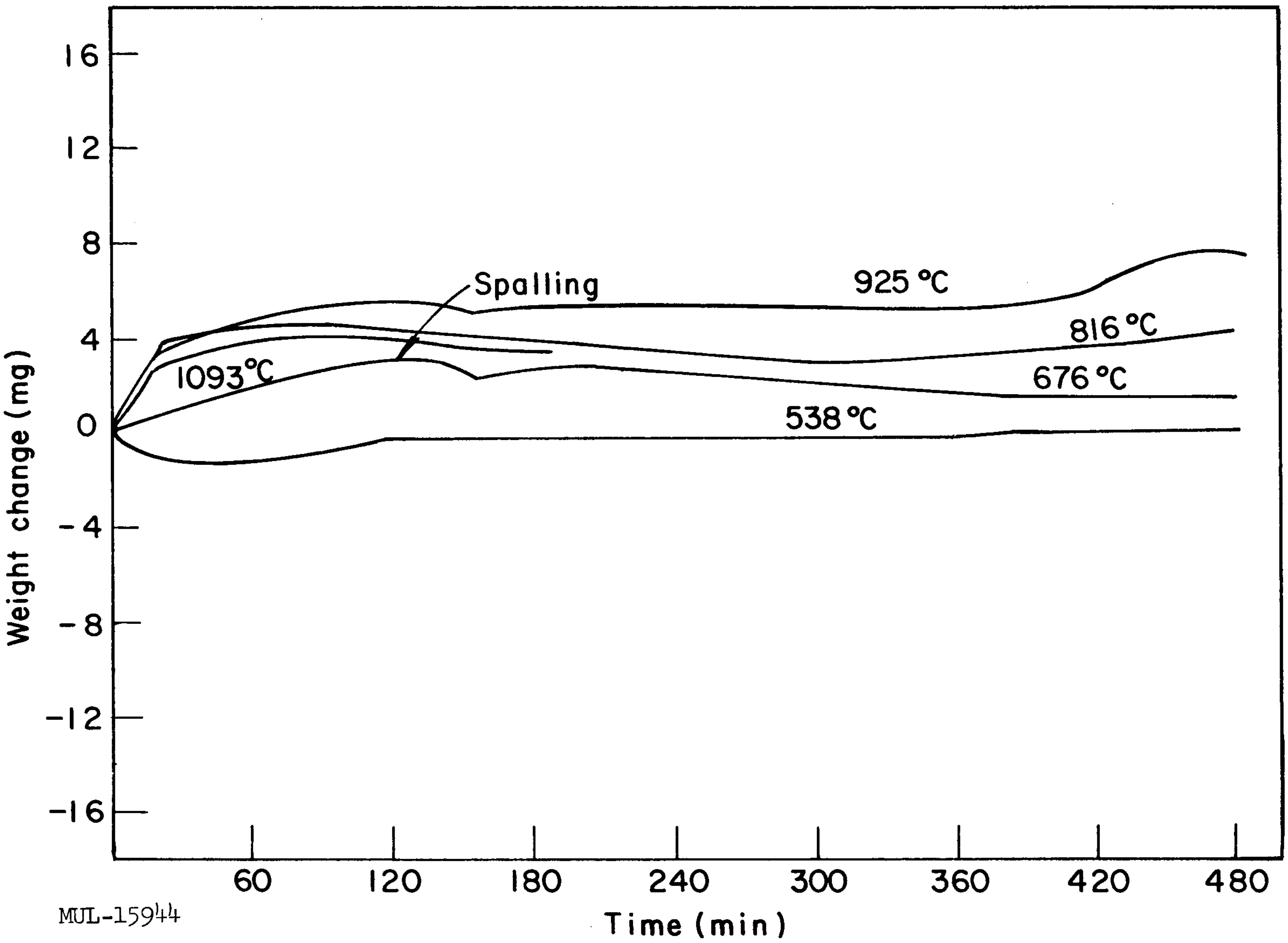

Fig. II-15. Weight change of coated F-48 alloy (coated with Supplier #2's coating) as a function of time at several different temperatures under oxygen at 1 atm. Surface area, 5.10 cm^2.

Table II-27. Heating Data for Supplier #1 II-IX Coated F-48 Specimens in 1 atm Oxygen.[a]

	Pretreatment[b]		Isothermal heating for 2 hours		
Sample designation	Δwt (mg)	Remarks	Temp (°C)	Δwt (mg)	Remarks
CC-1	4.0	Turned gray.	593	-1.5	No change in texture or color.
			650	-29.7	Heavy spalling of coating from sides and edges, exposing metallic surface.
CC-2	9.2 14.2[c]	Gray to gray-yellow. Vitreous appearing.	704	+34.4	Coating deteriorated to powdery mass. Yellow scale on outside with gray powdered subsurfaces. Specimen was black with conchoidal fractures.

[a] Specimens were prepared by 1260°C (2300°F) treatment for 16 hours each cycle. A "semipermeable" seal was used during the second cycle. Conditioning consisted of 1093°C (2000°F) heating for 1 hour and 1260°C (23))°F) heating for 1/2 hour, both in air.

[b] Pretreatment at LRL: 5°C/min to 1260°C (2300°F) in 1 atm oxygen.

[c] Sample temperature maintained at 1260°C for 1 hour before removing from furnace, with 14.2 mg total weight change for the entire pretreatment.

Table II-28. Heating Data for Supplier #2 Coated F-48 Specimens in 1 atm Oxygen.[a]

		After 2 hours[b]		After 8 hours[b]	
Sample	Temperature (°C)	Δwt (mg)	Remarks	Δwt (mg)	Remarks
CB-1	This sample was used for metallographic, x-ray, and analytical analysis.				
CB-2[c]	816	+0.6	No failure. One area exposed.	--	--
CB-3[d]	This sample was given special treatment described in footnote d.				
CB-4[e]	538	-0.3	No change.	0.0	Little change in texture. Slight vitreous appearance. Dark-green and tan color.
CB-5[e]	676	+3.2	Less vitreous. Intact.	1.6	Spalled badly at edges.

Table II-28. (Continued)

		After 2 hours[b]		After 8 hours[b]	
Sample	Temperature (°C)	Δwt (mg)	Remarks	Δwt (mg)	Remarks
CB-6[e]	816	+4.5	Mottled green and tan. Intact.	4.5	Slight green and tan. Intact.
CB-7[e]	925	+5.5	Mottled green and tan. Intact.	6.7	Slightly powdery surface, green and tan. Intact.
CB-8[e]	1093	+4.0	Mottled green and tan. Intact.	3.4[f]	Slight powdery deposit. Green and tan surface. Intact.

[a] All specimens had surfaces area of ~5.1 cm^2.

[b] Samples were removed from furnace after 2 hours, examined, and returned to furnace at same temperature for 6 hours.

[c] Pretreatment consisted of heating at 5°C/min to 1360°C, with 3.7 mg total weight change. Edges were all intact. Surface had a nearly glazed appearance with a few areas where oxidation products from substrate were visible.

[d] Pretreatment consisted of heating at 5°C/min to 1260°C with a 1-hour soak at 1260°C. No oxidation products from substrate. Nearly vitreous appearance. The total weight change was +11.1 mg.

[e] Heatings were preceded by a 2-hour heating at 1260°C which resulted in a weight gain of 3.5 ±0.2 mg. No change other than a more vitreous and darker colored surface resulted.

[f] Three hours total time.

As a result of the tests, the following comparisons may be made of these suppliers coated samples (the present Supplier #1 process cannot be evaluated because process variables have been altered and optimum conditions have not been re-established): The previous Supplier #1 (II-IX process) samples offered high temperature protection (1100 to 1300°C), but were subject to intermediate temperature (~700°C) failure in less than 1 hour. Supplier #2 coated samples offer acceptable protection at 1300°C, but are reactive with many materials. At intermediate temperatures (~700°C), lifetimes are greater than 6 hours. The protective layer appears to be somewhat mobile and seems to have some healing characteristics.

Microscopic Examination of Coated F-48 Samples

Polished sections have been prepared and microstructures analyzed for a number of coated F-48 samples. Silicide-type coatings are characterized by a thick (~5-mil)columnar structure overlaying a thin diffusion zone over the base metal (see Fig. II-16). The diffusion zone varies in thickness; observed under 200X magnification, it appears to be 0.1 mil or less. It is believed to be mainly Nb_5Si_3. X-ray analysis shows the columnar material to be of the same structure as $NbSi_2$, but with slightly different lattice parameters. Other constituents are believed to be present in solid solution in the $NbSi_2$ phase, e.g., W, Mo, and Zr from the base alloy, and/or constituents from the overlay coating.

The Supplier #1 Cr-Al overlay coatings are currently under study; they appear to be very complex. Oxidation of the coatings gives rise to additional structures which have not yet been identified. Grain and crystallite boundaries are not as well defined as in the first cycle (silicide) coatings.

Cracks in the coatings are almost invariably present. These cracks occur at irregular intervals and penetrate from the overlay coating down into the columnar structure. The extent of penetration ranges all the way from very slight to complete penetration through the columnar region to the base metal. It is believed that these cracks are inherent to the silicide-coated F-48, and are the same cracks which appear on surfaces as a crack mosaic upon etching with $HF-HNO_3$ solutions (see Fig. II-17).

Pack Application of Coatings on F-48

Most of the effort has been on silicide coats, to find out the effect of varying pack composition, temperature, time, and type of vacuum system used. Pack compositions were either 60% Si, 30% Al_2O_3, 10% NaF or 67% Si, 33% Al_2O_3. Temperatures from 900 to 1325°C and times from 2 to 8 hours were used. Most of the runs were done in the dry box apparatus, with an Al_2O_3 crucible and a graphite susceptor. A few coatings runs were done in the hot press furnace using either an all-graphite system or an Al_2O_3 crucible with a graphite susceptor and radiation shields. The specimens were 1.0 × 1.3 × 0.3 cm with rounded edges and ~4 cm^2 surface area. They were cleaned and weighed before and after coating. Those coated in NaF-free pack material were dipped in either saturated aqueous NaF or else fused NaF before coating. During a coating run, the specimens were heated at less than 1 micron Hg

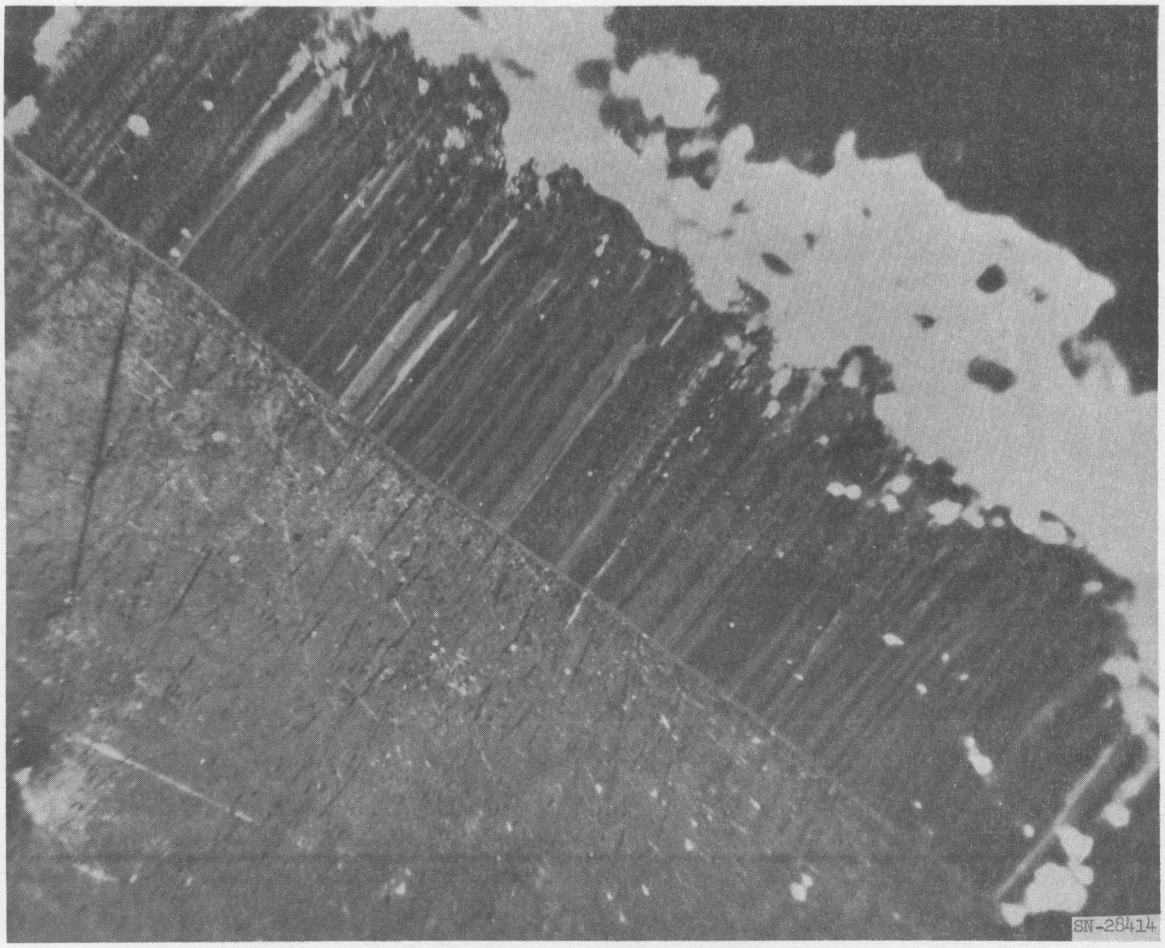

Fig. II-16. Metallographic polished section of Supplier #1 II-IX coated F-48 alloy. Specimen was conditioned for 1 hour at 1260°C in air followed by an additional 6 hours in air at 1090°C. Light areas at the top are oxidation products. Note crack which penetrates to diffusion zone. Photograph was taken with polarized light and represents a magnification of 200×.

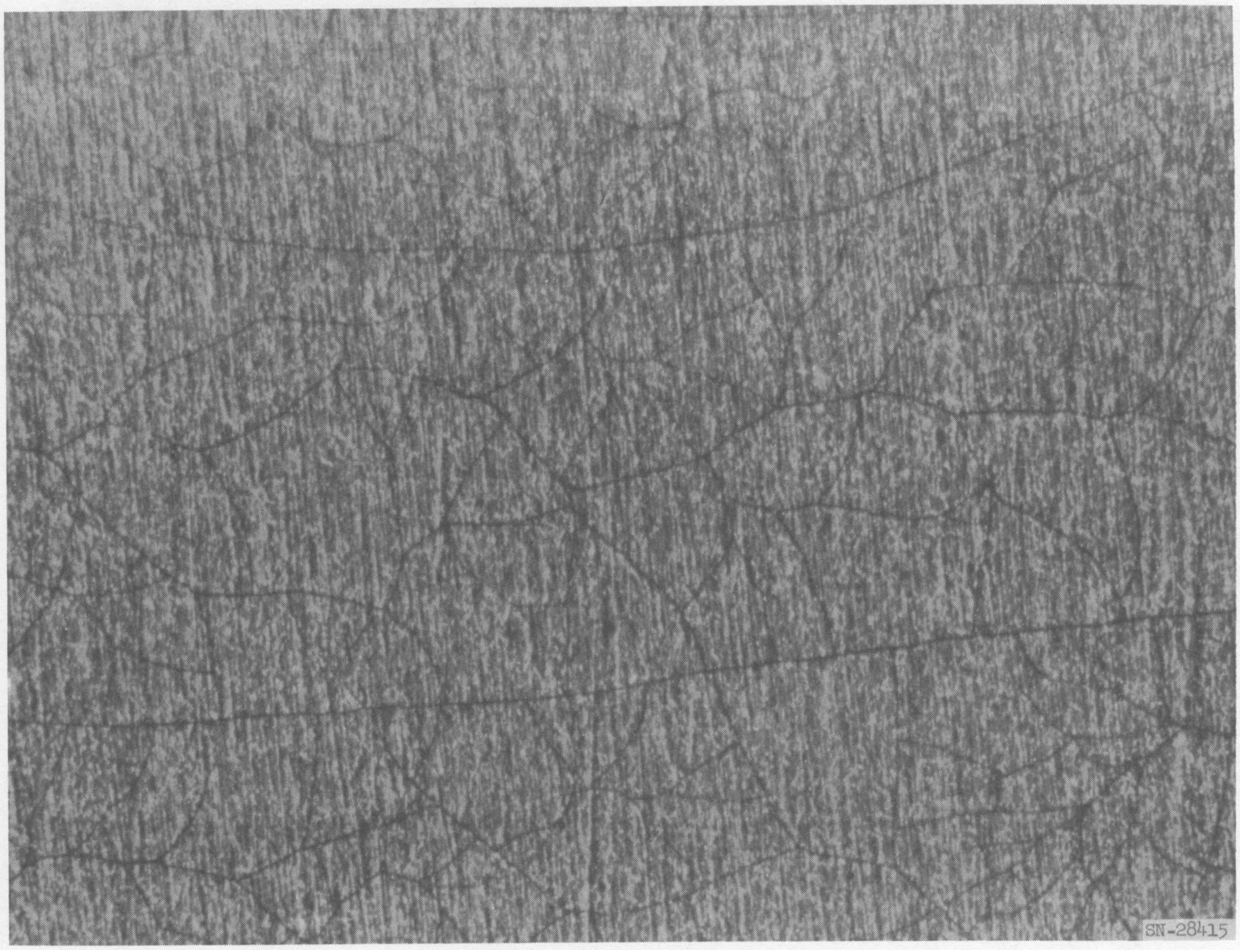

Fig. II-17. Crack mosaic pattern on the surface of silicide-coated F-48. The pattern was brought out by etching for a few minutes in 2:1 concentrated HF-HNO_3 solution. The sample was coated by the pack cementation process at 1174°C for 4 hours under 1 atm argon, to give a 3-mil-thick silicide coating. Magnification is 26×.

pressure up to ~1000°C. One atm argon was then admitted, and the run continued. Most coated specimens were etched with $HF-HNO_3$ solution to study the surface structure. A few were sectioned for metallographic examination. A few were also coated with an overlay of Cr-Al to explore conditions for Supplier #1 type coatings.

The coating thickness for the silicide coatings, d_c, was calculated from the weight gain during coating, Δwt, the surface area, A, and the assumption of an $NbSi_2$ density of 5.29 g/cm^3 for the coating:

$$d_c = \frac{0.1975\ \Delta wt}{A} \quad . \tag{1}$$

The temperature dependence of d_c for 4 and 8 hours is given in Figs. II-18 and II-19, and the time dependence by replotting points from their straight-line plots onto Fig. II-20. The corresponding equation is:

$$d_c = k\tau^n , \tag{2}$$

where k and n depend on the temperature (Fig. II-21). The variation of n indicates that the coating process is not simply controlled by the rate of diffusion of Si into the F-48. Other factors such as the depletion of pack material near the sample may be important.

Omitting NaF from the pack decreased d_c by about a factor of 4, and so did pretreatment with aqueous NaF (Fig. II-19). Pretreatment with fused NaF seemed to cause little decrease in d_c (Fig. II-19). Heating in the hot press furnace in graphite crucibles gave samples with lower d_c than those prepared in the dry box, and a run with an Al_2O_3 crucible gave still lower d_c values (Fig. II-19). Because of this, and the greater convenience of the dry box, no other coating runs were made in the hot press.

Measurements at 80× on polished cross sections have shown that

$$d_0 = 1.24\ d_c , \tag{3}$$

where d_0 is the directly observed thickness. This is in satisfactory agreement with the measurements at ~400× after further polishing the surface. In almost all cases, the surface of the etched samples showed a crack mosaic structure (Fig. II-17).

Cr-Al coatings were applied from a pack of nominal Supplier #1 IX composition: 25% Al, 35% Cr, 33% Al_2O_3, 7% KI. Preliminary results in Table II-29

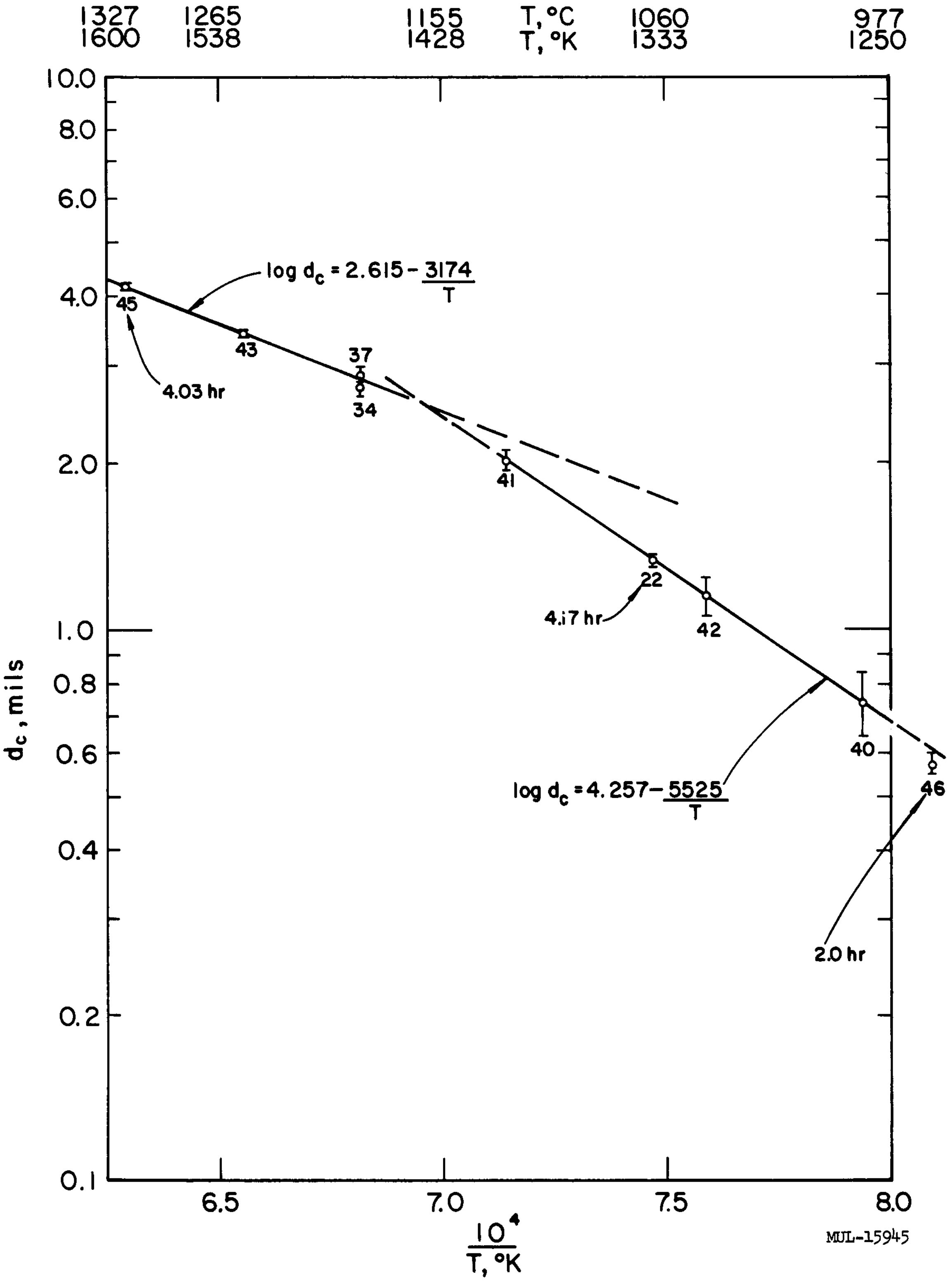

Fig. II-18. Coating thickness of silicide, d_c, on F-48 as a function of temperature. Conditions: 4 hours in dry box unless otherwise noted.

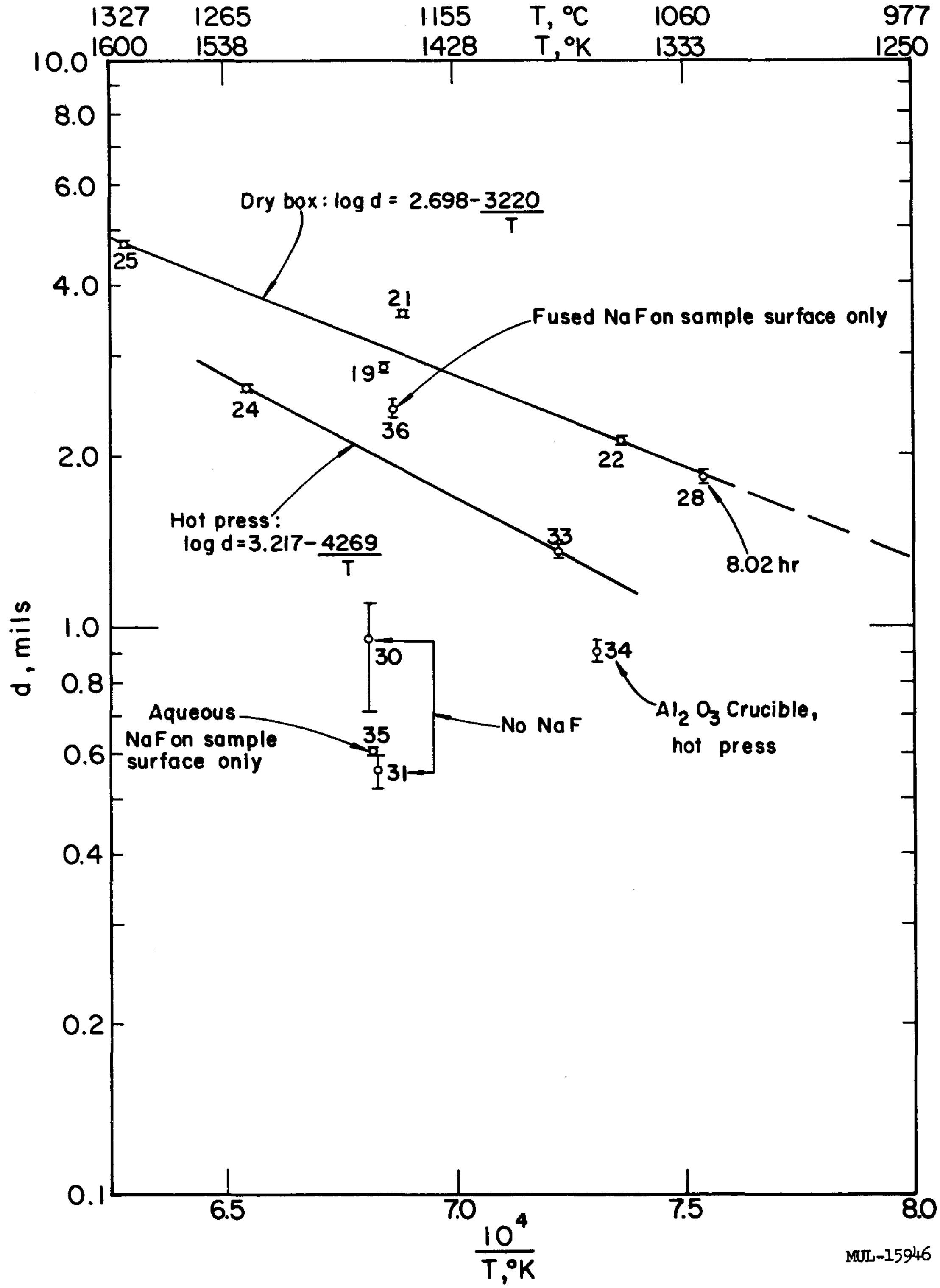

Fig. II-19. Coating thickness of silicide, d_c, on F-48 as a function of temperature. Time: 8 hours unless otherwise indicated.

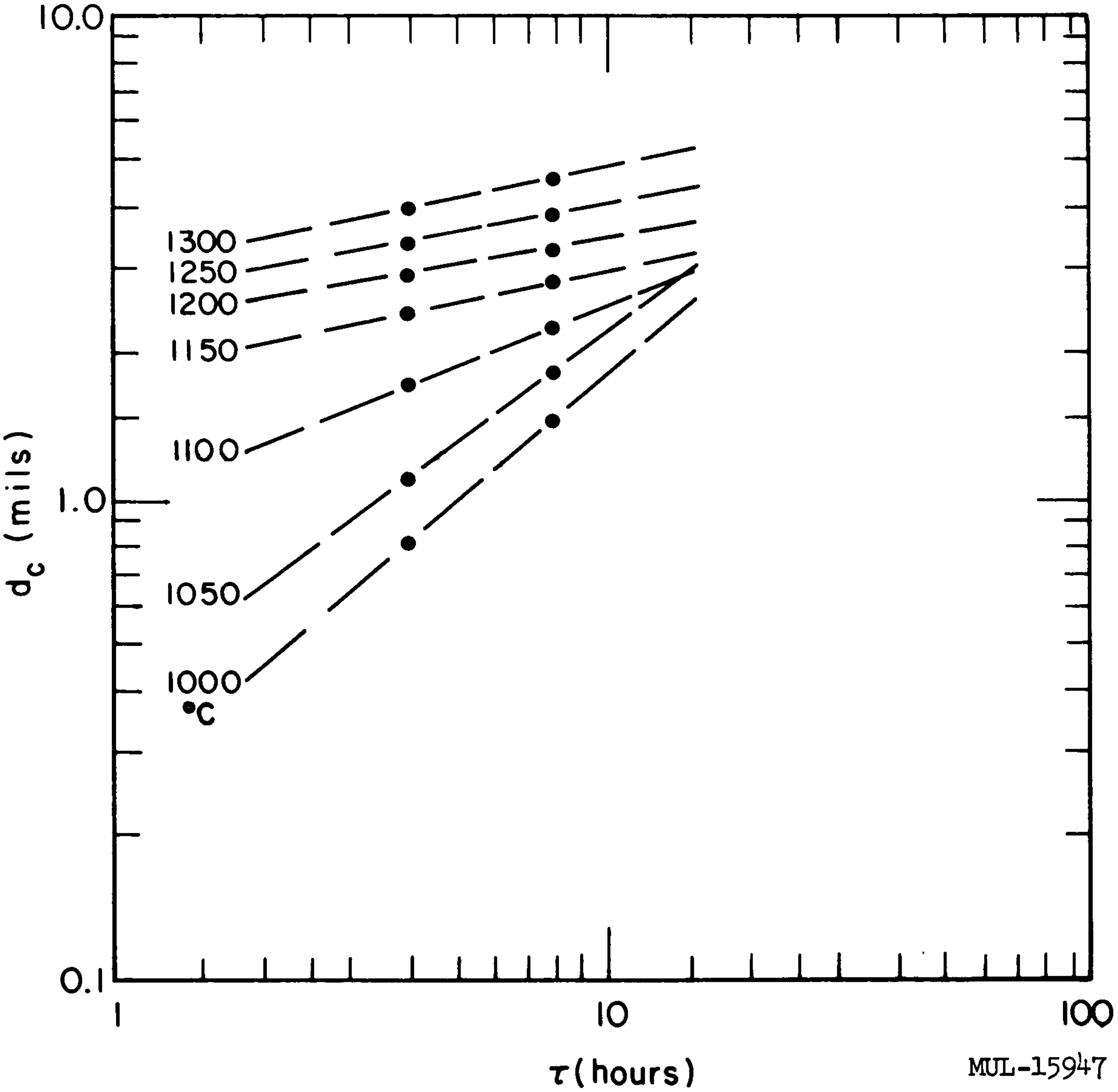

Fig. II-20. Coating thickness of silicide, d_c, on F-48 as a function of time, for several different temperatures.

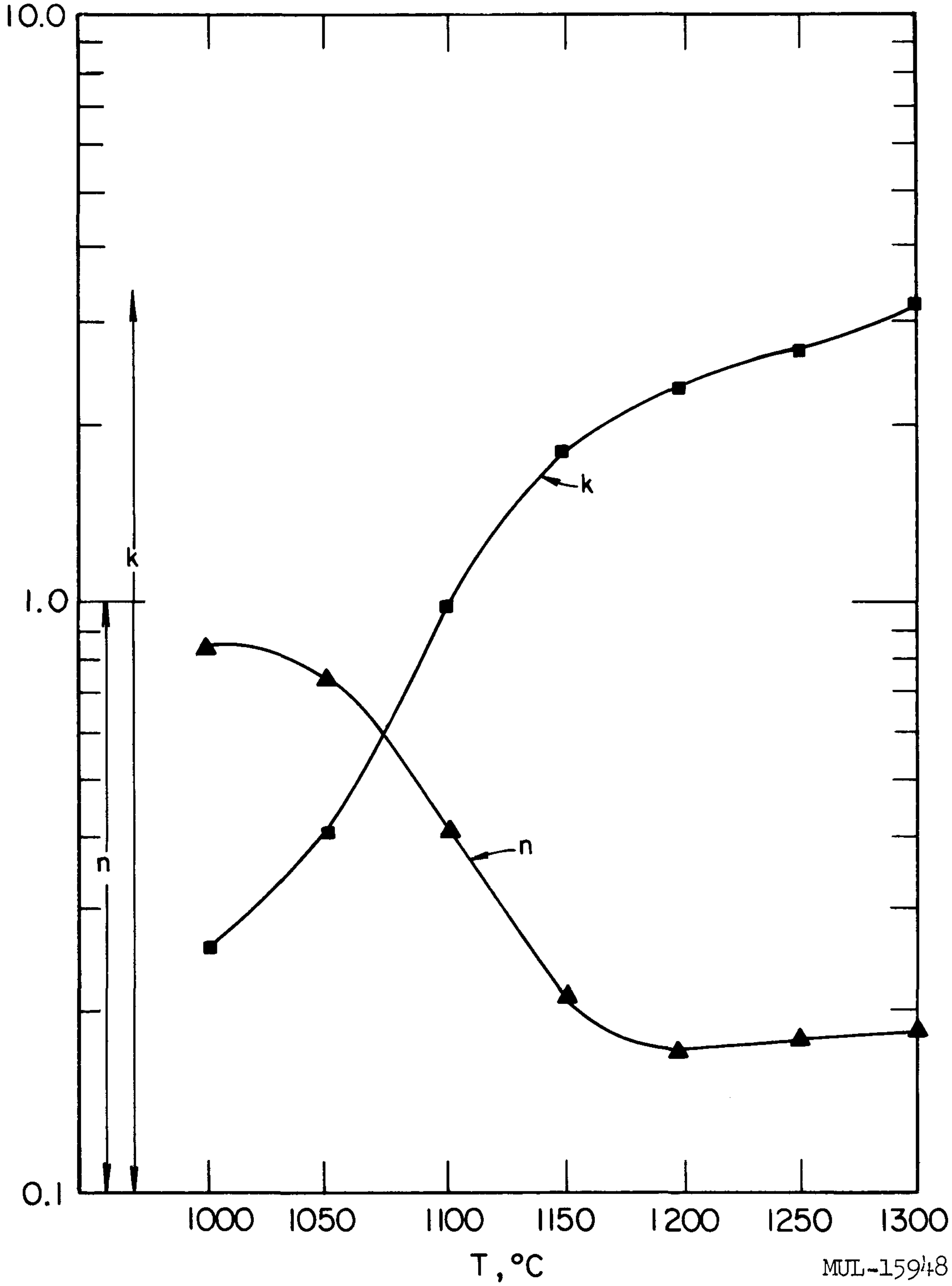

Fig. II-21. Temperature dependence of k and n in the formula $d_c = k\,\tau^n$.

Table II-29. Cr-Al Overlays on Silicide Coatings

Sample	Time (hr)	Temperature (°C)	Silicide coating thickness (mils)	Wt of Cr-Al coating (grams)
56-2	4	940	0.547	0.0002
73-2			4.12	0.0002
77			None	0.0057
78			None	0.0061
58-2	8	949	0.881	0.0008
71-2			4.11	0.0003
79			None	0.0105
80			None	0.0098
67-2	4	1046	3.29	0.0036
74-2			0.552	0.0025
81			None	0.0088
82			None	0.0065
31-2	8	1030	1.84	0.0059
29-2			1.93	0.0066
50-2			2.82	0.0041

show no correlation between the thickness of the silicide undercoating and the deposited weight of Cr-Al. More Cr-Al deposited on uncoated than on silicide-coated F-48. Also, the temperature coefficient of the weight of Cr-Al coating was much smaller for deposition on uncoated than on silicided F-48. Under microscopic examination, coatings on unsilicided F-48 appear smoother, more uniform, softer, and duller in appearance than those on silicided F-48. Cr-Al coatings reproduce the crack mosaic where it is present in the silicide coats.

Pack Application of Cr-Al Coatings Using a Cr-Al Alloy

When elemental aluminum is used in pack application of Cr-Al coatings, problems are encountered from the presence of molten metal in the pack. To avoid this problem, an alloy of 60% Cr, 40% Al was employed as a pack material for coating F-48 alloy. This Cr-Al alloy is reported to melt at approximately 1350°C. The alloy was prepared by arc-melting pressed compacts of Cr-Al powder mixtures. The ingots were then crushed to pass a -100 mesh screen. A pack mixture was made up of 55% Al_2O_3, 40% Cr-Al alloy, and 5%

NaF . The pack was used to coat three F-48 samples at 1175°C and four F-48 samples at 1330°C. Both batches were heated for 5 hours under 1 atm argon. The coating thicknesses were ~0.001 in. in all of the samples, as evidenced by weight gain, dimensional changes, and microscopic examination. The coatings appeared to be of uniform thickness and free from flaws.

One sample from each batch was tested for oxidation resistance under 1 atm slowly flowing oxygen. The sample from the 1175°C batch survived a 5°C/min heating from 300 to 1260°C followed by 2 hours at 1260°C, but failed after an additional 2 hours at 750°C. Failure was caused by spalling after cooling from the 750°C test. The sample from the 1330°C batch was tested by heating from 300 to 1260°C, followed by 2 hours at 750°C, and 3 hours at 1260°C. Examination after the final test showed three small eruptions of oxidized F-48 along the sample edges. Total weight gains for both samples were ~10 mg for a sample area of 4 cm^2. Most of the weight gain occurred in the 1260°C tests. A thickness increase of 0.0005 in. was noted for the 1330°C sample.

Application of Aluminide Coatings to F-48 by the Melting Process

Molten aluminum has been observed to wet niobium very readily at temperatures of ~1000°C and higher. The molten metal spreads itself uniformly over the surface of the niobium, then reacts to form an adherent uniform coat. Aluminum does not wet F-48 under the same conditions, however.

Experiments were done to observe the wetting of aluminum on the surface of Zr, W, and Mo, the principal metallic constituents of F-48 other than niobium. Wetting did not occur on the Mo surface.

In an effort to reduce the concentration of molybdenum at the surface, samples of F-48 were refluxed in aqua regia for several days. The samples were coated with aluminum by painting with a slurry of aluminum powder suspended in a mixture of Duco cement and ethyl acetate. The aluminum was then melted on at 1100°C in vacuum. Although the aluminum flowed better than on untreated specimens, the coatings were grainy and porous. X-ray diffraction pictures of the coating showed a phase identical with $NbAl_3$, but with a slightly smaller lattice constant.

F-48 samples silicide-coated to a depth of 4-5 mils by the pack cementation process were very easily wetted and coated with aluminum. The best of these samples oxidized badly when heated for 2 hours at 825°C, after conditioning at 1260°C for 2 hours in still air. The other sample failed during the conditioning process.

Oxidation of $NbSi_2$ and $(F\text{-}48)Si_2$

Fitzer (UCRL-Trans 725(L)) has observed that $MoSi_2$ shows unusual behavior in its oxidation. The material is extremely oxidation-resistant at high temperatures, but disintegrates rapidly at lower temperatures.

The low temperature failure of silicon-coated F-48 pieces shows precisely this behavior pattern. The following experiments were done to demonstrate the similarity of $MoSi_2$ and the Nb alloy silicides.

Preparations of $NbSi_2$ and $(F\text{-}48)Si_2$ were made by weighing and blending the correct proportions of powder, pressing the powder mixes into compacts, and arc-melting these compacts in an argon atmosphere on a cooled copper hearth. The buttons were remelted several times to insure homogeneity, then sawed into waferlike samples. X-ray analysis showed only one phase present.

Samples of $(F\text{-}48)Si_2$ were exposed to gently flowing air at several temperatures. The results are given in Table II-30.

To see if the protective coating formed at high temperatures affords subsequent protection at low temperatures, a sample of $(F\text{-}48)Si_2$ was tested first at high temperature and then at lower temperatures, with the following results:

Temperature (°C ±10)	Time (hr)	Δwt (mg)	Remarks
1350	1	+1.8	Yellowish coat. Piece looks good.
840	1-1/4	+12.6	Piece completely reduced to powder.
810	65	+104.1	Powder from above had further decomposed to leave very fine powder.

Since the F-48 contains Mo, it is conceivable that this element could be responsible for the low temperature failure. To check this hypothesis, a sample of $NbSi_2$ was exposed for 1 hour at 850°C. The piece was completely reduced to powder; the ~0.5-g sample gained 13.7 mg in the process.

It is concluded that Nb and Nb alloy silicides are subject to the same failure phenomenon as was observed for $MoSi_2$. As with $MoSi_2$, the most remarkable aspect of the attack is that complete loss of integrity of the piece is brought about by only a comparatively small uptake of oxygen. For example, the piece of $NbSi_2$ weighed 0.4752 gram before exposure and 0.4889 gram after, a gain of 13.7 mg. This weight gain corresponds to oxidation of only ~4% of the silicide, yet was sufficient to reduce the sample to a granular mass of powder.

Table II-30. Oxidation of (F-48)Si_2 in 1 atm Gently Flowing Air.

Sample	Temperature (°C ± 10)	Time (hr)	Initial wt (g)	Δwt (mg)	Remarks
1	712	1	0.7907	+2.0	Blackened on surface. Looks undamaged.
2	825	1	1.2524	+38.7	Completely reduced to powder.
3	910	1	1.2754	+24.0	Reduced to granular powder.
4	1230	1	Neglected to weigh.		Coat formed on surface. Piece looks fairly satisfactory.
5	1340	1	0.8629	+1.9	Yellowish coat on surface. Piece looks good.

Al-Nb-O System

A study of the Al-O-Nb system has been started. It is hoped that the study of this system will help in the identification of the complex phases which have been observed in the oxidized aluminum coatings on niobium alloys.

Mixtures of αAl_2O_3 (corundum) and αNb_2O_5 (high-temperature form) powders were made up in mole ratios of 1:3, 1:1, and 3:1. Three pellets 1/4 in. in diameter were pressed from each mixture. These, with control pellets of Nb_2O_5, were placed in an Al_2O_3 dish and heated for 1, 2, and 4 hours at 1290° C.

All the x-ray powder diffraction analyses showed three phase mixtures, indicating that none of the samples had reached equilibrium in 4 hours. A new phase, isostructural with $AlTaO_4$, was observed. The intensity of the new phase increased with increasing concentration of Al_2O_3. The mixture $Nb_2O_5 + Al_2O_3$ showed predominantly the new phase.

MgO-U_3O_8-O_2 System

An investigation of methods of reducing the volatility of urania in air by compound formation has been undertaken. The system chosen for initial investigation is the magnesia-urania system.

Pellets prepared from mixtures of 3 MgO/U_3O_8 were heated at various temperatures up to 1600°C in air, and their weight changes, crystallographic parameters, infrared transmission, and the oxidation state of uranium were compared with pure urania and with the published literature on the magnesia-urania system.

At temperatures below 700°C, a 0.1% loss in weight resulted from heatings as long as 3 days and the color of the pellet remained black. The weight loss agrees with an investigation of Lynch, Handwerk, and Hoenig [J. Am. Ceram. Soc. 43, 520 (1960)] who found that weight losses of this magnitude result from oxygen release:

$$UO_{2.67} \rightarrow UO_{2.65} + 0.01\ O_2\ (g).$$

From 700 to 1050°C, the system gains weight in the following manner:

$$MgO + UO_{2.67-x} + (0.165 + 0.5x)O_2\ (g) \rightarrow MgUO_4.$$

The black color of the original pellet is converted to bright orange, characteristic of magnesium uranate. The maximum weight gain is consistent with the above reaction, which has also been confirmed by x-ray powder diffraction patterns and coulometric determination of the oxidation state of uranium by the method of Strommatt and Connally [Anal. Chem. 33, 345 (1961)].

At 1050 °C and above, the system loses weight because of the reaction

$$MgUO_4\ (s) \rightarrow MgO\ (s) + UO_3\ (g)$$

and the orange color changes to brown although the uranium oxidation state is apparently unchanged. Between 1260 and 1320°C, the uranium oxidation state decreases and approaches that of U_3O_8. A summary of the analytical work is given in Table II-31. The transition is accompanied by a further color change from brown to black. The x-ray patterns show the material to change from the orthorhombic $MgUO_4$ phase at the lower temperatures to a mixture of $MgUO_4$ and a cubic phase which appears to be a solid solution of MgO and O_2 in UO_2.

An infrared investigation of several magnesium uranate samples was also carried out. Absorption characteristic of UO_2^{+} ion in other uranyl compounds at ~900 cm^{-1} [L. H. Jones, Spectrochim. Acta 15, 409 (1959)] has been found in samples prepared at 1135°C but not at 1267 or 1293°C.

In separate heatings of U_3O_8 and magnesium uranate in platinum boats exposed to air, dark deposits believed to be U_3O_8 were observed to accumulate in the cold parts of the furnace tube. The resulting weight losses from $MgUO_4$ and from U_3O_8 are compared in Fig. II-22. As expected, the uranium weight loss from $MgUO_4$ is less than from U_3O_8, but the difference is small.

Table II-31. Uranium Valence in U-Mg-O System at Different Temperatures.

Temperature (°C)	Uranium valence
837	5.76
1005	5.96
1025	6.04
1261	6.04
1285	5.94
1320	5.54
1425	5.38
1570	5.42

Spinel Coatings on BeO-UO_2 Tubes

Spinel coatings are being applied to BeO surfaces by a process developed by an outside organization. The process begins with application of Al_2O_3 to a BeO surface by means of a vapor transport process to form chrysoberyl on the surface. In the second (separate) step, MgO, transferred by a similar process, reacts with the chrysoberyl to form a surface coating of spinel ($MgAl_2O_4$). Both vapor transport processes are accomplished by placing rods of pure oxide close to the BeO surface to be coated, then heating to a given temperature, usually ~1600°C, in a hydrogen atmosphere. Application of the process to BeO tubes of the type developed by LRL shows the chrysoberyl formation step to be exceedingly slow, approximately 1/50 the rate reported by the above-mentioned organization on it own tubes.

Various methods of accelerating the rate of chrysoberyl formation are being tried. The outside organization obtained a chrysoberyl layer formation of 25 microns thickness in 12 hours on BeO tubes containing 0.5% MgO. These results suggest that application of a small amount of MgO to the BeO surface might accelerate the formation of chrysoberyl. Accordingly, an attempt was made to put a small amount of MgO into solid solution with the BeO at the surface, using the vapor transport process. A 30-minute treatment was used on two samples and a 60-minute treatment on one sample, all at a temperature of 1700°C. Upon applying the Al_2O_3, it was found that the rate of chrysoberyl formation was unaffected, or possibly even reduced, by the prior MgO treatment.

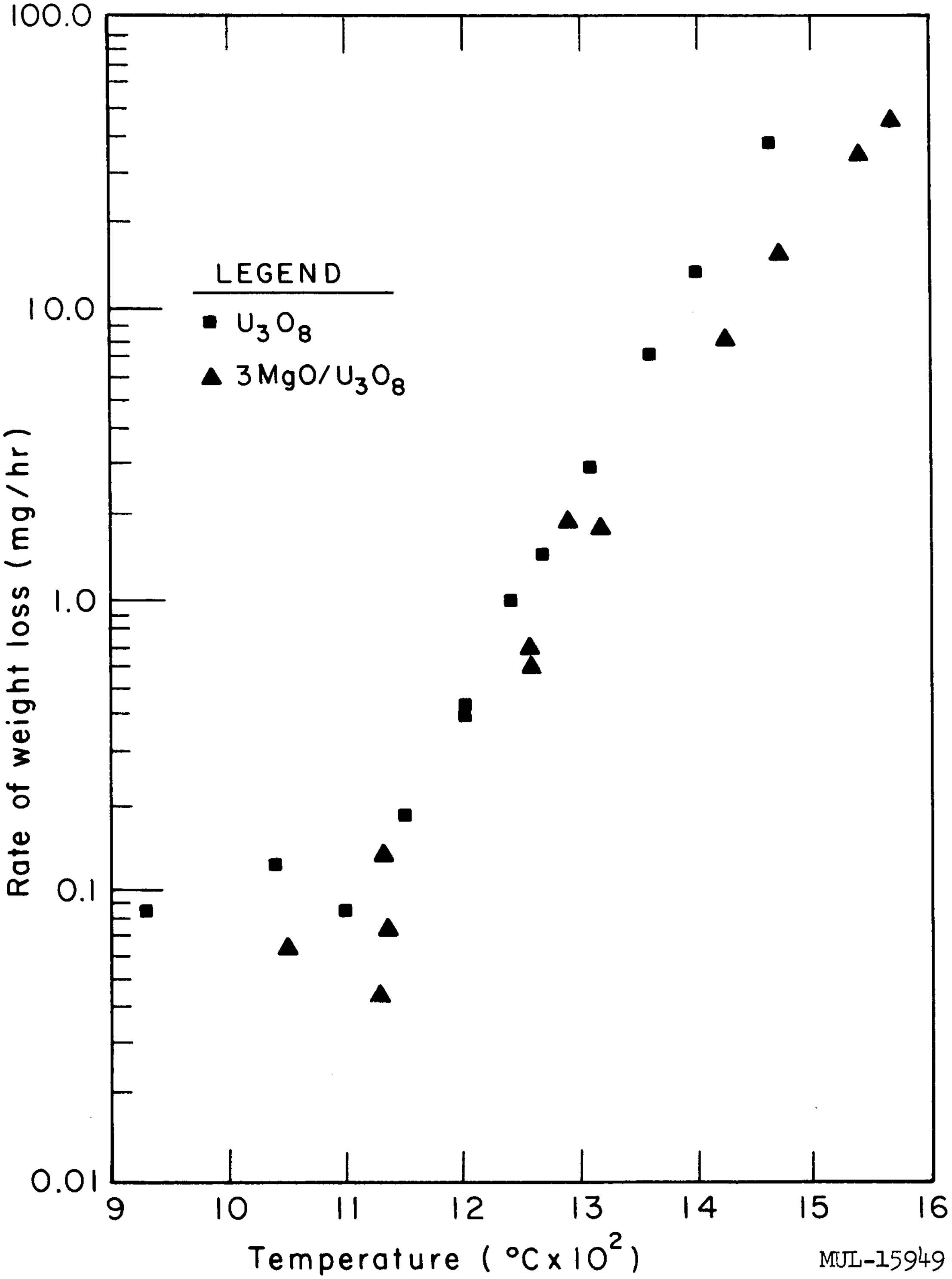

Fig. II-22. Rate of weight loss as a function of temperature, for separate heatings of U_3O_8 and 3 MgO/U_3O_8.

Two experiments were also tried with the original process, but with a higher temperature, 1700°C rather than 1600°C. This nearly doubled the initial rate of chrysoberyl formation. The advantage was lost at longer times, however, as the coating thickness leveled off at less than 5 microns after several hours. It is believed that the higher processing temperature leads to excessive grain growth in BeO. The development of large grains may then reduce the rate of diffusion of the reactant species.

Thermodynamics of the Beryllia-Water Vapor Reaction

Thermodynamic studies of the beryllia-water vapor reaction reported in the literature show a discrepancy between second-law and third-law treatments of the data. Agreement is obtained if a nonlinear model for the beryllium hydroxide gaseous species is assumed. The JANAF tables list free energy functions assuming a linear model, and these are compared in Table II-32 with those obtained using a nonlinear model analogous to that shown for hydrogen peroxide, having the following parameters:

Stretching frequencies	
γ OH	3610 cm^{-1} (2)
γ BeO	855, 1835 cm^{-1}

Bending frequencies	
δ OH	1350, 1266 cm^{-1}
torsion	520 cm^{-1}
δ BeO	800 cm^{-1} (2)

$r_{(BeO)} = 1.36$ Å

$r_{(OH)} = 0.97$ Å

H-O-Be angle 100°

Dihedral angle 95°

$$I_1 = 107.4 \times 10^{-40} \text{ g-cm}^2$$
$$I_2 = 4.929 \times 10^{-40} \text{ g-cm}^2$$
$$I_3 = 120.9 \times 10^{-40} \text{ g-cm}^2$$

Both sets of data were applied to a set of transpiration data [L. Grossweiner and R. Seifert, J. Am. Chem. Soc. 74, 2701 (1952)], and the results are given in Table II-33. Grossweiner and Seifert report a heat of reaction of 41.5 kcal/mole from their second-law plot. This compares with a third-law value of 32.0 kcal/mole using the linear model and 41.3 kcal/mole using the nonlinear model treated here. Experimental work by other investigators is in fair agreement with that of Grossweiner and Seifert, so that the same conclusions should apply to the other studies.

Table II-32. Free Energy Functions for $Be(OH)_2(g)$.

Temperature (°K)	$-(F_T{}^0 - H^0_{298})/T$ (e.u.)	
	JANAF tables	Nonlinear model
1400	64.306	69.900
1500	65.287	70.903
1600	66.240	71.873
1700	67.165	72.813
1800	68.063	73.772
1900	68.936	74.602

Table II-33. Third-Law Treatment for the Reaction: $BeO(c) + H_2O(g) - Be(OH)_2(g)$.

Temp (°K)	log K(a)	Linear model		Nonlinear model	
		$-\Delta(F_T{}^0 - H^0_{298})/T$	ΔH^0_{298}	$-\Delta(F^0_T - H^0_{298})/T$	ΔH^0_{298}
1472	-4.4214	2.117	32.9	7.726	41.2
1488	-4.3125	2.095	32.5	7.708	40.8
1534	-4.2684	2.037	33.1	7.658	41.7
1586	-4.0070	1.973	32.2	7.603	41.1
1623	-3.9101	1.930	32.2	7.566	41.3
1623	-3.9508	1.930	32.5	7.566	41.6
1663	-3.7773	1.885	31.9	7.527	41.3
1668	-3.7447	1.879	31.7	7.522	41.1
1673	-3.7190	1.874	31.6	7.517	41.0
1673	-3.7799	1.874	32.1	7.517	41.5
1748	-3.4895	1.793	31.0	7.446	40.9
1823	-3.2899	1.717	30.6	7.377	40.9
1873	-3.2865	1.668	31.3	7.332	41.9
			Av = 32.0 ± 0.7		Av = 41.3 ± 0.3

(a) $K = p_{Be(OH)_2}/p_{H_2O}$.

Structure of Ru_3Be_{17}

The intensities of 506 independent reflections of Ru_3Be_{17} were measured on the spectrometer using Mo Kα radiation. The 3-dimensional Patterson synthesis was computed and the positions of the 24 Ru atoms were deduced. A 3-dimensional Fourier was computed, using the phases of the Ru atoms, and the positions of 136 Be atoms were obtained. The structure, in a body-centered cubic unit cell of edge 11.337 A, is compatible with space group I_m3. Each Ru atom has 16 Be neighbors at 2.37 to 2.61 A; 12 of these neighbors are at the vertices of a truncated tetrahedron, the other 4 are in the centers of the hexagonal faces of this polyhedron. This type of coordination about the heavy atom is familiar from the structures of $NbBe_2$, $NbBe_3$, and $ReBe_{22}$. There are 6 types of Be atoms: Be_1 has 2 Ru and 13 Be neighbors, 4 of the Be neighbors being at 2.73 A; Be_2 has 2 Ru and 10 Be neighbors; Be_3 has 3 Ru and 9 Be neighbors, 1 of the Be neighbors being at 2.73 A; Be_4 has 3 Ru and 6 Be neighbors; Be_5 has 3 Ru and 10 Be neighbors; Be_6 has 3 Ru and 6 Be neighbors. Least-squares refinements resulted in a reliability factor of 5.2%, demonstrating excellent agreement between the observed and calculated structure factors. A troublesome and at present inexplicable feature of the structure is the presence of two holes of radius 2.8 A in the unit cell. If two Be atoms could be placed in each hole — and there is room for this — the composition would be Ru_6Be_{35}. If only one Be atom were in each hole the composition would be Ru_4Be_{23}. Occupancy of the holes would improve the coordination of Be_4 and Be_6. However, the Fourier maps and difference syntheses show nothing at these positions, and if atoms are postulated in them the least-squares calculations result in very high temperature factors. In all other known intermetallic beryllides the volume of the unit cell is very nearly the sum of the atomic volumes of the elements; the discrepancy in this case is approximately the volume of four Be atoms.

CHAPTER III. HOT BOX

INTRODUCTION

The series of experiments with bare BeO assemblies at the Hot Box facility has been extended to include assemblies with the moderator-to-fuel (BeO/U^{235}) molecular ratio of 1120:1 in addition to the 560:1 and 280:1 ratios reported in UCRL-6625. These experiments have been used to check the accuracy of the ANGIE diffusion code in predicting the temperature dependence of reactivity.

EXPERIMENTAL RESULTS

The experimental method employed with the 1120:1 BeO/U^{235} assemblies is the same as that used for the other two ratios; details are given in UCRL-6625. To give the 1120:1 ratio, two 1-mil-thick oralloy fuel-element foils were used for each 1-inch-thick layer of BeO blocks in a 12-inch-wide quadrant. The two 9-inch-wide foils of each pair were arranged to fill the full width of a slot. This produced two 3-inch-wide regions of half-loading on each side of a quadrant and a central region 6 inches wide within the slot with full-loading. The blocks were stacked tight against the outside graphite box, leaving a 90-mil gap in each quadrant along the cruciform. The results obtained from experiments with all three moderator-fuel ratios are given in Table III-1.

ANGIE CALCULATIONS

A series of problems based on the experiments with BeO/U^{235} ratios of 560:1 and 1120:1 have been solved by the 9-ANGIE neutron diffusion code as a check on the accuracy of the calculated temperature dependence of reactivity. These problems were set up with the following conditions.

The effective density of BeO was taken as 2.86 g/cm^3 for a 1 × 6 × 6-inch block, and the effective uniform density of BeO in each quadrant was calculated by multiplying 2.86 by the ratio of the quadrant length in terms of number of blocks to the experimentally measured length in inches.

The fuel loading was treated by taking the average weight per fuel element pair, multiplying by the quadrant length in terms of number of blocks, and dividing by the quadrant volume ($L_Q \times 24 \times 12\ in.^3$), to give the average density of oralloy in each quadrant. The density in the two 3-inch-wide half-fueled strips is $\frac{2}{3}\rho_{av}$ and that in the 6-inch-wide center strip is $\frac{4}{3}\rho_{av}$.

Table III-1. Bare-BeO High-Temperature Critical Experiments.

				Length[a] at 70°F				
BeO/U^{235}	Description	N,	S	L_n (in.)	L_s (in.)	T_c (°F)	Average weight per fuel element pair (g)	Effective thickness of graphite pusher plates (in.)
280:1	Blocks against side walls							
	short	14,	13-1/2	14-27/32	14-11/32	90	489.75[b]	1.141
	long	14,	14-1/2	14-27/32	15-3/8	850	489.75[b]	1.156
560:1	Blocks against cruciform							
	short	15,	15	15-23/32	15-23/32	360	247.1	1.176
	long	16,	16	16-3/4	16-3/4	1115	247.1	1.214
560:1	Blocks against side walls							
	short	15,	16	15-23/32	16-3/4	420	247.1	1.195
	long	16,	16	16-3/4	16-3/4	785	247.1	1.214
1120:1	Blocks against side walls							
	short	19,	19	19-13/16	19-13/16	65	124.1	1.356
	long	21,	21	21-7/8	21-7/8	630	124.1	1.478

[a] Measured length of BeO in quadrant.

[b] Extra stainless steel present in these experiments.

The concentration of U^{235} is 93.2% of the oralloy, the remainder being U^{238}. The conversion from discrete fuel foils of finite thickness to a homogeneous fueling is made through the use of appropriate, group-averaged, self-shielding and flux depression factors.

The concentration of stainless steel from the fuel element envelope was based on a weight of 105.23 g per fuel element and smeared uniformly over the fueled regions in proportion to the fuel concentration. Self-shielding factors were used appropriate to the flux depression at the surface of the fuel element in the half-fueled region; in the full-fueled region, half the steel was treated in this way and the other half, represented by the steel between fuel elements in the overlapped region, was shielded with the average flux depression over the fuel element.

The void region in the graphite control-vane cruciform, and the 90-mil gap left between the BeO blocks and the cruciform for differential thermal expansion allowance, have been treated by the smear technique, which requires conservation of all masses (UCRL-6625, p. 8). In the case of the cruciform, it was assumed the graphite was reduced to half normal density ($\frac{1}{2} \times 1.74$ g/cm^3); in the case of the 90-mil gap, fueled BeO was smeared in from the bordering areas to give a uniform density for the resultant regions.

The density of graphite in the 1.63-inch-wide box sides and in the pusher plates was taken as 1.74 g/cm^3.

The experiments were arranged with spaces between stacks of blocks to allow for a higher thermal coefficient of expansion for BeO than for graphite. This means that as the temperature of the assembly is raised the box dimensions change according to the graphite expansion, and the higher rate of expansion of the BeO decreases the spacing between stacks and decreases the original 90-mil gap between blocks and cruciform. One extra inch has been added to the height (24 + 1 inches at 70°F) to allow for neutrons reflected from the structure under the assembly. The assembly height also changes with BeO expansion. The thermal coefficient of expansion for graphite was taken from the curve in UCRL-6516, assuming expansion took place parallel to the extrusion axis. The coefficient for BeO was taken to be 2.73 times that for graphite.

A series of seven problems were solved for each moderator-to-fuel ratio. Three of these used the density and dimensions as calculated at the lowest critical temperature, and standard library-tape transfer coefficients for oralloy, BeO, and graphite at temperatures of 300, 650, and 1000°K. A second set of three problems used the density and dimensions calculated for the high critical temperature and the same three sets of transfer coefficients. The k_{eff} was plotted against temperature for each set of three, and the proper value of k_{eff} at the experimental critical temperature was read off in each case. The seventh problem had the low-temperature density and dimensions except that the length had been increased to the number of blocks reported for the high-temperature critical assembly. The difference between k_{eff} for this seventh problem and the first one provides a measure of the reactivity overcome experimentally by raising the temperature.

RESULTS

The results of the ANGIE calculations for these two BeO/U^{235} ratios are summarized in Table III-2. (Calculations are also being done for the 280:1 ratio.) The calculations agree very well for the 560:1 ratio, but the temperature effect is overpredicted by 44% for the 1120:1 ratio. The effect of representing the cruciform as half-density graphite has been investigated by using the more accurate void treatment presented in UCRL-6625. The gross effect on k_{eff} as calculated for a single critical assembly is quite large (of the order of 1%), but the differential effect between assemblies critical at high and low temperatures as studied here is very small and is within the 0.05% uncertainty in estimating it.

Table III-2. Results of ANGIE Calculations.

BeO/U^{235}	T_c (°F)	k_{eff}	Δk_{exp} (experimental reactivity difference at low temperature)	ANGIE over-prediction (%)
560	420	0.9968	0.0099	- 2.0
	785	0.9970		
1120	65	0.9889	0.0243	44.5
	630	0.9781		

CHAPTER IV. TORY II-C

SECTION I. NEUTRONICS

Significant advances were made towards the development of a final fuel distribution pattern. Quarterly report No. 8 (UCRL-6516, June, 1961) outlined the general method and the other considerations which enter into spatial allocation of fuel classes. In that report the simplified assumption was made that control rods were fully withdrawn from the reactor, whereas the present study considers the realistic case where control rods penetrate the core to a predetermined depth to render the reactor operational during the changing character of its useful life.

Fuel class assignments resulting from this study are shown in Fig. IV-1. Corresponding fuel tube requirements are listed in Table IV-1. This information, which supersedes that in quarterly report 9 (UCRL-6625, Sept., 1961, Fig. IV-5 and Table IV-1), is still to be considered as preliminary pending final specification of reactor components.

PREPARATION OF REFINED FUEL LOADING MAP

Reactivity of the reactor is controlled in main by 12 centrally arranged shim rods (cf. Fig. IV-23b, UCRL-6516). This mode of control has a pronounced effect on the power profiles of the reactor. Although it is conceivable to compensate fully for disturbances of idealized radial and axial power profiles due to a certain control rod position, the time-dependent variation of the insertion depth demands a compromise solution. At this point it is in order to recall neutronic requirements of control rod worth during the specified 10-hour operating period of the reactor. These are given in Table IV-1a.

Here, insertion depths are shown at the indicated average core temperature, and are measured from the forward face of the forward reflector. A graphic illustration of the control curve is given in Fig. IV-2.

In UCRL-6625 (p. 115) is shown the disturbance of the idealized power distribution due to a rod insertion depth equivalent to 1.59% in the multiplication factor; there results an 8% increase above the average power density in the downstream regions of the active core. Further insertion of control rods, of course, causes a still greater distortion of the power profile, where the design power densities are exceeded still further. This implies a subsequent limitation on the overall reactor power one could safely demand from the nuclear ramjet.

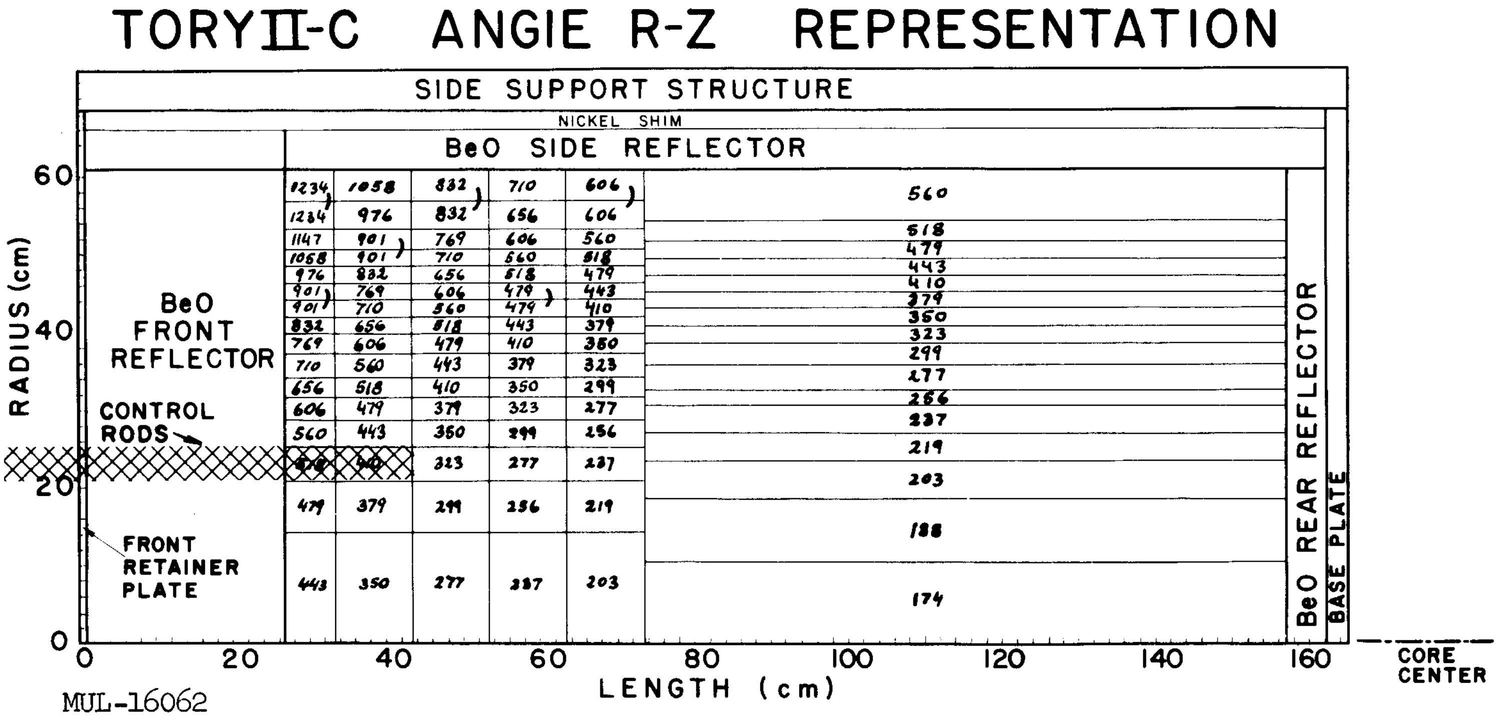

MUL-16062

Fig. IV-1. Spatial allocation of fuel classes for control rods at the 5-hr position. Fuel classes are characterized by the nominal quantity of OyO_2 in grams per inch length of tube. Class numbers are scaled by 10,000, i.e., class 128 has 0.0128 gram OyO_2/inch of tube.

Table IV-1. Fuel Element Requirements for Tory II-C Reactor. (Revised)

R	Fuel class[a]	Approx. No. tubes per class	Approx. No. inches per class
1	128	---	---
2	138	---	---
3	149	---	---
4	161	---	---
5	174	5,394	21,171
6	188	11,044	43,346
7	203	10,219	40,108
8	219	9,153	35,927
9	237	11,758	46,149
10	256	8,406	32,995
11	277	14,018	55,021
12	299	12,919	50,708
13	323	11,493	45,112
14	350	13,712	53,820
15	379	13,226	51,913
16	410	13,449	52,789
17	443	15,394	60,421
18	479	17,006	66,749
19	518	17,727	69,578
20	560	41,656	163,500
21	606	9,276	36,409
22	656	5,089	19,974
23	710	5,866	23,023
24	769	3,323	13,043
25	832	6,759	26,530
26	901	4,261	16,723
27	976	3,039	11,929
28	1058	3,501	13,741
29	1147	1,005	3,946
30	1243	3,265	12,816
		271,958	

[a] Fuel classes are characterized by a number 10^4 times the nominal quantity of OyO_2 in grams per inch length of tube: i.e., class 128 has 0.0128 g OyO_2/inch of tube.

Table IV-1a. Neutronic Requirements of Control Rod Worth.

	Startup, 27 °F	Startup, 2331 °F	5-hr point, 2331 °F	10-hr point, 2331 °F
Δk (shutdown)	-0.025	---	---	---
Δk (temp effect)	-0.075	---	---	---
Δk (xenon)	-0.025	-0.025	-0.012	---
Δk (supercritical)	-0.005	-0.005	-0.005	-0.005
Δk (total)	-0.13	-0.03	-0.017	-0.005
Insertion depth				
(in.)	40	20.53	16.58	10.00
(cm)	101.60	52.15	42.12	25.40

Of course, at some particular insertion depth a median disturbance takes place. It is for this condition that the fuel distribution of the reactor should be determined. Therefore, to explore the situation, an insertion depth commensurate with the specified neutronic worth of control rods after 5 hours of high power operation was chosen. Fuel class assignments were made for this case to counteract the upheaval in power profile. The resulting local power densities have been compared against the idealized shape and are shown in Fig. IV-3. Most of the reactor is seen to hover about the average power density, as desired. There exist, however, some hotspots in the upstream region of the core which show a local excess above the average by as much as 6%. In contrast to the comparison made on page 115 of UCRL-6625, these hotspots appear only very locally and are of lesser magnitude. Thus the particular fuel arrangement marks a great improvement, although it does not represent the final version.

Given the fuel arrangement which has been optimized above for the 5-hour control rod position, it is desirable to inquire into the changes in the power profile when control rods are moved to the zero-hour and 10-hour operating positions. This change can be represented in two ways: (1) By a comparison of local power densities resulting from these two cases with ideal power profiles, as was done before (Figs. IV-4 and IV-5); (2) by a comparison with the power profile realized at the 5-hour point (Figs. IV-6 and IV-7). The latter renders the percent deviation from the assumed compromise position of control rods for which the fuel loading has been optimized.

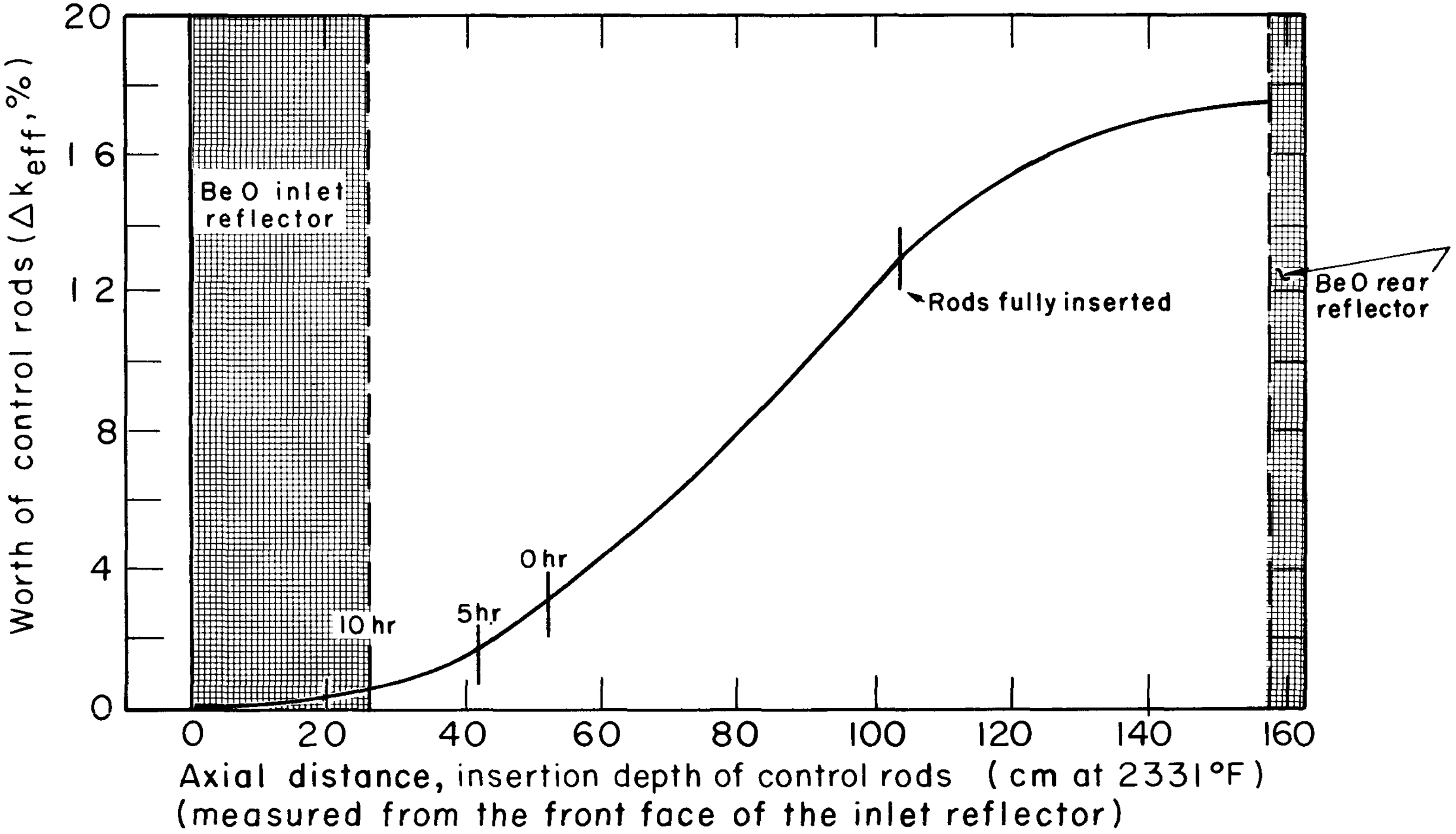

MUL-15950

Fig. IV-2. Shim-rod control curve for Tory II-C. Distances measured from front face of inlet reflector.

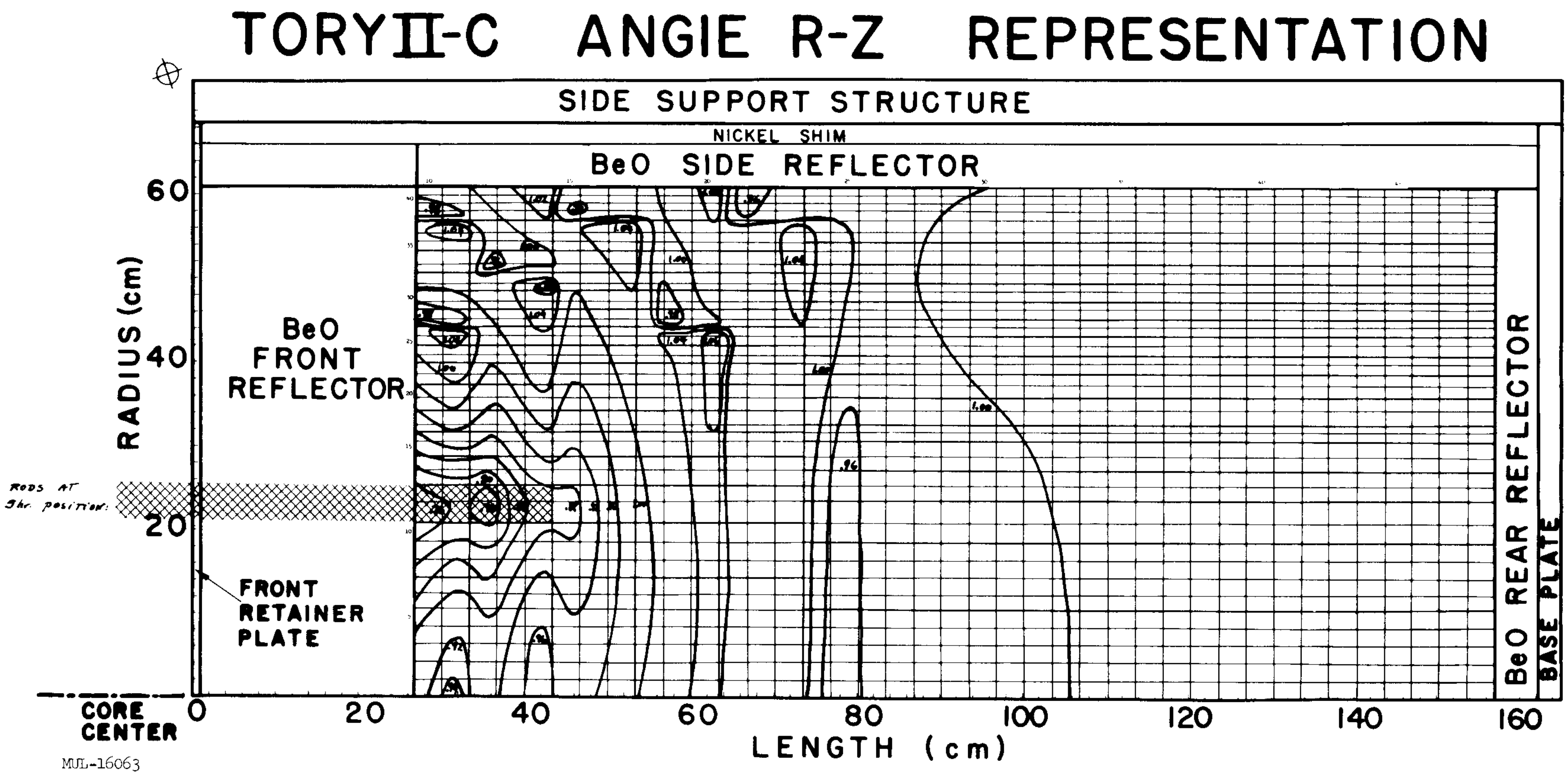

MUL-16063

Fig. IV-3. Power profile deviation of fuel loading for 5-hr control rod position, compared with ideal power shape.

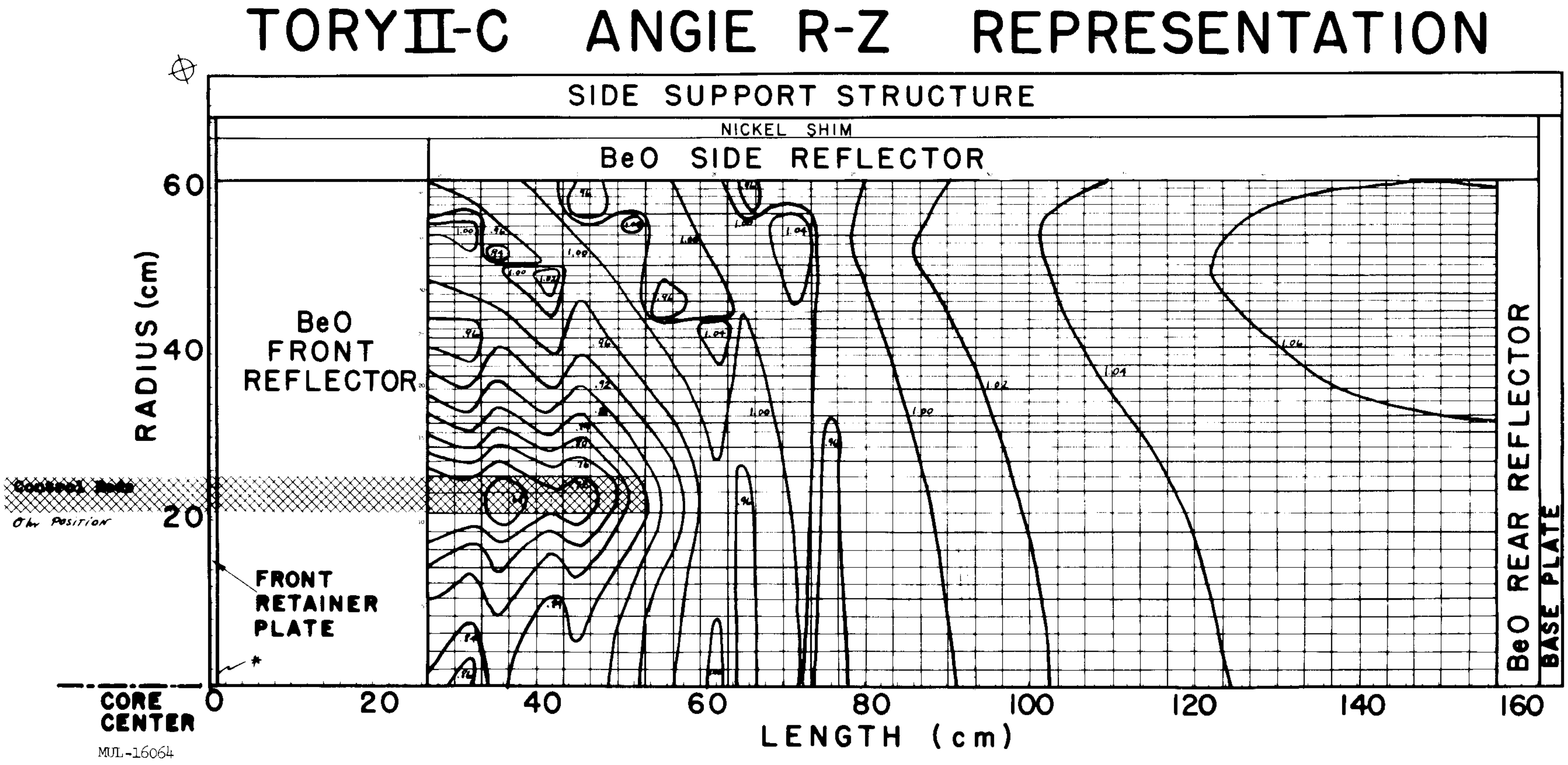

Fig. IV-4. Power profile of zero-hour control rod position compared with ideal power profile with all rods withdrawn.

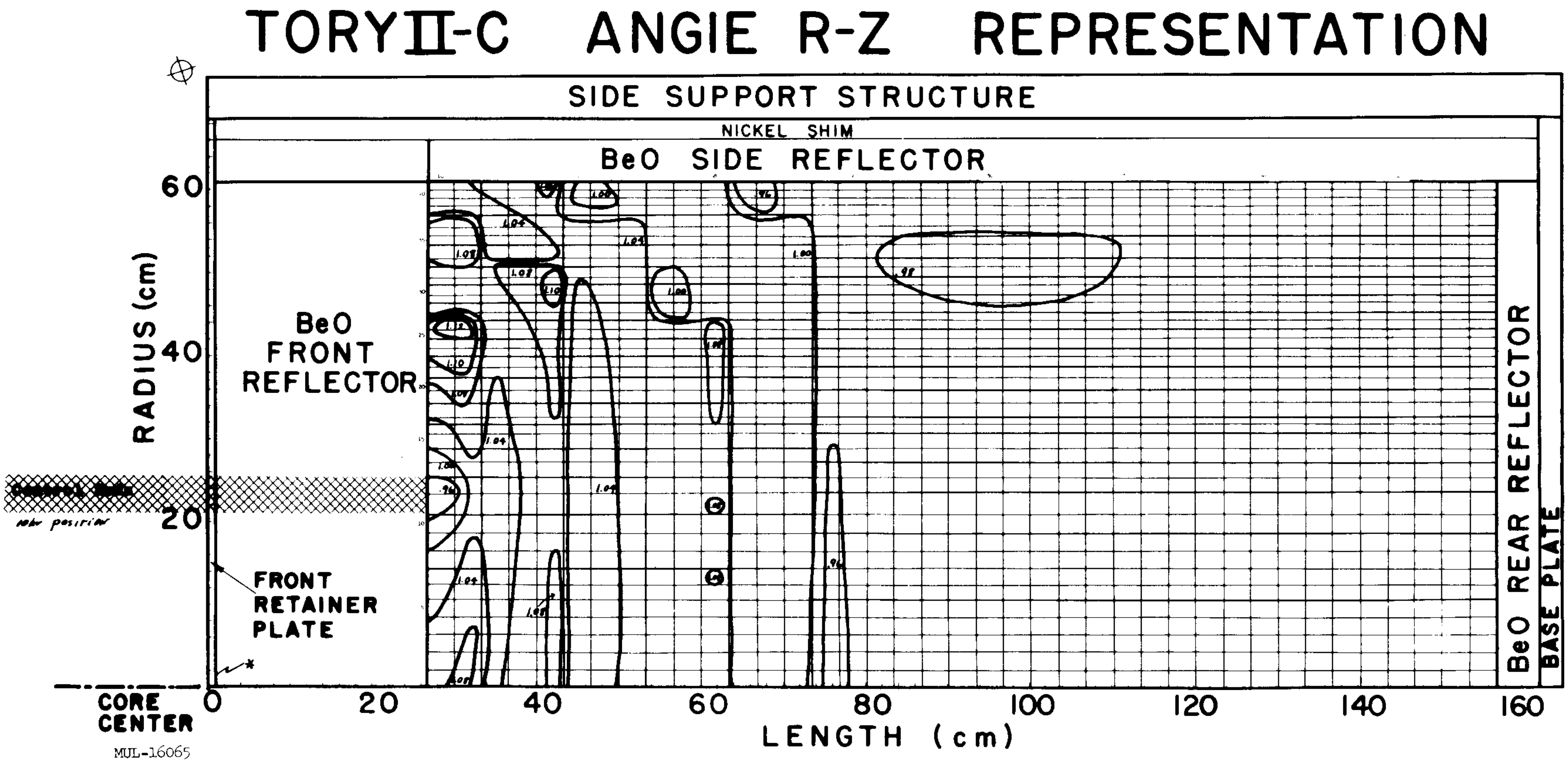

Fig. IV-5. Power profile of 10-hr control rod position compared with ideal power profile with all rods withdrawn.

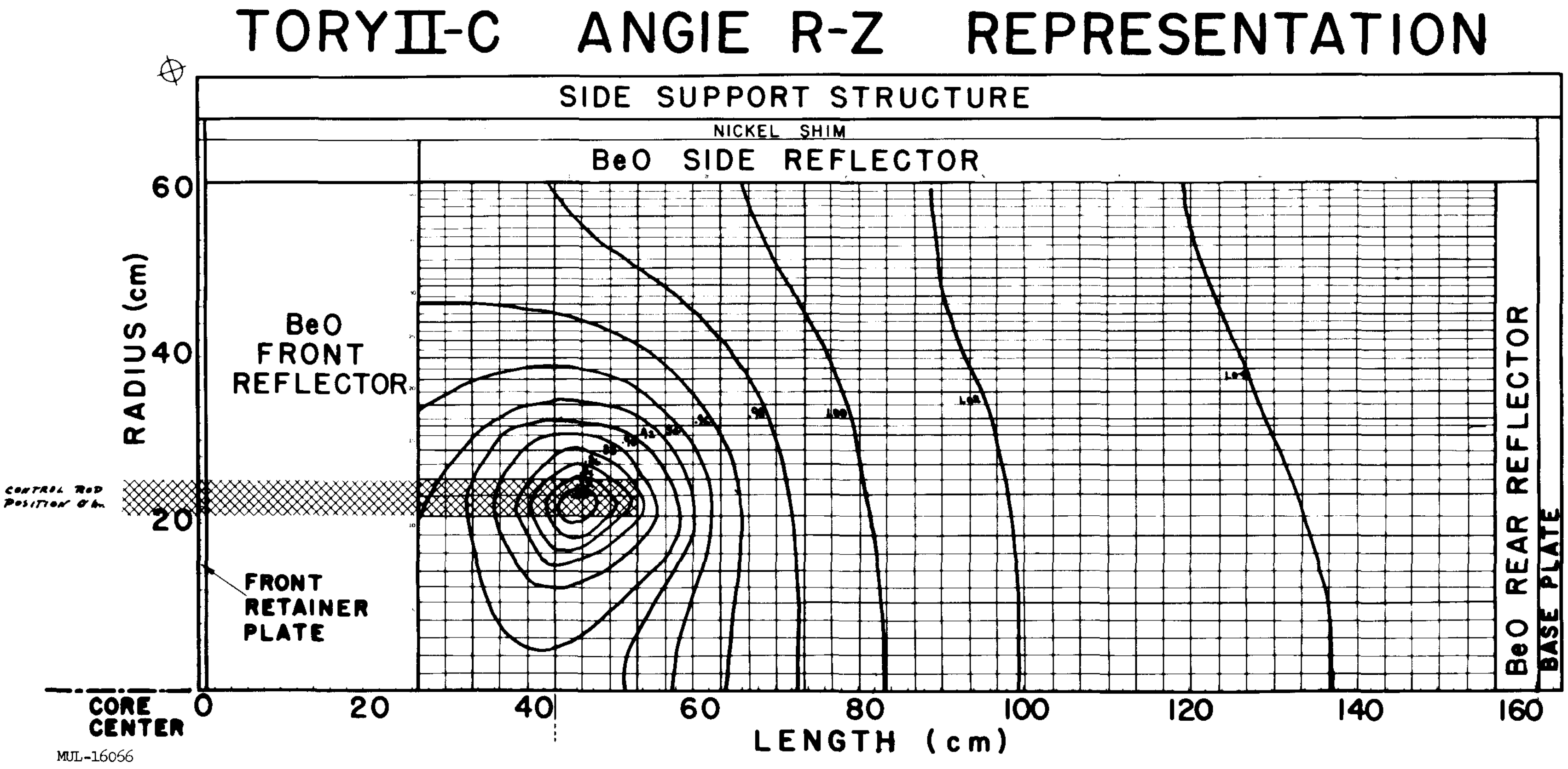

MUL-16066

Fig. IV-6. Power profile perturbations of the zero-hour control rod position, normalized to the 5-hr position.

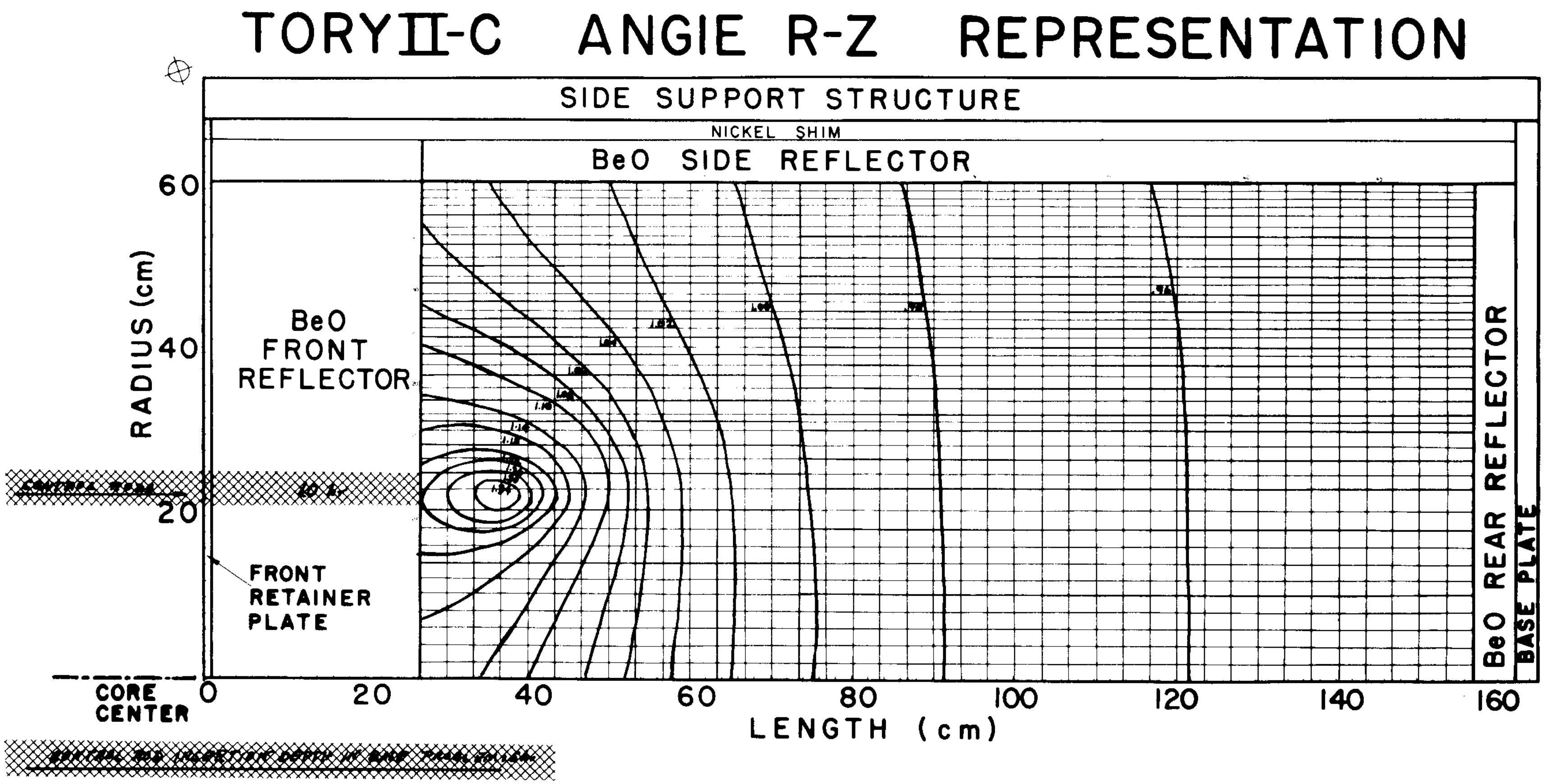

MUL-16067

Fig. IV-7. Power profile perturbations of the 10-hr control rod position, normalized to the 5-hr position.

Comparisons with the ideal power profile show hotspots of 12% above the average for the 10-hour case and hotspots of only 6% for the zero-hour case. The 12% hotspots appear in the forward end of the active core where temperatures are below average; hence hotspot occurrence there is not too serious. From these findings, and in consideration of other parameters which cause stresses in fuel tubes, an optimum position of control rods can be chosen for which the final fuel class assignment in the reactor should be made.

EFFECT OF NICKEL SHIMS ON NUCLEAR HEATING OF PERIPHERAL REGIONS

The thickening of the nickel shims to approximately 1 inch, at the expense of the side reflector BeO, has changed the radiation heating environment of the peripheral regions of the Tory II-C reactor. The energy distribution analysis was made for the current side-support structure configuration. In view of the fact that the side support design may undergo further changes, the results given in this report should be considered to be preliminary. It is not expected, however, that the changes considered will greatly affect the distribution given.

Extensive use of the YOGI and ANGIE codes has been made in the evaluation of the gamma heating distribution in the BeO side reflector, the nickel shims, and the side support structure. The total heating density distribution is given in Fig. IV-8 for both cases: with and without the nickel shims in the side support structure. The results are normalized to unit power density averaged over the fueled core volume of 53.4 ft^3.

The results of this analysis show a net reduction in the heating density of side-support structure components of about 30%.

NUCLEAR HEATING OF UNFUELED BeO AND TIE RODS

Nuclear heating of the unfueled BeO inserts and of the tie rods in both standard and control modules was calculated with the aid of the YOGI Monte Carlo code [Pluto Quarterly Progress Report No. 8, UCRL-6516, June, 1961]. The heating values of the control module components are based on problems that were run in conjunction with the hafnium control rod analysis [Pluto Quarterly Progress Report No. 9, UCRL-6625, Sept., 1961]. Two additional problems were run to determine the heating of the standard module components. The cell descriptions used closely approximated the actual configurations.

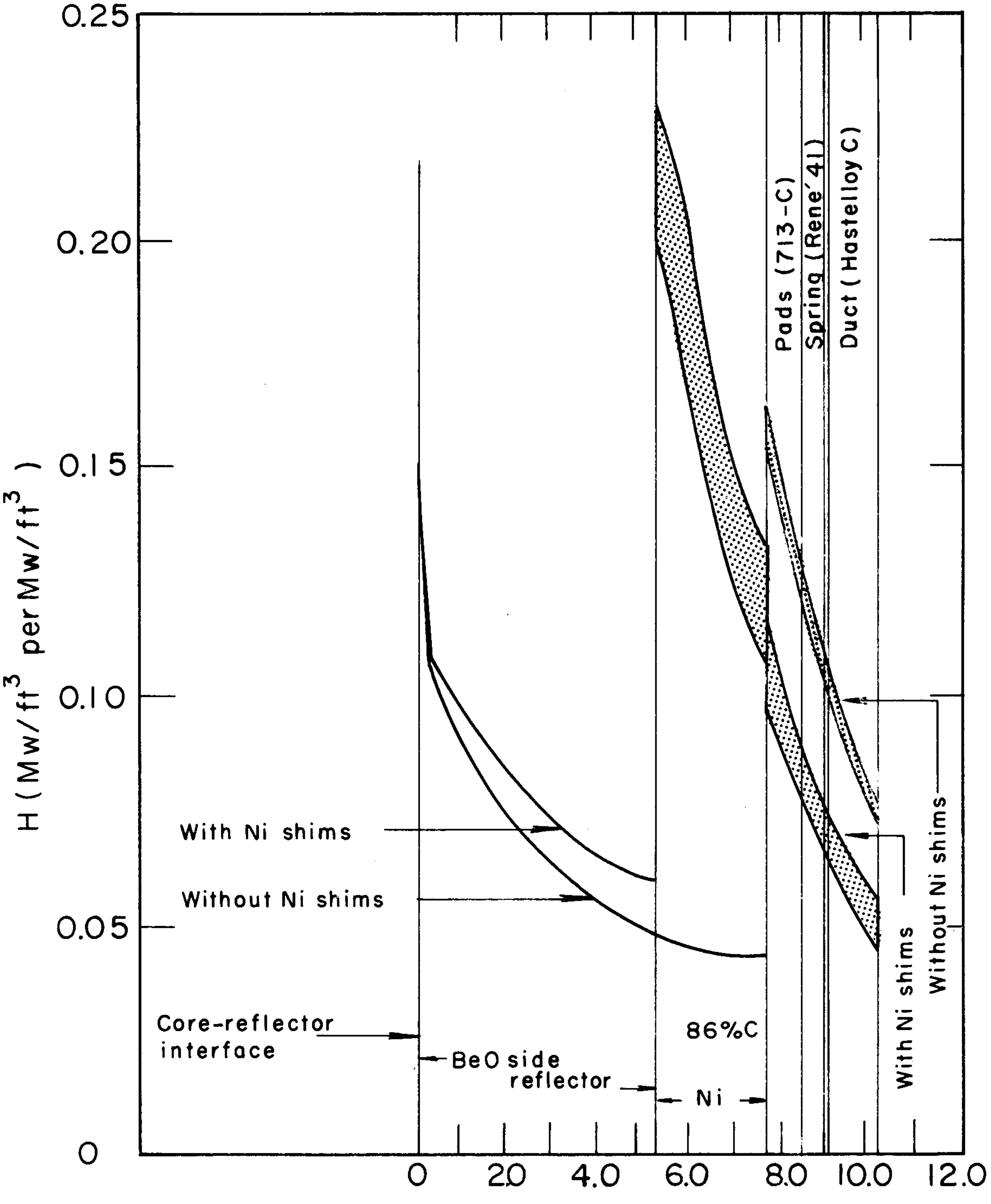

Fig. IV-8. Total heating density distribution in the peripheral regions of Tory II-C in reactor midplane. Uncertainty of results ~± 10%. Upper and lower limits of heating in shims and side support structure determined by uncertainty in the neutron absorption in nickel. Results are given for 90% fission product saturation (10-hr run); at 66% saturation (10-min run) the heating is approximately 5% lower.

The results of the problems run are listed in Table IV-2 and the heating values obtained are given in Table IV-3. The axial distributions of tie rod and BeO heating in both standard and control modules are shown in Figs. IV-9 through IV-12. The radial dependence was compiled from earlier calculations.

Control Module

Nuclear heating of the control module components was calculated for the case of a René 41 rod located at R = 8.5 in. Two conditions were investigated: one with the hafnium control rod inserted 13 in. into the core, the other with the control rod inserted 40 in. into the core. The former represents a typical operating condition, the latter a scram conditions. It was determined that replacement of the René 41 tie rod by an R-235 tie rod decreases the peak heating of the tie rod by ~8% and that of the BeO insert by ~4%. The two curves in Fig. IV-13 indicate that the heating of the control module components at R = 17.2 in. is reduced from the heating at R = 8.5 in. by ~30% for the tie rod and ~20% for the BeO insert.

The effect of removal of the hafnium control rod from its module was determined from Monte Carlo calculations. The following results were obtained:

a Effect on the control tie rod heating:
  - External core gamma heating increases by 40%
  - Internal control tie rod (n, γ) heating increases by 15%;

b Effect on the control module BeO insert:
  - External core gamma heating increases by 26%
  - Internal control tie rod (n, γ) heating increases by 23%.

Standard Module

The heating of standard module components was calculated for the case of the central module (R = 0). Both tie rod materials were considered. The total heating of the René 41 tie rod is 15% higher than that of the R-235 tie rod; the heating of the BeO inserts surrounding René 41 is 6% higher than that of the inserts surrounding R-235.

The fast neutron and beta heating distribution in all components considered is the same as in the earlier analyses.

The uncertainties in these calculations can be approximated more precisely than in earlier calculations, since the standard deviation of the energy deposition per zone is calculated in the YOGI code. The statistical uncertainty

Table IV-2. Summary of YOGI Problems; the Fueled Moderator Medium has a BeO:U Ratio of 423:1.

		Energy fraction deposited in				
		Control module[a]			Standard module[b]	
Source	YOGI	Hf control rod	R-235 tie rod	BeO insert	R-235 tie rod	BeO insert
Control Module						
External core gamma	40	0.0894	0.019	0.061	---	---
Internal Hf (n, γ)	41	0.257	0.034	0.075	---	---
Internal tie rod (n, γ)	42	0.154	0.057	0.089	---	---
Standard Module						
External core gamma	201	---	---	---	0.032	0.065
Internal tie rod (n, γ)	202	---	---	---	0.0896	0.1043
Component area in cell (in^2)	---	0.0586	0.0296	0.293	0.0221	0.195

[a] Total cell area is 8.00 in^2. The component areas in cell are based on earlier control module design.
[b] Total cell area is 4.49 in^2.

Table IV-3. Summary of Results of YOGI Calculations of Total Heating.[a]

	Control module (at R = 8.5 in.)				Standard module (at R = 0)	
	René 41 tie rod (Hf control rod insertion)		BeO insert (Hf control rod insertion)		René 41 tie rod	BeO insert
	13 in.	40 in.	13 in.	40 in.		
Peak heating density (Mw/ft^3 per Mw/ft^3)	0.953	1.143	0.319	0.360	1.065	0.285
Peak-to-average ratio[b]	1.47	1.60	1.46	1.55	1.50	1.50
Average heating density[b] (Mw/ft^3 per Mw/ft^3)	0.648	0.714	0.218	0.232	0.712	0.190
Considered component volume[c] (ft^3)	0.00417	0.00417	0.0424	0.0424	0.00329	0.0294
Total component power (kw per Mw/ft^3)	2.70	2.98	9.26	9.85	2.34	5.58

[a] All heating density values are given in Mw/ft^3 of solid component material normalized to 1 Mw/ft^3 of average core power density, based on the hot fueled volume of the core, $V_c = 53.4\ ft^3$. The heating calculations were performed for 90% fission product saturation, equivalent to a 10-hr steady operation.

[b] Average was taken over the full length of the hot reactor ($L_R = 63.5$ in.).

[c] In the normalization, the components were assumed to be hot and to extend the full length of the hot reactor.

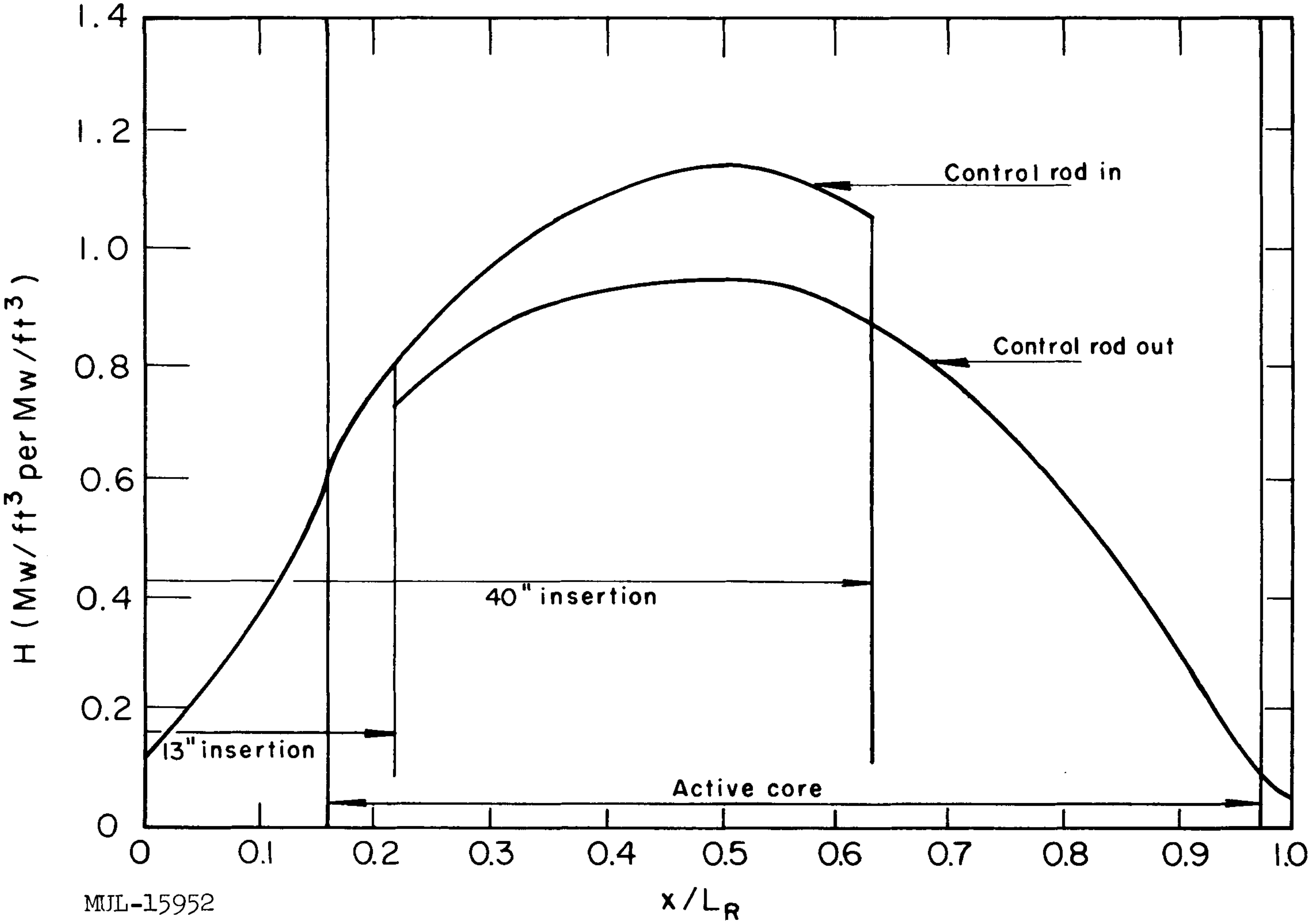

MUL-15952

Fig. IV-9. Nuclear heating of René 41 tie rod in control module at R = 8.92 in.

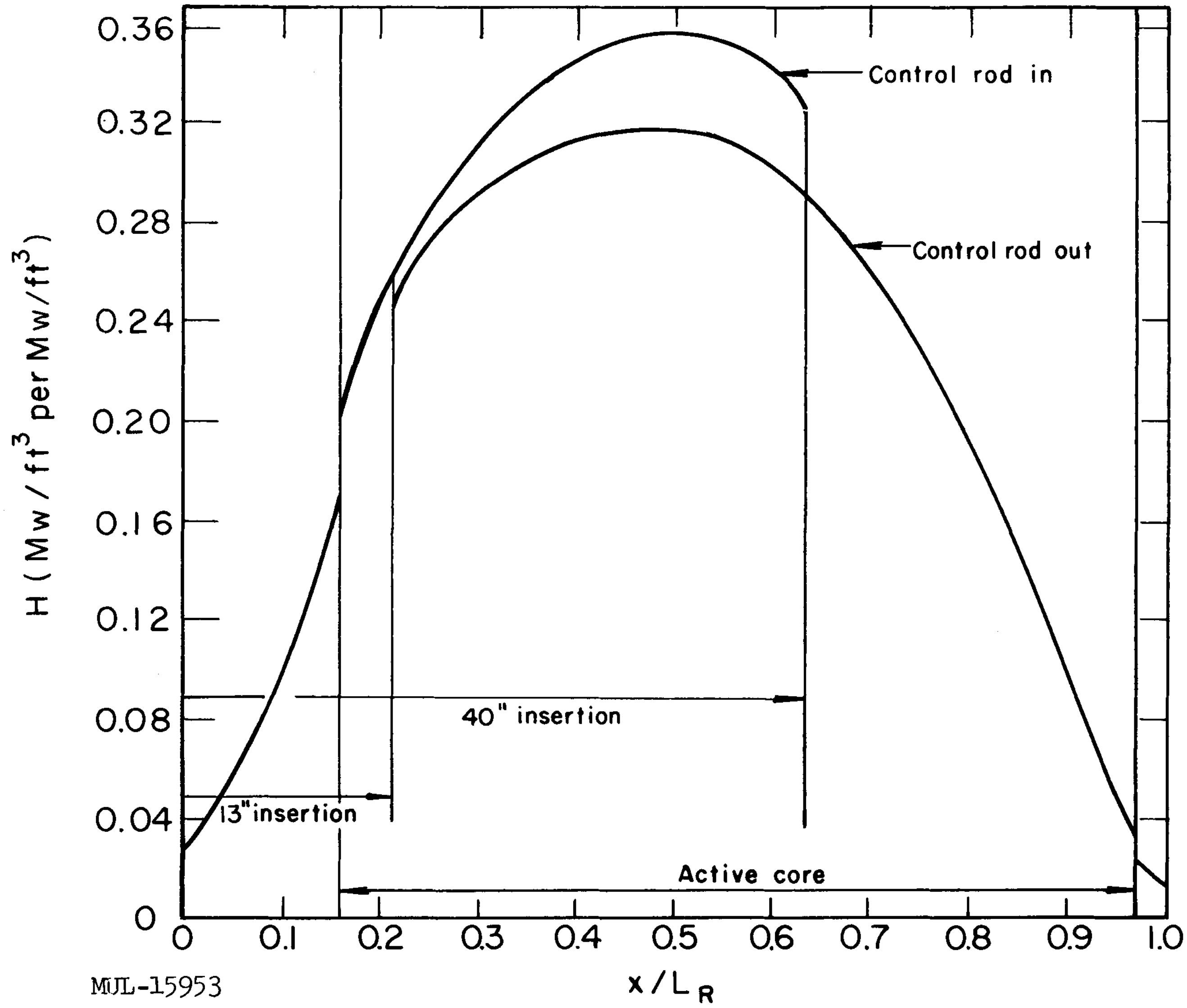

Fig. IV-10. Nuclear heating of BeO insert in control module at R = 8.92 in.

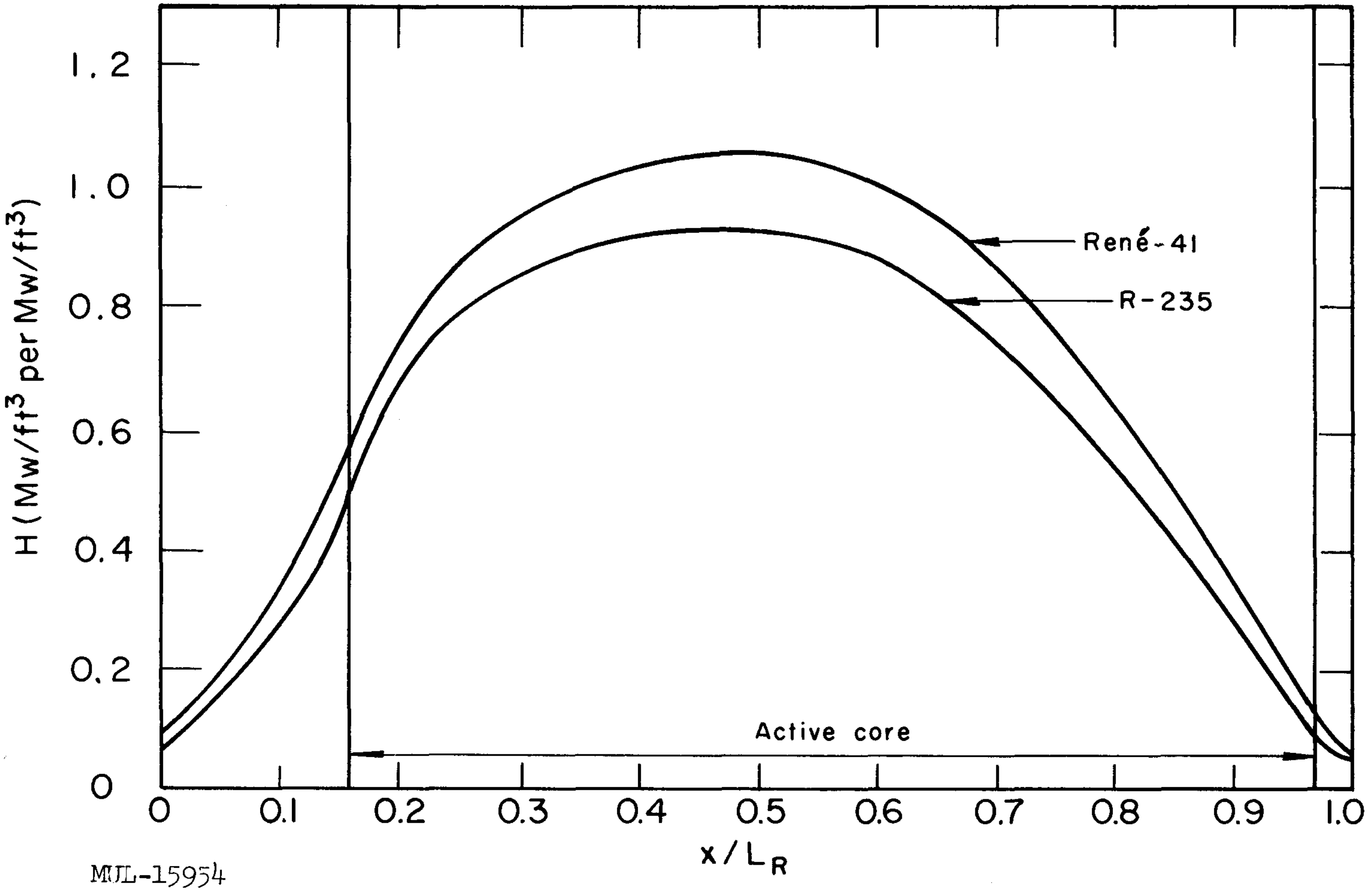

MUL-15954

Fig. IV-11. Nuclear heating of standard tie rods at R = 0.

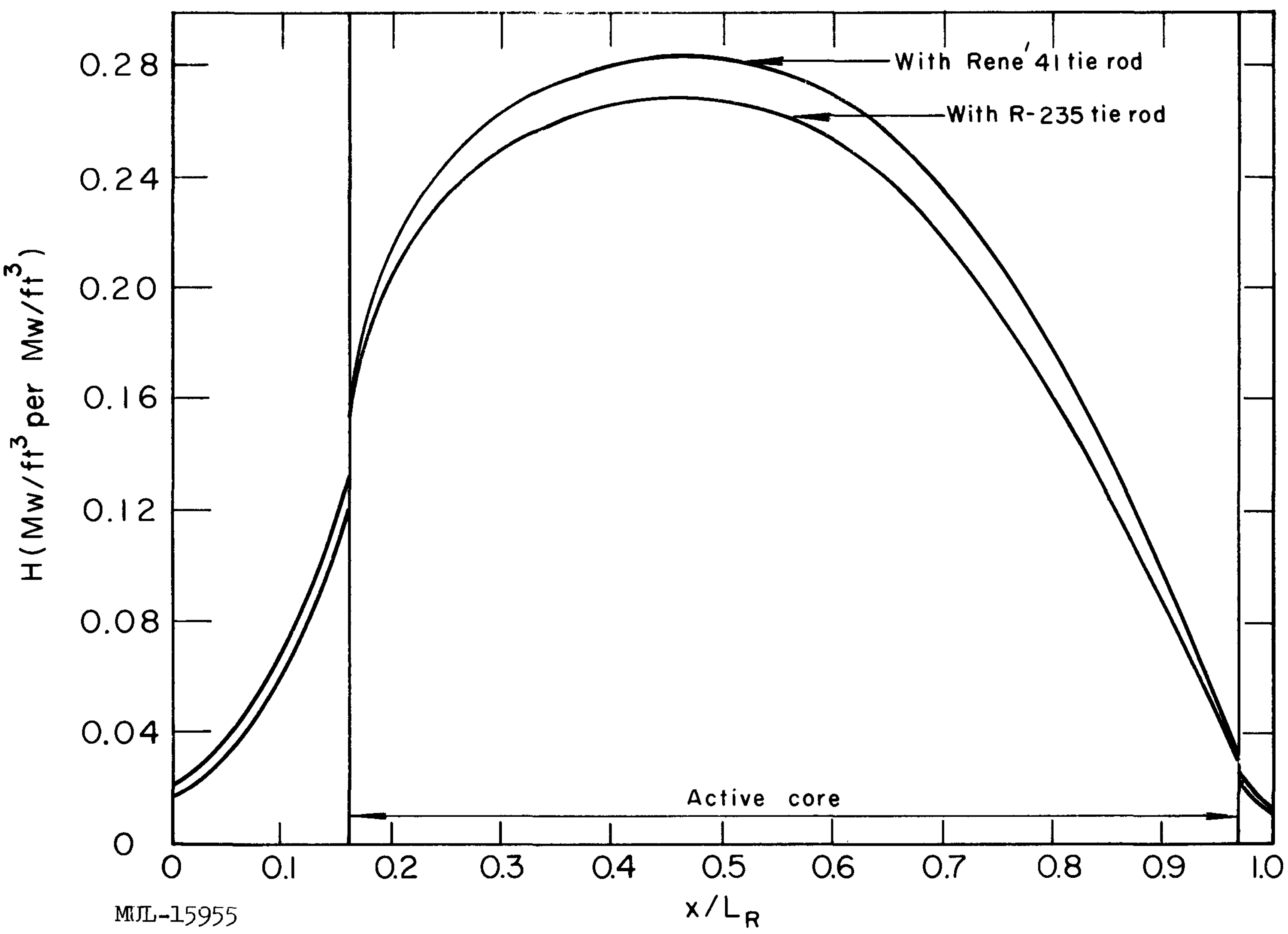

MUL-15955

Fig. IV-12. Nuclear heating of BeO insert in standard module at R = 0.

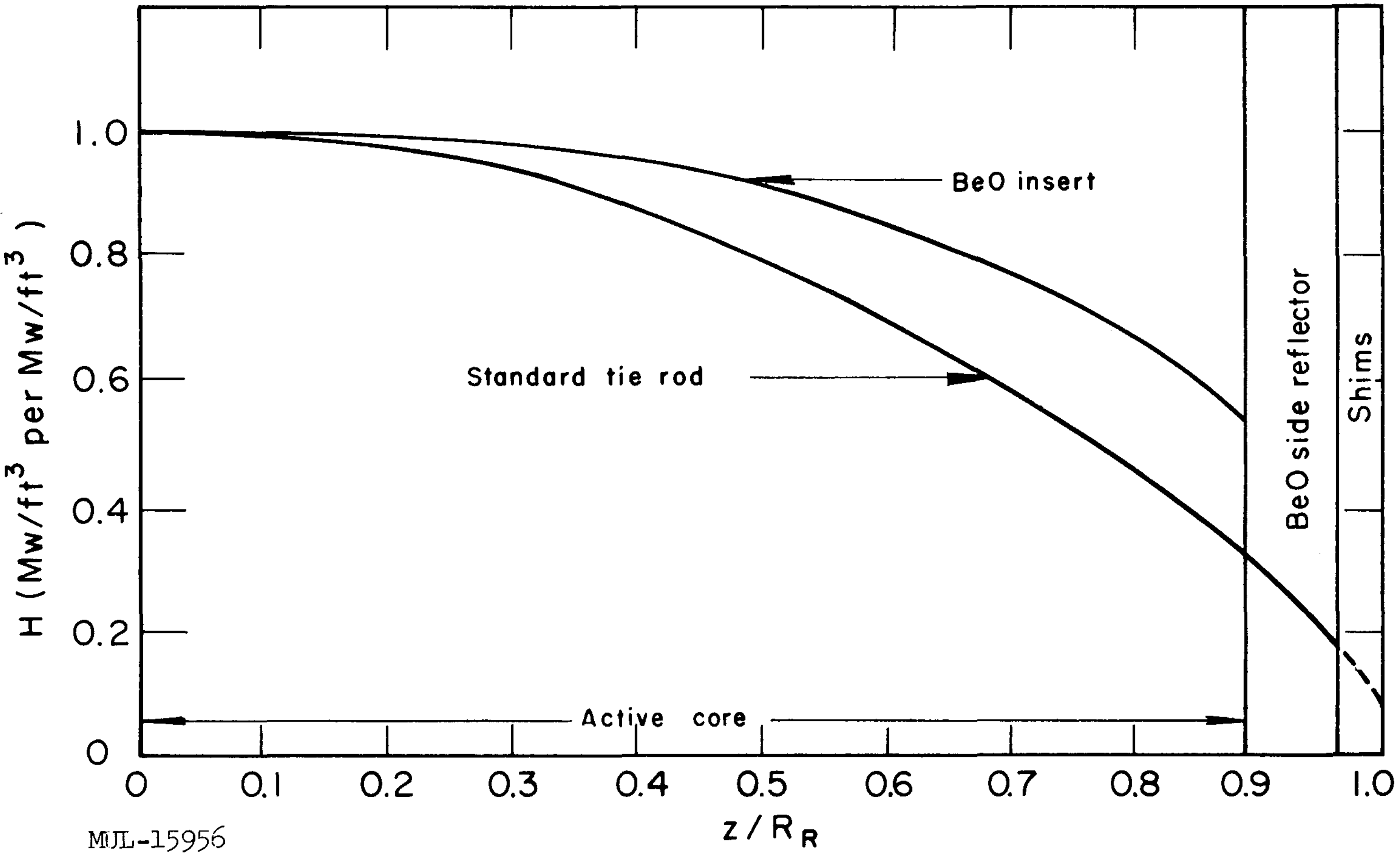

MUL-15956

Fig. IV-13. Radial dependence of standard module component heating.

of the results of the YOGI problems ranges from 5% to 10%. An additional error arises from the uncertainties existing in the input quantities for both gamma and neutron heating; these are on the order of 10%. The spatial distributions, which are derived analytically, introduce further uncertainties; these can range from a few percent to about 20%, depending on the accuracy of the model used in the analytical calculations. The total error in the values given in this analysis are thus seen to be in the range of 20 to 30%.

CONTROL ROD SYSTEMS

Experiments completed in the present quarter permit a redetermination of the neutronic worths of the hafnium shim rods and the $B_4^{10}C$ safety rods. Worth comparisons were made also with the assembly poison rods. (See Pluto Quarterly Progress Rept. No. 9, UCRL-6625, Sept., 1961, pp. 129-33.)

Control Rod Studies at Hot Box

A graphite bare assembly, with a molar ratio of $C/U^{235} = 1200$ was employed for this study at the Hot Box facility. This loading value was chosen in order to approximate the spectrum found in the Tory II-C core.

A vertical coolant hole 0.968 in. in diameter and reasonably far from the control rod system was chosen to accommodate the various test rods in turn. The reactivity worth was determined for each test rod in units of the worth of the fine vane. This worth was simply given as proportional to $\int_{\pi/2}^{\theta_1} \cos^2 \theta \, d\theta$, where $\theta = \pi x/(L + 2\Delta)$, x being measured from the central plane. Here, L is the geometric height and Δ is the extrapolation length. The procedure has been verified [O. C. Kolar and F. A. Kloverstrom, UCRL-6070 (Aug. 25, 1960)]. The comparison was repeated in a second coolant hole, where all rods were worth less. The results are given in Table IV-4.

From experiments 4-6 one can determine the variation of worth of a rod with diameter. It is necessary to interpolate between experiments 4 and 5, giving proper attention to self-shielding (KAPL-1262 was employed in this respect). Some conclusions which follow from Table IV-4 are:

1. A cruciform whose tips fall on the same circle as a rod is worth 1.44 times the rod (diam ~1.00 in., blade thickness ~0.080 in.).
2. An asterisk whose tips fall on the same circle as a rod is worth 1.60 times the rod (diam ~1.00 in., blade thickness ~0.080 in.).

Table IV-4. Comparative Reactivity Values for Various Test Control Rods.

			Ratios			
Expt. No.	Type	Material	Series 1	Series 2	Average	Description
1	Asterisk	Hafnium	1.00	1.00	1.00	(a)
2	Cruciform	"	0.93	0.913	0.92	
3	Rod	"	0.64	0.612	0.626	
4	Tube, i.d. 0.305 in.	B^{10}	0.78	0.777	0.78	(b)
5	Tube, i.d. 0.305 in.	B^N	0.58	0.564	0.57	(c)
6	Tube, i.d. 0.498 in.	B_4^NC	1.11	1.12	1.11	(d)

(a) The three rods had six, four, and two blades, respectively. These blades were 0.080 in. thick. The rod tips in all cases but one fell on a circle 0.875 in. in diameter; the exception was one arm of the cruciform which was 0.90 in. wide. These rods were inserted 40.0 in. into the assembly, which was approximately 48 in. high.

(b) The B^{10} tube was inserted 39.5 in. Into 54 in. of tube length, 52 g of metal was placed. Of this, 84.35% was B^{10}. The resultant density of B^{10}, $\rho(B^{10})$, was 0.676 g/cc.

(c) The B^N tube also was inserted 39.5 in. The density of B^{10} was 0.181 g/cc.

(d) This tube is representative of the assembly poison rods. The B^4C has a density of 2.47 g/cc, giving $\rho(B^{10}) = 0.372$ g/cc. The tube was inserted 40.0 in.

3. Given two rods filled with B^{10} of density 0.372 g/cc, the worth is increased by a factor of 1.52 in going from a diameter of 0.305 in. to 0.498 in. (i.e., factor of 1.64 increase in diameter).
4. An assembly poison rod (i.d. = 0.498 in.) is worth 1.01 of a hafnium asterisk rod (diam = 1.00 in.).
5. A dense $B_4^{10}C$ safety rod, 0.35-in. i.d., inserted 45 in. into Tory II-C is worth 1.05 of a hafnium asterisk rod of 0.875-in. diameter. The $B_4^{10}C$ density is assumed to be 2.32 g/cc. The $B_4^{10}C$ rod is worth 0.94 of a 1.00-in. hafnium asterisk rod.

Shim Rod System

The worth of the 12 rods has been re-evaluated, and Δk is found to be -0.134. Recall that $\Delta k = -0.13$ is required, where $\Delta k = -0.075$ is due to temperature effects, $\Delta k = -0.025$ is due to xenon poisoning after a 10 hour run, $\Delta k = -0.025$ is needed for shutdown, and $\Delta k = -0.005$ is desired for supercriticality.

The procedure will now be outlined.

1. ANGIE R-θ calculations have been performed in which 12 flat bar-type shim rods are represented. For 80-mil rods, $\Delta k_{12} = -0.134$.
2. It has been established by comparing ANGIE calculations with Spade experiments that the worth of hafnium bars is overpredicted by ANGIE by 10%. Therefore $\Delta k_{12} = -0.120$.
3. The rods are inserted only 40 in., which is 73% of the total worth. Therefore $\Delta k_{12} = -0.0875$.
4. The asterisk shape is 1.6 times as effective. Therefore

$$\Delta k_{12} = -0.140$$

One small factor which is not yet evaluated is the enhanced coupling between rods when one goes from step 3 to step 4. Coupling is implicit in step 1, and was seen to degrade the worth of a rod by ~12% in comparison with a single rod in the core. It would appear reasonable to reduce the latter value of Δk by 5% to

$$\Delta k_{12} = -0.134.$$

The earlier estimate of $\Delta k_{12} = -0.19$ has been reduced primarily because the worth ratio of asterisk to bar was smaller than anticipated.

The Tory II-C reactor has been modified slightly to permit the accommodation of four more standard shim rods in the "N" ring. Four tension tubes in the "M" ring will be of the control tube variety. These rods are worth 30% of the shim rods, or

$$\Delta k_4 = -0.3 \times 0.134 = 0.040.$$

The extra rods will be added only if it is found that the 12 normal shim rods give inadequate reactivity swing.

Reactor Safety System

A more accurate determination of the worth of the reactor safety system is now possible. The Hot Box comparison studies show that the $B_4^{10}C$-filled tube, 0.35 in. in inner diameter and inserted to a depth of 45 in., is worth 0.94 of a hafnium asterisk rod inserted 40 in. at the same core position. Six safety rods in the "L" ring will, because they are closer to the core center than the asterisk rods of the "M" ring, be enhanced by a factor of 1.08. The safety rods are then worth

$$\frac{0.94 \times 6 \times 1.08}{12} = 0.51$$

of the 12 shim rods. The relative coupling effect has to be evaluated; it is expected to be unimportant.

The decision has been made to utilize only six safety rods in the "M" ring, to avoid the additional and considerable complexity which would arise in a more extensive system. The above findings indicate that the safety system can protect the reactor in the event of failure of one or two actuators (where three shim rods are connected to each actuator).

Assembly Poison Rods

The assembly poison rods are seen from the Hot Box comparison studies to be worth 1.01 as much as a normal hafnium asterisk rod. With approximately 100 poison rods in the empty tension tubes, the reactor should be very subcritical.

ANGULAR DISTRIBUTION OF LEAKAGE NEUTRONS

FLANG, a FORTRAN code for the IBM 709/7090, calculates the vector flux emerging from the end of a semi-infinite slab. The equation solved is

$$F_i(x_2, \mu) = (\mathrm{Sum})_j \; \frac{1}{2\mu} \int_{x_1}^{x_2} \Sigma^{ij}(x)\, \phi^j(x)\, e^{-\Sigma^i(x)(x_2 - x)/\mu}\, dx$$

where $F_i(x_2, \mu)$ is the vector flux (energy group i) emerging into the interval $[\mu, \; \mu + d\mu]$,

$\phi^j(x)$ is the group j scalar flux (input quantity),

$\Sigma^{ij}(x)$ is the macroscopic cross section for transferring neutrons from j to i by scatters and fissions,

$\Sigma^i(x)$ is the total cross section for group i.

FLANG also calculates the scalar flux at the boundary and the current at the boundary:

$$\phi^i(x_2) = \int_0^1 d\mu \; F(x_2, \mu),$$

$$J^i(x_2) = \int_0^1 d\mu \; \mu F(x_2, \mu).$$

Results

A three-group, homogeneous, 72-cm semi-infinite slab (C/235 = 1000) was run on ZOOM (our one-dimensional diffusion code) and on BANZAI (our one-dimensional transport code). The scalar flux from BANZAI was put into FLANG, and the vector flux emerging from the end of the slab was calculated. This vector flux, for one thermal group, is plotted below (Fig. IV-14). Also plotted is the reactor flux calculated from diffusion theory $[F(x,\mu) = \frac{1}{2}\phi(x) + \frac{3}{2}J(x)\mu]$ for the same slab with the same power level. It is seen that the angular agreement is reasonable, though the magnitudes differ (possibly an indication that the diffusion constant is too large).

The above considerations are particularly pertinent to the Tory II-C reactor if accurate estimates of radiation heating of external components such as the side support structure are needed.

POWER-REFLECTOR THICKNESS STUDY

The maximum total power delivered to the airstream by a reactor is a function of many variables. Limitations are imposed by the technology of fabrication of materials and the extremes of temperature and stress the materials can withstand, but within these limits it is possible to vary the thickness of the reflector, the radial fuel distribution, and the porosity of the core. The design of the Tory II-C reactor is based on a flat radial power distribution with a 3-inch radial reflector. The object of this study is to determine what combination of radial power profile and reflector thickness will lead to the maximum power being delivered to the airstream.

Method

The variations are carried out subject to the following restrictions:

1. The length and total radius (core + reflector)are fixed at Tory II-C values.
2. The critical mass of oralloy dioxide must be 50 kilograms.
3. The maximum fuel concentration cannot exceed 10% by weight.
4. The core porosity must be kept uniform.
5. The maximum temperature in the core cannot exceed that for Tory II-C.

Restriction 5 is applied by saying that the maximum power density at any point cannot bear a greater ratio to the Tory II-C value than the ratio of the corresponding porosities (porosity is defined as 1 minus the volume of solid BeO

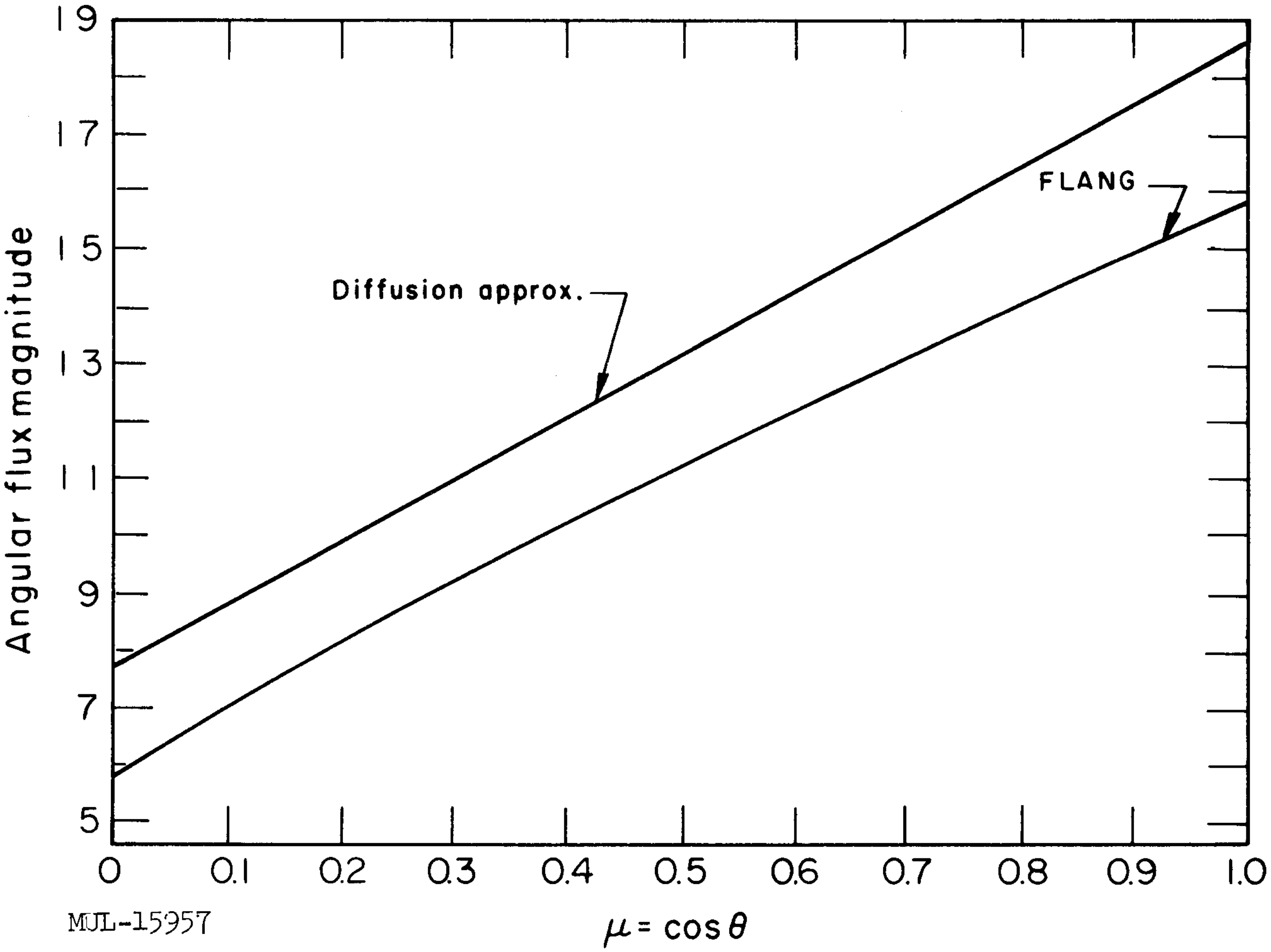

MUL-15957

Fig. IV-14. Comparison of angular flux from FLANG (using BANZAI scalar fluxes) and angular flux from diffusion approximation (using ZOOM scalar fluxes).

per cm^3). That is, $\left(\frac{dP}{dV}\right)_x$ × porosity (which is constant over all radial zones of Tory II-C), is not exceeded. Restriction 3 did not affect any of the problems since great extremes in fuel loading were prohibited by the condition of near-flat radial power for optimum operation, as will be brought out later.

The best representation of Tory II-C as of July, 1961, was used as a base problem with 9-ZOOM to give a value of the total power and porosity. This problem gave a radial power distribution flat to ±0.3% with a 3-inch BeO reflector.

The first question to arise is whether or not a flat radial power gives the maximum total power for a given reflector thickness. Condition 5 above (requiring a normalization to the peak power density) prohibits any radial fuel distribution leading to bumps or peaks of any magnitude in the power distribution. The question then applies to fuel movements producing only broad plateaus in the power curve.

The movement of fuel from a region of greater to one of lesser neutronic worth would result in a net decrease in total power: the fuel is then in a region of lower neutron flux and therefore undergoes fewer fissions. The lower value of k_{eff} would necessitate increasing the BeO concentration to bring k_{eff} back to the base value, and give a lower porosity for normalization. All of these effects produce a lower normalized total power, and prohibit such a fuel movement.

A more fruitful approach appears to be the movement of fuel from a region of lesser to one of greater neutronic worth. We now produce a locally depressed power area where the fuel has been removed, but in compensating for the higher k_{eff} produced, we reduce the BeO concentration and increase the porosity. If the effect of the gain through normalizing to the lower porosity is larger than that of the loss through local power depression, the normalized total power will be increased. This effect will be largest in the case where the neutronic worth changes the most. Since the effect of a side reflector is to even out the neutronic worth radially, the deviation from a flat radial power will be of most benefit with the thinnest reflector.

From these arguments it appears best to first examine the variation of total power (normalized through the porosity) with reflector thickness, if the radial power distribution is kept flat. The results of these calculations are shown in Fig. IV-15. The power curve has a shallow maximum between 2-1/2

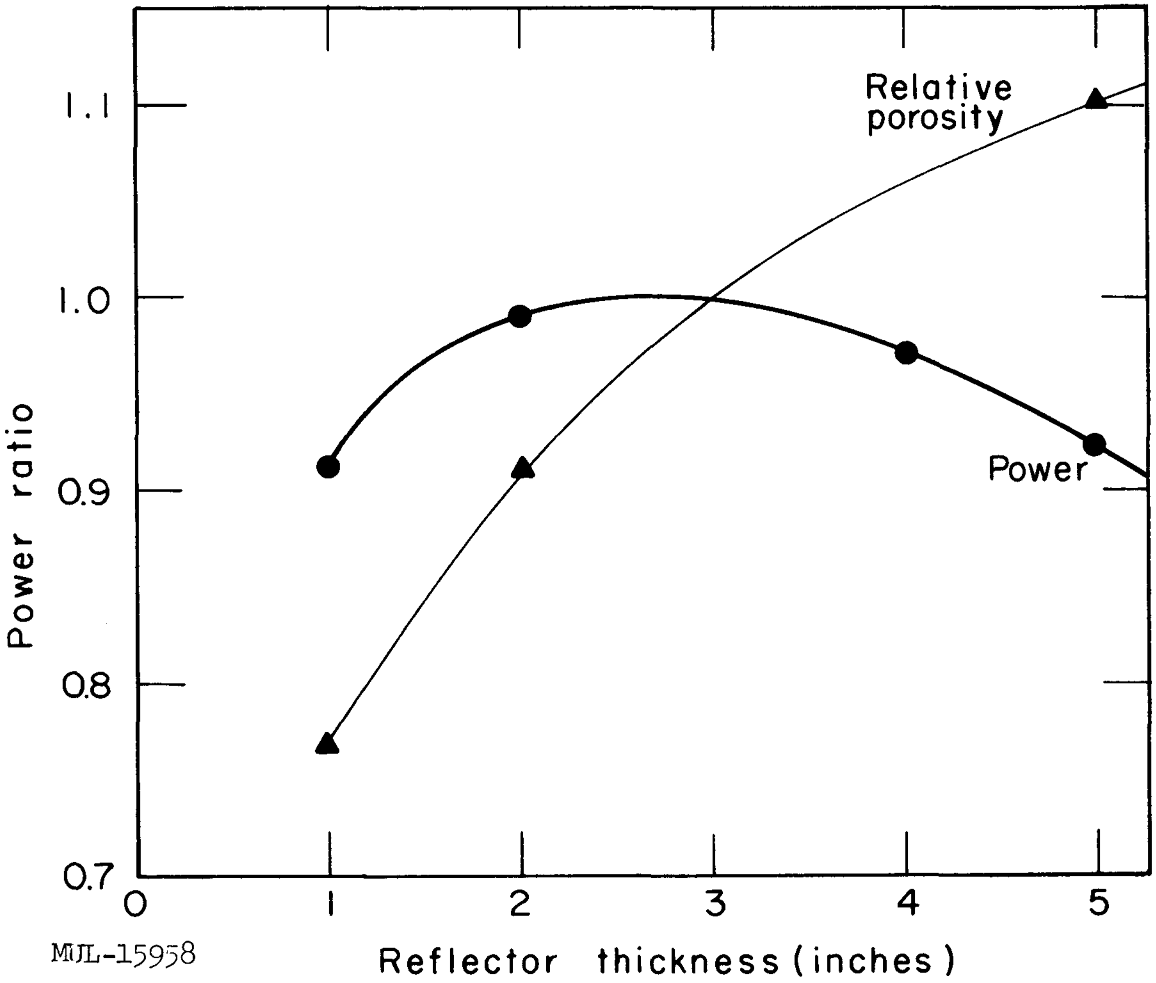

Fig. IV-15. Total power ratio vs reflector thickness. Powers are normalized through ratio of porosity to 3-inch case.

and 3 inches; while it appears that the present design is near optimum, any reflector thickness in the range 2-3 inches gives very nearly the same result.

Now we consider the variation of radial power from the flat distribution. Remembering that the benefits are greatest when fuel is moved from the region of lowest neutronic worth, we would move it from the outermost core region. This in effect is simply increasing the reflector thickness, and from Fig. IV-15 we see that increasing the reflector thickness does indeed help when the original thickness is below 2 inches. However, the reflector thickness added by removing fuel is of material of the density of the core, not as dense as the original reflector. The effect that movement of fuel has on total normalized power is therefore expected to be small.

A series of problems have been solved involving deviations from flat power for the 1-inch reflector case. The fuel was completely removed from core regions of various thickness nearest the reflector and redistributed over the remainder of the core so that the power distribution was flat. The results are shown in Fig. IV-16. The removal of the fuel from the outermost inch of core did indeed increase the total normalized power; but the effect is small, as expected, and does not raise the power to the level of the Tory II-C 3-inch-reflector reactor design (normalized power of unity).

Conclusions

With the restrictions imposed on this study, the total power delivered to the airstream by the reactor will be a maximum:

1. When the radial power distribution is flat.
2. With a reflector thickness of 2-1/2 inches.

Figure IV-15 has a shallow maximum, and it appears the power is not sensitive (<1% variation) to reflector thickness over the range 2-3 inches. For reflector thicknesses less than 2 inches, the maximum total power is obtained when the radial power distribution is not flat but has a minimum adjoining the reflector. This amounts to an effective increase in reflector thickness, and since the added reflector material has the low density of the core, the effect is small.

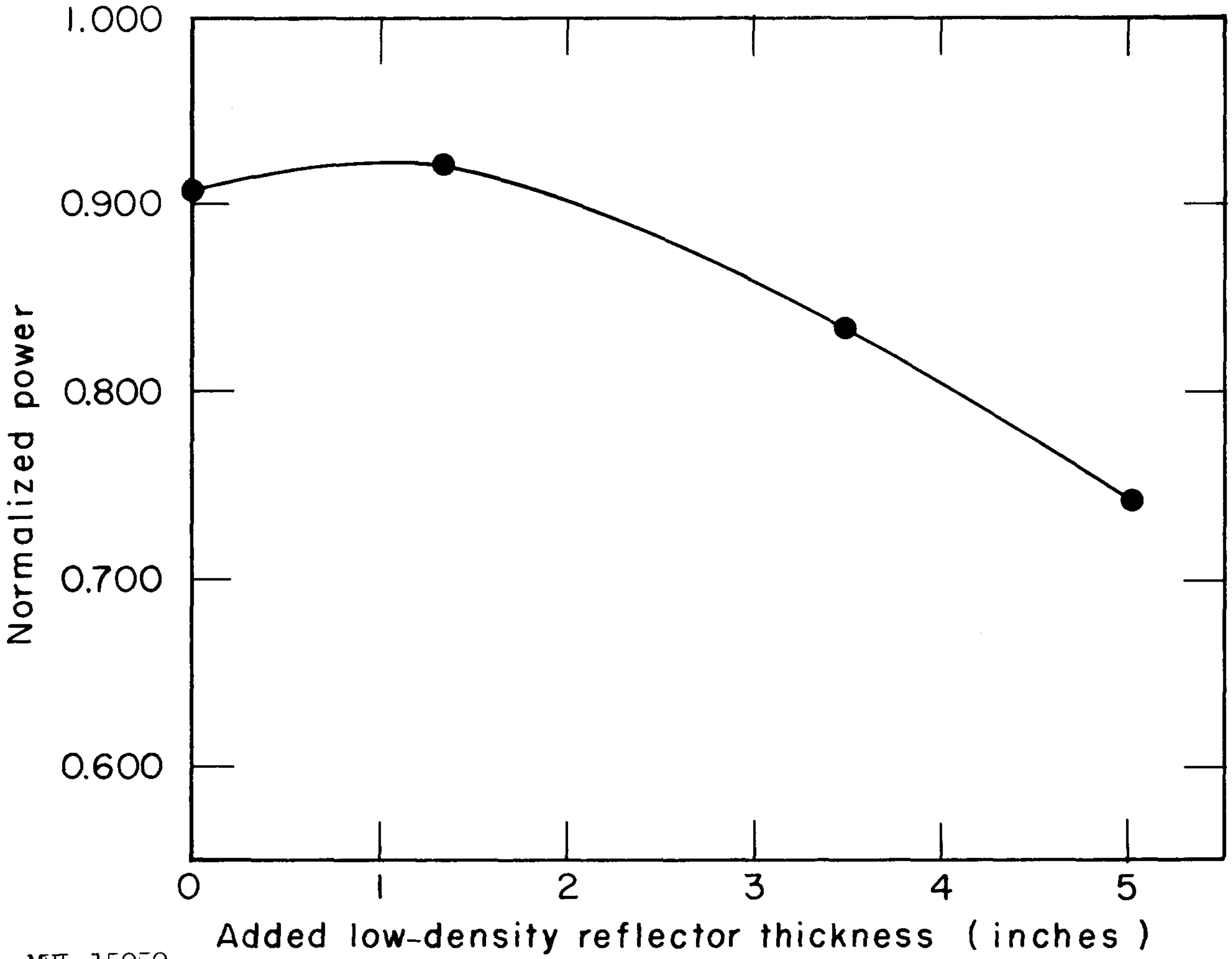

MUL-15959

Fig. IV-16. Effect on reactor power of removing fuel from core region nearest reflector and redistributing it over remainder of core (in effect, increasing reflector thickness by adding low-density reflecting material). Reflector thickness, 1 inch.

SECTION II. AEROTHERMODYNAMICS

PERFORMANCE ANALYSIS

Tory II-C is in the final design phase of development; however, until more detailed characteristics of the side support structure and aft transition region are obtained, it would not be appropriate to re-estimate the engine equivalent performance of the Tory II-C reactor. On the other hand, efforts are being devoted to improving techniques of performance analysis. Until recently ramjet performance calculations used in the designing of the Tory II-C air-cooled reactor and associated air ducting were based upon operational points determined for a reactor consisting of a single variety of fuel element flow channels. The effects of unfueled structural and control components were analyzed by hand correction and no attempt was made to reoptimize the resulting performance numbers.

A relatively simple modification of the NOMAC 2 digital computer code has made it possible, however, to consider up to 30 independent varieties of flow channels in a single performance calculation. (See UCRL-6146, Part II, for a description of NOMAC 2.) Thus it becomes feasible to carry out extensive parameterized optimization studies for more realistic engine configurations. This new performance code is called DASH-N. The specific effect of applying this code to Tory II-C is that exit plenum pressures are inclined to be higher than predicted by "single-tube ramjet" analysis. This higher pressure is caused by structure cooling dynamics and results in a lower flow rate and lower total reactor power for a fixed maximum fuel element temperature.

The thrust coefficients predicted by DASH-N include the effects of sudden expansions at the exit of the Tory II-C reactor, but such considerations as diffuser boundary layer bleed, entrance losses, offsets, control rod power depression, etc., must be accounted for independently. These latter effects produce about a 10% reduction in net performance of the engine.

At the time of this writing, the net design point thrust coefficient for Tory II-C is calculated to be 0.178 when based upon a diameter of 57 inches.

During this reporting period, major emphasis has been devoted to detailed component analysis. A new IBM 7090 code entitled SODOM has been developed to perform detailed thermal analysis of components with complex geometries. The temperatures at the interior points of a two-dimensional space are determined by the code using a relaxation method applied to the set of difference equations obtained from Poisson's equation. The maximum permissible nodal point number is 10,000. The temperatures at the space boundaries are fixed from the boundary condition appropriate for convective heat transfer.

INLET AND EXIT THROAT SIZES

The inlet grid and exit nozzle throat sizes have been specified. The inlet grid was sized so that at the Mach 3.0 hot-day operating condition the pressure at the test vehicle disconnect will not exceed 560 psia. This pressure limit is dictated by structural limitations of the air supply system. The required total throat area of the inlet grid is 246 in^2 at room temperature. Since there are 241 flow passages in the grid, each flow passage throat area will be 1.02 in^2 at room temperature. The expected critical reactor temperature ratio is expected to be 3.2.

The exit nozzle throat area will be 745 in^2 at ambient temperature. This value was selected on the basis of reactor thrust optimization. The choking flow rate of the exit nozzle for various stagnation bulk mean air temperatures is shown in Fig. IV-17. This graph was generated by utilizing the continuity relations, an atmospheric pressure of 12.5 psia, and a flow discharge coefficient of 0.98.

SIDE-SUPPORT STRUCTURE ANALYSIS

The purpose of the aerothermodynamic design analysis of the Tory II-C side support structure is to determine the local temperatures of the cooling duct walls and spring walls for various operating conditions, so that temperatures injurious to the materials can be avoided during actual operation of the reactor.

The heat transfer problems associated with the side support structure designs, shown schematically in Figs. IV-18 and IV-19, are concerned with the turbulent flow of gases in ducts having noncircular cross sections. Papers in the literature which investigated the pressure drop and heat transfer in ducts with noncircular cross sections indicate that turbulent pressure drop can be calculated from relations for circular ducts when the diameter in these relations is replaced by the "hydraulic diameter" of the particular cross section. This rule has also been used to calculate average heat transfer coefficients in noncircular ducts. It has not, however, been verified as well by experiments.

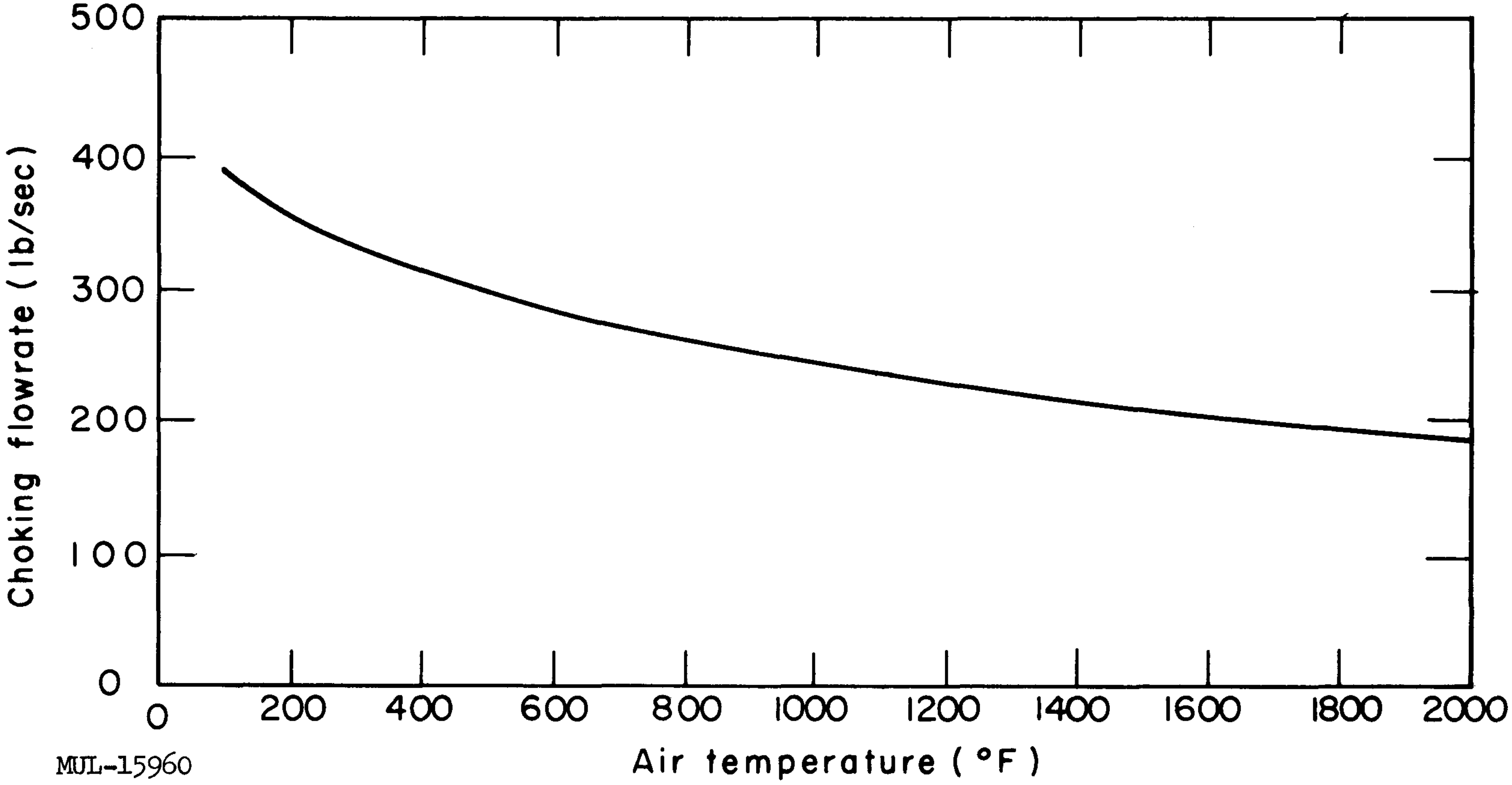

MUL-15960

Fig. IV-17. Flow rate required to choke Tory II-C exit nozzle. (Atmospheric pressure 12.5 psi.)

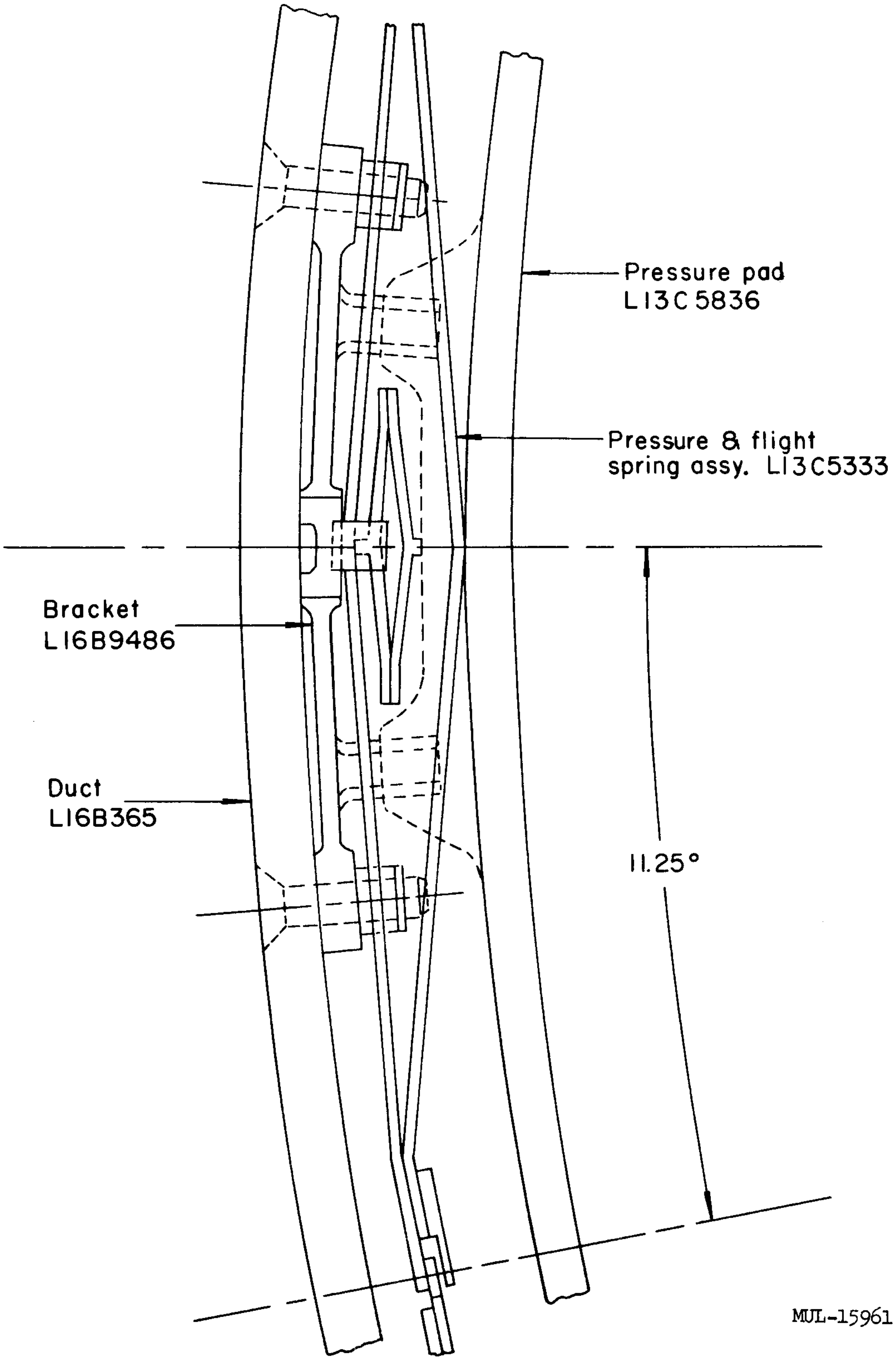

Fig. IV-18. Cross section of side support structure.

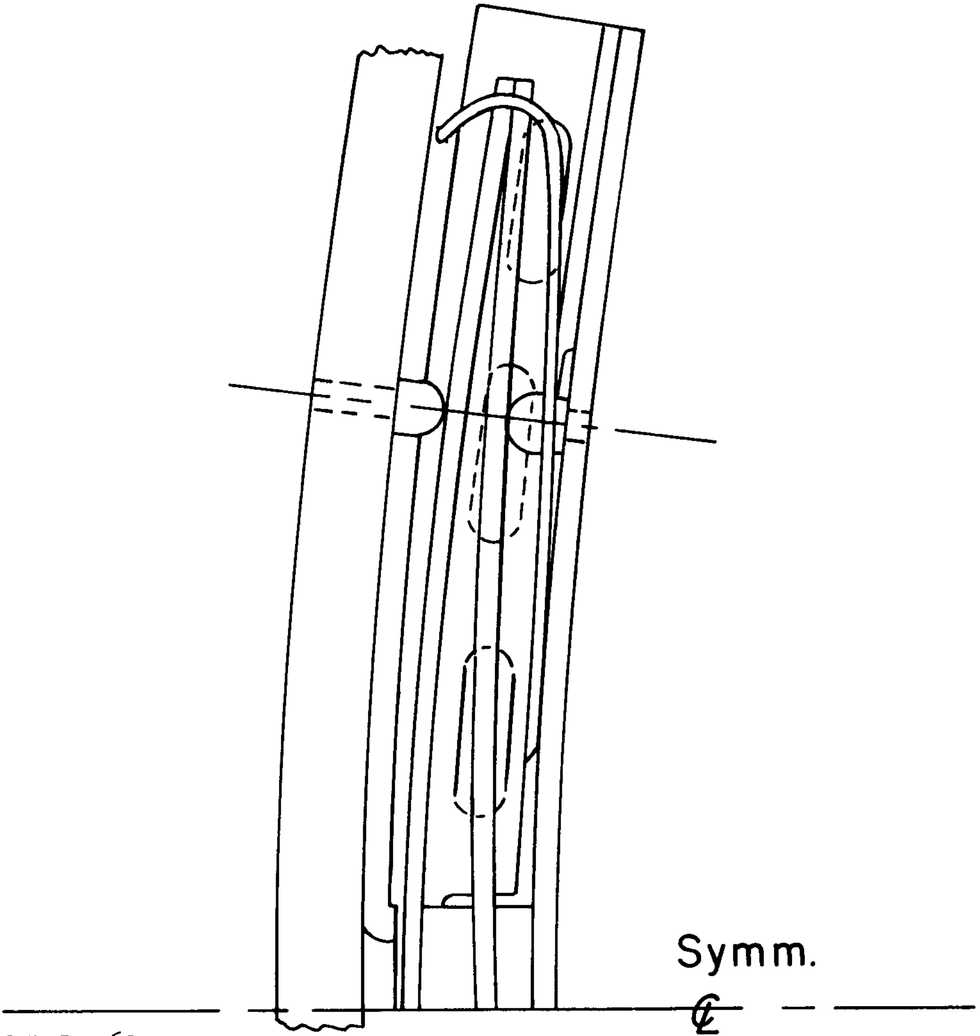

MUL-15962

Fig. IV-19. Cross section of side support structure.

The preliminary heat transfer analysis of the side support structure is based on the "hydraulic diameter" of that particular cross section. The heat transfers of the cross sections are individually calculated and then are made to satisfy a radial heat balance in order to correctly calculate average wall temperatures of the various components. The results of these analyses are then corrected for the calculated boundary conditions in turbulent flow for that particular geometry. These boundary conditions are calculated by Deissler and Taylor's procedure which determines the local heat transfer coefficient around the periphery of the duct. The results of the calculations of local heat transfer coefficient related to the average coefficient based on "hydraulic diameter" are presented in Fig. IV-20.

The results of the calculations to determine the maximum wall temperatures in the side support for the configuration shown in Fig. IV-18 for the Mach 3.0 operating condition and a mass flow of 130 lb/sec are as follows: duct, 1510°F; pressure pad, 1609°F; springs, 1240°F; bracket, 1330°F. The maximum wall temperature of the nuts and bolts fastening the bracket to the duct is 1670°F.

The preliminary results of the calculations for the configuration shown in Fig. IV-19 for the same operating condition stated above show that the maximum wall temperatures are as follows: duct, 1440°F; pressure pad, 1520°F; springs, 1332°F; spring clip, 1520°F; fittings, 1550°F.

It is important to match the pressure through the side support with that of the core in order not to apply large pressure forces on either the core or the side support. In order to accomplish this the pressure through the side support may be dissipated by introducing sudden expansion losses designed to match, as closely as possible, the core pressure. If for both side-support designs pressure losses are accomplished at the beginning, middle, and end of each pressure pad, the typical axial pressure distribution through the side support compared to the core pressure for the Mach 3.0 operating condition is presented in Fig. IV-21.

Also completed during this report period was calculation of a chart to determine transient temperatures in the reactor duct due to a step input of power deposited in the duct. That is, the equation

$$\frac{\partial^2\theta(x,t)}{\partial x^2} = \frac{1}{\alpha}\frac{\partial\theta(x,t)}{\partial t} - \frac{q_0}{k}$$

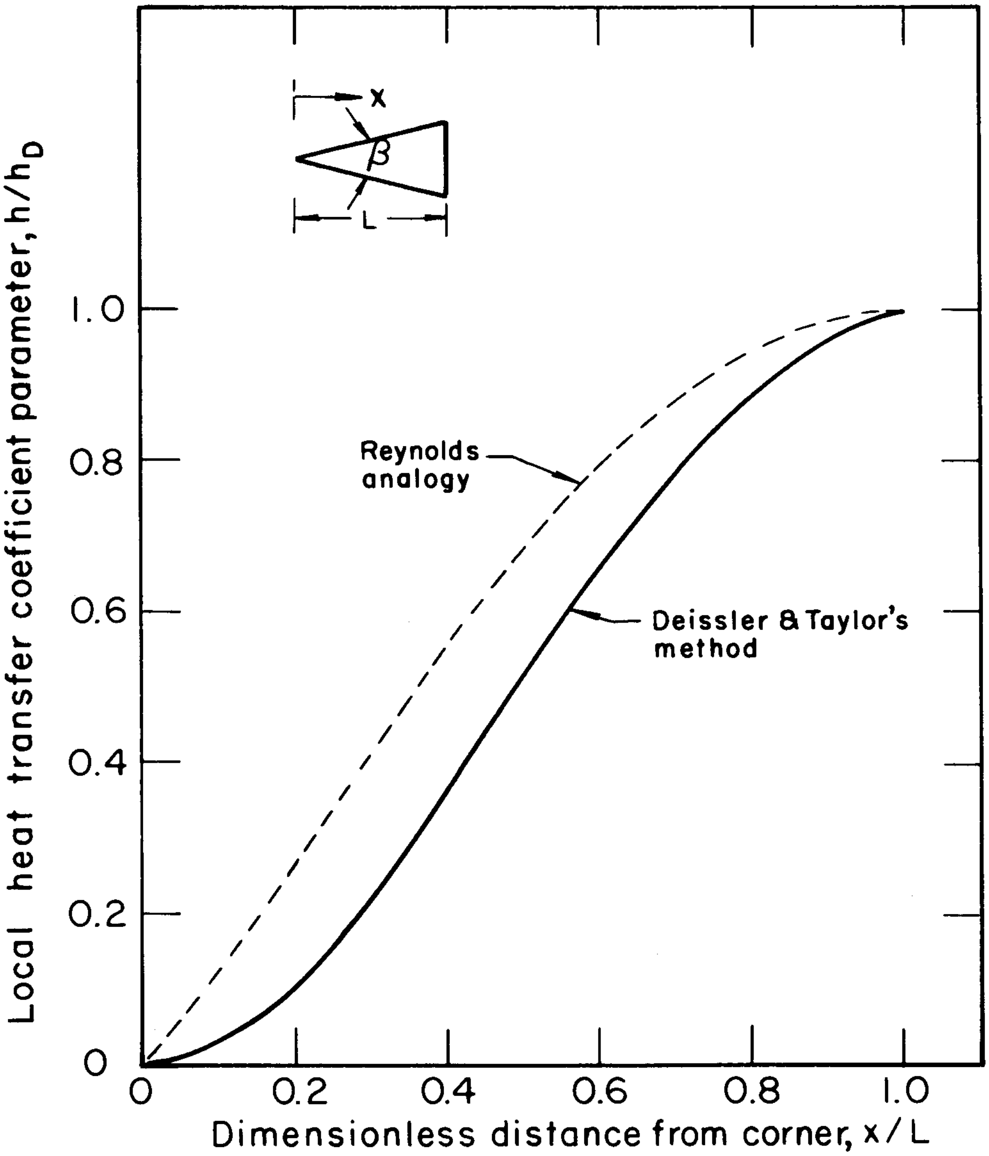

MUL-15967

Fig. IV-20. Local heat transfer coefficient parameter for a triangle with apex angle β = 10°, for Reynolds number from 25×10^3 to 900×10^3; h_D is heat transfer coefficient based on hydraulic diameter.

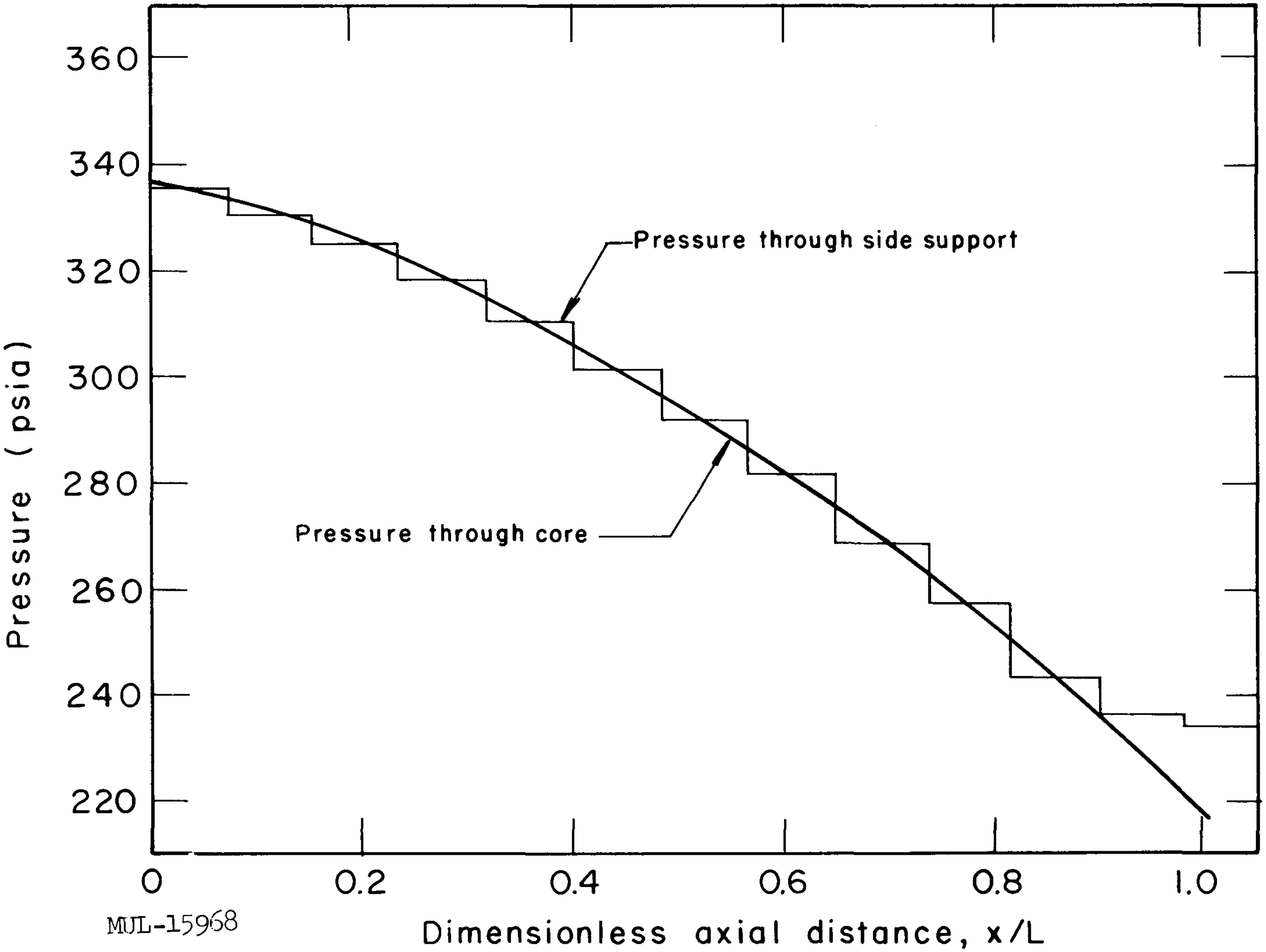

MUL-15968

Fig. IV-21. Typical pressure through core and side support.

with appropriate boundary conditions was solved to yield the transient

$$\theta_1(x,t) = -\left(\frac{2q_0a^2}{k}\right)\sum_{i=1} \frac{\cos\left(\frac{x}{a}X_i\right)\exp\left(-\frac{\alpha t}{a^2}X_i^2\right)}{X_i^3\,[af\sin X_i + X_i\cos X_i + \sin X_i]} ,$$

where the values of X_i are given by

$$\cot X_i = X_i/af.$$

This solution was programmed and calculated on the IBM 650 computer.

EXIT TRANSITION CONFIGURATION

A series of experiments have been performed to evaluate pressure losses and flow nonuniformities for five different types of exit transition regions. Figure IV-22 is a sketch of the proposed Tory II-C transition configuration. As derived from the experiments, a total pressure loss of 2.8% due to the transition is presently predicted for design point operating conditions. Flow nonuniformity due to exit pressure nonuniformity should be negligible.

FRONT SUPPORT GRID

Calculations have been performed to ascertain the maximum temperatures to be expected in the redesigned front support grid. Pertinent maximum temperatures for Mach 3.0 hot-day operating conditions are as follows:

Maximum internal temperature (trailing edge) $\approx$1500°F,
Average internal temperature $\approx$1350°F,
Maximum wall temperature (trailing edge) $\approx$1430°F
Average wall temperature $\approx$1300°F.

Except at the leading edge, the effect of axial conduction was found to be negligible.

A maximum nuclear power density of 1.0 Mw/ft^3 and a leading-edge power density of 0.5 Mw/ft^3 with linear interpolation along the beam axis was used as the source function for the calculations.

Nonrecoverable pressure losses across the grid are expected to be less than 1% of the reactor inlet pressure.

TIE RODS

Tie rod aerothermodynamic parameters have been computed for Tory II-C operating limits. Included here are tie rod parameters for René 41 and

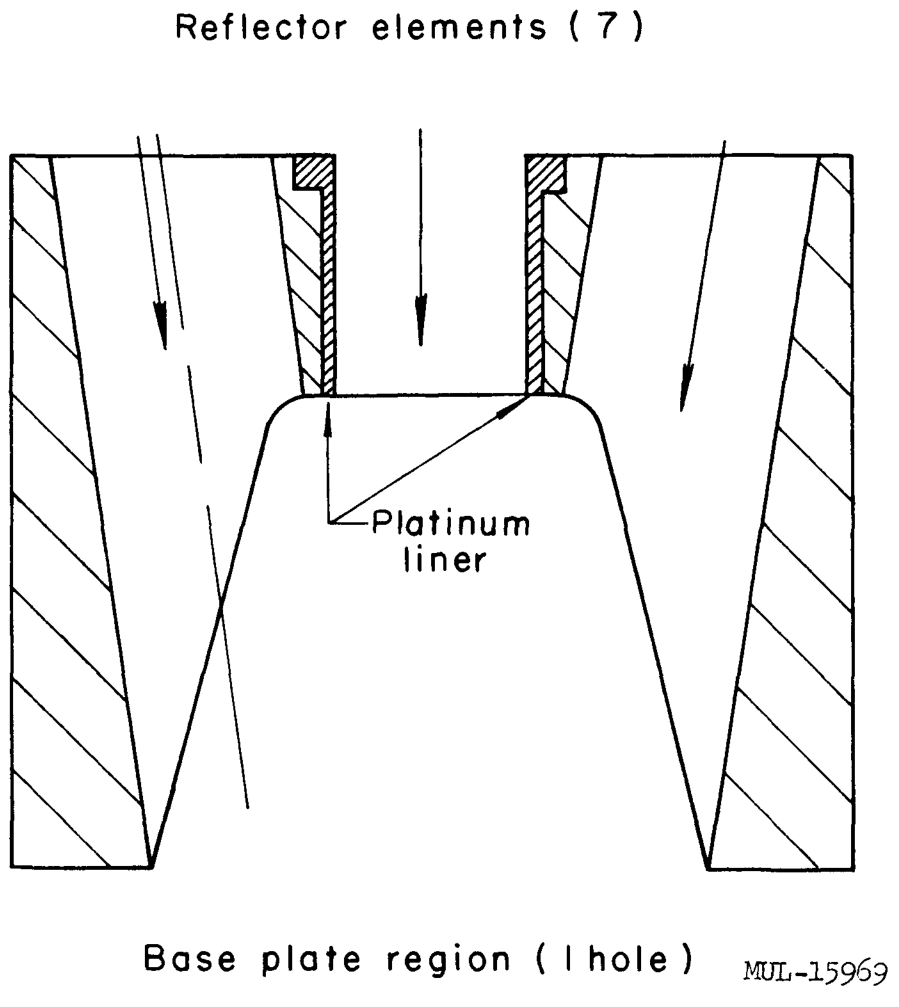

Fig. IV-22. Proposed exit transition configuration for Tory II-C. Arrows indicate flow.

Hastelloy R-235 at seven radial positions. Figures IV-23 through IV-36 show the axial variation of wall temperature, stagnation gas temperature, and the peak-to-average power density ratio for the rods. Figures IV-37 and IV-38 show the axial variation of total pressure, static pressure, and Mach number for the same operating conditions.

Including the effects of thermal radiation from the insert tubes, internal (maximum) material temperatures were found to be within 2% of the wall temperatures shown.

CONTROL ROD

The present control rod design consists of six sections of 40-mil curved hafnium sheet with provision for flow down the center of the rod. The general characteristics when operating at Mach 3.0 hot-day conditions are as follows:

Total power = 24.7 Kw (full insertion),
Length of rod = 40 in.,
Hydraulic radius = 0.177 in.,
Flow area (total) = 0.887 in^2.

For this new control rod design, the internal temperatures will be close to the surface temperatures at any axial position.

The maximum wall temperature of the control rod has been calculated to be about 1600 °F. The maximum gas temperature in the control rod channel will be about 1300 °F.

TRANSIENT REACTOR PERFORMANCE

The transient aerothermodynamic performance of a reactor may be described in terms of the temperature variations with time of various portions of the reactor. The temperature-time history of a given part of the reactor is a function of the heat input from fission, radiation absorption; heat removal by means of conduction, convection, and radiation; material properties such as density, specific heat, etc.; and location in the reactor itself.

The transient aerothermodynamic analysis of Tory II-C that is currently under way takes all these various factors into account. The principal tool is the SEA LION code which solves the heat balance equation for up to 50 elements (5 types of flow channels, each divided into 10 axial zones) of the reactor simultaneously.

Some results obtained to date with this code are presented in Fig. IV-39. The time-temperature histories for the fuel elements, the BeO inserts between

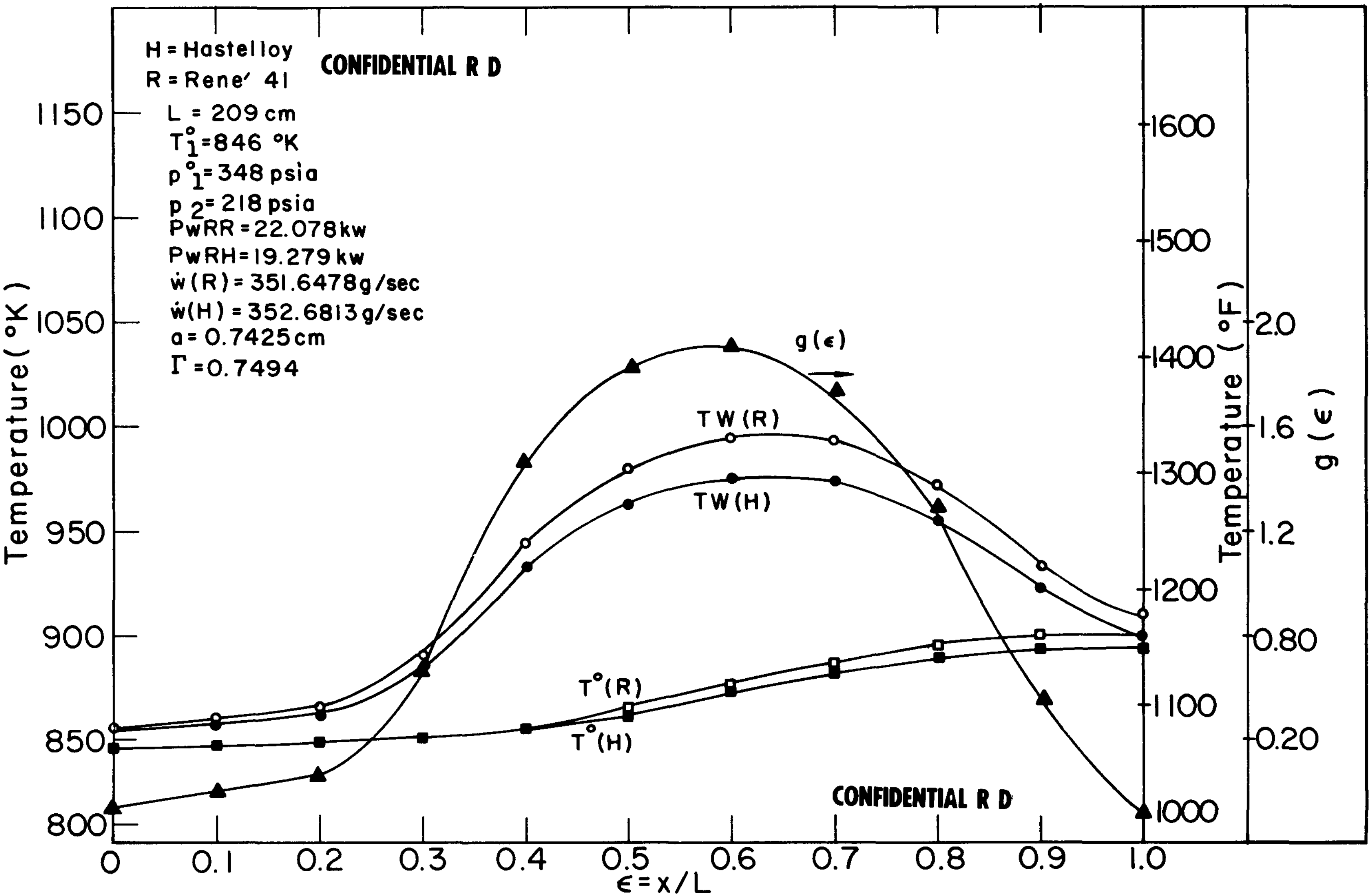

MUL-15970-A

Fig. IV-23. Tory II-C tie rod parameters at Mach 3.0, radial position 0 inches.

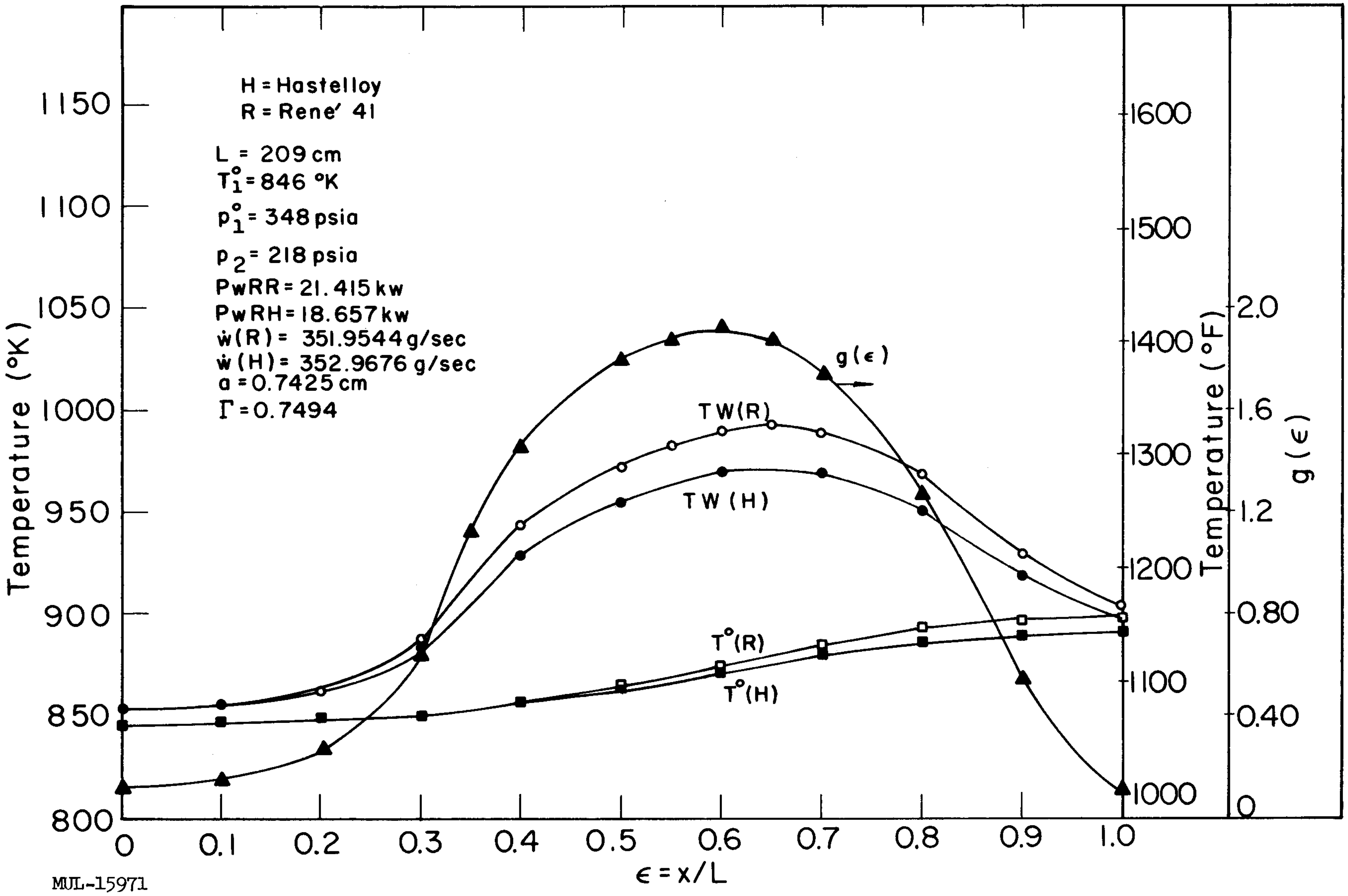

Fig. IV-24. Tory II-C tie rod parameters at Mach 3.0, radial position 5.35 inches.

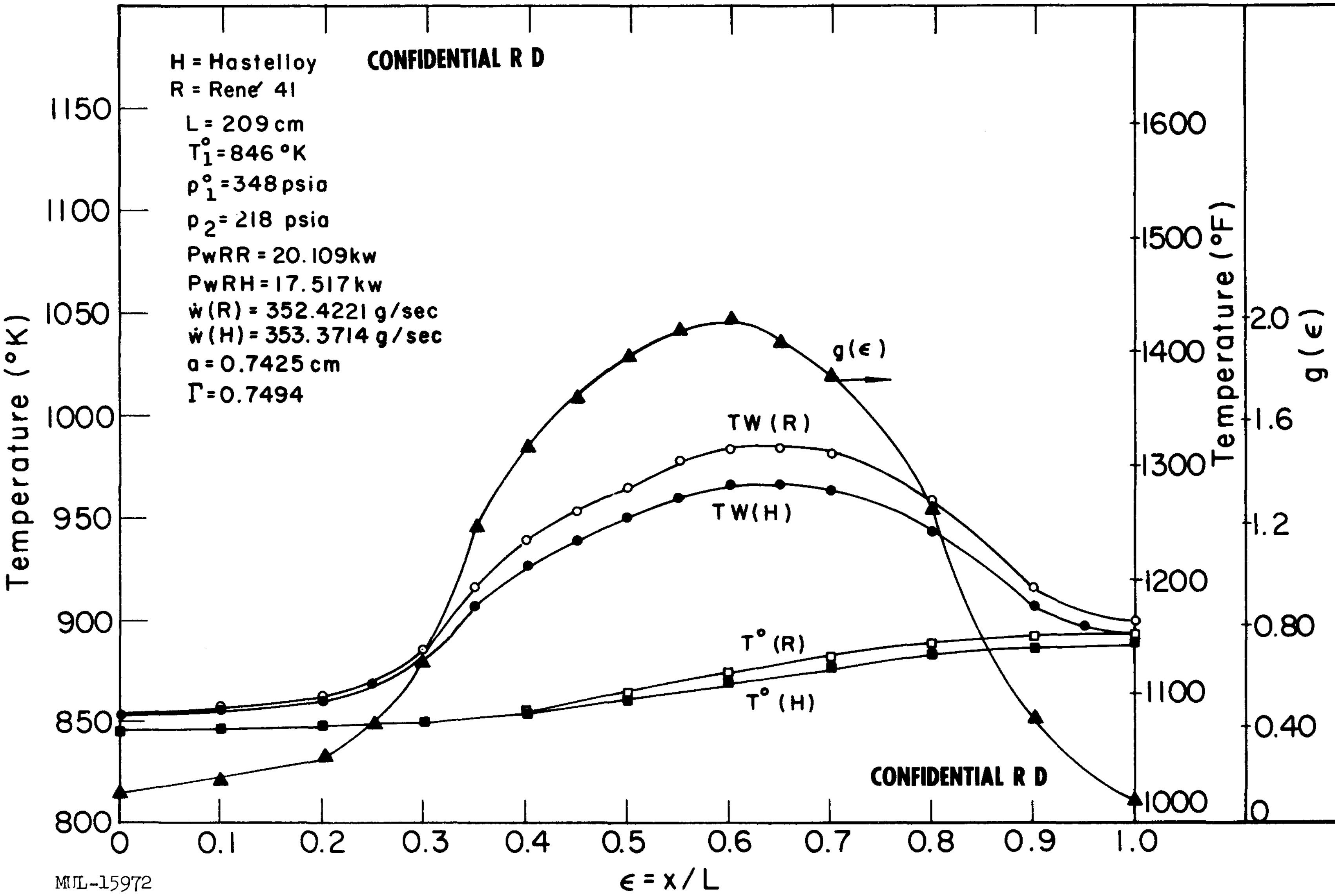

MUL-15972

Fig. IV-25. Tory II-C tie rod parameters at Mach 3.0, radial position 9.25 inches.

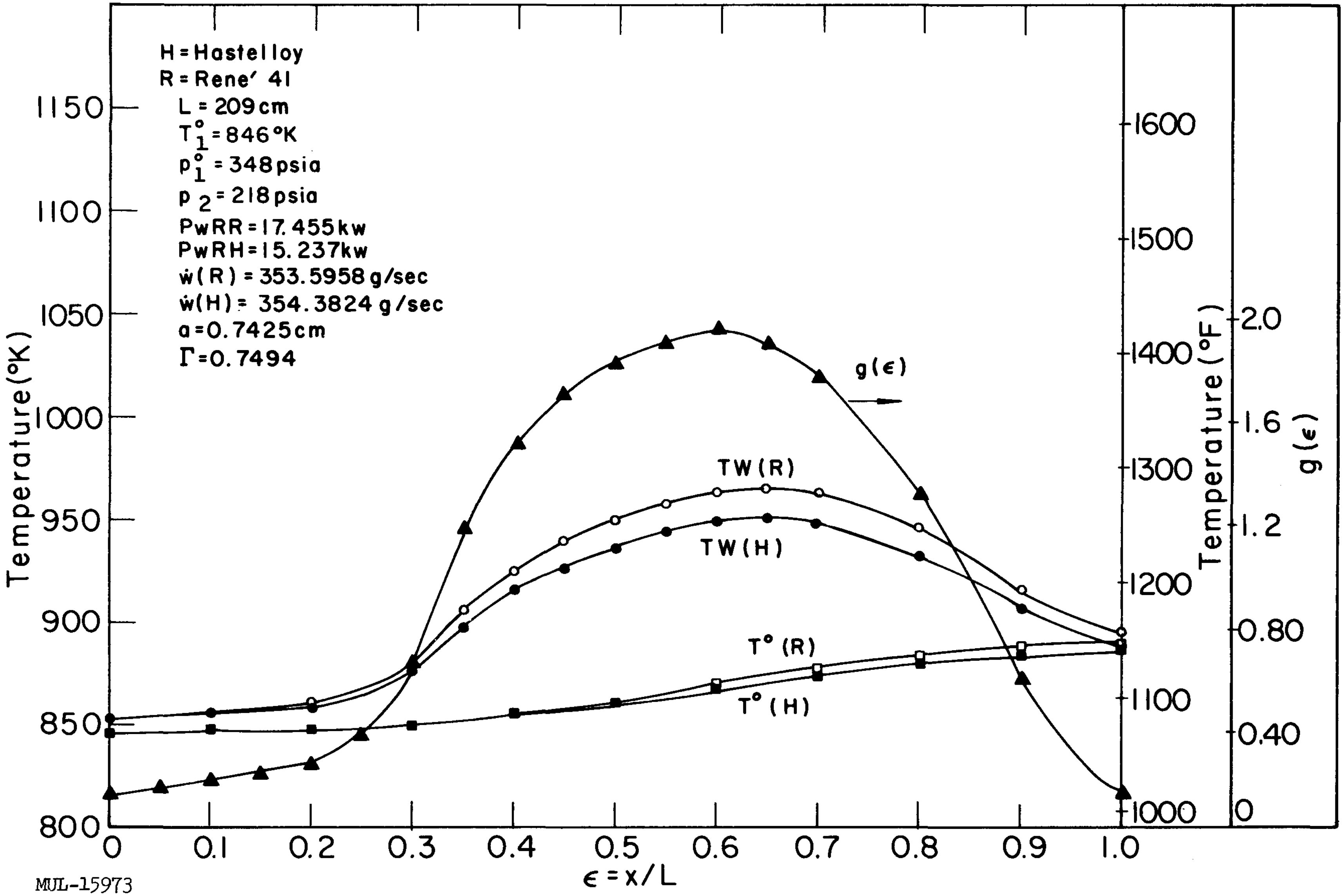

MUL-15973

Fig. IV-26. Tory II-C tie rod parameters at Mach 3.0, radial position 13.11 inches.

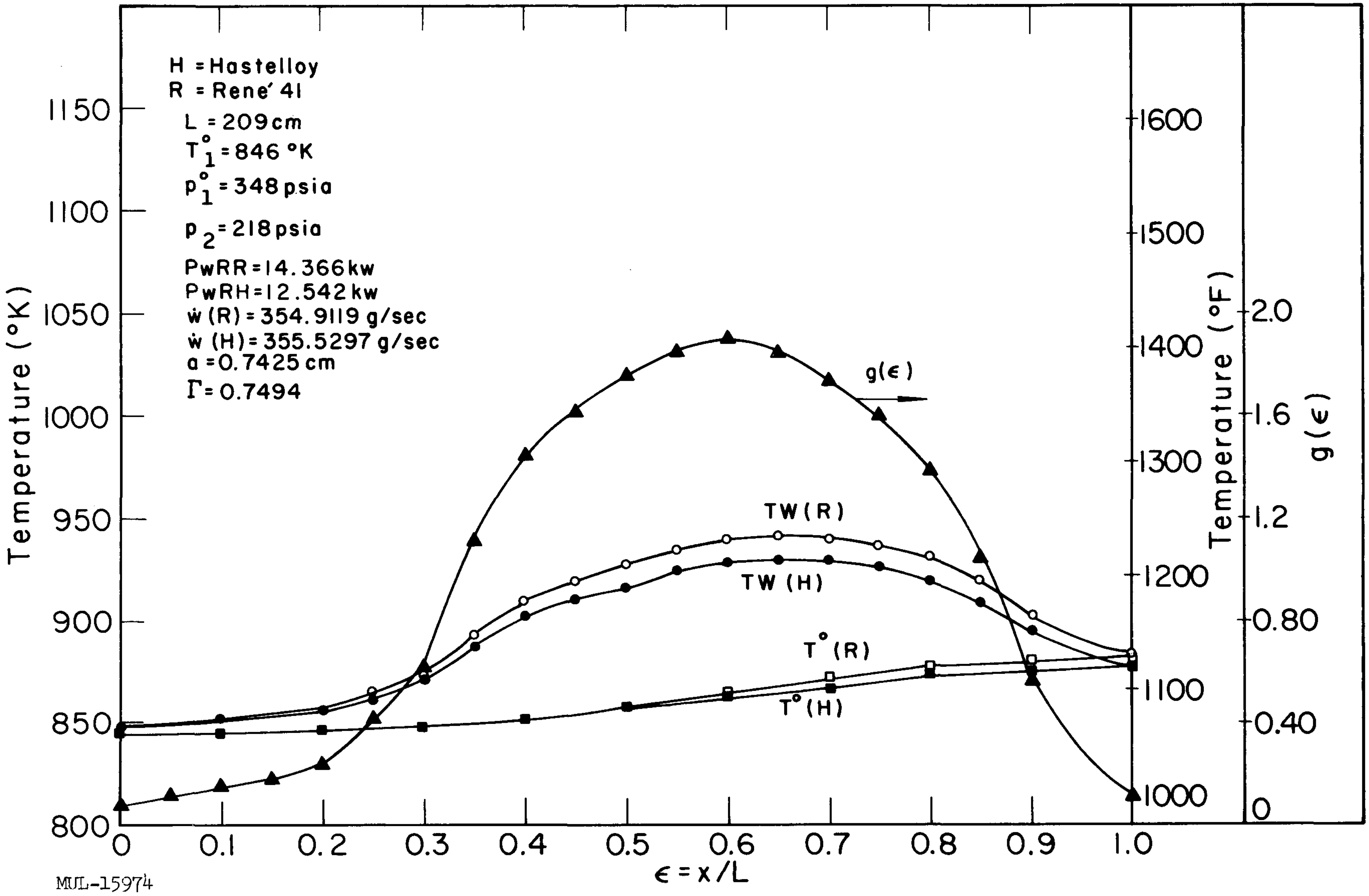

Fig. IV-27. Tory II-C tie rod parameters at Mach 3.0, radial position 17.8 inches.

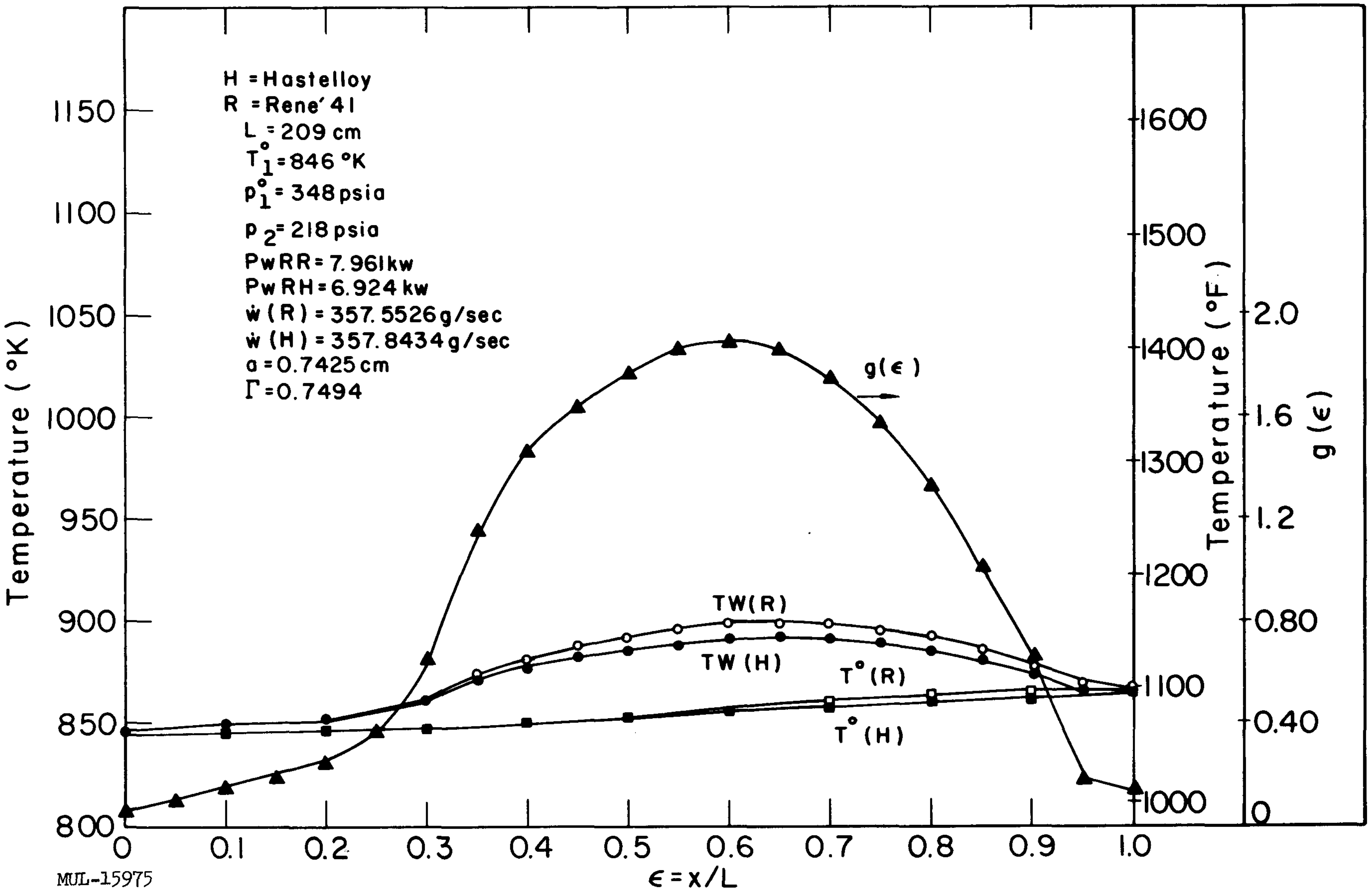

MUL-15975

Fig. IV-28. Tory II-C tie rod parameters at Mach 3.0, radial position 23.92 inches.

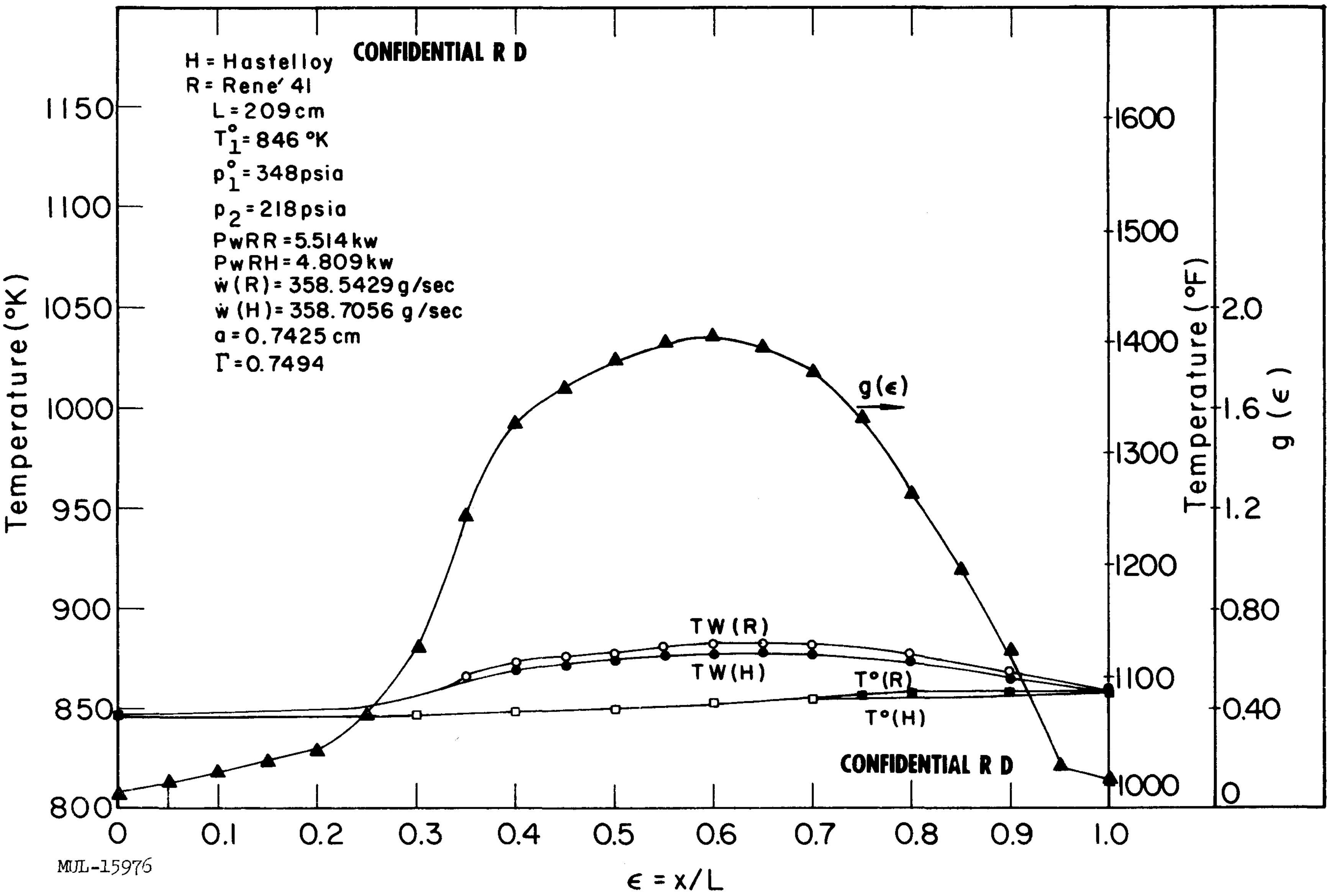

Fig. IV-29. Tory II-C tie rod parameters at Mach 3, radial position 26.70 inches.

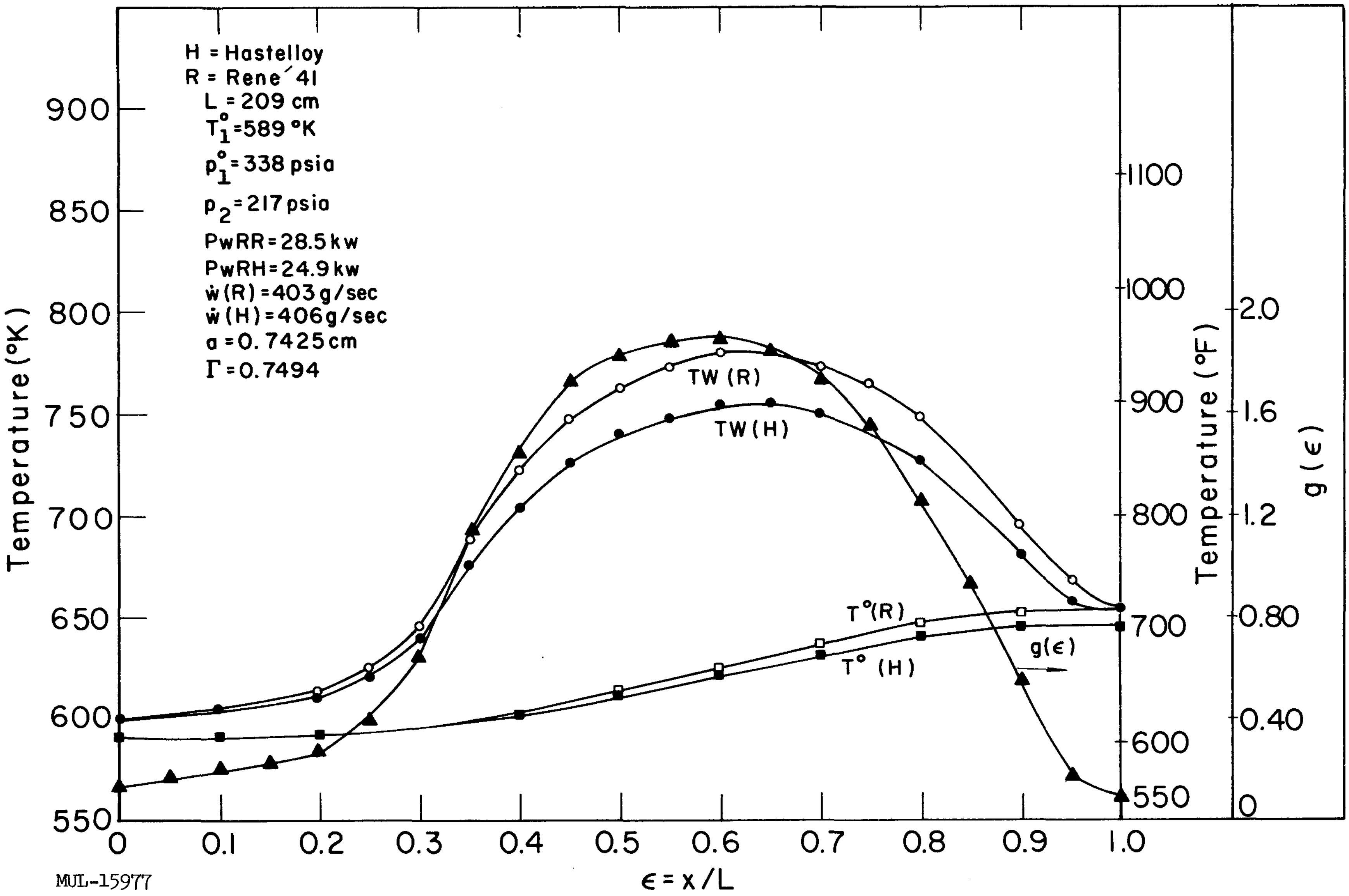

Fig. IV-30. Tory II-C tie rod parameters for 600°F inlet air, radial position 0 inches.

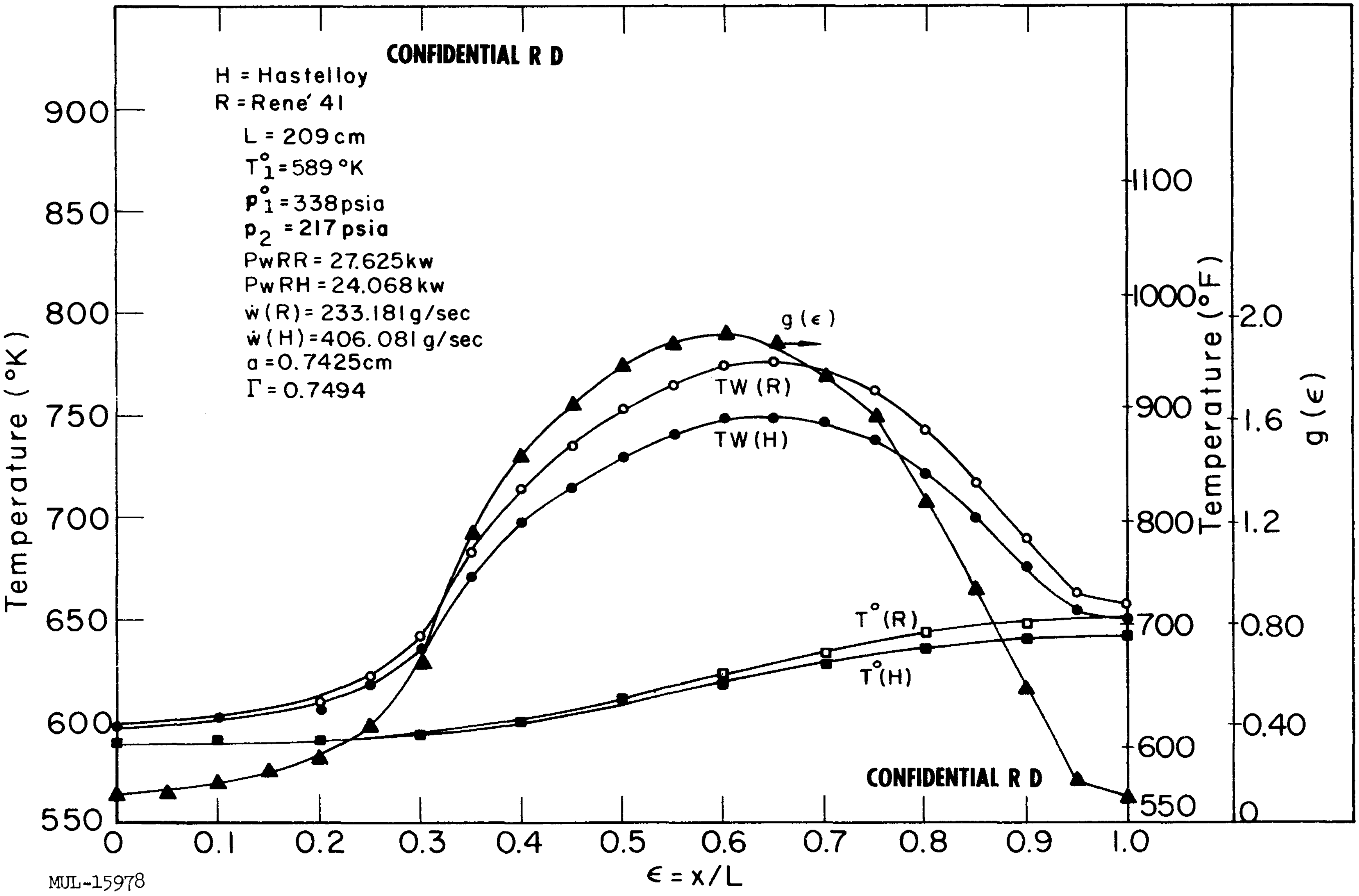

MUL-15978

Fig. IV-31. Tory II-C tie rod parameters for 600°F inlet air, radial position 5.35 inches.

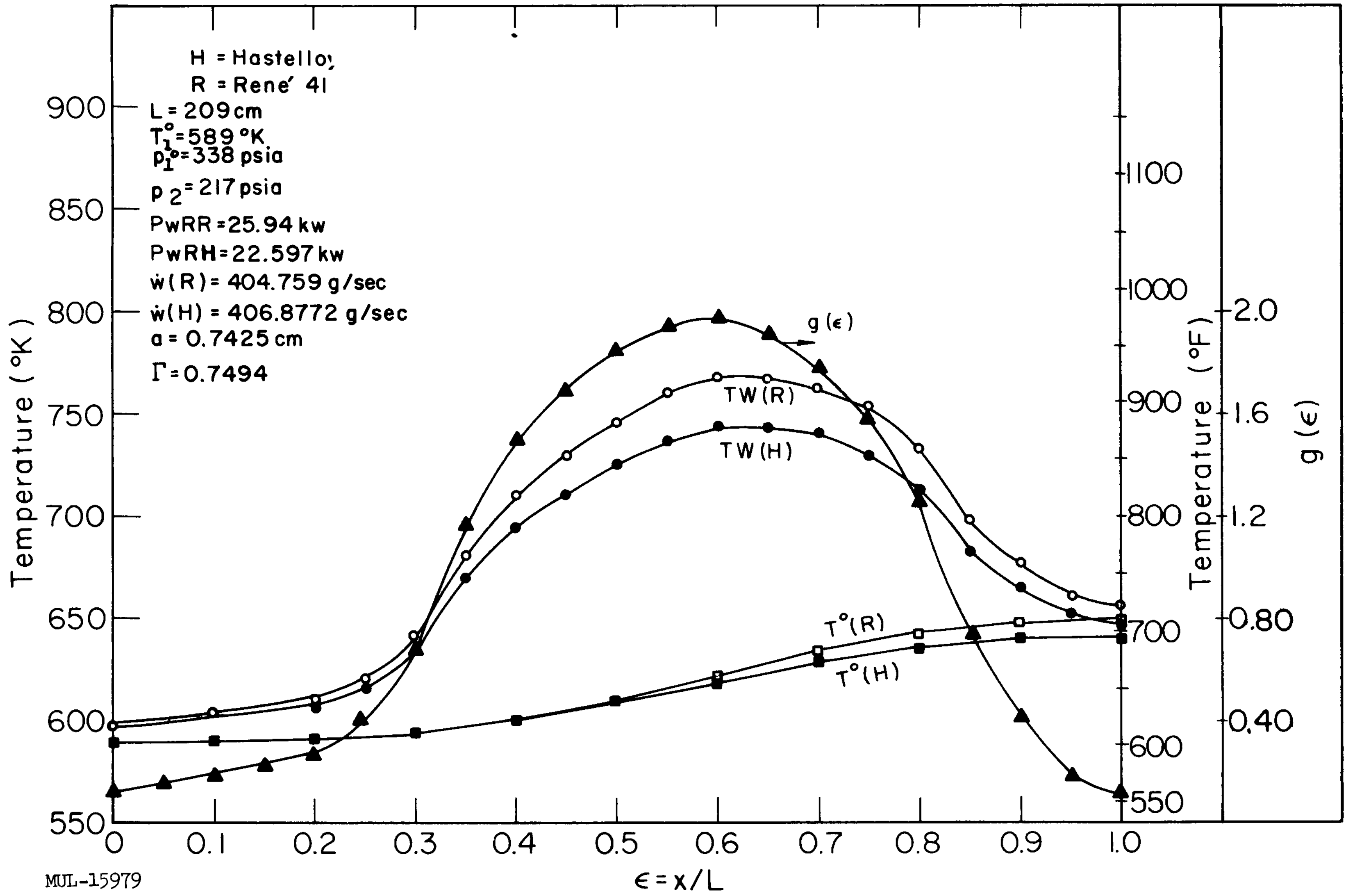

Fig. IV-32. Tory II-C tie rod parameters for 600 °F inlet air, radial position 9.25 inches.

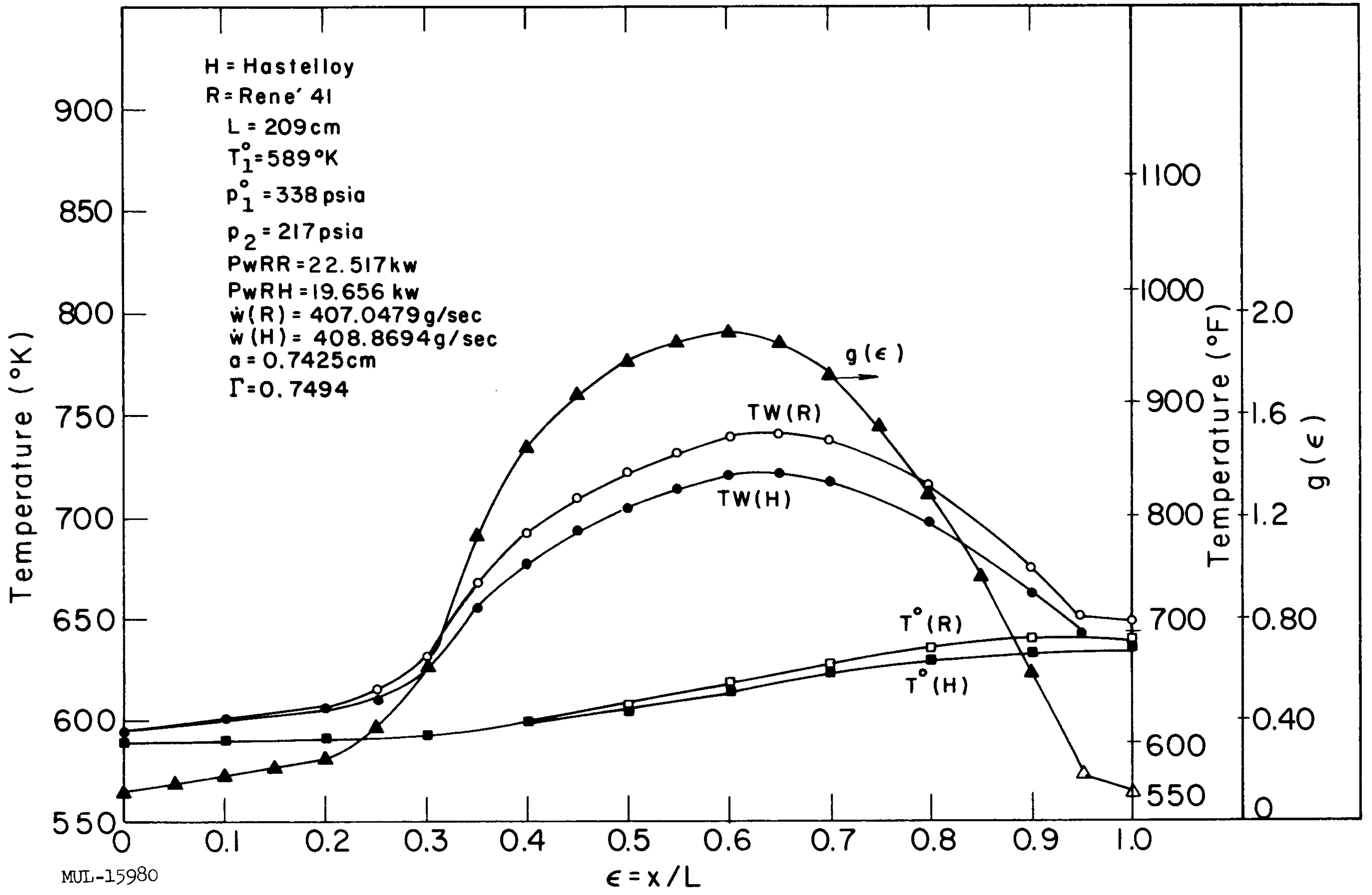

MUL-15980

Fig. IV-33. Tory II-C tie rod parameters for 600 °F inlet air, radial position 13.11 inches.

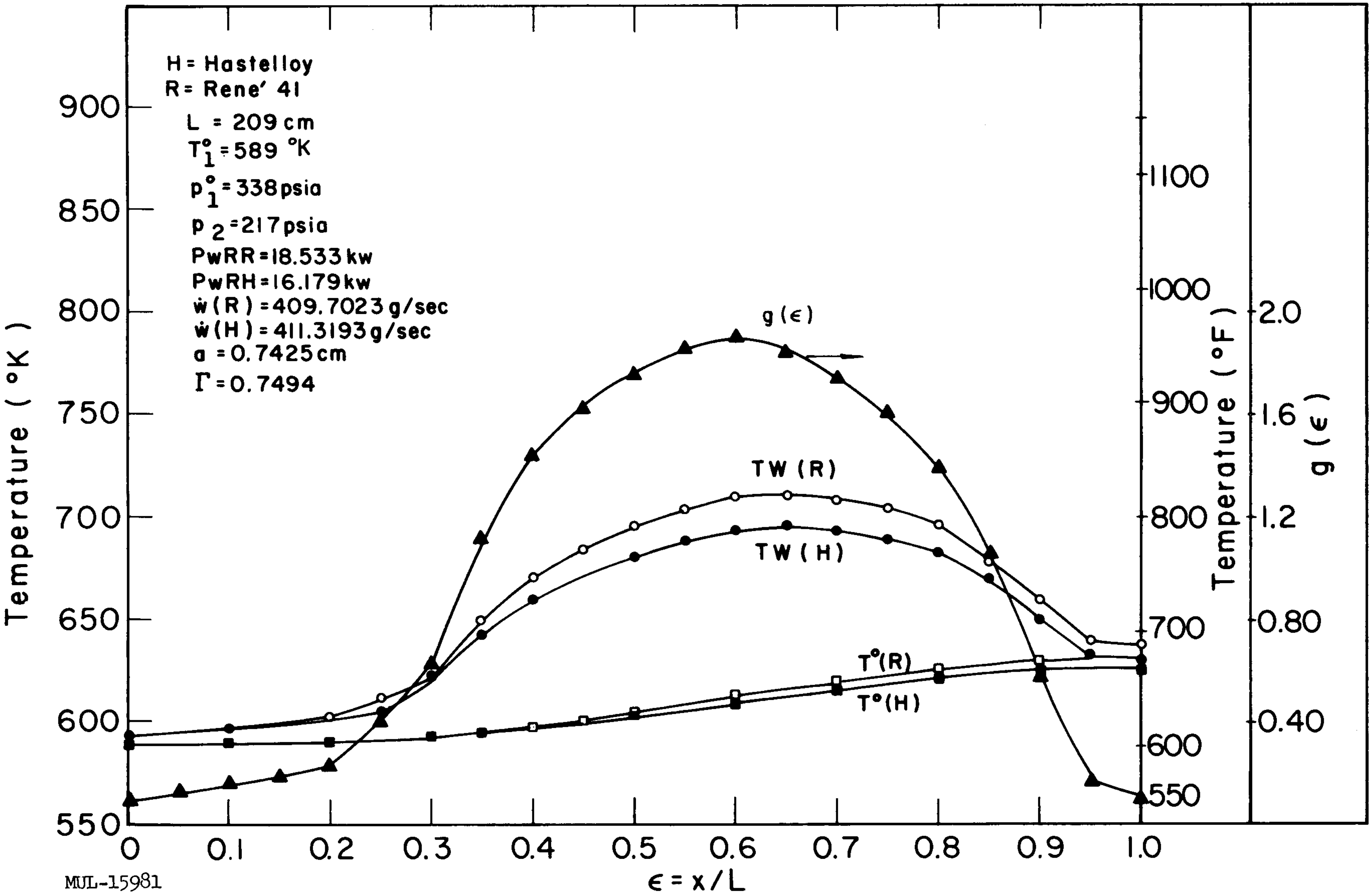

MUL-15981

Fig. IV-34. Tory II-C tie rod parameters for 600°F inlet air, radial position 17.8 inches.

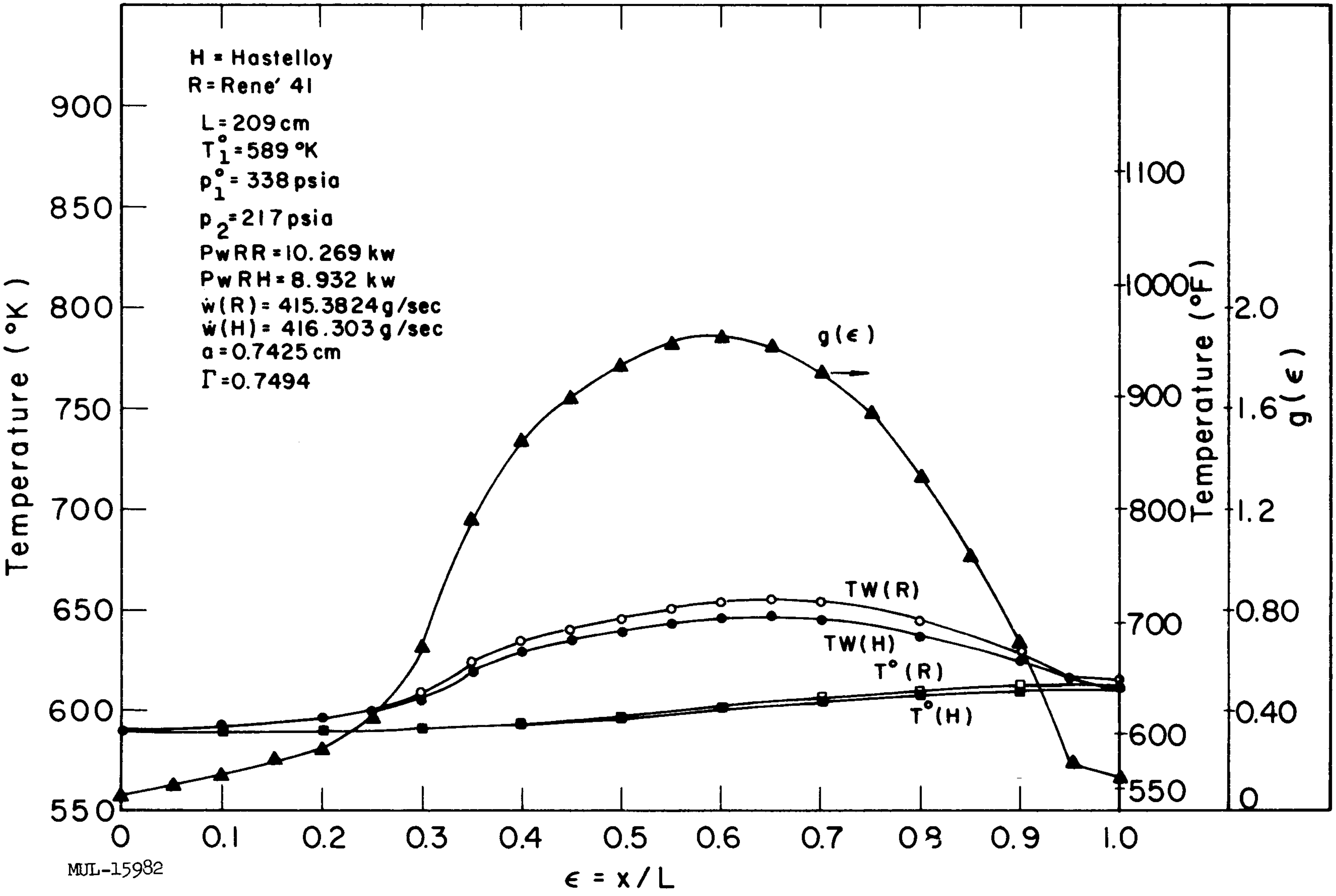

Fig. IV-35. Tory II-C tie rod parameters for 600 °F inlet air, radial position 23.9 inches.

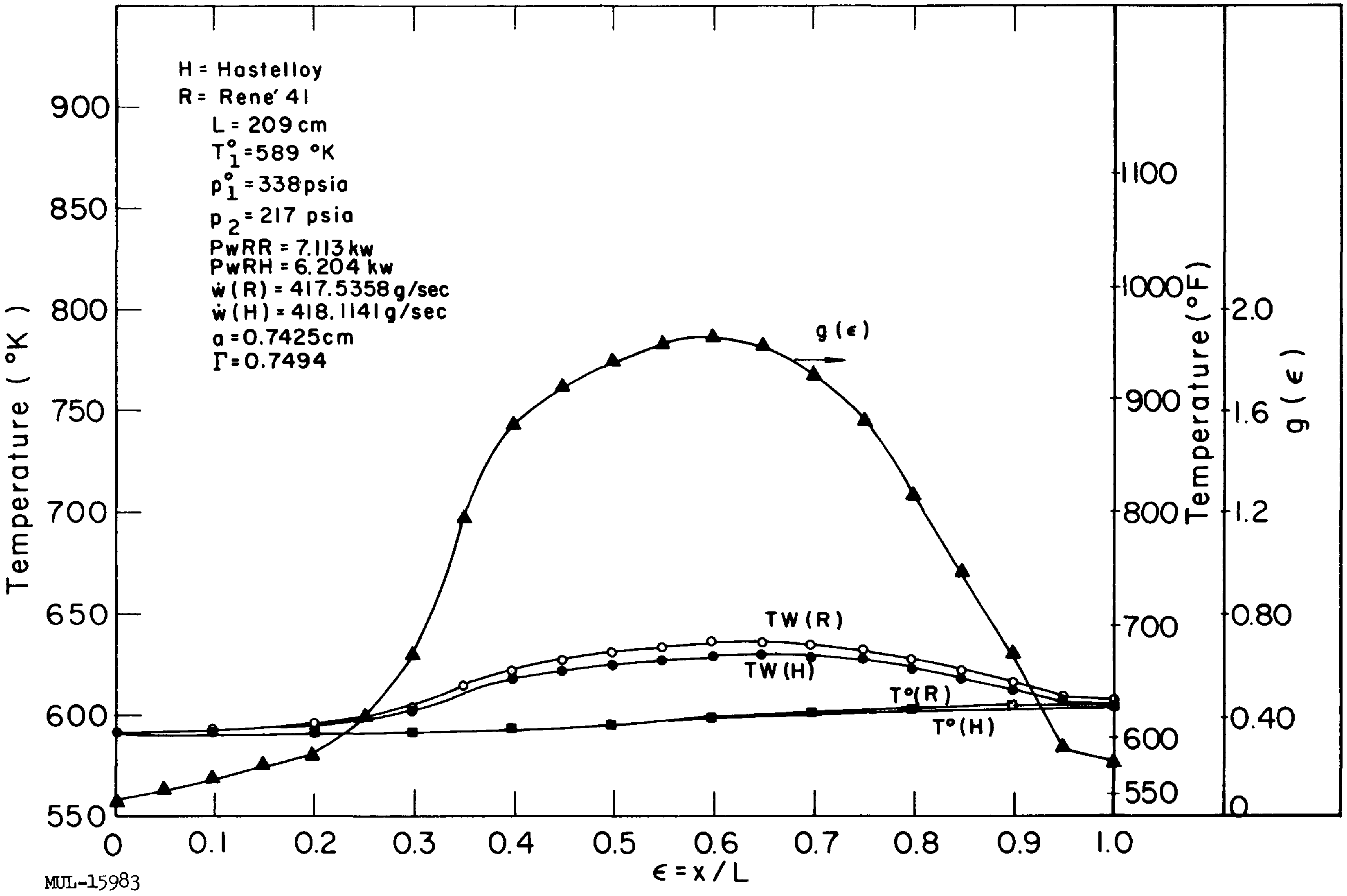

Fig. IV-36. Tory II-C tie rod parameters for 600°F inlet air, radial position 26.7 inches.

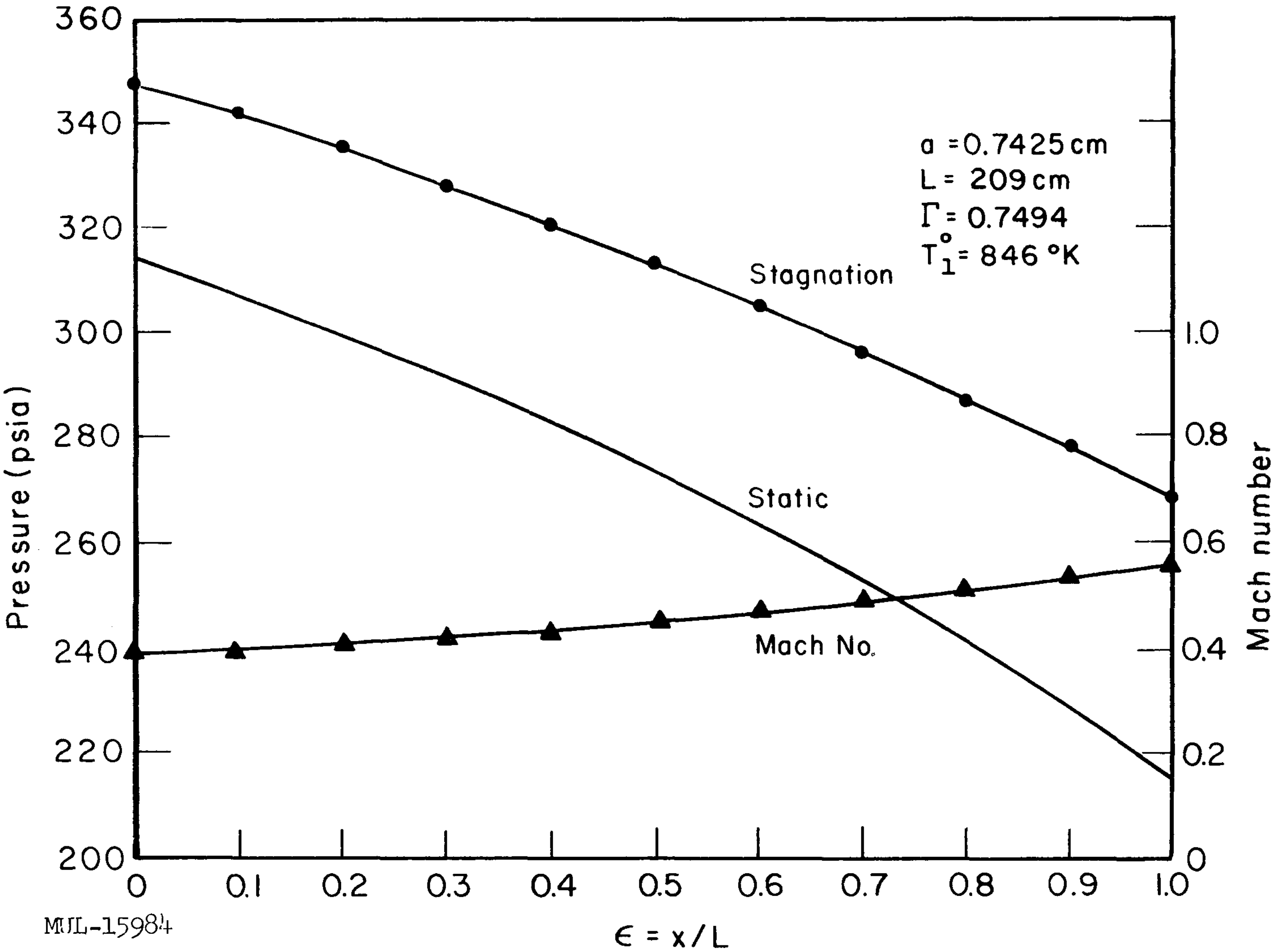

MUL-15984

Fig. IV-37. Tory II-C tie rod parameters at Mach 3.0. Values are independent of material and radial position.

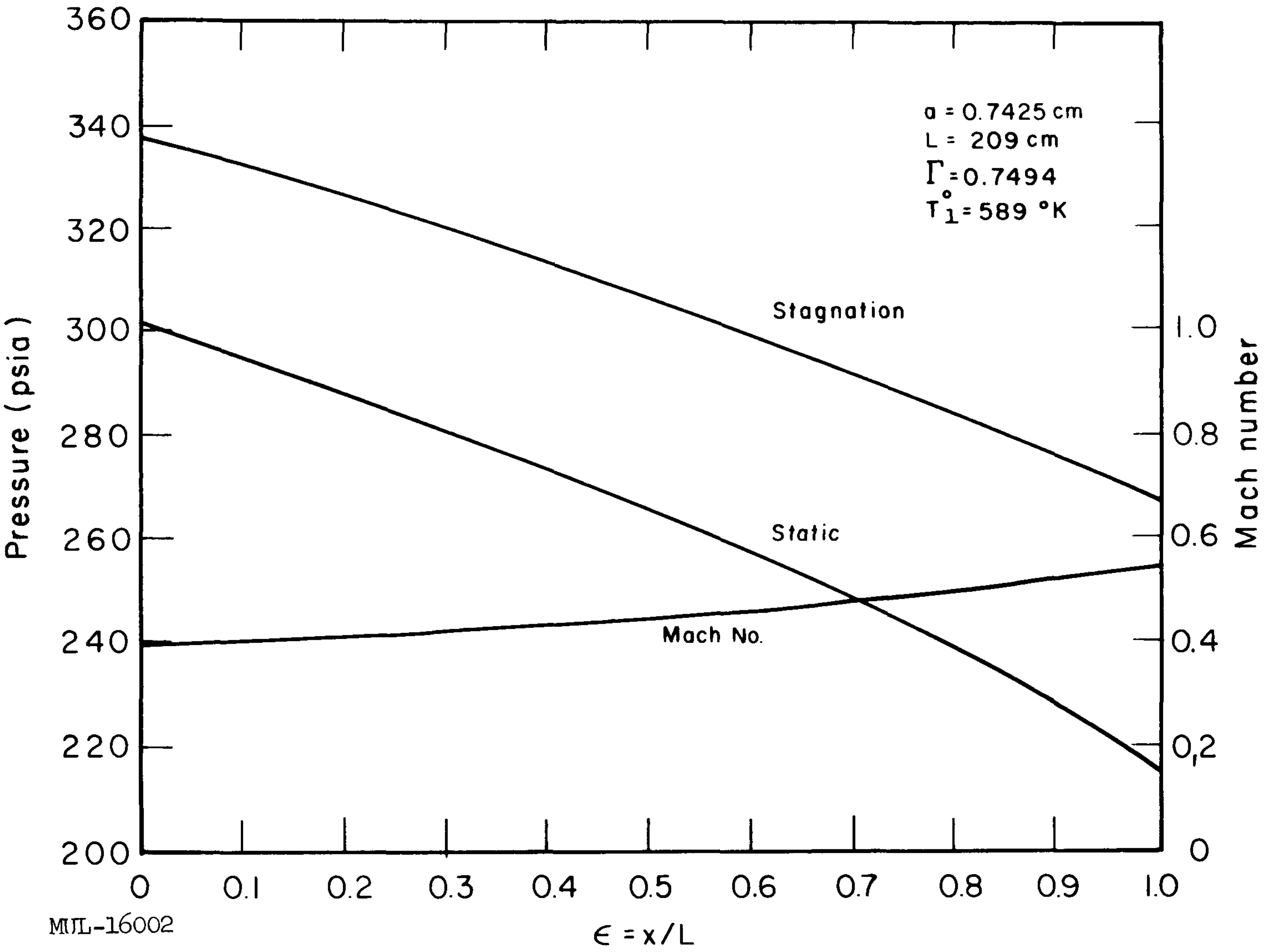

Fig. IV-38. Tory II-C tie rod parameters for 600°F inlet air. Values are independent of material and radial position.

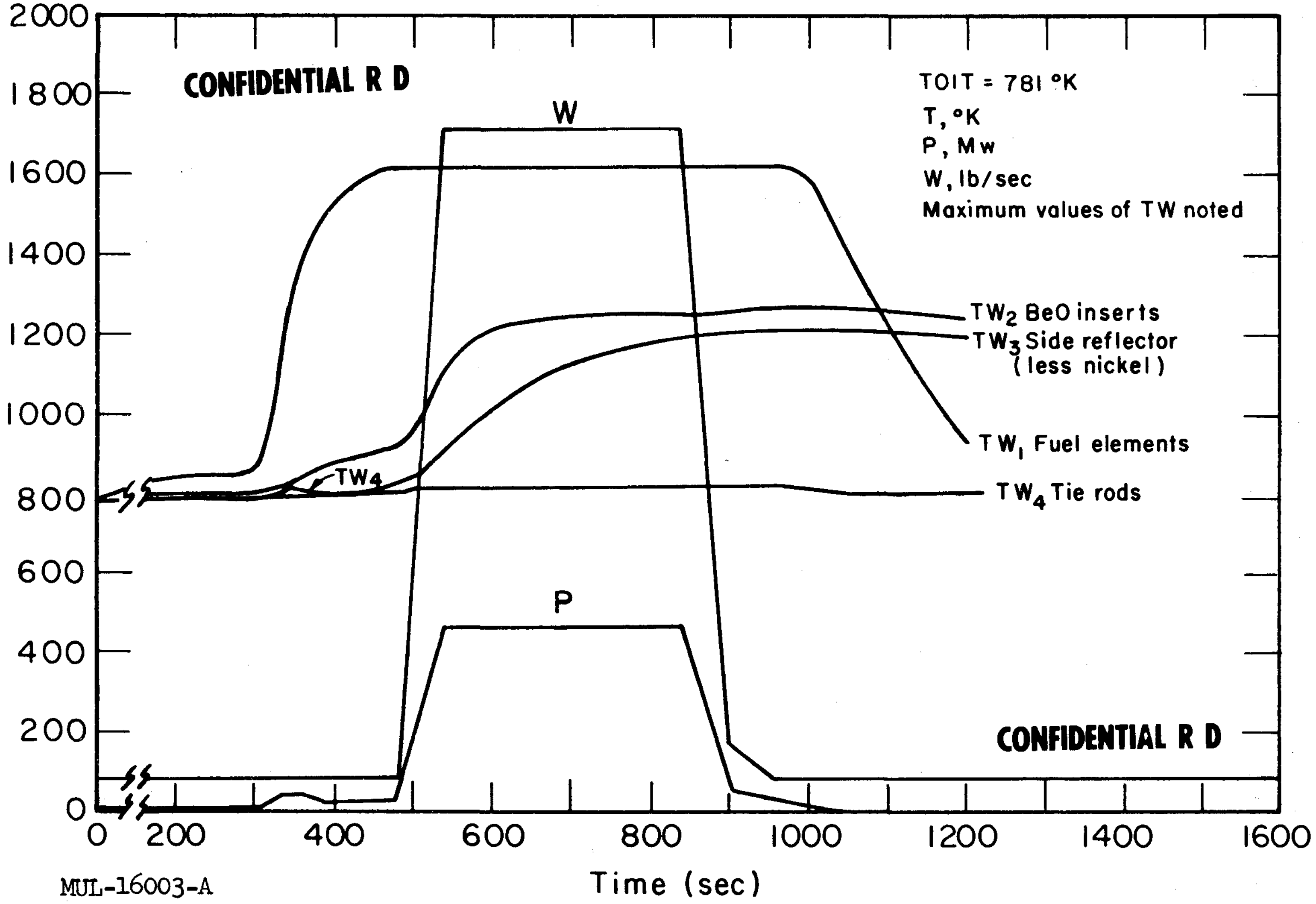

MUL-16003-A

Fig. IV-39. SEA LION analysis of NTS power run of Tory II-C.

the fuel elements and the tie rods, the BeO portion of the side reflector, and the tie rods are presented for a typical full-power run of Tory II-C at NTS. These curves and other analyses show that the tie rods are the quickest to respond to new conditions, followed by the fuel elements, the BeO inserts, and the side reflector, in that order. The transient analysis of the side support structure is more complex. The pads and springs respond rather quickly while the pressure shell surrounding the reactor is relatively sluggish.

The time-temperature histories of different portions of the reactor have various uses. That of the fuel elements is of principal importance to the control system studies and is the major factor in overall reactor performance. The major structural items must be studied to insure that temperature limits of materials are not exceeded. An even more complex problem is that of relative thermal expansion of the various parts of the reactor, which do not heat up to the same temperatures, and furthermore, do not heat up at the same rates. A prime example is that of the differential expansion of the active core and side reflectors. As shown in Fig. IV-39, the side reflector does not get up to equilibrium temperatures until near the end of a 5-minute full-power run.

The above transient studies are on the basis of airflow through the reactor. It is also of interest to know how the reactor temperature will vary without cooling airflow. The Tory II-C temperature transients in this case are such that a temperature increase from room temperature to 2500°F will take about 80 minutes at 1 Mw, 8 minutes at 10 Mw, 50 seconds at 100 Mw, and 10 seconds at the design power of 510 Mw.

SECTION III. CONTROLS

Significant breakthroughs have been made during this quarter on critical components of the Model 1240 actuator; this is a prototype of the Tory II-C control rod actuator and must operate in a 1200°F high-radiation environment.

The Model 1240 has been simulated in an exact model on the analog computer. Analog studies have determined practical methods of improving the steady-state characteristics of the Model 1240 valve and motor. These methods have been verified in room temperature tests at LRL and in high temperature tests at the contractor's facility. The analog model provides, as well, for measurement of many variables not available on the actual hardware at both design and off-design conditions.

The Tory II-C control system electronics and simulation has been fabricated and is undergoing acceptance tests by LRL personnel at the contractor's facility. This equipment is built with solid-state, analog-computer-type components and provides improved reliability and flexibility in all control systems. A semiautomatic checkout system has been designed which will provide rapid and complete checkout of all control systems during test operations. Included in this method is automatic logging of all measured variables in a convenient digital form.

An analytical study of the Tory II-C air supply process has been completed which provides the accurate mathematical model of the flow and air temperature processes. Using an analog of this model, both air flow rate and air temperature control systems have been designed.

MODEL 1240 ACTUATOR DEVELOPMENT

This program has as its objective development of a control rod servomechanism which can operate for extended periods of time at temperatures as high as 1200°F and in a high nuclear radiation field. Early tests on the Model 1240 prototype resulted in successful operation for limited periods of time in a laboratory-controlled 1200°F environment.

Four serious problem areas were uncovered during these tests: (1) Inoperability of electropneumatic servo valve whenever valve body temperature differed by more than 100°F from temperature of servo valve air supply (i.e., valve spool temperature), (2) Failure of position transducer after several minutes of high temperature operation, (3) Wearout of Model 1240 motor carbon sideplates after short-time cycling at high temperature (about one-fifth required Tory II-C life), (4) Failure of ring springs used for scram snubbing following several hot scram cycles. During this quarter, emphasis has been placed on solving each of these problems in addition to adapting the Model 1240 to the shim rod actuation problem. It is recalled that the Model 1240 has been built to actuate the fine (vernier) control rod.

Three of the problem areas noted above have been alleviated by component refinements. Environmental system tests are required before the problems can be considered as solved. These refinements are next described.

1. Electropneumatic Servo Valve

A refined servo valve has been built and tested which operates reliably throughout the Tory II-C environment despite a large variation in the temperature of the air supplied to the valve.

2. Position Transducer

The 40-in. linear variable differential transformer has been rebuilt and has successfully undergone the complete Tory II-C life test including 30 thermal cycles.

3. Motor Improvement

A new motor design has been built and tested which eliminates the carbon side plates that have given so much trouble in previous endurance tests. This motor demonstrates greatly improved performance and does not have the short-life limitations of the previous design.

The scram snubbing system is the major remaining Model 1240 problem area. (The scram time specified for the Model 1240 is 0.25 sec for full 40-in. travel of the rod.) The first method used to perform this snubbing action employed conical ring springs which absorbed the energy of the high velocity rack and control rod, dissipating it in the form of friction heat. With solid film lubrication the coefficient of friction between adjacent spring sections is of the order of 0.1 and the method is satisfactory. However, following several thermal cycles, it was found that the lubricant "boiled off" and the coefficient of friction increased rapidly to values ≥ 0.7. Locking of adjacent spring sections followed with ultimate failure from high impact loads. Two approaches are being pursued to attempt a solution to this problem.

Ring spring with pneumatic damper. This method employs the previously used ring spring principle for final snubbing but uses a pneumatic snubber to reduce the velocity of the inertia load prior to engaging the ring springs. Improved lubricants are also introduced. Using this method, the Model 1240 endured a total of 37 scrams during one thermal cycle. It was found that the lubricant was dissipated by four or five thermal cycles with resulting failure of the snubbing system. Work has been stopped on this approach, since it is felt that a complete evaluation of its usefulness has been made. This method could fulfill the minimum Tory II-C requirements.

Complete pneumatic snubber. A method which employs all-pneumatic snubbing has been proposed and analytically demonstrated to be possible. This method does not involve springs with lubricants for its damping action but rather uses the pressure force of compressed air to effect the snubbing. This method has no apparent dependence on thermal cycles and should be able to perform the snubbing action independently of temperature.

A major portion of the effort on the high-temperature servomechanism development program has been devoted to adapting the Model 1240 for shim rod actuation. Two areas are receiving particular emphasis.

Transmission and clutch. In the shim rod actuator a transmission is needed to mechanically limit the maximum velocity of the shim rod, which will use the Model 1240 motor. A torque-limiting clutch permits scramming "against" the servo valve in addition to limiting the torque applied to the control rod load. Both 7.5:1 and 56:1 transmissions have been designed and built and are now being prepared for high temperature test. Both transmissions are of planetary type and similar versions have undergone tests successfully to 600°F. A high-temperature torque-limiting clutch has been built and is currently being prepared for test.

Design finalization. A shim rod actuation system has been designed using the Model 1240 modified with the transmission and clutch described above. Following completion of the component tests outlined, the entire shim rod actuator will be assembled and tested.

DUPLICATE MODEL 1240

A duplicate Model 1240 actuation system was delivered to LRL. This system has already been checked out at temperatures up to 1200°F at the contractor's facility. It will undergo room- and high-temperature endurance tests in the LRL test facility to determine its acceptability for Tory II-C. In conjunction with the Tory II-C electronics hardware, it will be used for initial nuclear control system close-loop tests.

MODEL 1240 ANALYSIS

Previous progress reports have outlined improvements recommended for the Model 1240 as determined from an accurate analog computer representation of the system.

Several of these improvements have been proven on the room temperature motor at LRL and on the Model 1240 at the contractor's facility. Most notable of these improvements is a method for improving the null torque gain of the motor-valve combination. This is done by interrupting all leakage flow paths connecting the motor pressure ports, P_1 and P_2, and porting the leakage flow to P_0, in this case ambient pressure. The null torque gain has been raised by a factor of 4 or more by this simple expedient, improving the actuator resolution and stiffness accordingly. Other improvements derived from the analog solution will be attempted on the duplicate Model 1240 at LRL.

A simplified version of the Model 1240 has been simulated on the TR-10 solid-state analog computer. This simulation has been incorporated into the overall Tory II-C solid-state electronics PC-12 equipment. In addition, the shim rod servo system has been simulated on this equipment using the 7.5:1 transmission for speed reduction.

ELECTRONICS

Nuclear Control System

Figure IV-40 is a block diagram of the nuclear control system. The blocks entitled Dual Mode Controller, Compensation, Fast-Reset Logic, Manual Control, Isolation Amplifiers, and Simulation have been fabricated. These units are made up of solid-state analog-computer-type components. Their proven reliability should greatly improve the control system and their flexibility should be a real advantage as operational requirements are changed. Figures IV-41 and IV-42 are photographs of some of these systems.

A semiautomatic checkout system is also shown in Fig. IV-40. This provides automatic logging of all dc voltages. In addition, it permits complete isolation of any subsystem from the rest of the system. Various stimuli can then be applied to this system and output variables can be recorded on an 8-channel strip chart recorder. The output variables can also be monitored by an oscilloscope or a digital voltmeter.

A 1632-point patch board is included in the checkout system. All input, output, and other critical signals from all subsystems come into this board. The cables from the control point, wires from the checkout system, and all control wiring also come to this patch board. There are several advantages with this patch board:

a) All subsystems are interconnected through this patch board. They can, therefore, be easily isolated for checkout and troubleshooting.
b) Change of control from bunker to control point is easily accomplished by inserting the properly programmed board.
c) System operation with full simulation can be readily changed to operation with real actuators by merely changing program boards.
d) System modifications can be more readily accomplished since most wiring changes will only involve partial reprogramming of the board.

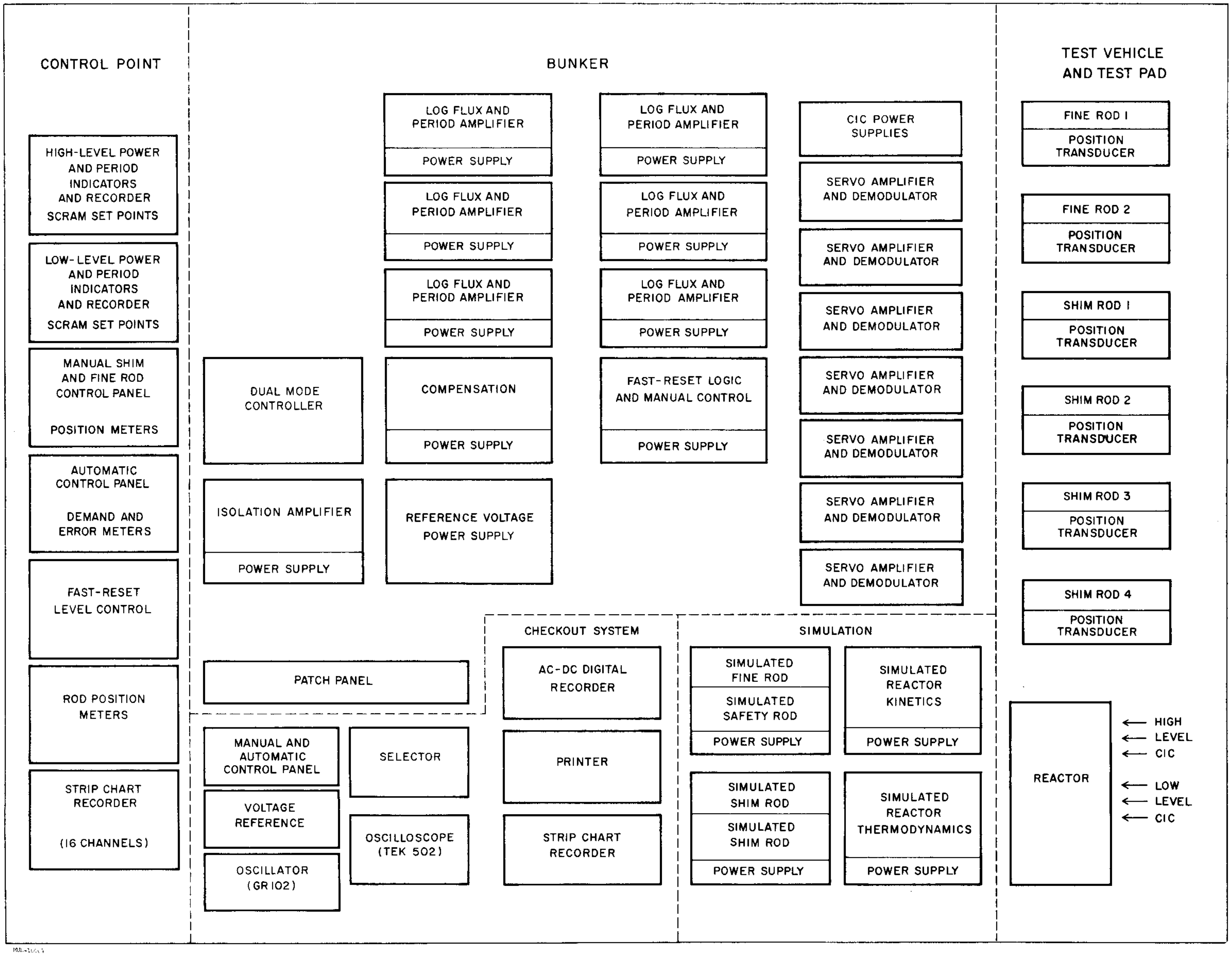

Fig. IV-40. Block diagram of Tory II-C reactor control system.

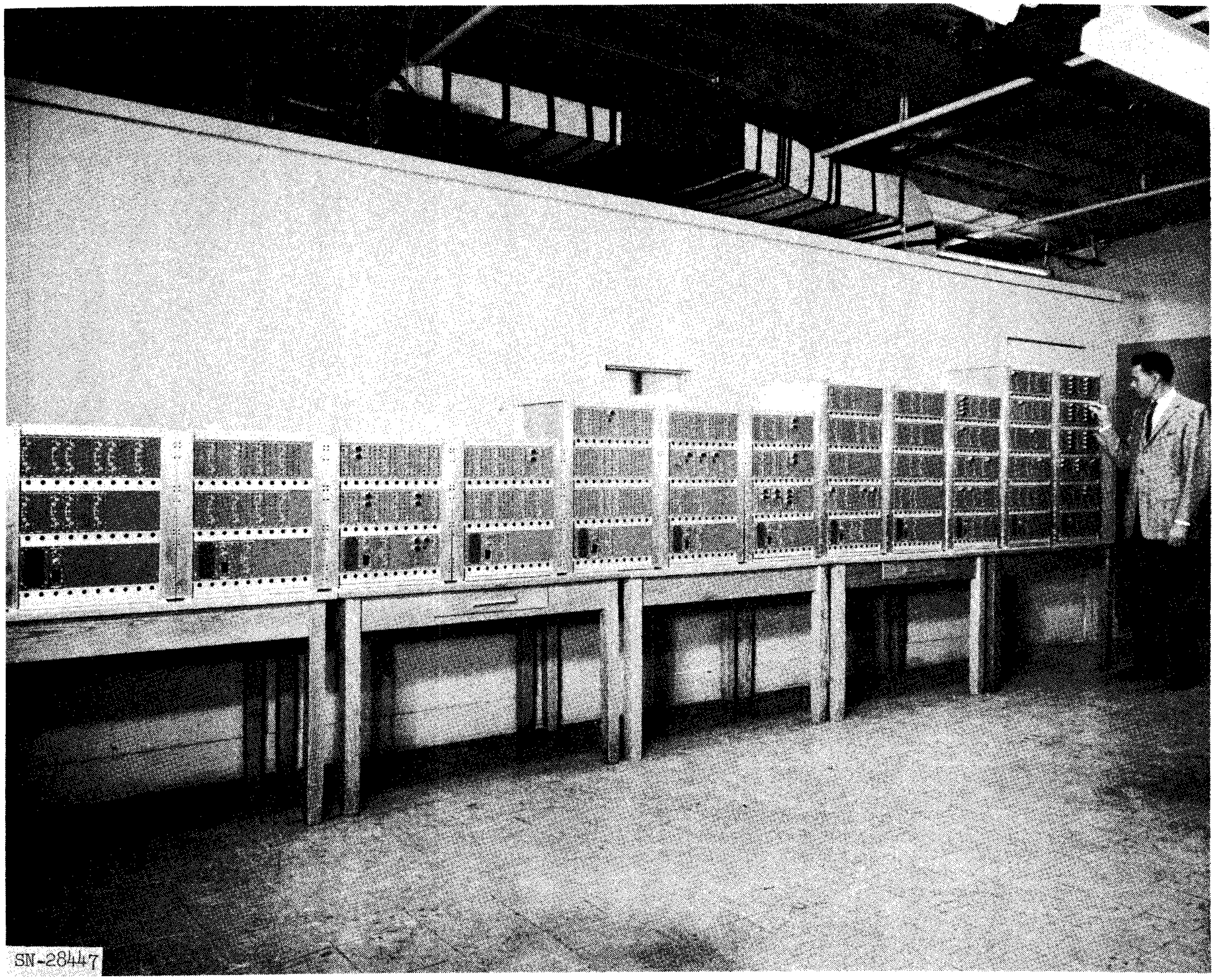

Fig. IV-41. Part of Tory II-C nuclear control system.

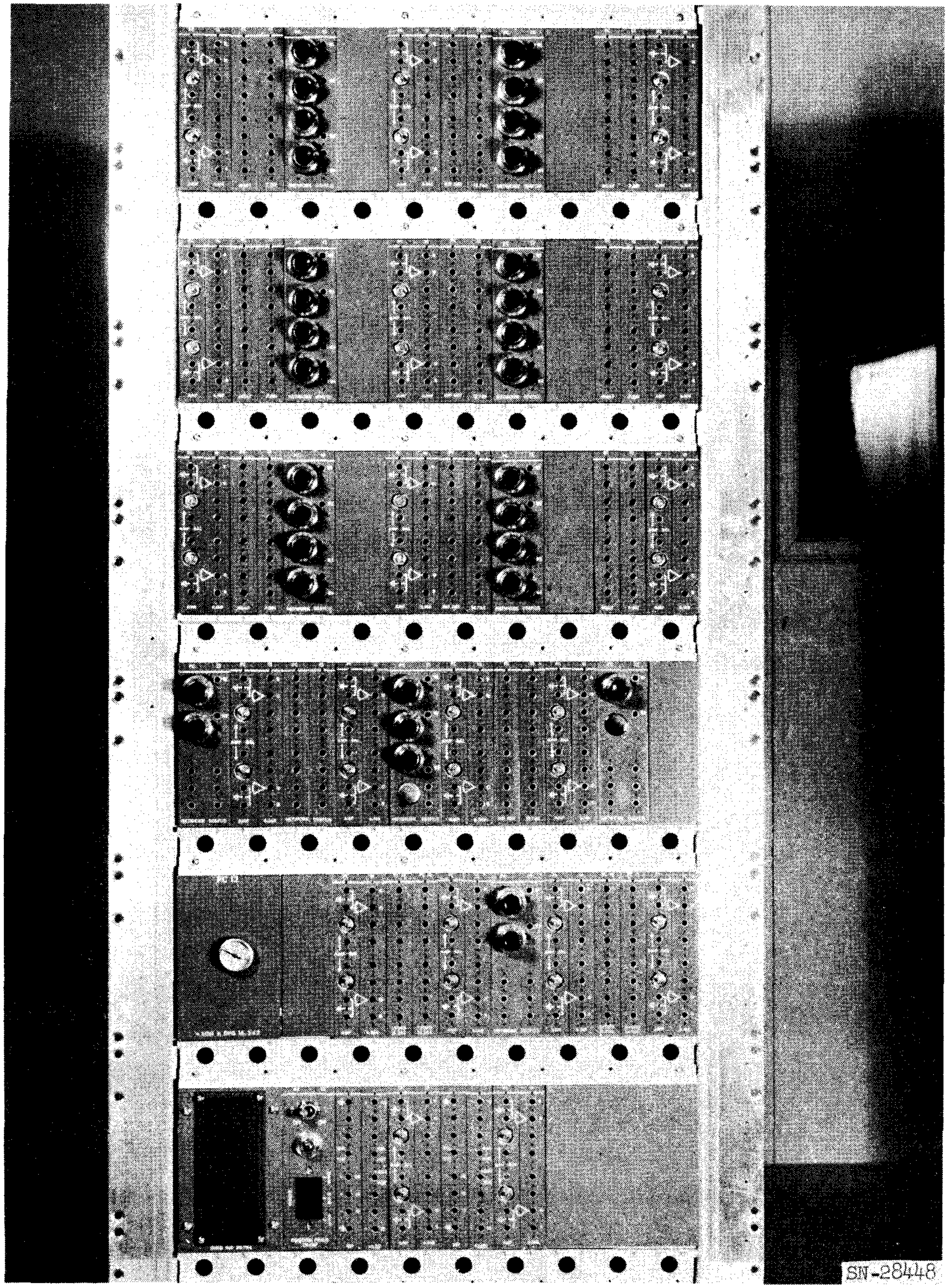

Fig. IV-42. Close-up view of one unit of control system.

The overall nuclear control system design has not yet been finalized. One significant aspect is presented, however.

There will be two ranges of automatic log power control. The high range, covering the top five or six decades of power, will utilize a set of three compensated ion chambers located approximately 50 feet from the core. The low range, covering five or six decades of power, will utilize a set of three compensated ion chambers normally located close to the core. They will be movable to enable withdrawal at high power levels. This system will permit automatic control over a total range of at least eight decades with high and low ranges overlapping at least two decades. Switching between ranges will be simple, safe, and "bumpless."

Air Flow and Temperature Control System

Figure IV-43 is a block diagram of the air flow and air temperature control systems. The blocks entitled Flow Rate Computer, Flow Controller, Temperature Controller, and Analog Simulation have been fabricated and are ready for acceptance testing. These units are made up of solid-state analog computer components, whose characteristics are mentioned above.

The semiautomatic checkout system and patch panel are similar to that of the reactor control system. The above description is also applicable to this system.

SYSTEM DESIGN AND ANALYSIS

Nuclear Control System

Reactor process. For purposes of overall control system studies a ±100-v analog kinetics simulation has been set up on the analog computer. A six-precursor model has been selected as representative of the reactor behavior based on Tory II-A experiments. This has been checked using transient and frequency response techniques and has been verified with the aid of the digital YO routine.

The mathematical basis for this simulation was developed using a set of differential equations describing reactor behavior.

$$\frac{dn}{dt} = \frac{\delta_k n}{\ell^*} - \frac{\beta_t n +}{\ell^*} \sum_{i=1}^{6} \lambda_i C_i, \tag{1}$$

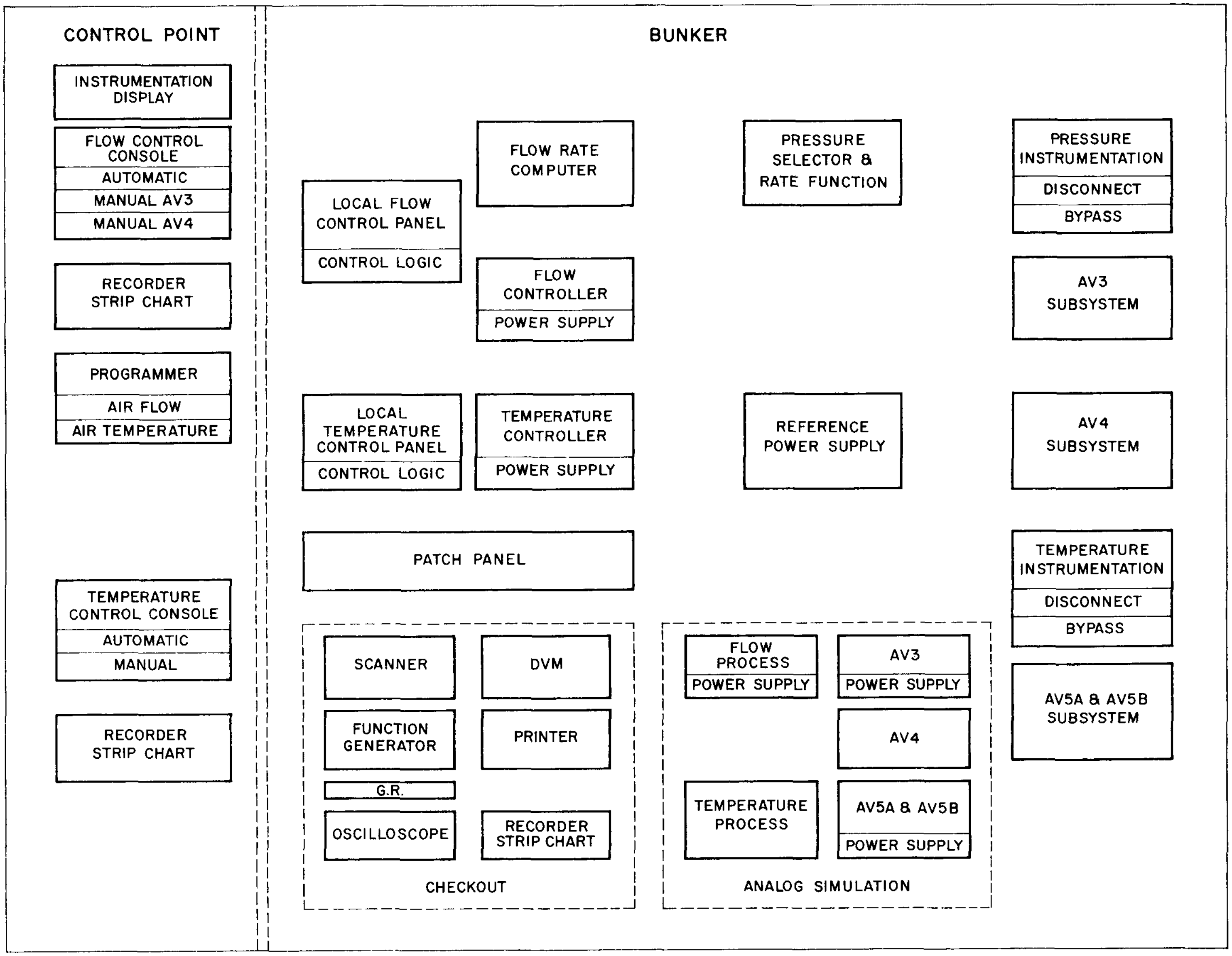

Fig. IV-43 Block diagram of Tory II-C air control system.

$$\frac{dC_i}{dt} = \frac{\beta_i n}{\ell^*} - \lambda_i C_i \,, \tag{2}$$

$$\text{Reactor period} = \frac{1}{\frac{1}{n}\frac{dn}{dt}} \,,$$

$$\text{Inverse reactor period} = \frac{1}{n}\frac{dn}{dt} \,.$$

Dividing (1) and (2) by n:

$$\frac{1}{n}\frac{dn}{dt} = \frac{\delta_k}{\ell^*} - \frac{\beta_t}{\ell^*} + \sum_{i=1}^{6} \lambda_i \frac{C_i}{n} \,, \tag{3}$$

$$\frac{1}{n}\frac{dC_i}{dt} = \frac{\beta_i}{\ell^*} - \lambda_i \frac{C_i}{n} \,.$$

Substituting $U = \frac{1}{n}\frac{dn}{dt}$, $V = \frac{C_i}{n}$, then (4)

$$\frac{dV_i}{dt} = \frac{n\frac{dC_i}{dt} - C_i\frac{dn}{dt}}{n^2} = \frac{1}{n}\frac{dC_i}{dt} - \frac{C_i}{n}\frac{1}{n}\frac{dn}{dt} \tag{5}$$

or

$$\frac{dV_i}{dt} = \frac{\beta_i}{\ell^*} - \lambda_i V_i - V_i U \,, \tag{6}$$

and

$$U = \frac{\delta_k}{\ell^*} - \frac{\beta_t}{\ell^*} + \sum_{i=1}^{6} \lambda_i V_i \,. \tag{7}$$

The constants for use in these seven equations are listed below:

$\lambda_1 = 3.01$; $\beta_1 = 302 \times 10^{-6}$; $\beta_1/\ell^* = 2.82$; $V_1 = (\beta_1/\ell^*)/\lambda_1 = 0.934$

$\lambda_2 = 1.13$; $\beta_2 = 790 \times 10^{-6}$; $\beta_2/\ell^* = 7.40$; $V_2 = (\beta_2/\ell^*)/\lambda_2 = 6.55$

$\lambda_3 = 0.301$; $\beta_3 = 2710 \times 10^{-6}$; $\beta_3/\ell^* = 25.4$; $V_3 = (\beta_3/\ell^*)/\lambda_3 = 84.4$

$\lambda_4 = 0.111$; $\beta_4 = 1346 \times 10^{-6}$; $\beta_4/\ell^* = 12.6$; $V_4 = (\beta_4/\ell^*)/\lambda_4 = 113.0$

$\lambda_5 = 0.031$; $\beta_5 = 1500 \times 10^{-6}$; $\beta_5/\ell^* = 14.0$; $V_5 = (\beta_5/\ell^*)/\lambda_5 = 452.0$

$\lambda_6 = 0.012$; $\beta_6 = 226 \times 10^{-6}$; $\beta_6/\ell^* = 2.1$; $V_6 = (\beta_6/\ell^*)/\lambda_6 = 175.0$

$\beta_t = 6874 \times 10^{-6}$

$$\ell^* = 107 \times 10^{-6};\ \frac{\beta_t}{\ell^*} = \frac{6874 \times 10^{-6}}{107 \times 10^{-6}} = 64.3$$

For a real time solution only amplitude scaling is required and the seven scaled equations are as follows:

$$10U = 10\,\frac{\delta_k}{\ell^*} - 10\,\beta_t/\ell^* + 10\sum_{i=1}^{6}\lambda_i V_i, \tag{8}$$

$$10\,\frac{dV_1}{dt} = 10\,\beta_1/\ell^* - 10\lambda_1 V_1 - 10V_1U, \tag{9}$$

$$10\,\frac{dV_2}{dt} = 10\,\beta_2/\ell^* - 10\lambda_2 V_2 - 10V_2U, \tag{10}$$

$$\frac{dV_3}{dt} = \beta_3/\ell^* - \lambda_3 V_3 - V_3U, \tag{11}$$

$$0.1\,\frac{dV_4}{dt} = 0.1\,\beta_4/\ell^* - 0.1\lambda_4 V_4 - 0.1V_4U, \tag{12}$$

$$0.1\,\frac{dV_5}{dt} = 0.1\,\beta_5/\ell^* - 0.1\lambda_5 V_5 - 0.1V_5U, \tag{13}$$

$$0.1\,\frac{dV_6}{dt} = 0.1\,\beta_6/\ell^* - 0.1\lambda_6 V_6 - 0.1V_6U. \tag{14}$$

A 100-v analog configuration for the solution of these equations is shown in Fig. IV-44. The integration of -I0U yields 4.33 $\ell n\ n$, which in turn is operated upon by the diode function generator giving 0.2 linear n, to be used later in the solution for the reactor heat transfer. The open-loop, reactor-kinetics, frequency-response experimental data is plotted in Fig. IV-45.

Reactor aerothermodynamics. For Tory II-C the reactor heat transfer equation is that for a single zone approximation. This was obtained from the Aerothermodynamics Group and is the result of the digital SEA LION routine. This equation is the following:

$$5.6\,\frac{d\overline{Tw}}{dt} = 1.425P_g - (1 + 0.928\phi)(\overline{Tw} - Tgi), \tag{15}$$

For fixed Tgi and variable $P_g\phi$, where

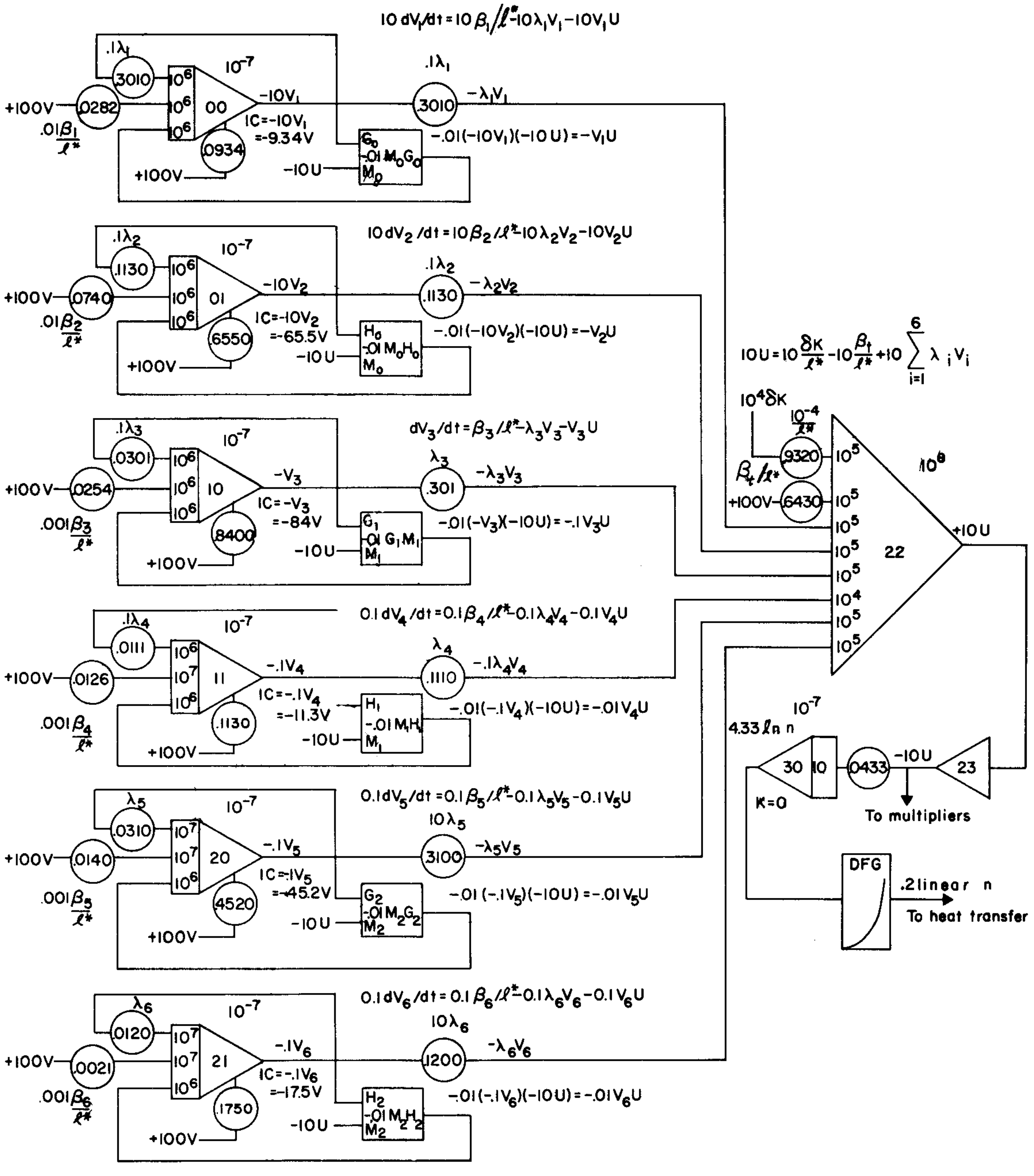

MUL-16024

Fig. IV-44. Tory II-C reactor kinetics simulation.

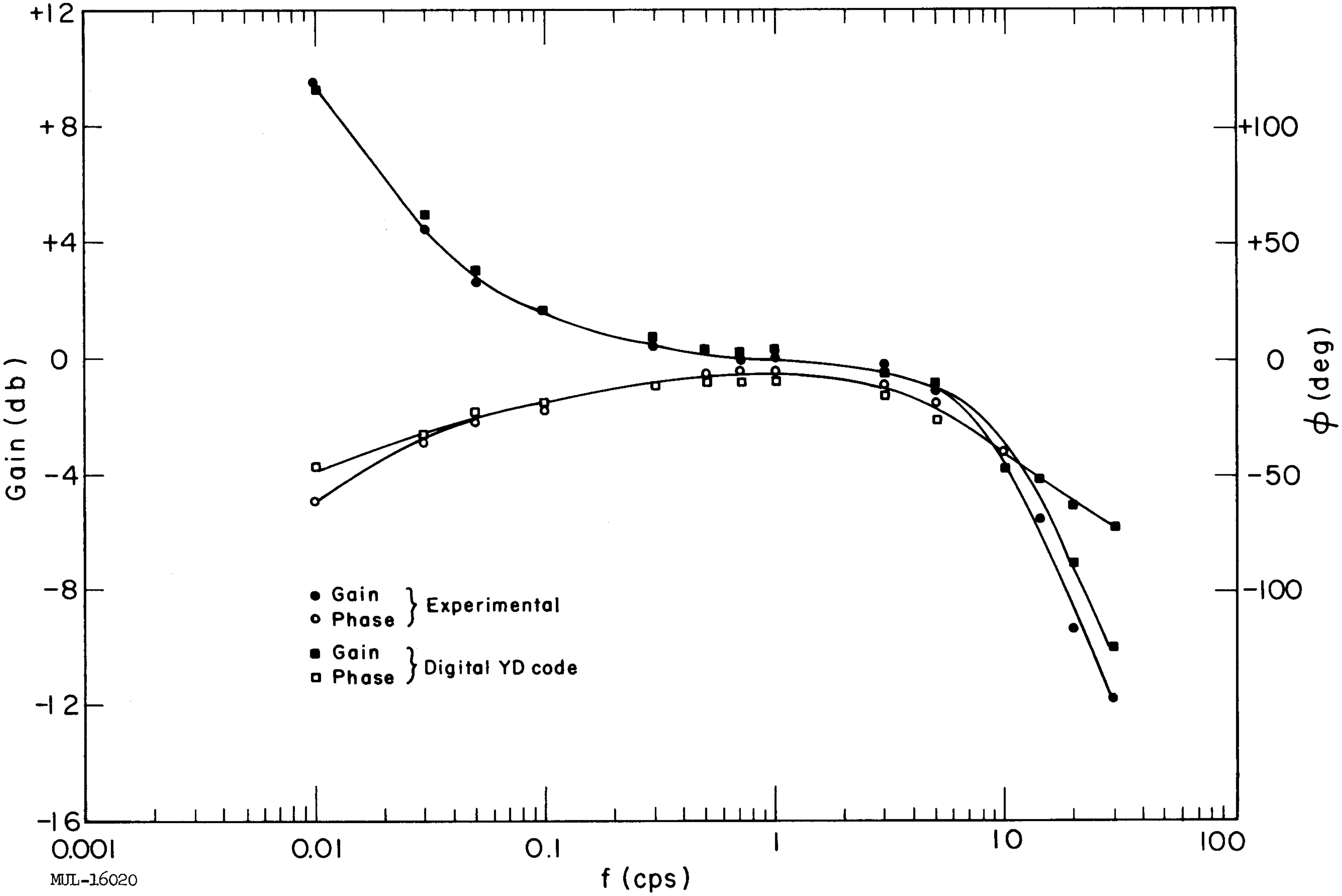

Fig. IV-45. Tory II-C reactor kinetics transfer function.

$\overline{Tw}$ = reactor wall temp (°K),
P = power (Mw),
W = air flow rate (lb/sec),
Tgi = inlet air temp (°K).

This new mathematical model is currently being added to the reactor process analog.

Simulation for system checkout and operator training at the Nevada Test Site. For checkout and operator training at the Nevada Test Site a solid state ±10-v simulation of reactor kinetics has been fabricated. This version is identical with that described above and its diagram is the same as Fig. IV-44 except the voltages are scaled down by 10 since these components are based on a ±10-v reference. TR-10 solid-state components in our analog facility were used to specify the circuits as well as to verify the frequency response.

A simplified one-zone temperature approximation is employed to simulate reactor thermodynamics. The equations to be simulated are:

$$\frac{d\bar{T}'}{dt} C_p' = 3.69\bar{P} - 1.13\dot{w}C_p gn(\bar{T}' - T_1^0), \tag{16}$$

$$\bar{T}^0 \approx \frac{T_1^0 + \bar{T}'}{2}, \tag{17}$$

where

$\bar{T}'$ = average fuel temp (°F),
T_1^0 = inlet air temp (°F),
$\bar{T}^0$ = average air temp in reactor (°F),
$\dot{w}$ = air flow rate (lb/sec),
P = power (Mw),
C_p' = specific heat of core material,
$C_p g$ = specific heat of air,
n = impedance to flow.

Equations (16) and (17) scaled for use on the process control hardware are:

$$0.0005 \frac{d\bar{T}'}{dt} C_p' = 0.00185\bar{P} - 0.000565\dot{w}C_p gn(\bar{T}' - T_1^0), \tag{18}$$

$$0.004\, \bar{T}^0 \approx \frac{0.004(T_1^0 + \bar{T}')}{2}. \tag{19}$$

SECTION IV. ENGINEERING

SUPPORT GRID

The reactor support grid for Tory II-C now differs from the one previously reported. The new grid weighs only 1000 pounds and uses solid beams in place of the drilled beams of the previous design.

The new design is shown in Fig. IV-46. It consists of a Hastelloy-C ring which is notched to locate and support 12 René 41 beams ($\frac{1}{2}$ in. wide × 7-3/4 in. deep). The René 41 front plate rests on the ring and beams and is attached with bolts. The front plate transfers the tie rod load to the beams and laterally supports and prevents the beams from buckling. Spacers are installed between the beams near the aft edge to increase stability and natural frequency of the beams.

The front plate fabrication starts with a wrought 7/8-in.-thick by 56-in.-diameter plate. This plate is first flattened and surfaced to 3/4 in. thick and then 70% of the material is removed by rough machining or chemical milling. Figure IV-47 shows the results of chemical milling through a 3/4-in.-thick René 41 plate for a typical section. Finish machining will consist of drilling, tapping, and deburring the chemical-milled edges. The Hastelloy-C rings have been rolled and welded.

The porosity of the front plate with respect to total air flow is 74%, and in the beam area the average porosity is 83%. Structural characteristics of the support grid are given in Table IV-5. These characteristics apply at the structural design point: 1000 ft altitude, hot day, Mach 3 flight.

REACTOR CONTROL AND SAFETY SYSTEM

Figure IV-48 is a drawing of the reactor control and safety systems showing the general arrangement of components. The two vernier control rods and the four groups of shim control rods are driven by linear actuators in the duct. The safety rods are actuated from outside the duct. The main structural member of this system is a tube coaxial with the duct. Ways for the shim rod sliders are mounted on the outside of the tube, and guide tubes for the safety rods are mounted on the inside. The two vernier rod sliders have individual tubular mounts.

Figure IV-49 shows the radial position of the control and safety rods within the reactor. All control rods (shim and vernier) insert into the control

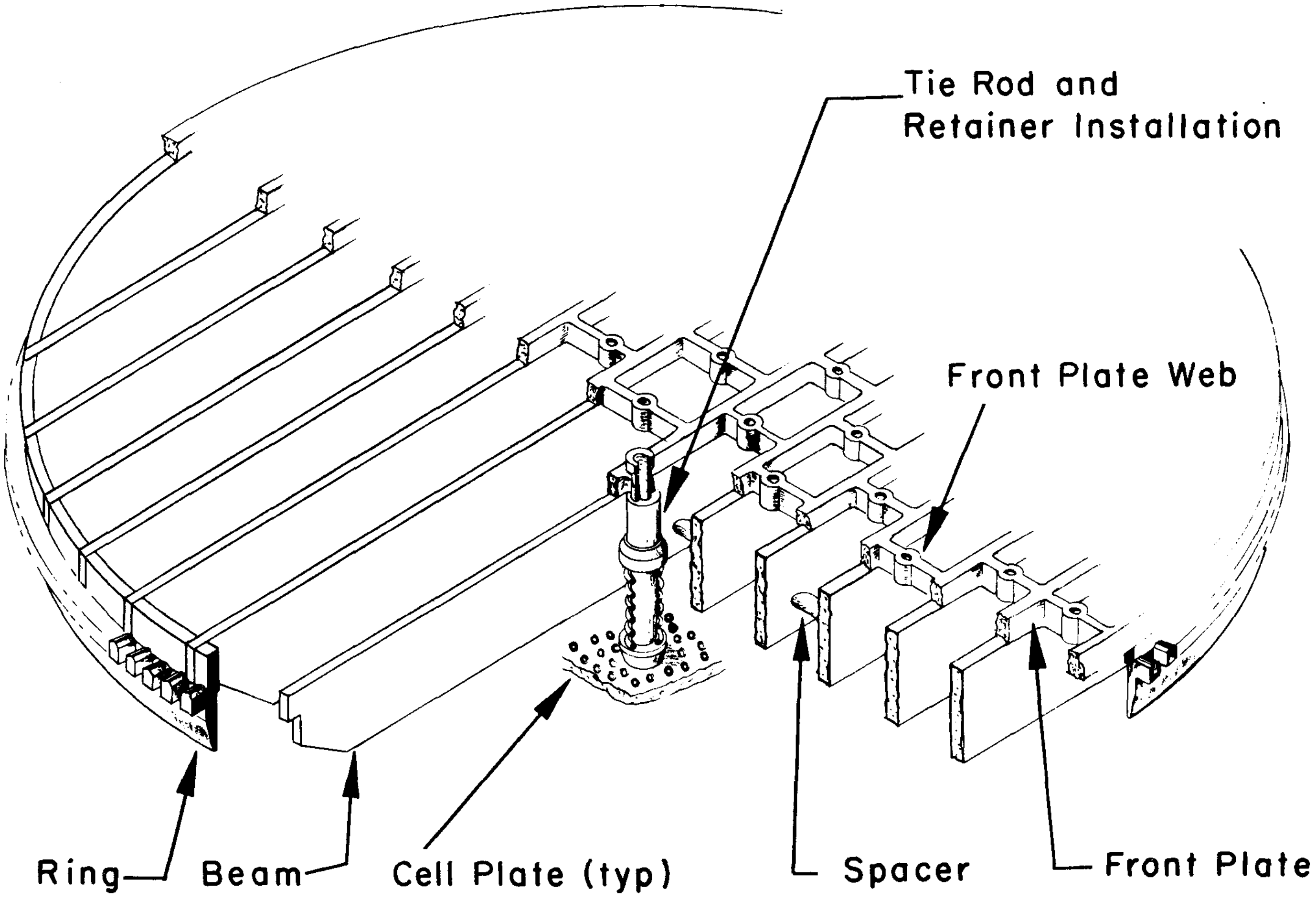

MUL-14727
Rev. 2/13/62

Fig. IV-46. Tory II-C reactor support grid, new design.

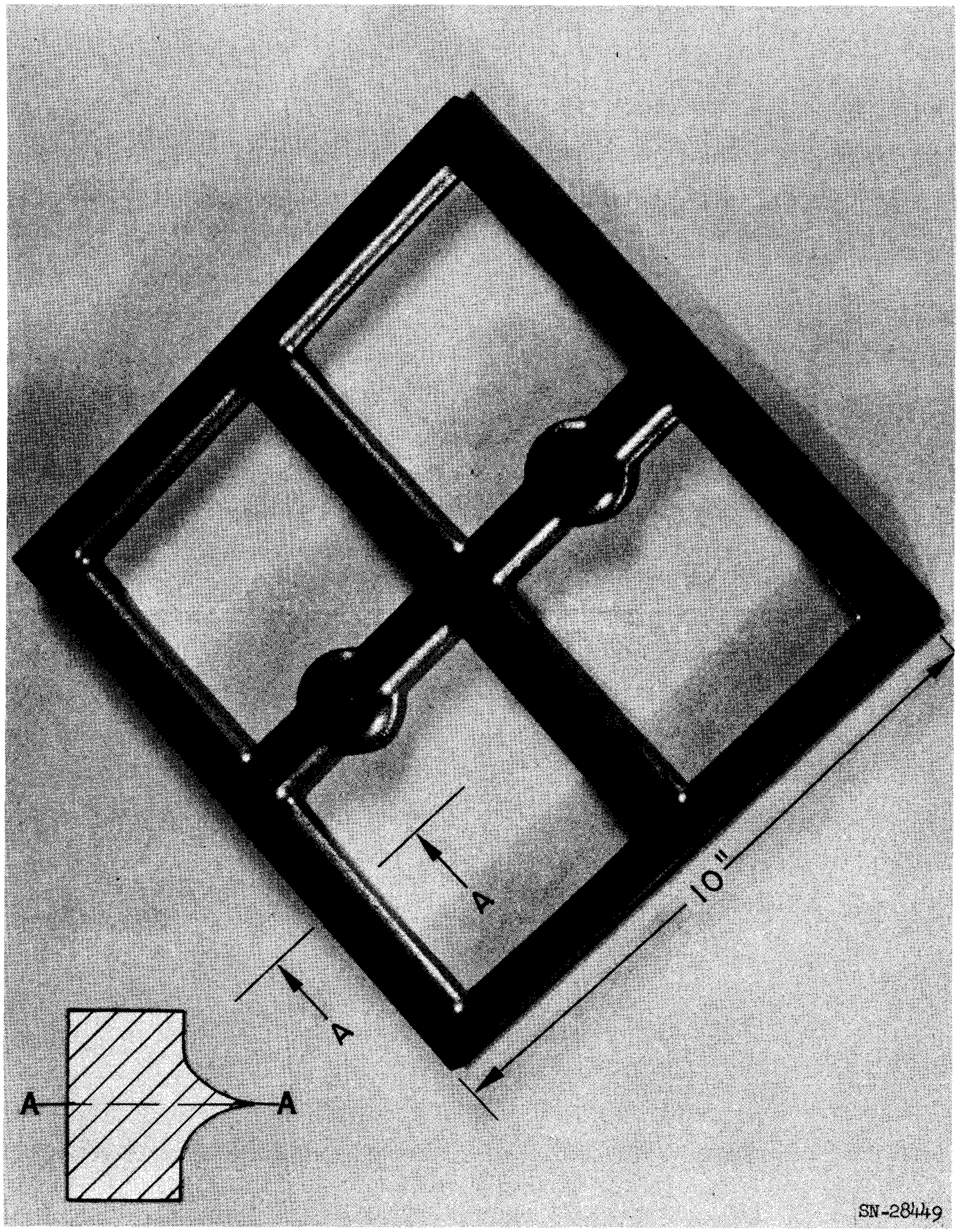

Fig. IV-47. Specimen of support grid material (3/4-inch René 41 plate) showing results of chemical milling.

Table IV-5. Support Grid Structural Characteristics.

	Center beam		Front plate	
Location	Aft surface	Fwd. surface (@ bolt hole)	Web at tie rod hole	Tie rod bolt hole
Bending stress	+38 ksi[a]	-38 ksi	±39 ksi	-34 ksi
Thermal stress	+10 ksi	None	-5 ksi	0
Stress conc. factor	None	2.0	2.0	2.4
Maximum elastic stress	+48 ksi	-76 ksi	-68 ksi	-82 ksi
Min yield strength, 0.2% offset	+105 ksi	+110 ksi	+110 ksi	+110 ksi
Approx temperature	1340 °F	1200 °F	1200 °F	1200 °F
$\frac{\text{Yield strength}}{\text{Max elastic stress}}$	2.2	1.4	1.6	1.35
Beam deflection (max)	0.125 in.			
Lateral natural frequency of beams	> 300 cps			
Design load	30,000 lb			
Minimum buckling load	100,000 lb			

[a] Means 1000 psi.

tie tods (1.222-in. o.d.). The safety rods insert into standard tie rod (0.670-in. o.d.) and are inserted only during nonnuclear, low power, or emergency conditions.

REFLECTED CORE

The reflected core design underwent several changes during this quarter. Results of the cross-section test and other investigations indicate that ground hexagonal tubes with a dimension across the flats of 0.2970 in. will result in gross stack dimensions that indicate an apparent element across-the-flats dimension of 0.2980 in. at cold assembly. This buildup affects dimensions of shims, base blocks, the support grid, and the side support system. Neutronics calculations are also affected.

To provide more control in case it is needed, four additional control rod spaces have been added, as shown in Fig. IV-50. The associated tie rods, base blocks, fueled and unfueled tubes, fuel loading maps, front retainer plates, springs, and spacers have been changed.

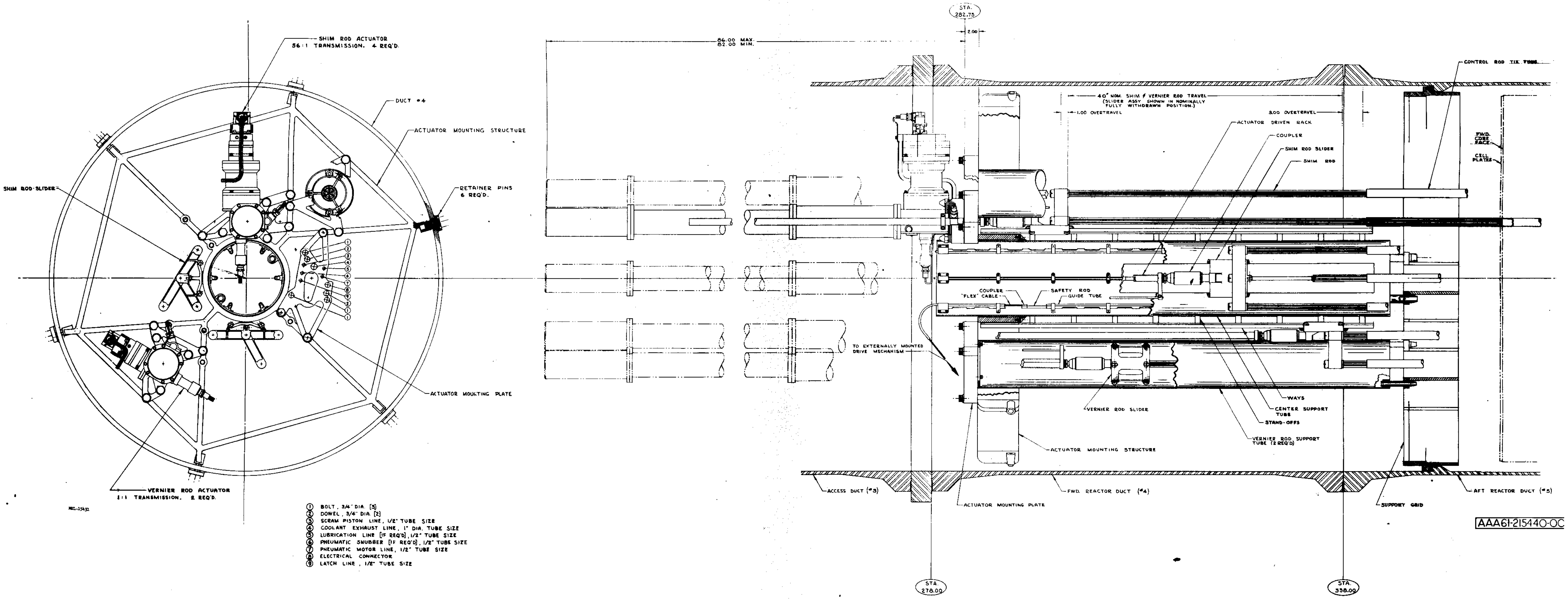

Fig. IV-48. General arrangement of the forward reactor duct housing control rods, safety rods, and supporting components.

~~CONFIDENTIAL-RD~~

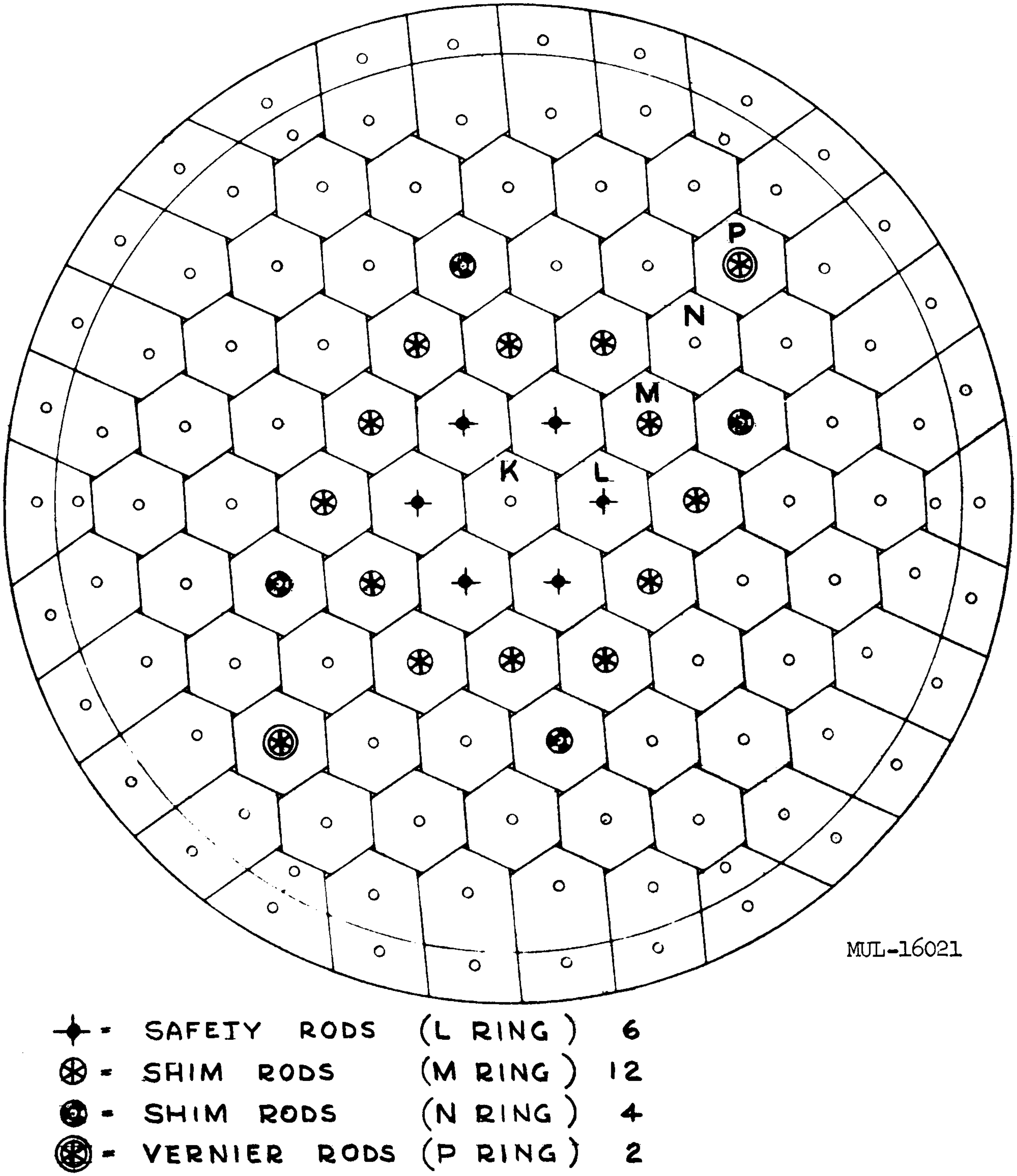

Fig. IV-49. Control and safety rod positions, view looking aft from face of cell plates.

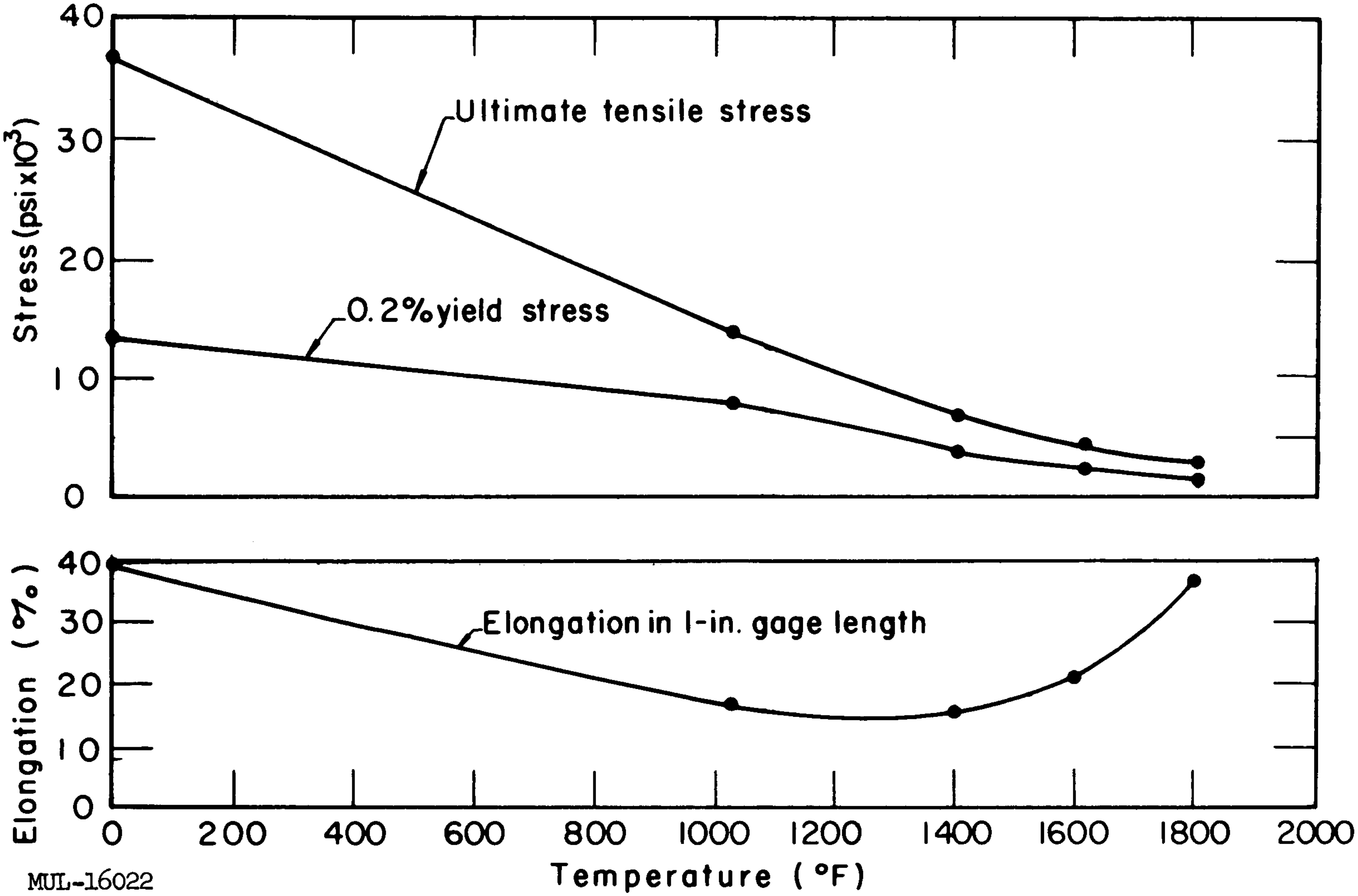

Fig. IV-50. Tensile strength of as-cast electrolytic nickel (99.95%).

Recent analysis revealed a high thermal stress in the BeO cartridge design shown heretofore. For purposes of stress calculation it was assumed that the temperatures of adjacent channels impinging on the same cartridge might differ by 300 °F. Several new designs are under consideration which reduce thermal stresses generated in this way to an acceptable level.

The nickel shims forming the outer periphery of the reflected core are designed to be a precision investment casting of electrolytic nickel.

High-temperature tensile tests on cast nickel test specimens have been completed. The results shown in Fig. IV-50 reveal a surprising strength and ductility for an as-cast, unworked material.

TIE RODS

Tubing Evaluation

Tests on R-235 welded-to-size control-tie-rod tubing (full tube test specimens) show adequate strength and ductility at the design temperature of 1080 °F. Figures IV-51 and IV-52 show creep rupture results plotted on Larsen-Miller coordinates for tests at 1080 and 1400 °F, respectively. Compare the lower ductility recorded for the 1400 °F tests with ductility recorded for the 1080 °F tests. Figure IV-53 shows short-time strength and elongation data obtained for R-235 and René 41 at 1080 and 1400 °F. Advertised curves have been superimposed. René 41 control-tie-rod tubing tests show adequate strength and ductility in creep rupture at 1080 °F but somewhat lower short-time tensile ductility than R-235. These data are shown in Figs. IV-53. and IV-54. Creep rupture tests on René 41 at 1400 °F are now being performed. Figure IV-55 shows creep test results on R-235 standard-tie-rod welded-to-size tubing. The strength and ductility are considered adequate at the design temperature of 1400 °F.

Brazing Study

The development of brazing cycles for R-235 and René 41 tie rod fittings using alloy J-8100 is proceeding satisfactorily. The latest group of brazed parts yielded over 80% acceptable brazes. Sample brazes with Premabraze 128 (72 Au, 22 Ni, 6 Cr) show promise in filling joints at a lower temperature than J-8100 requires. This prevents reduction of tensile properties in the parent material due to carbides going into solution at the higher temperature range. Premabraze 128 is a ductile alloy in the as-brazed condition and is available in sheet and wire, whereas the brittle J-8100 is only available in powder.

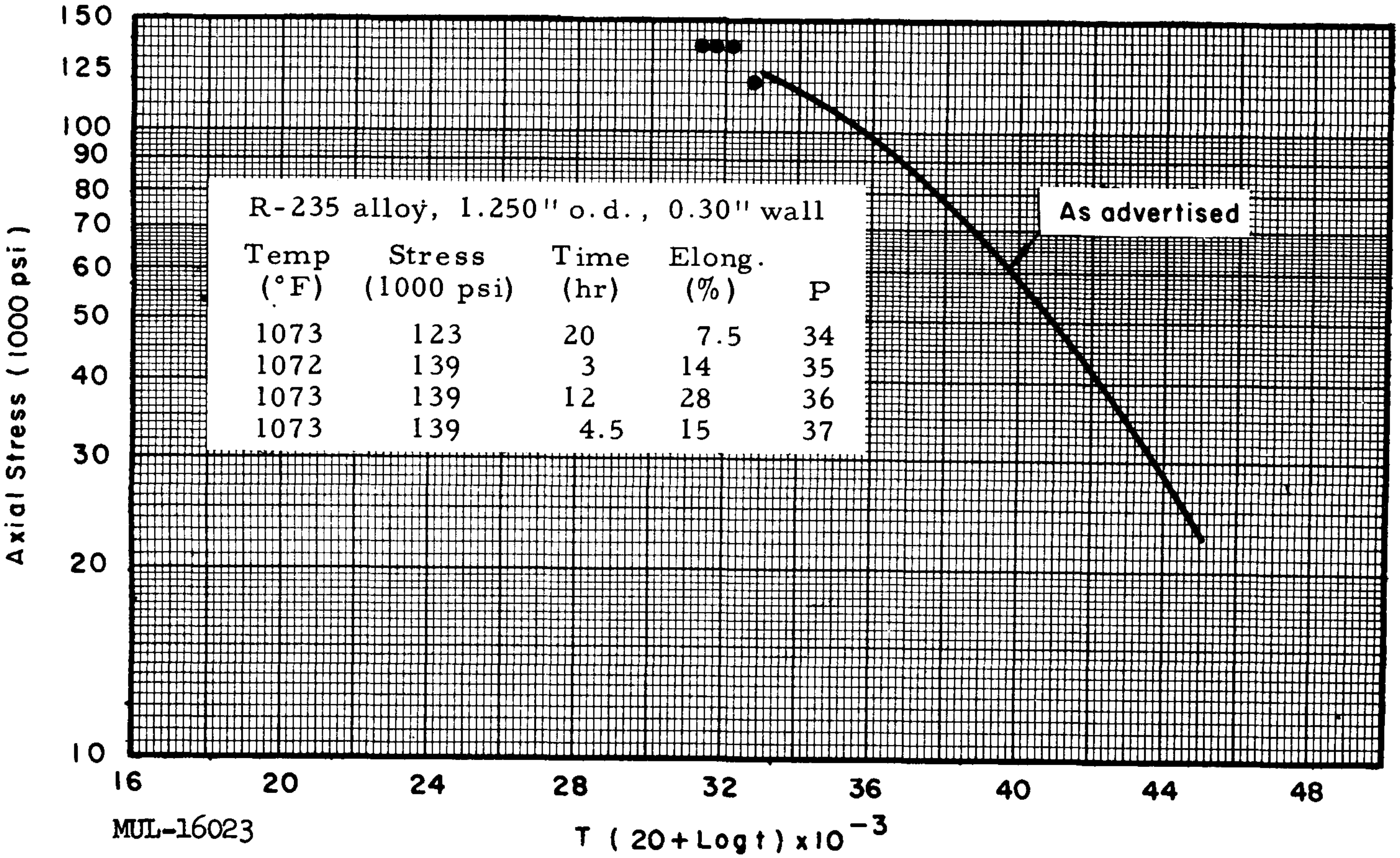

R-235 alloy, 1.250" o.d., 0.30" wall

Temp (°F)	Stress (1000 psi)	Time (hr)	Elong. (%)	P
1073	123	20	7.5	34
1072	139	3	14	35
1073	139	12	28	36
1073	139	4.5	15	37

Fig. IV-51. Results of creep rupture tests on R-235 welded-to-size control-tie-rod tubing (full tube test specimens). Specimens heat-treated 1975°F/30 min and air-cooled, 1400°F/16 hr and air-cooled, before testing.

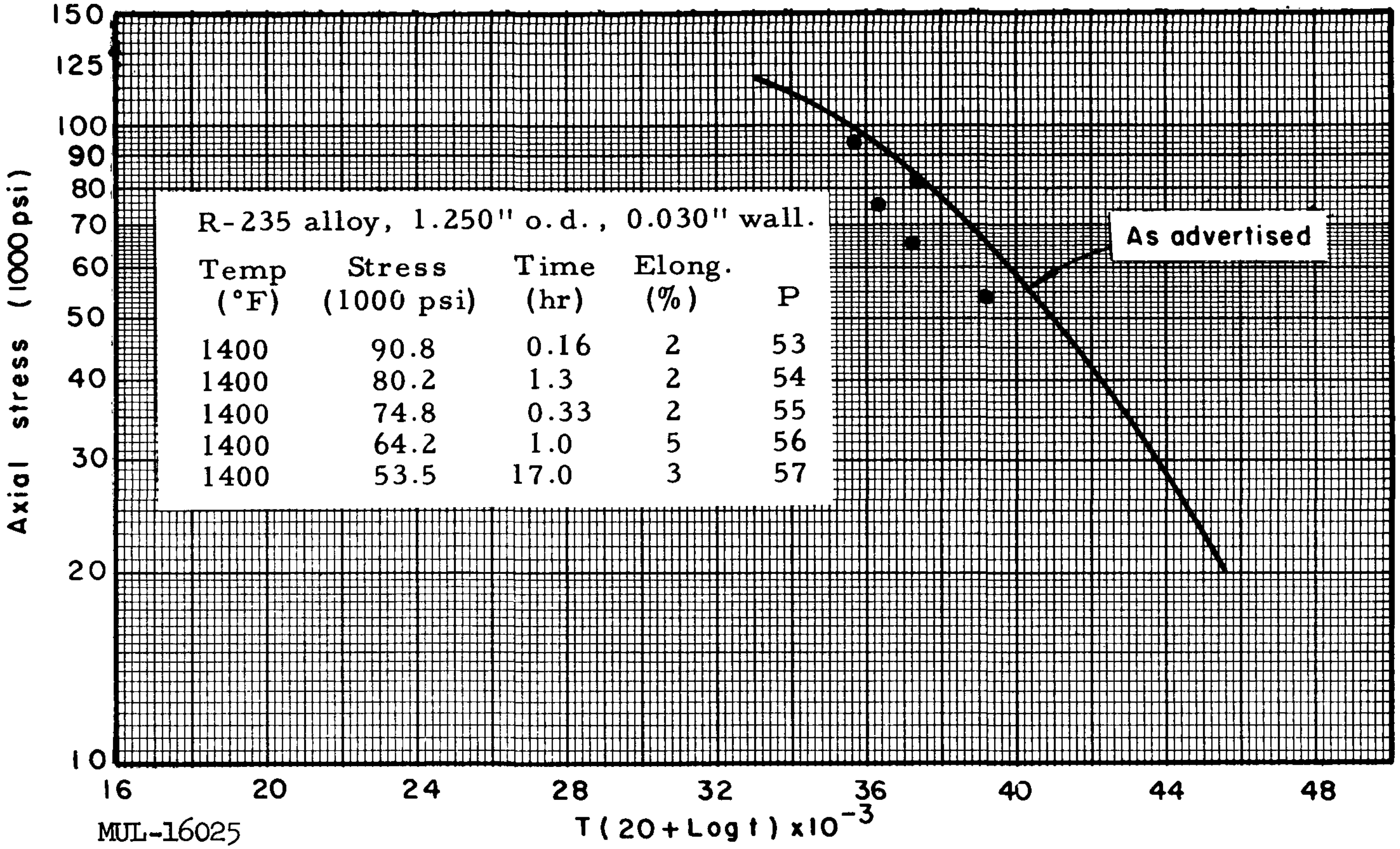

R-235 alloy, 1.250" o.d., 0.030" wall.

Temp (°F)	Stress (1000 psi)	Time (hr)	Elong. (%)	P
1400	90.8	0.16	2	53
1400	80.2	1.3	2	54
1400	74.8	0.33	2	55
1400	64.2	1.0	5	56
1400	53.5	17.0	3	57

Fig. IV-52. Results of creep rupture tests on R-235 welded-to-size control-tie-rod tubing (full tube test specimens). Specimens heat-treated 1975°F/30 min and air-cooled, 1400°F/4 hr and air-cooled, before testing.

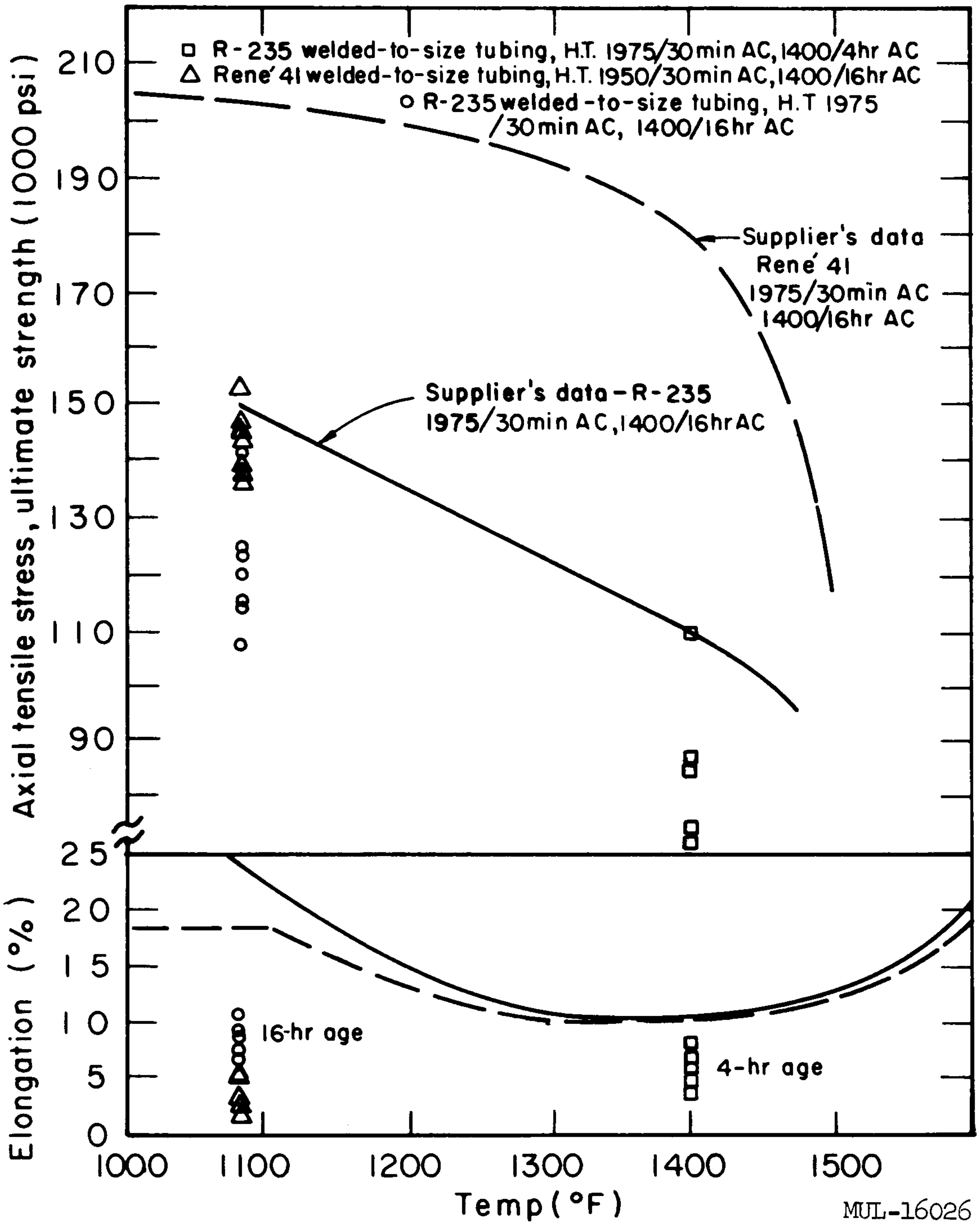

Fig. IV-53. Short-time strength and elongation data for R-235 and René 41, with advertised curves superimposed. Full tube test specimens, welded-to-size control-tie-rod tubing, 1.250-in. o.d., 0.030-in. wall.

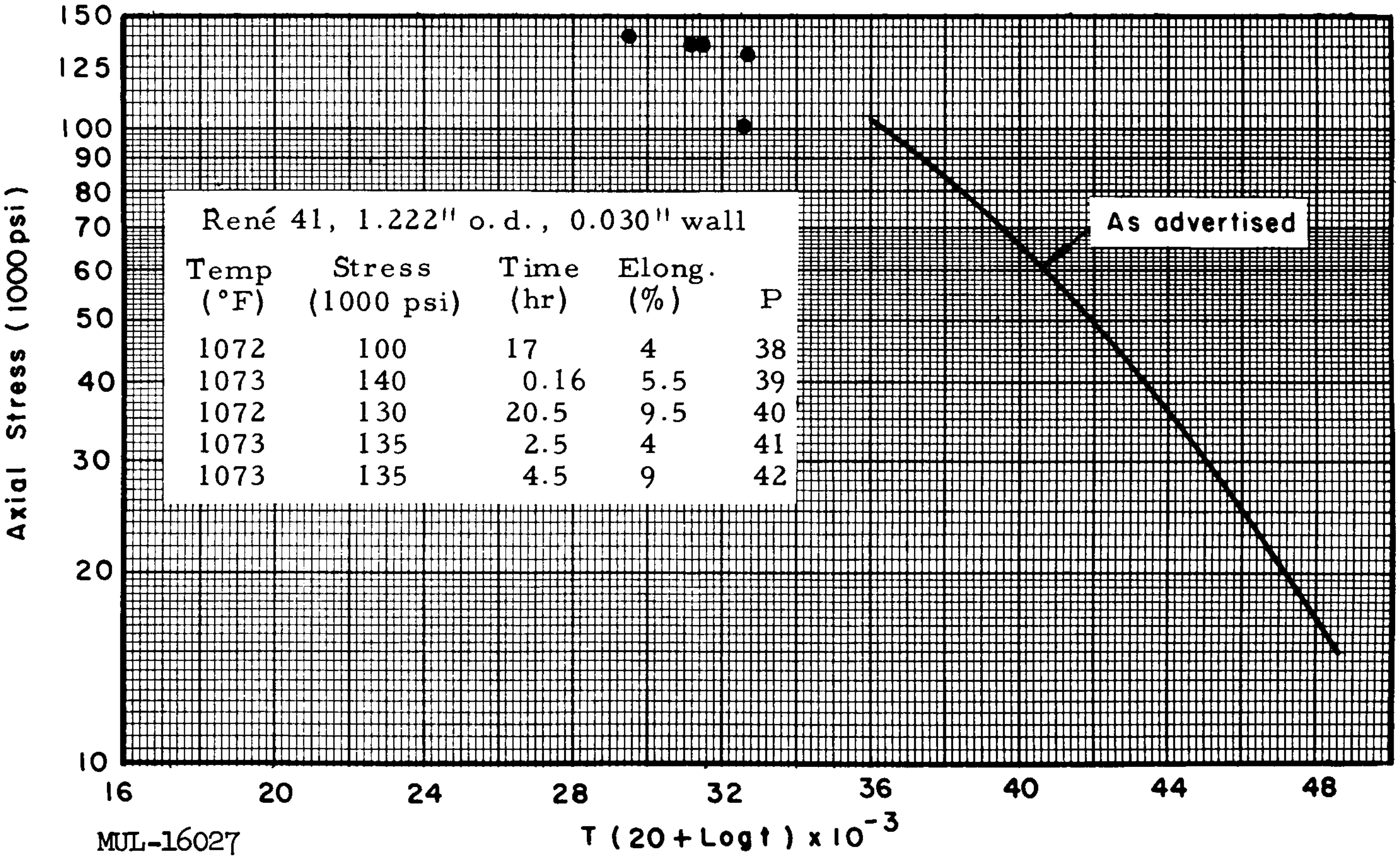

René 41, 1.222" o.d., 0.030" wall

Temp (°F)	Stress (1000 psi)	Time (hr)	Elong. (%)	P
1072	100	17	4	38
1073	140	0.16	5.5	39
1072	130	20.5	9.5	40
1073	135	2.5	4	41
1073	135	4.5	9	42

MUL-16027

Fig. IV-54. Results of creep rupture tests on René 41 welded-to-size control-tie-rod tubing (full tube test specimens). Specimens heat-treated 1950°F/30 min and air-cooled, 1400°F/16 hr and air-cooled, before testing.

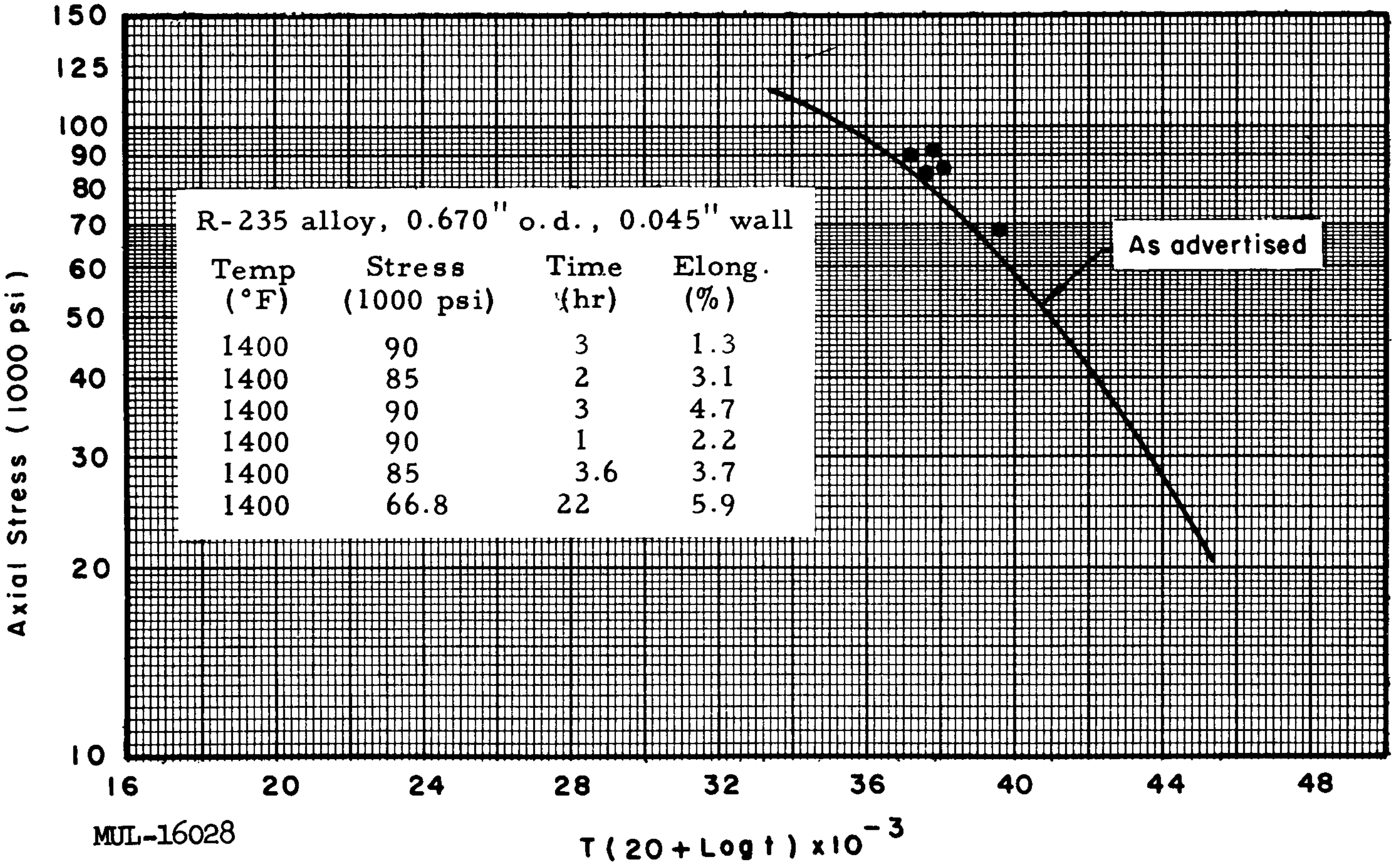

R-235 alloy, 0.670" o.d., 0.045" wall

Temp (°F)	Stress (1000 psi)	Time (hr)	Elong. (%)
1400	90	3	1.3
1400	85	2	3.1
1400	90	3	4.7
1400	90	1	2.2
1400	85	3.6	3.7
1400	66.8	22	5.9

MUL-16028

Fig. IV-55. Results of creep rupture tests on R-235 welded-to-size standard-tie-rod tubing. Specimens heat-treated 1975°F/30 min and air-cooled, 1400°F/16 hr and air-cooled, before testing.

Recent strength tests of the J-8100 brazed joints in R-235 tie rods continue to show 100% joint efficiency even at 1700 °F. The full tensile strength of the tubing can therefore be realized.

BASE BLOCKS

Alloy Procurement

Eight 5-inch plates and four 9-inch plates were produced during this quarter. All of these plates exhibited less room-temperature ductility than the 4% required by specification. Studies conducted by several vendors and LRL demonstrate that the ductility can be increased by a post-rolling anneal at 2500 °F for 1 hour. A post-rolling anneal at 2200 °F for 1 hour was previously used. The 2500 °F annealing temperature reduces the high temperature strength by an acceptable amount. Specifications have been revised accordingly, and fabrication of further quantities is proceeding.

Protective Coatings

Studies were conducted on the oxidation rate in air of uncoated F-48 for temperatures ranging from 600 °C (1110 °F) to 1300 °C (2375 °F). The data are given in Table IV-6. A graph (Fig. IV-56) based on these data shows time for a constant 5-mil metal recession vs temperature. This curve provides a conservative means of estimating expected life for the uncoated material. The observation can be made that in the temperature region (1250 °F) where the disilicide pest is most detrimental to the protective coating which will be applied to the base metal, the base metal itself is more than adequate for reactor use. At 2300 °F the base metal has a minimum life of almost 2 hours which may be safely added to the protective coating life in determining the total useful life. Coatings have been produced which provide at least 10 hours and as much as 46 hours protection at 2300 °F. These same coatings in the disilicide-pest region have an expected life of about 2 hours.

Based upon this information, the minimum expected life of a coated base block at any temperature up to 2300 °F is 4 hours. This minimum life results from exposing the part first at 1250 °F for 2 hours and subsequently at 2300 °F for 2 hours. Any other combination of time and temperature would yield a significantly greater life.

Disilicide Pest

The first observation of the disilicide pest was made in the previous quarter. The niobium disilicide compound, which is one of the products of the

Table IV-6. Oxidation Rate of F-48 (Cb 15-W 5-Mo 1-Zr) vs Temperature.

Temperature (°C)	(°F)	Time (hours)	Wt change (mg/cm ^{2})	Surface recession (mils)
600	1110	2	0.15	0.015
600	1110	5	0.39	.040
600	1110	10	0.62	.064
650	1200	2	0.24	.025
650	1200	5	0.49	.051
650	1200	10	2.21	.229
700	1290	2	0.45	.047
700	1290	5	4.10	.423
700	1290	10	18.8	1.95
800	1470	2	20.1	2.08
900	1650	2	15.3	1.58
1000	1830	2	17.8	1.85
1100	2010	2	19.0	1.97
1100	2010	4	28.7	2.97
1100	2010	2	16.3	1.69
1100	2010	4	26.8	2.78
1170	2140	2	26.6	2.76
1170	2140	4	37.2	3.85
1200	2190	2	24.7	2.56
1200	2190	4	35.9	3.72
1270	2320	2	44.7	4.62
1270	2320	4	69.3	7.18
1300	2370	2	69.9	7.23
1300	2370	4	101.8	10.60

Cr-Al/Si coating process, is generally a highly oxidation-resistant material. However, at temperatures of about 1250°F this compound undergoes an oxidizing decomposition which results in total loss of the coating material in a few hours. The decomposition is characterized by the formation of a voluminous, loose brownish powder. Little progress has been made in understanding the reaction; however, progress has been made in alleviating the condition in two different ways. The first has been to provide a chromium barrier between the niobium and the silicon, forming a chrome silicide. The second has been to provide a more dense Cr/Al oxide barrier between the environment air and the niobium disilicide.

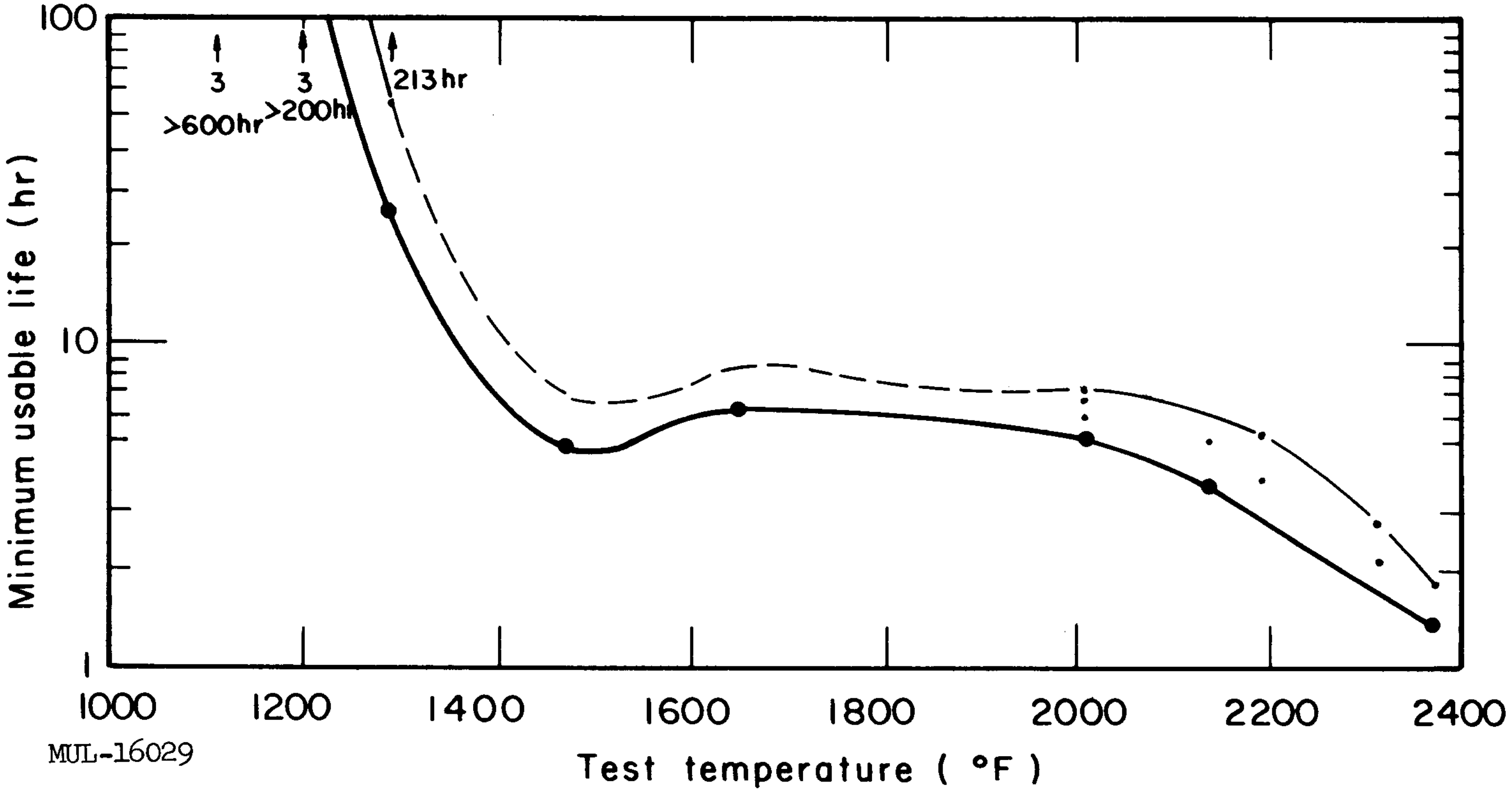

Fig. IV-56. Minimum usable life (time for oxidizing outer 5 mils) of uncoated F-48 columbium alloy in air, as a function of temperature. Upper curve: constant exposure. Lower curve: 2-hour cycles, with oxide removed between cycles.

SIDE SUPPORT SYSTEM

The details of the Tory II-C side support system are being reviewed. The present system is shown in Fig. IV-57.

The Inco 713C cast pressure pad has been replaced by a single sheet of 0.125-inch thick René 41 stiffened by three brazed ribs. These ribs are perforated and hence serve dual purposes — as pad stiffeners and flow screens. A 0.750-in.-diameter shear pin keys each pad to the duct.

The brazed pressure/flight spring combination has been replaced by two simply supported 0.090-in.-thick René 41 rectangular leaf springs. The spring system remains approximately linear through an average initial deflection of 0.750 in. As the leaves roll together, however, the spring becomes progressively stiffer, thereby assuming nonlinear characteristics.

Figure IV-58 presents load-deflection characteristics of these side support springs.

Brazing studies for the previous spring requirement continued in light of the rib-to-pressure-pad braze application. The braze alloy AMS-4778A has proven to be superior to J-8100 for the temperature requirements on the side support system. Tensile specimens subjected to the AMS-2778A braze cycle exhibit approximately 20% higher tensile strength and 400% greater ductility than those carried through the J-8100 cycle. The higher solution temperature required for J-8100 (2160°F vs 1975°F) forms a continuous grain boundary film of a complex metallic carbide which, in addition to reducing tensile strength and ductility, significantly decreases fatigue life. Braze No. 128 is being considered for this application as well as the tie rod application.

Photomicrographs of the fracture zone of the two René 41 tensile specimens are presented as Fig. IV-59 and IV-60. The specimen of Fig. IV-59 was heat-treated with the same thermal cycle used in brazing with AMS-4778A. The specimen in Fig. IV-60 was subjected to heat treatment according to the thermal cycle required for brazing with J-8100.

Brazed René 41 buggy springs were fatigue-tested at 1400°F, with maximum stress level of 100,000 psi and alternating stress levels of 60,000 psi. The alternating deflections which were imposed were on the order of 0.300 in. Three types of brazes were used — J-8600, J-8100, and AMS-4778. Some difficulty was encountered with stress concentration at a holding-clip guide. It is essential that uniform cross sections be maintained wherever possible.

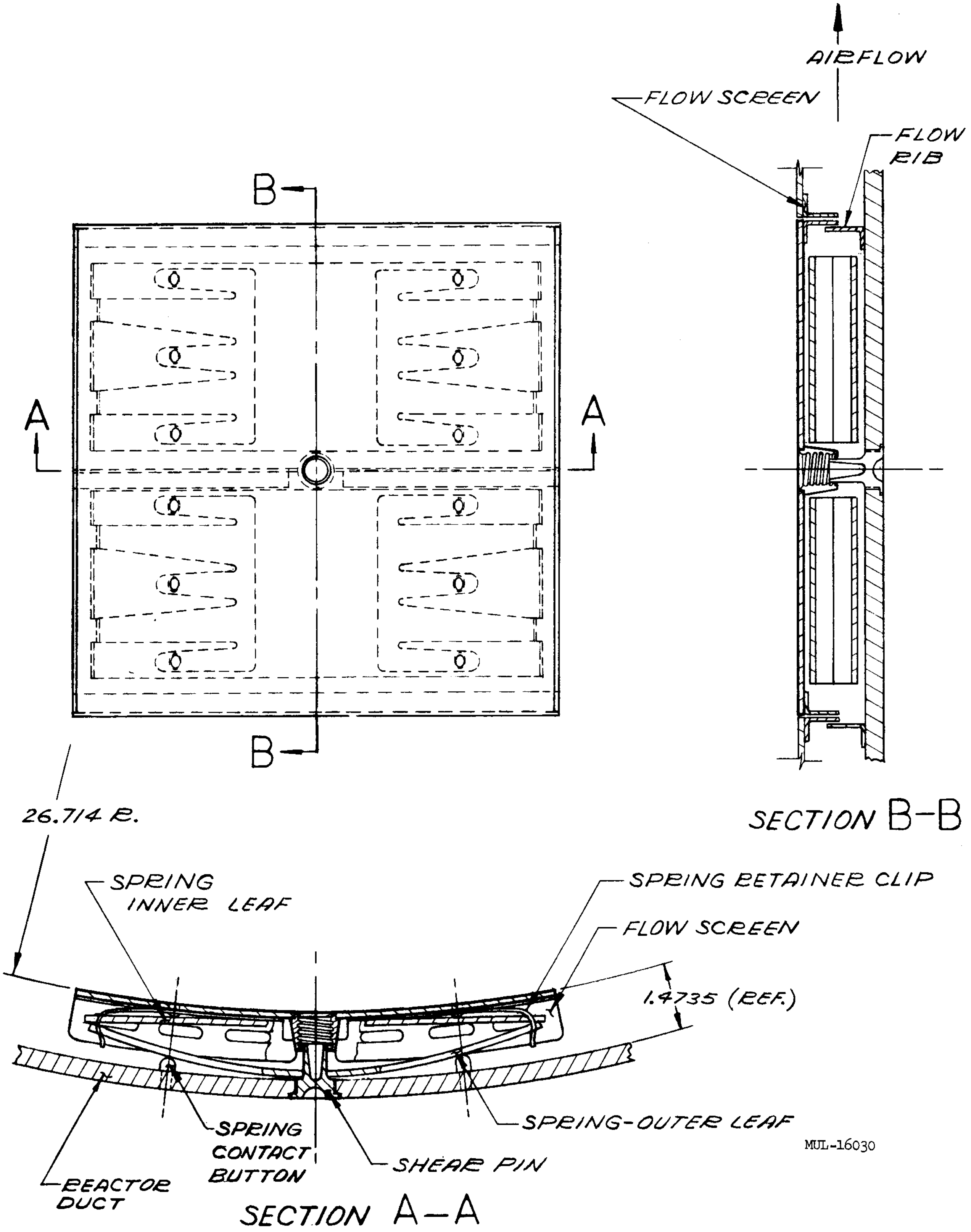

Fig. IV-57. Tory II-C side support system, 22-1/2° sector.

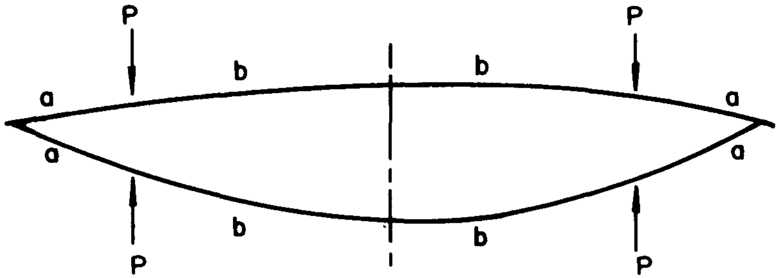

w = 4.00 in.
t = 0.09 in.
σ(max) = 98,600 psi
E(R.T.) = 3.0×10^7 psi
E(1400°F) = 2.5×10^7 psi
arc a = 1.68 in.
arc b = 3.12 in.

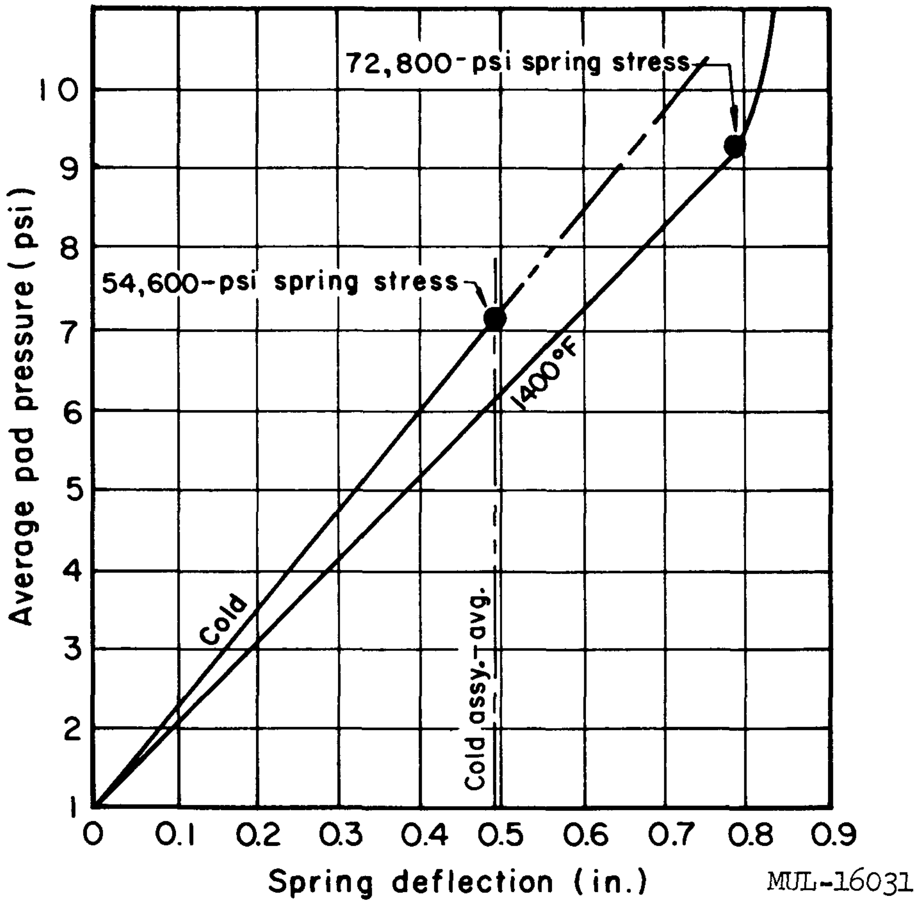

MUL-16031

Fig. IV-58. Load deflection characteristics of Tory II-C side support springs.

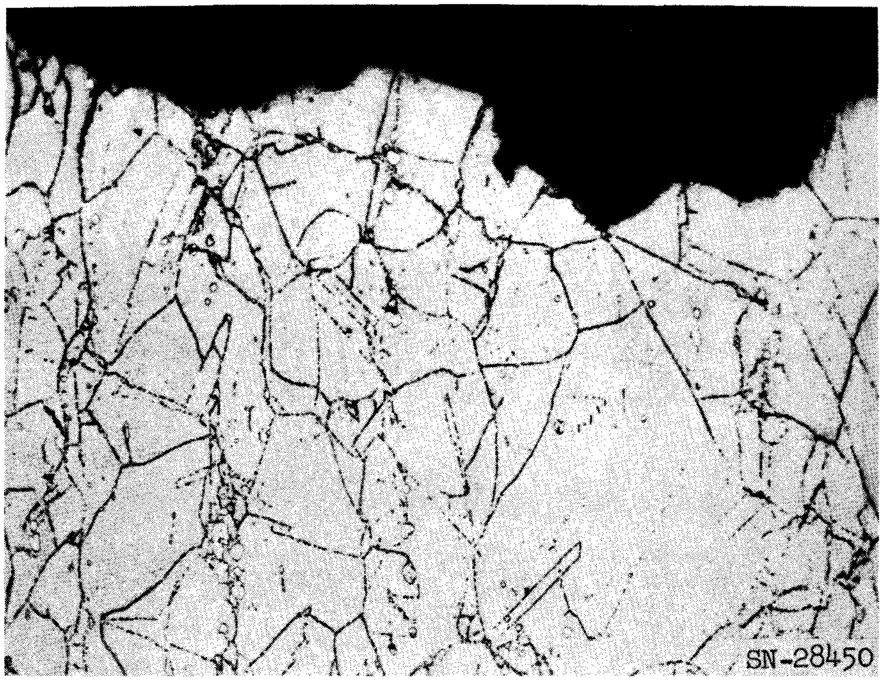

Fig. IV-59. Photomicrograph of René 41 tensile specimen (AMS-4778A thermal treatment). Magnified 250×; etchant, oxalic acid.

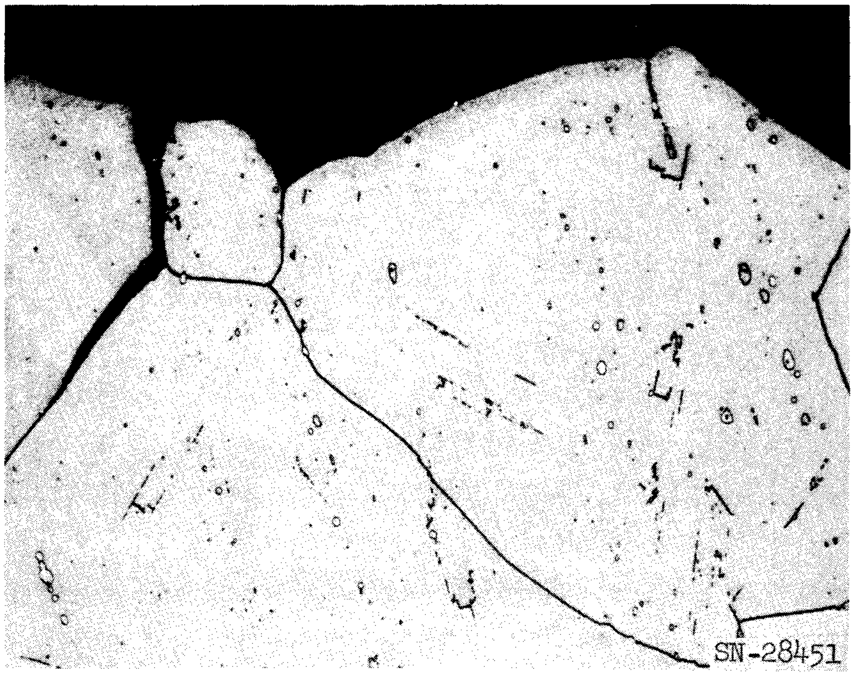

Fig. IV-60. Photomicrograph of René 41 tensile specimen (J-8100 thermal treatment). Magnified 250×; etchant, oxalic acid.

The AMS-4778 braze was again found to be superior to the others. Specimens with this braze withstood the imposed stresses for 500,000 cycles without failure.

ASSEMBLY-DISASSEMBLY EQUIPMENT

A contract was placed for the design and fabrication of a special handling vehicle. This equipment will be used for assembly, disassembly, and handling of the reactor and all duct sections used on the test vehicle. The assembled duct system can be removed directly from this assembly equipment and placed on the test vehicle.

Figures IV-61, IV-62, and IV-63 are an artist's conception of the various functions of the main handling vehicle (vehicle 5). Vehicle 5 handles the aft reactor duct (duct 5), the nozzle, and the forward reactor duct (duct 4). Figure IV-61 shows the 4-5 duct assembly tilted to the vertical position. In this attitude, actuators and control packages may be worked on by slave manipulators. Duct 5, containing the partially assembled reflected core, will be placed on the vehicle while it is in this vertical position and then tilted to the horizontal for installation of tie rods and base blocks. The vehicle can be jacked up to provide a rigid assembly jig.

Figure IV-62 shows the reactor in traveling position. The vehicle is capable of self-propulsion up to 1.25 mph, or of being towed up to 5 mph. It is narrow enough to be loaded on a standard motor vehicle trailer (Fig. IV-63) for highway transportation.

UNIT CELL TESTS

To date three unit-cell tests have been conducted. These tests consisted of flowing direct propane-fired air through an assembly representing in various degrees a Tory II-C unit cell. The unit cell consists of a bundle of ceramic tubes supported by a tie rod and coated metal base block. A typical bundle of tubes is shown in Fig. IV-64. The whole assembly is contained in a section of refractory-lined high-pressure pipe.

The purpose of these tests is (1) to demonstrate that the components are compatible in an environment similar to the one they are intended to operate in, and (2) to demonstrate, at the earliest possible date, that the structure can operate for extended periods in such an environment.

The first cell consisted of a steatite tube bundle, a standard tie rod, and a coated 1% Zr-Nb base block. The coating was the dual-cycle Si-Cr/Al coating.

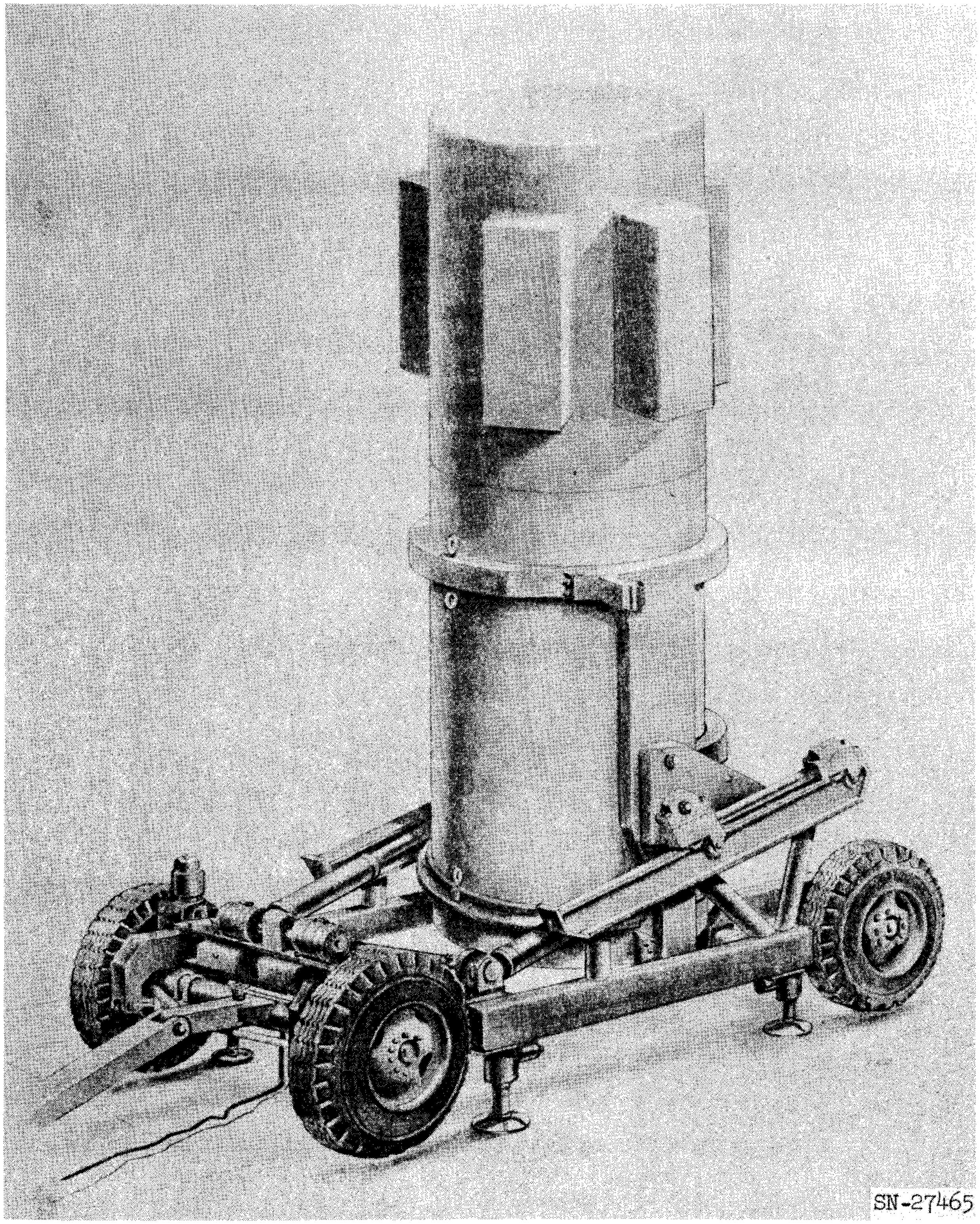

Fig. IV-61. Vehicle No. 5, ducts 4 and 5 erected.

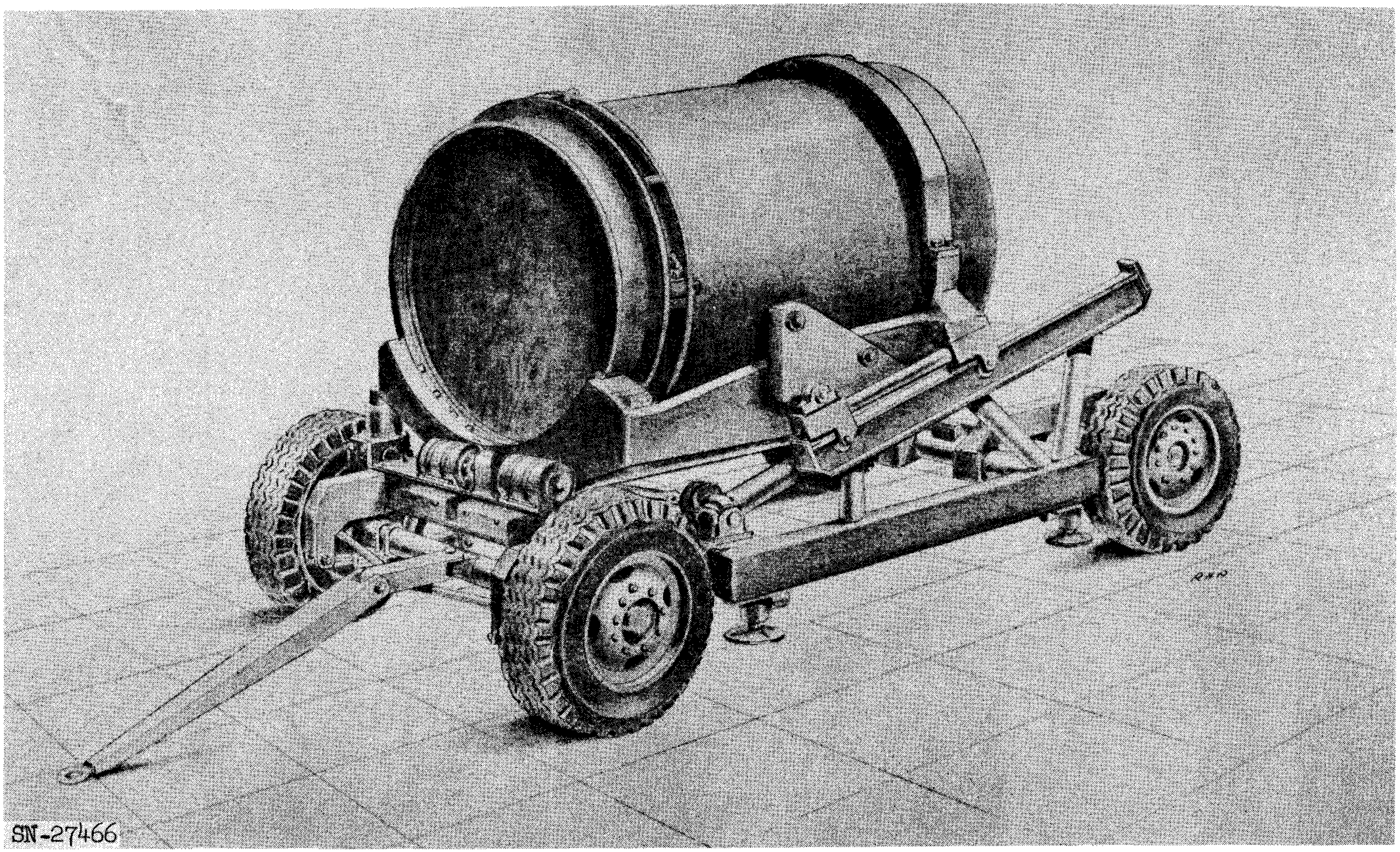

Fig. IV-62. Vehicle No. 5, towing mode.

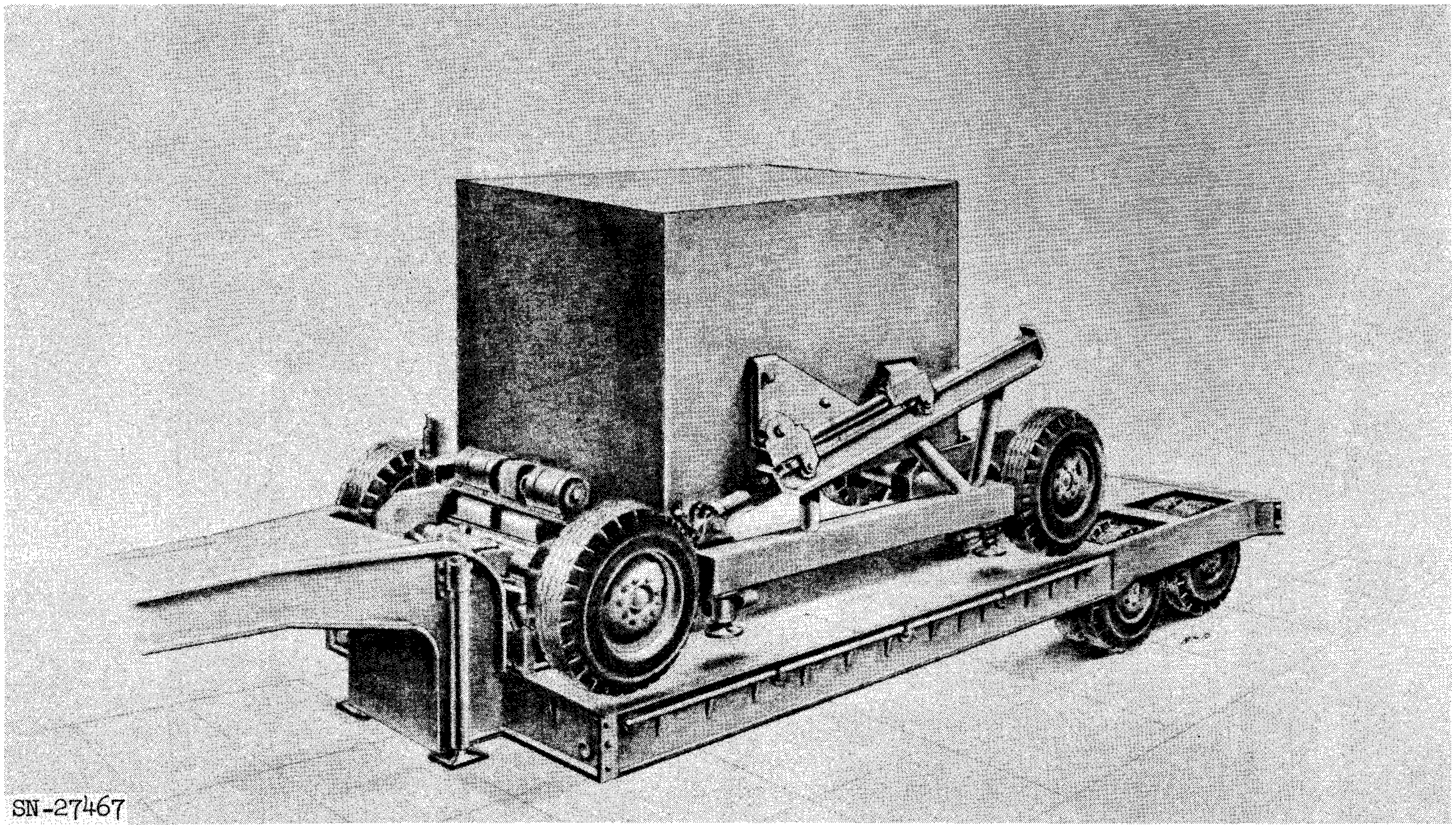

Fig. IV-63. Vehicle No. 5, highway transportation mode.

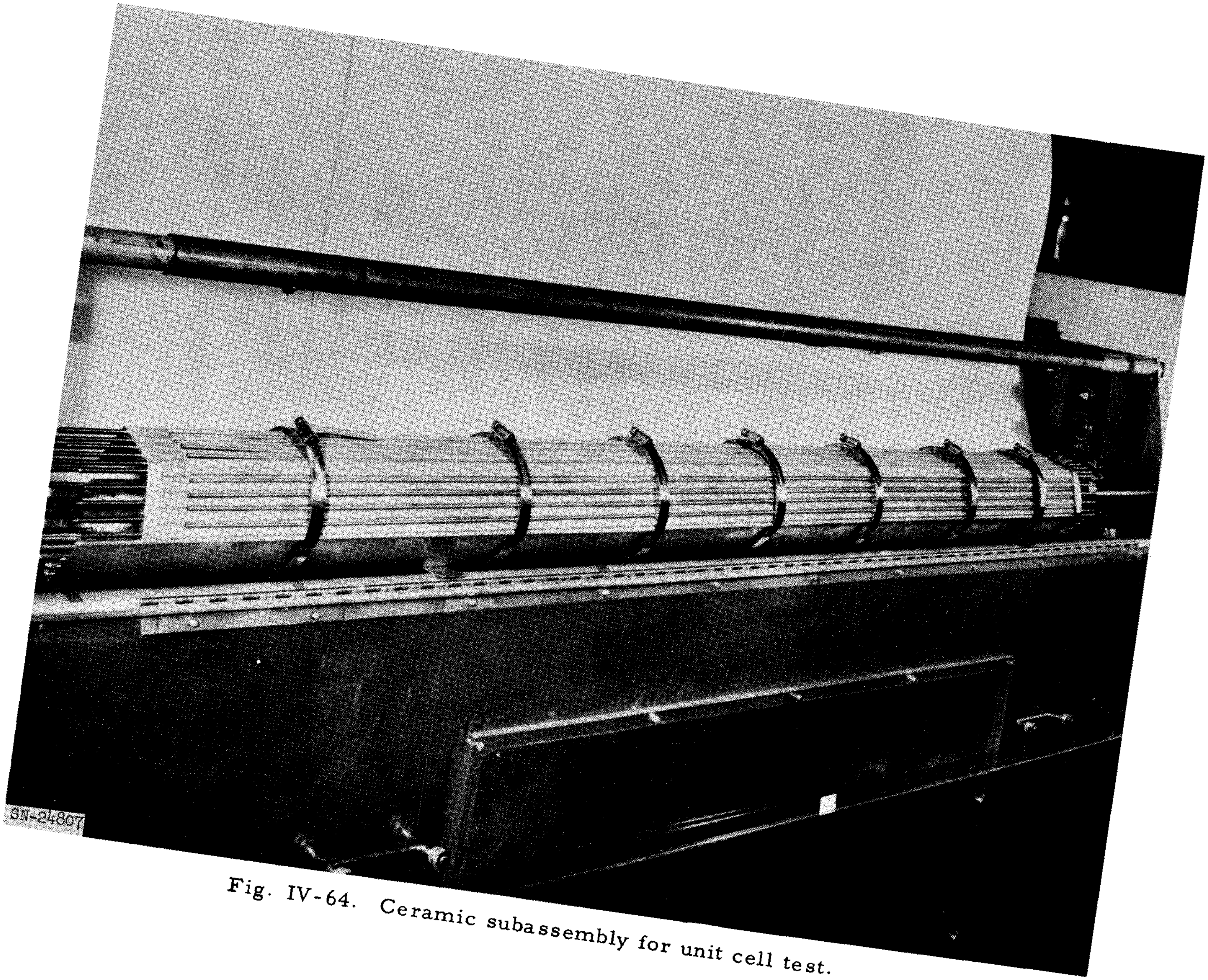

Fig. IV-64. Ceramic subassembly for unit cell test.

The base block had individual flow passages corresponding to the steatite tubes. The primary purpose of this cell was to check out instrumentation, test equipment and operation, and cell design. This cell ran for 38 minutes in cold air, 15 minutes in 1100°F air, and 15 minutes in 2000°F air.

Subsequent examination revealed that the refractory pipe liner had failed due to erosion in the high-velocity air stream. With the exception of some already obsolete components, all simulated reactor components were intact except for the coating of the base block. The failures noted on it were due to sandblasting by particles from the eroding liner.

A second liner was cast and covered with a 1/16-inch nickel shield and the test repeated with identical components. This cell was operated for 2-1/2 hours, 2-1/4 hours of which was at 2000°F.

This time the only damage noted was on the base block coating at a few points where it was subjected to direct air blast. Otherwise, the base block could not be distinguished visually from a new base block. Again it was evident that the damage resulted from a sandblasting effect, but the source of the particles could not be determined with certainty. The phenomenon does not occur in a direct air blast when the ceramic tubes are absent, so the possibility that dust is generated in the tubes cannot be discounted. However, a direct blast of this sort will not occur in the reactor as presently designed, so this is not a source of major concern. Conceivably the eroding agent could have come from the hot air supply system.

The third cell tested was much closer to the actual configuration of a reactor unit cell than the first two. The tube bundle consisted of 204 BeO tube columns. This is fewer than a unit cell by one row of tube columns around the periphery. The reduction was required in view of the continuous run capability of the facility. These tubes were backed up by a 1-inch BeO plate, thirty-six 1-inch-long flow transition sections (seven to one hole except on the periphery of the cell), and a modified base block. A proprietary coating had been applied to the base block. The transition sections consisted of 17 BeO sections and 1 chrome-cermet section. The remaining 18 sections were composed of modified tie rod inserts since the transition sections were in short supply.

Since the base block was the component of most concern, the test conditions were selected to give a close approximation to design temperature, pressure drop, Mach number, and oxygen partial pressure in the base block region. All design conditions could not be achieved due to the fact that this is a different type of flow (no heat addition) and that the facility air flow rate is limited.

The test commenced with 10 minutes of cold air flow followed by 45 minutes of hot air flow, during which the air temperature was 2180 ± 20°F. The base block region was then visually inspected through an inspection port. No damage was noted except for a cracked tie rod insert. The run was continued for another 44 minutes until failure of the refractory pipe liner forced a shutdown.

Post run inspection revealed that none of the reactor structural components suffered damage except the weakened outer transition sections. (Fig. IV-65.

The base block coating performance was generally satisfactory. The downstream face of the block and the area within the holes of the block showed no loss of coating. Loss of the coating occurred in approximately six small areas on the upstream periphery of the plate and on two small places on the edge of one hole of the second row on the upstream side (Fig. IV-66). The loss of the coating on the periphery was considered due to a chemical/mechanical abrading action of aluminum silicate insulating material incidental to the test. This material became dislodged upstream and was entrained in the air. Subsequent testing of the coating in contact with aluminum silicate showed that a reaction occurred which softened the coating. The pinhole loss of coating at the interior hole could have been caused in the same way but it is more likely attributable to a minor coating defect that was there initially.

There was no evidence of chemical incompatibility between the coating and any transition section materials. The area between the tension rod bearing cup and the base block showed no interaction although some had been considered possible, either between the alumina and the coating or between the platinum rhodium cup material and the silicide in the coating.

During the run, data were taken from a photo panel every 3 minutes. Variations of 1 or 2% were noted among data sets, but each set of data is self-consistent. A typical set of data taken early in the first run of the third unit cell test is given in Table IV-7.

In addition to these data, noise level measurements were made immediately upstream and downstream of the cell. Figure IV-67 shows the upstream pressure pickup and the ratio of the downstream pressure to the upstream pressure. At the upstream conditions 1 psi corresponds to 170 decibels. Each decade on the graph corresponds to 20 decibels.

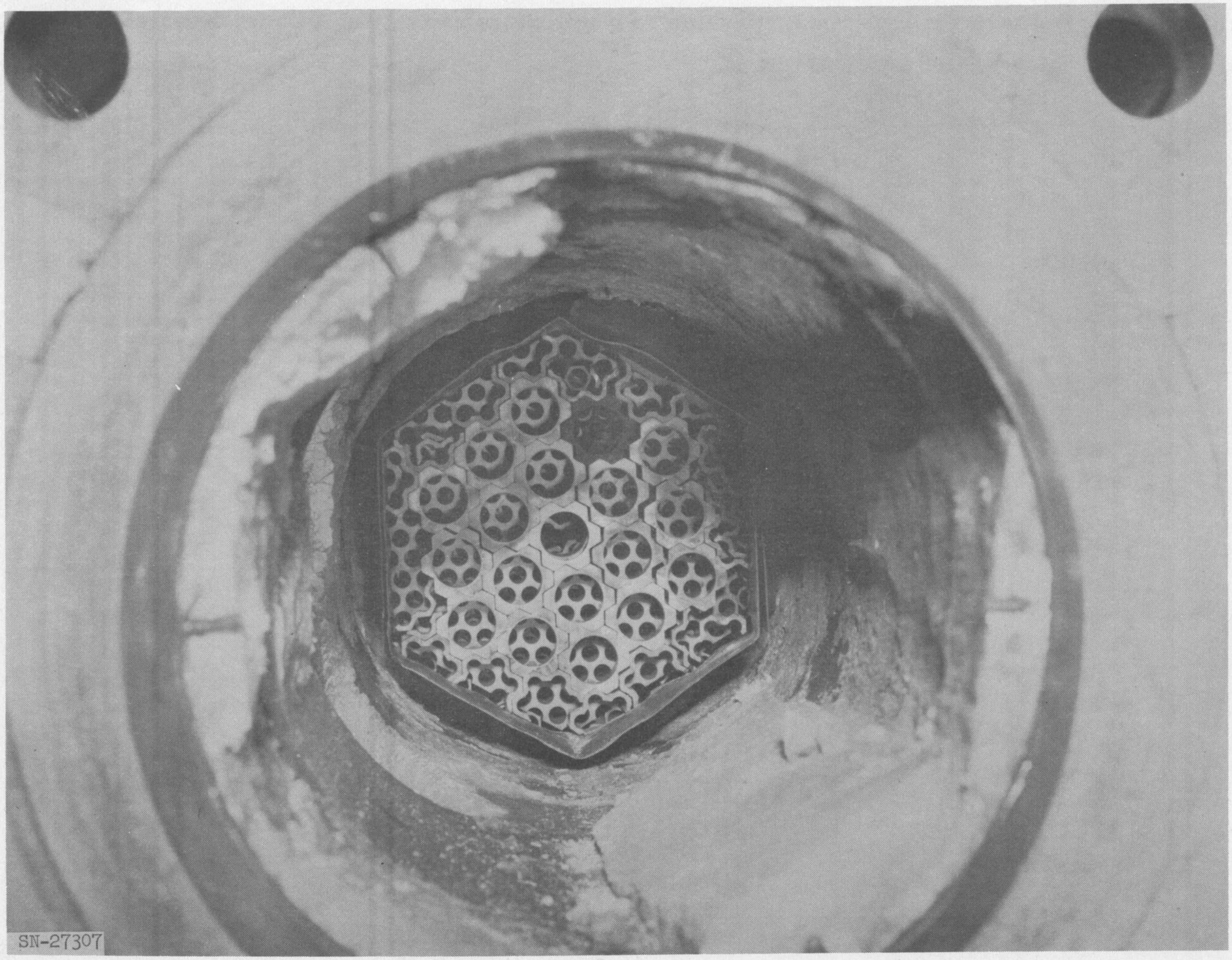

Fig. IV-65. Unit cell test, rear end after run No. 3. Base plate and tie rod removed.

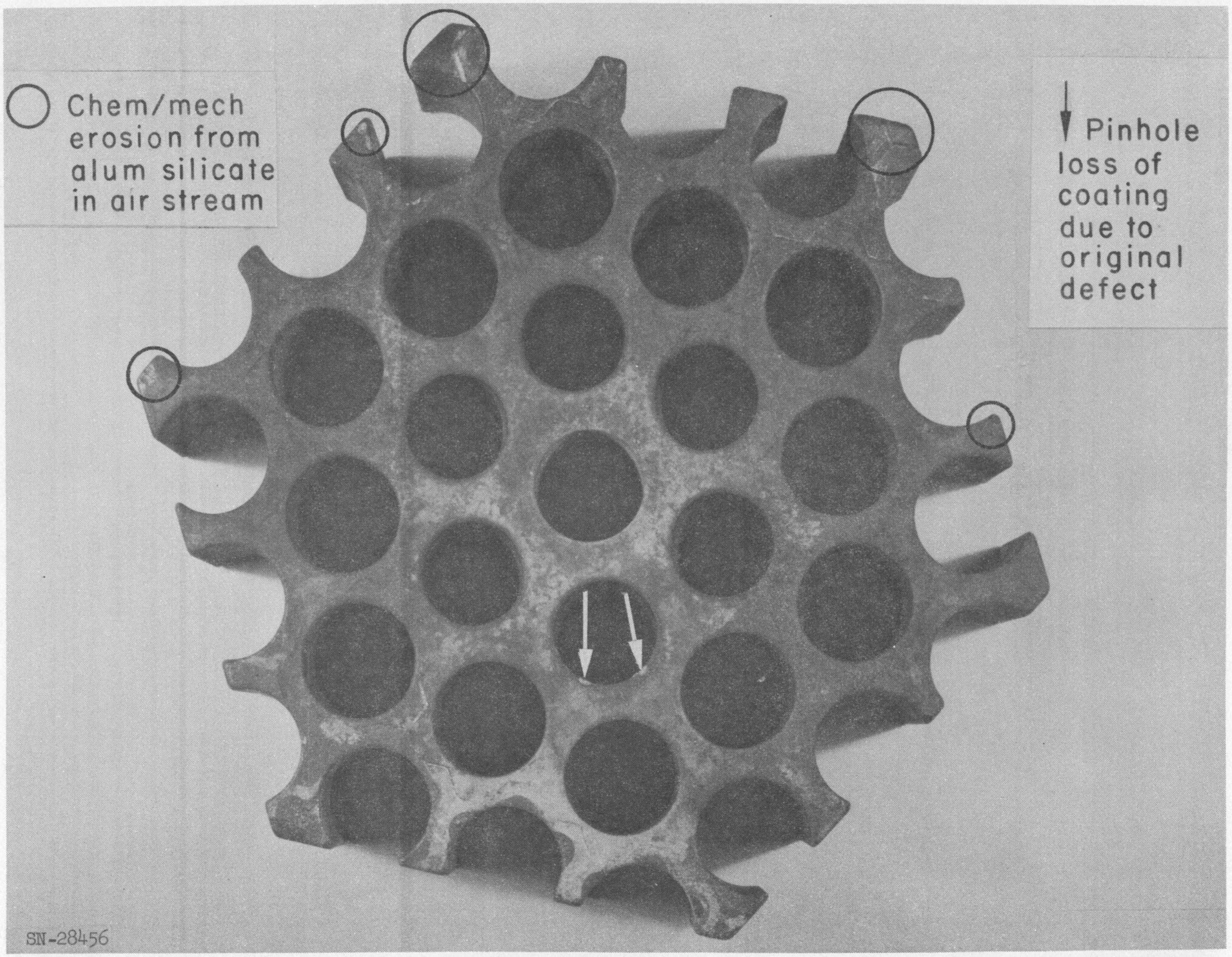

Fig. IV-66. Upstream face of base block after run 3 of unit cell test, showing areas (circled) where loss of coating occurred.

Table IV-7. Typical Conditions for Third Unit Cell Test.

Measured:	
Upstream total temperature (average of 3 thermocouples)	2195°F
Upstream total pressure (average of 3 probes)	248.3 psia
Downstream total pressure (average of 3 probes)	139.0 psia
Air flow rate	7.61 lb/sec
O_2 flow rate	2.32 lb/sec
Propane flow rate	0.329 lb/sec
Tie rod cooling air	0.259 lb/sec
Cooling air temperature	345°F at tie rod entrance
Tie rod temperatures	1164°F 1-1/2 in. from exit
	1084°F 5 in. from exit
	978°F 28 in. from exit
Calculated:	
Base block temperature	2195°F
Pressure drop across cell	109 psi
Mach No. at tube exit	0.52
Reynolds No.	1.05×10^5
Oxygen partial pressure equivalent to air at 180 psia in baseplate region	

ANNULAR FLOW TESTING

Due to the small difference between the temperature of the cooling air and the temperature limits of the side support springs, cooling is critical in the side support annulus.

Infrared photographic techniques have been employed to study the convective heat transfer mechanism in this region in detail.

A 3-foot-long, 22-1/2 degree segment of this annulus was fabricated with quartz walls in the center portion. Through these walls the temperature distribution of the resistively heated, convectively cooled springs could be photographed. Included in the photographs was a view of a heated calibration strip of the same material as the springs. The quartz walls and buggy springs are

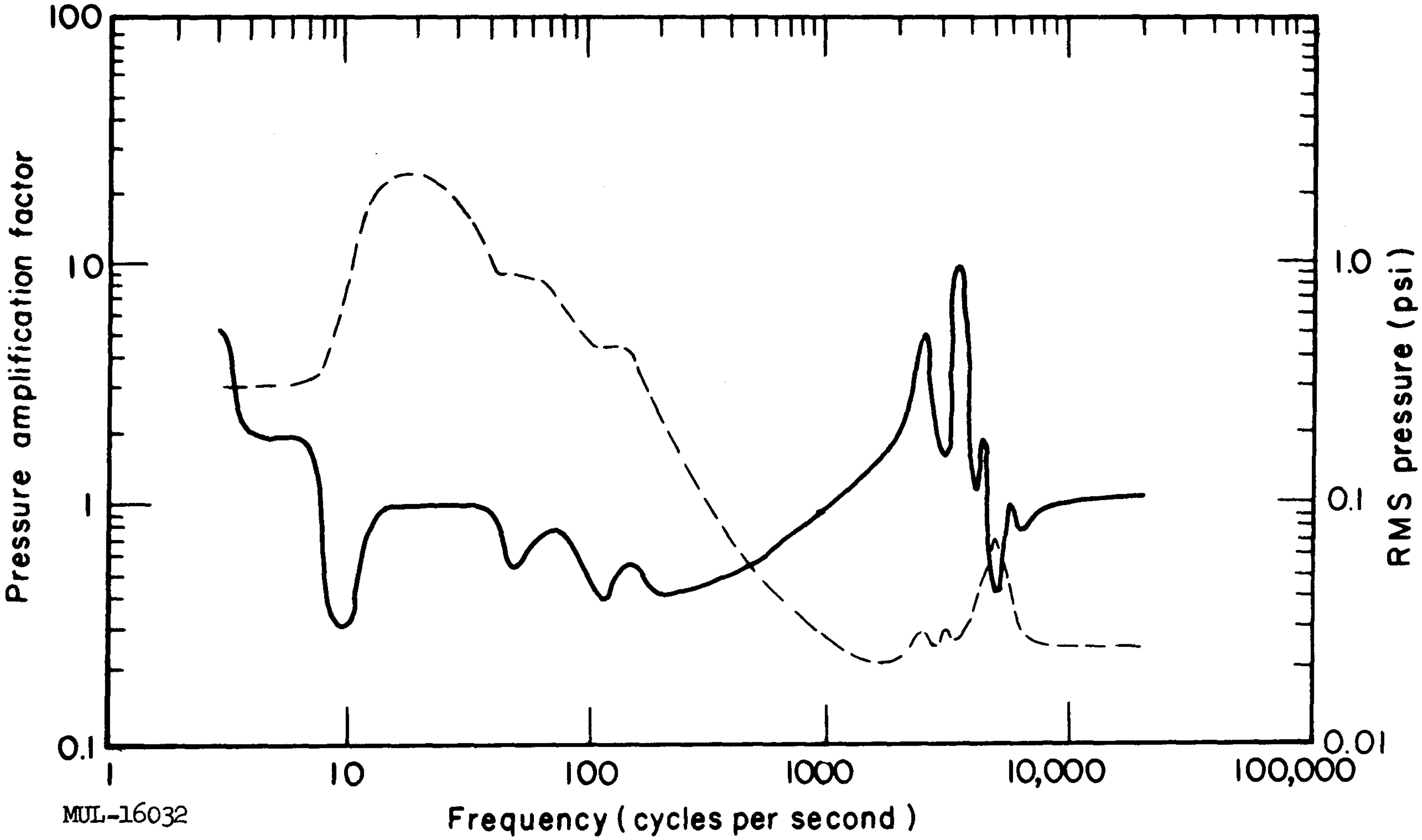

Fig. IV-67. Pressure amplification (ratio of downstream to upstream pressures, solid curve, left-hand scale) and upstream pressure (dashed curve, right-hand scale) as functions of frequency. From noise level measurements made immediately upstream and downstream of unit cell.

visible in the center of Fig. IV-68, together with the calibration strip and its instrumentation. The calibration strip was cut from the same sheet as the spring. The annulus contains three sets of springs and associated hardware forward and aft of the spring shown.

Figure IV-69 shows the test arrangement. The annular section is contained in the pressure vessel. Infrared cameras are positioned on each side, viewing the test through quartz windows. Densitometer traverses of the infrared negative can determine the local temperature to an accuracy of 4 to 5%. From the measured temperature distribution, radiation and conduction losses can be determined at any point. Voltage and current measurements across the springs determine the rate of heat generation. From this information the amount of heat removed by convection can be determined at any point.

The convection heat transfer mechanism governing this situation is assumed to be governed by a Colburn-type correlation:

$$q/A = \phi \frac{\dot{W}^{0.8}}{D^{1.8}} \frac{T_b^{0.8}}{T_f^{0.56}} (T_f - T_b),$$

where q/A = rate of heat removal (Btu/hr-ft^2),
$\dot{W}$ = air flow rate (lb/sec),
D = hydraulic diameter of the passage (ft) (arbitrary size factor),
T_b = air bulk temperature (°R),
T_f = local average of wall and bulk temperature (°R),
ϕ = local geometric factor.

Although each spring leaf is cooled on two sides, this effect cannot be separated in this test. The effect on both sides is lumped into one parameter as if cooling took place on one side only.

One brazed spring design has been tested so far, and other designs will be tested in the near future.

The results for the brazed spring were as follows:

Reactor side: $\phi_{mean} = 0.166$
$\phi_{max} = 0.382$
$\phi_{min} = 0.0764$
Duct side: $\phi_{mean} = 0.167$
$\phi_{max} = 0.220$
$\phi_{min} = 0.113$

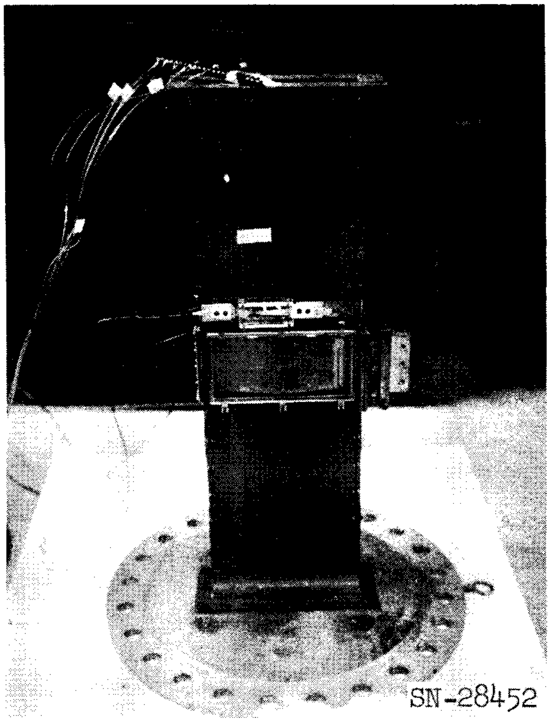

SN-28452

Fig. IV-68. Annular flow test assembly.

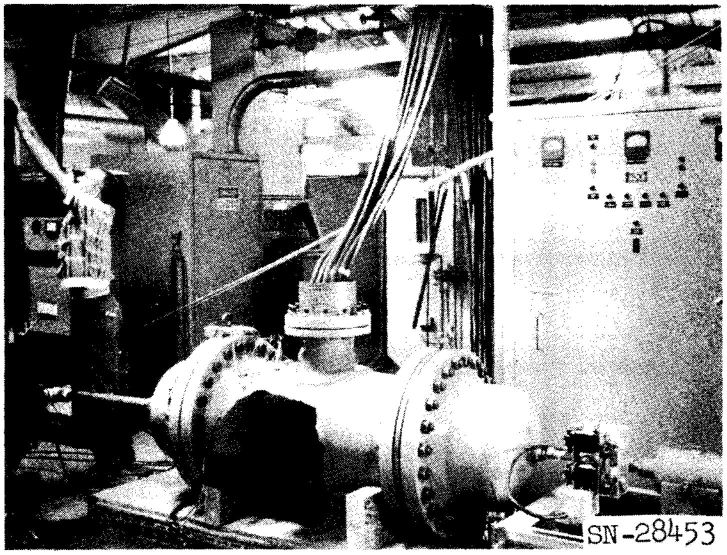

SN-28453

Fig. IV-69. Annular flow test setup.

Although the average values of the coefficient are almost identical for two leaves of the spring, the wide range of values on the reactor side is indicative of severe hot spots due to flow separation around supports, etc. These patterns are easily visible in the accompanying photographs (Fig. IV-70 and IV-71) where flow conditions and extremely high contrast printing have been used to exaggerate conditions.

Figure IV-71 shows the reactor side of the spring, and Fig. IV-70 shows the duct side. In each case only half of the spring is shown, the midpoint of the spring being toward the top. Flow symmetry was easily confirmed by visual observation. The calibration strips are visible behind their quartz windows (identical to the spring window). Flow in each picture is from the direction of the calibration strip. The lower hot spot is the brazed region where only one side of the leaf is available for cooling. The upper hot spot is due to a guide pin arrangement and interior flight spring (not visible).

SLICE TEST ASSEMBLY

Much effort during this quarter was devoted to study of the dynamic response of the side-support/reflected-core assembly. This study was required since the calculated low translatory mode was not observed in previous vibration tests of the slice test assembly (see UCRL-6625, p. 181 ff.). In addition, no information was available on the damping factors present in the system.

To study the side-support system dynamics alone, the steatite tubes in the slice test assembly were replaced by a rigid steel ring having the same diameter and weight as the steatite core. This assembly in position for test is shown in Fig. IV-72. Concurrently the steatite tubes were being used for dimensional studies with newly installed peripheral shims. The shims are accurately machined aluminum parts which simulate the nickel shims to be used in the reactor. The aluminum shims and steatite tubes can be seen in Fig. IV-73.

A series of transient dynamic tests were made on the side support system/rigid core assembly. The tests were of two types. In one test the ring mass was raised while the side support system was held fixed. The ring was instantaneously released and the resultant dynamics observed. In another test the entire test assembly was raised eight inches and instantaneously released. The test assembly impacted on a paper "hexcell" cushion. The paper hexcell was triangular in shape to give a sawtooth force input. Results from the first type

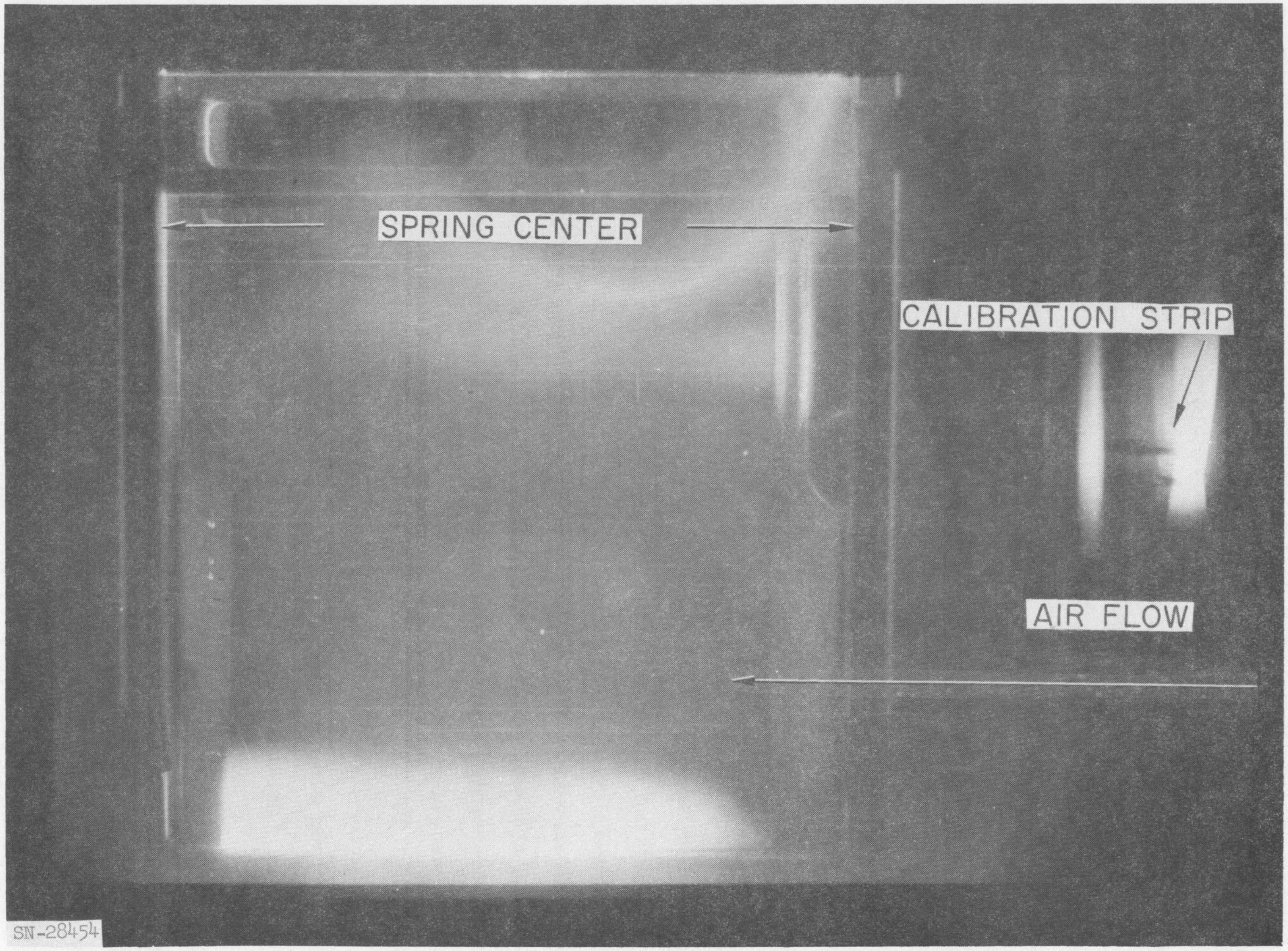

Fig. IV-70. Duct side, annulus flow test.

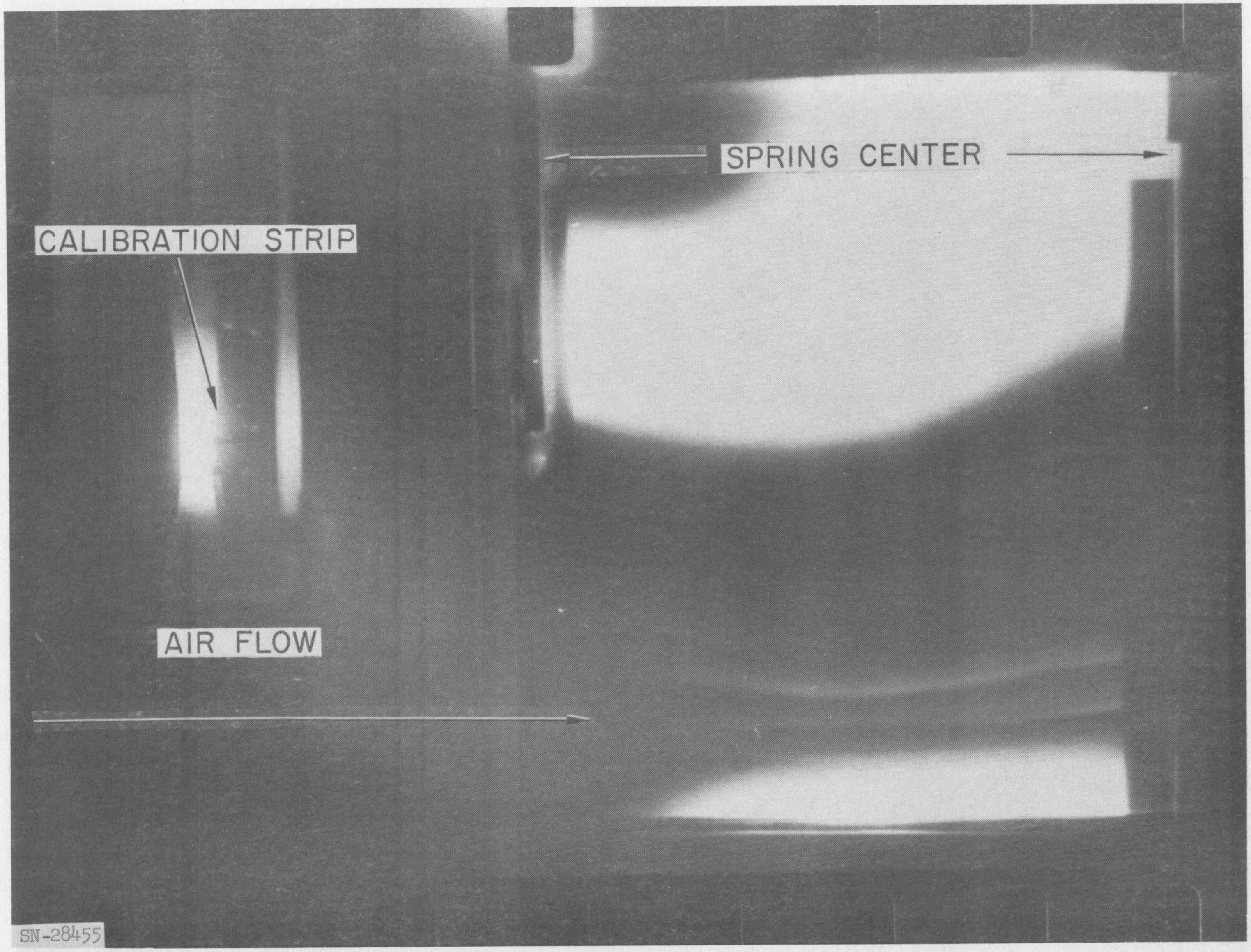

Fig. IV-71. Reactor side, annulus flow test.

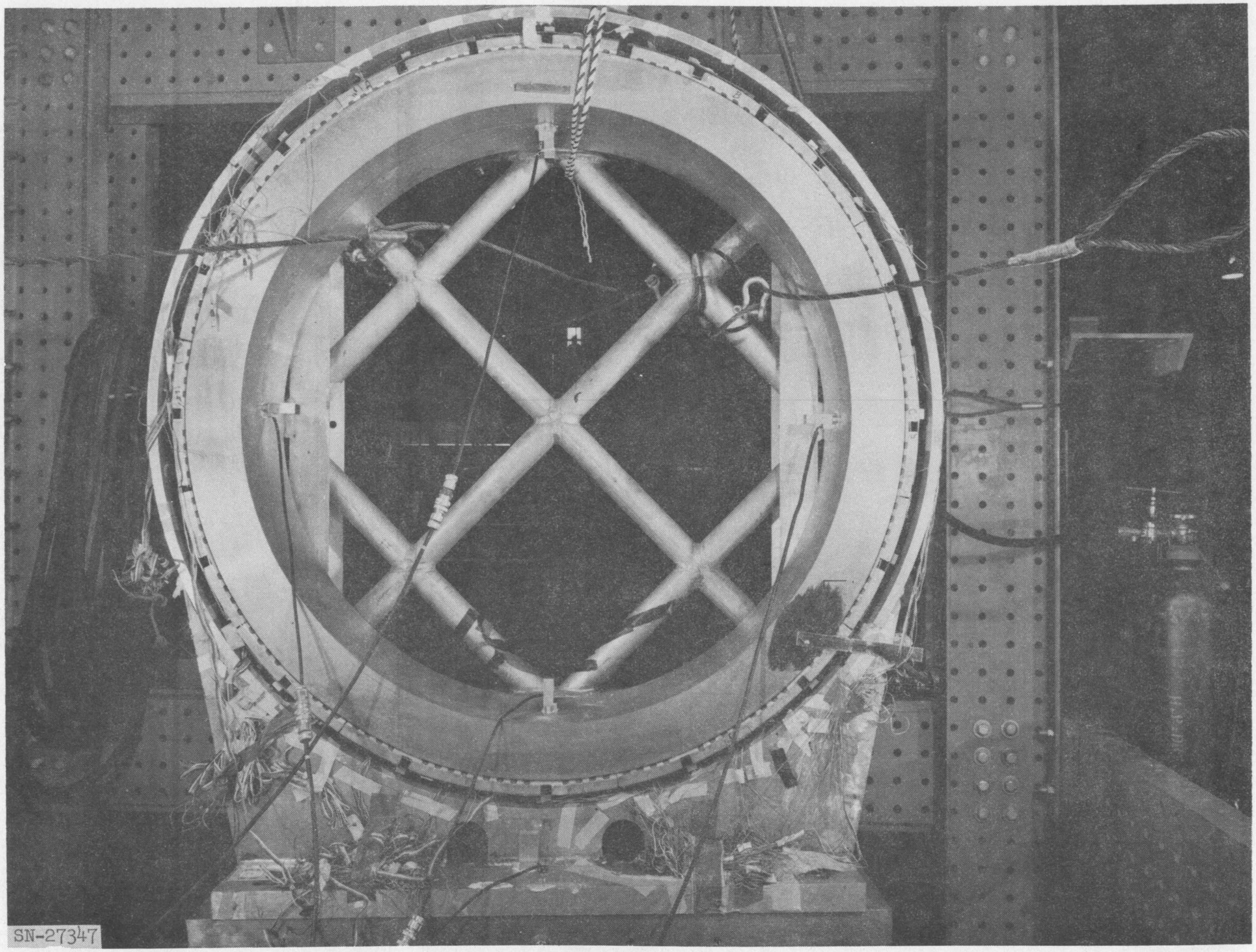

Fig. IV-72. Tory II-C full-scale cross section, rigid mass test.

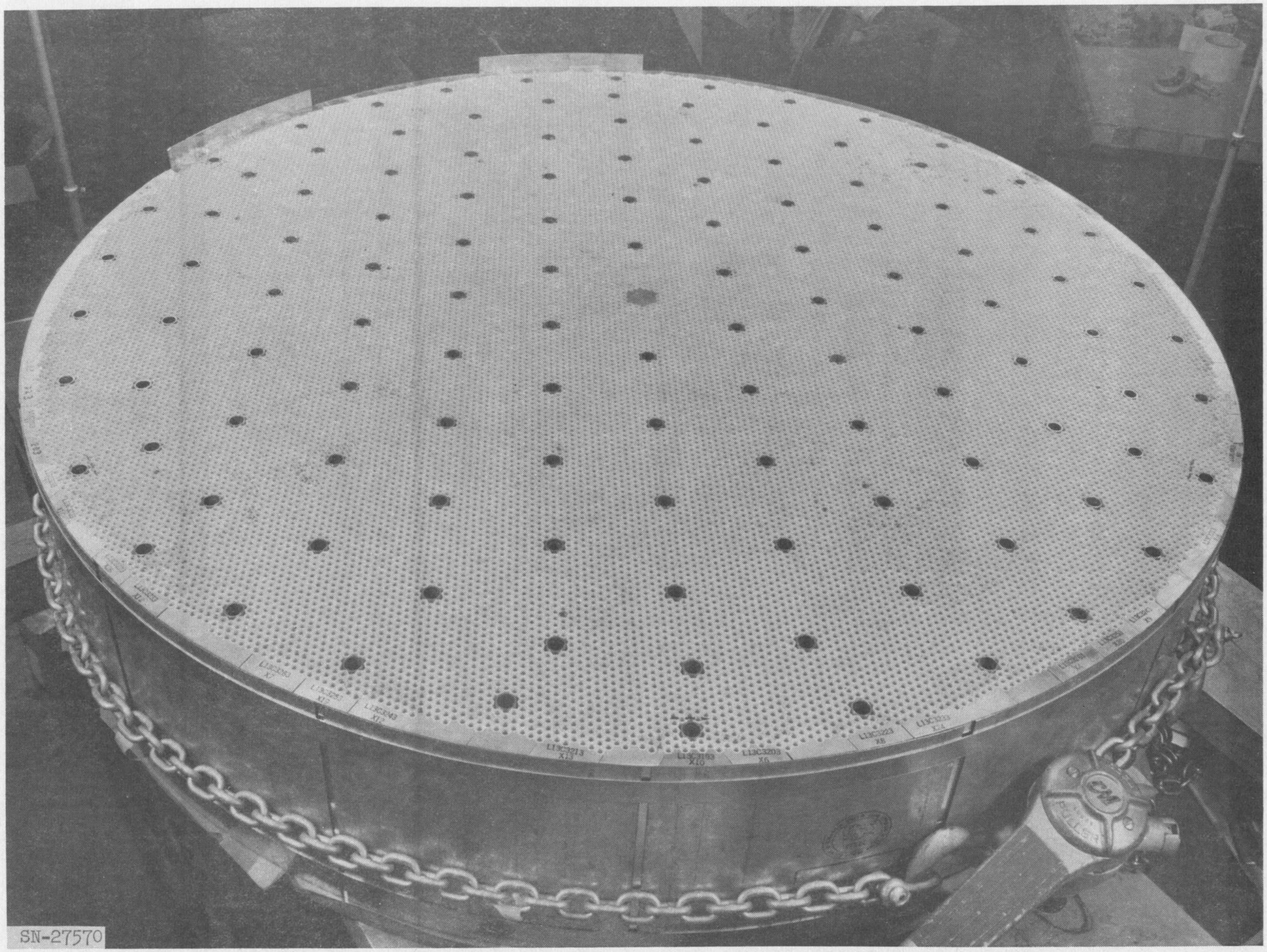

Fig. IV-73. Full-scale cross section with aluminum shims added.

of test are much easier to analyze. In both tests a rapid smooth release was obtained by using a bomb release mechanism.

Figure IV-74 shows some results obtained in the first type of test. The traces give the position of the ring as measured with two transducers. The damping observed is apparently only dry friction, estimated to be 25 $\text{lb-sec}^2/\text{ft}$. The natural frequency is approximately 16 cps. This mode is highly damped.

Figures IV-75, IV-76, IV-77 show results from the second type (drop) test. The peak acceleration was 3-1/2 to 4 times gravity.

A 5-inch-thick full-diameter cross section of the reflected core was assembled using 5-inch-long steatite tubes and thin, machined aluminum shims. This assembly was used for further studies of dimensional buildup and core stiffness. The assembly is shown in Fig. IV-78.

The distance across 165 tubes was measured along three diameters with no radial pressure on the assembly. The measurements gave this dimension to be 49.600 to 49.630 inches. Similar data from the 10-inch-thick assembly used in the dynamic tests at 3-psi radial pressure gave 165 tube dimensions varying between 49.530 and 49.600 inches. The effective mean tube across-flats dimension based upon these data ranges from 0.3002 to 0.3008 in.

A statistical sample (1624 tubes) of the steatite tubes used in these assemblies was measured for camber and flat dimensions. The results are shown in Figs.IV-79 and IV-80 and as probability distribution functions. The individual mean tube across-flats dimension is 0.2986 in. Thus there is an effective increase of 0.0016 to 0.0022 in. in the size of these tubes. This increase is due to (1) camber, (2) frictional effects, (3) across-flats dimension tolerance, and (4) twist. A statistical analysis shows that camber accounts for 0.0014 in. The distribution of across-flats dimensions accounts for another 0.0002 in. in buildup.

TUBE CRUSH

The ability of the LRL fuel elements to resist stress for a 10-hour period has been measured at 1100, 1800, and 2200°F. The specimens were 1-inch-long sections of fuel elements loaded on opposite flats. Initially, the short-time strength was determined; subsequent tests were to find the portion of this stress which the material would withstand for 10 hours.

Since all specimens were 1 in. long the nominal bearing area was about 0.173 in^2. The short-time strength of these specimens loaded across opposing

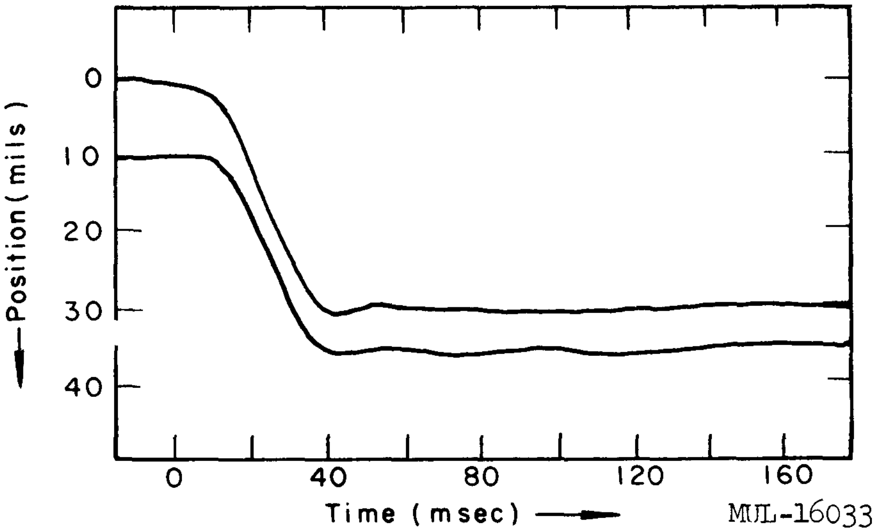

Fig. IV-74. Tracing of oscillogram from transient dynamic test type 1 (ring mass raised and released, side support system fixed).

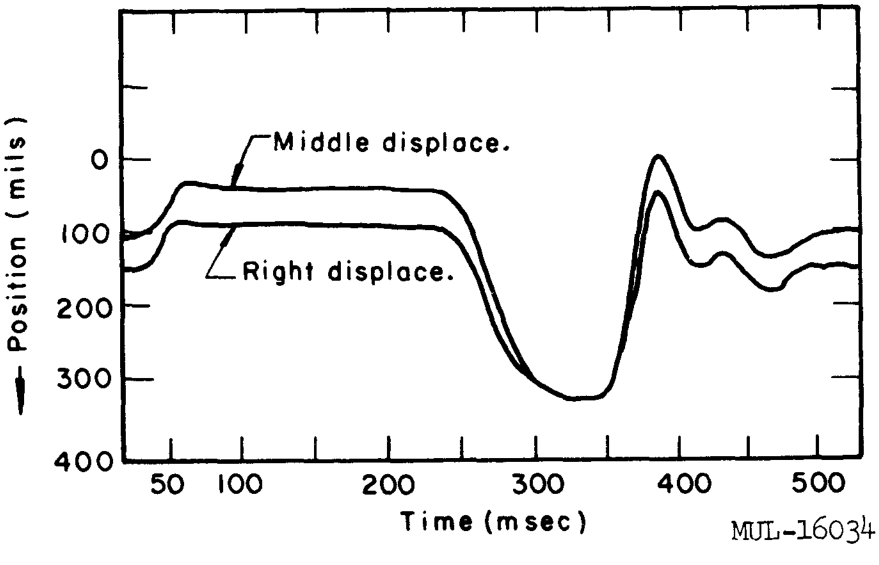

Fig. IV-75. Tracing of oscillogram from transient dynamic test type 2 (entire assembly raised and dropped).

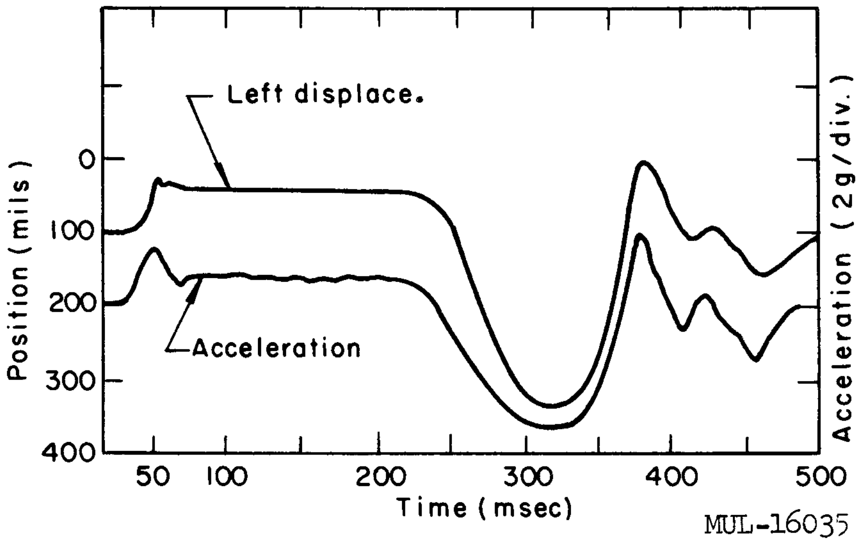

Fig. IV-76. Tracing of oscillogram from transient dynamic test type 2 (entire assembly raised and dropped).

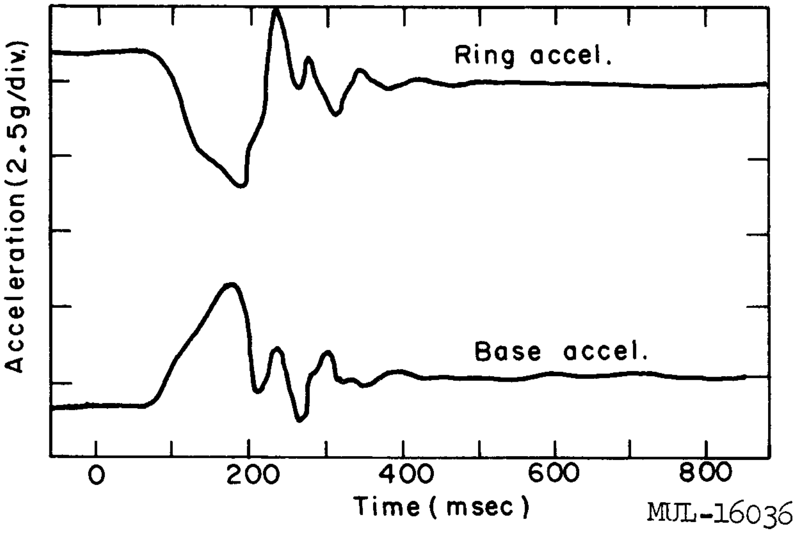

Fig. IV-77. Tracing of oscillogram from transient dynamic test type 2 (entire assembly raised and dropped).

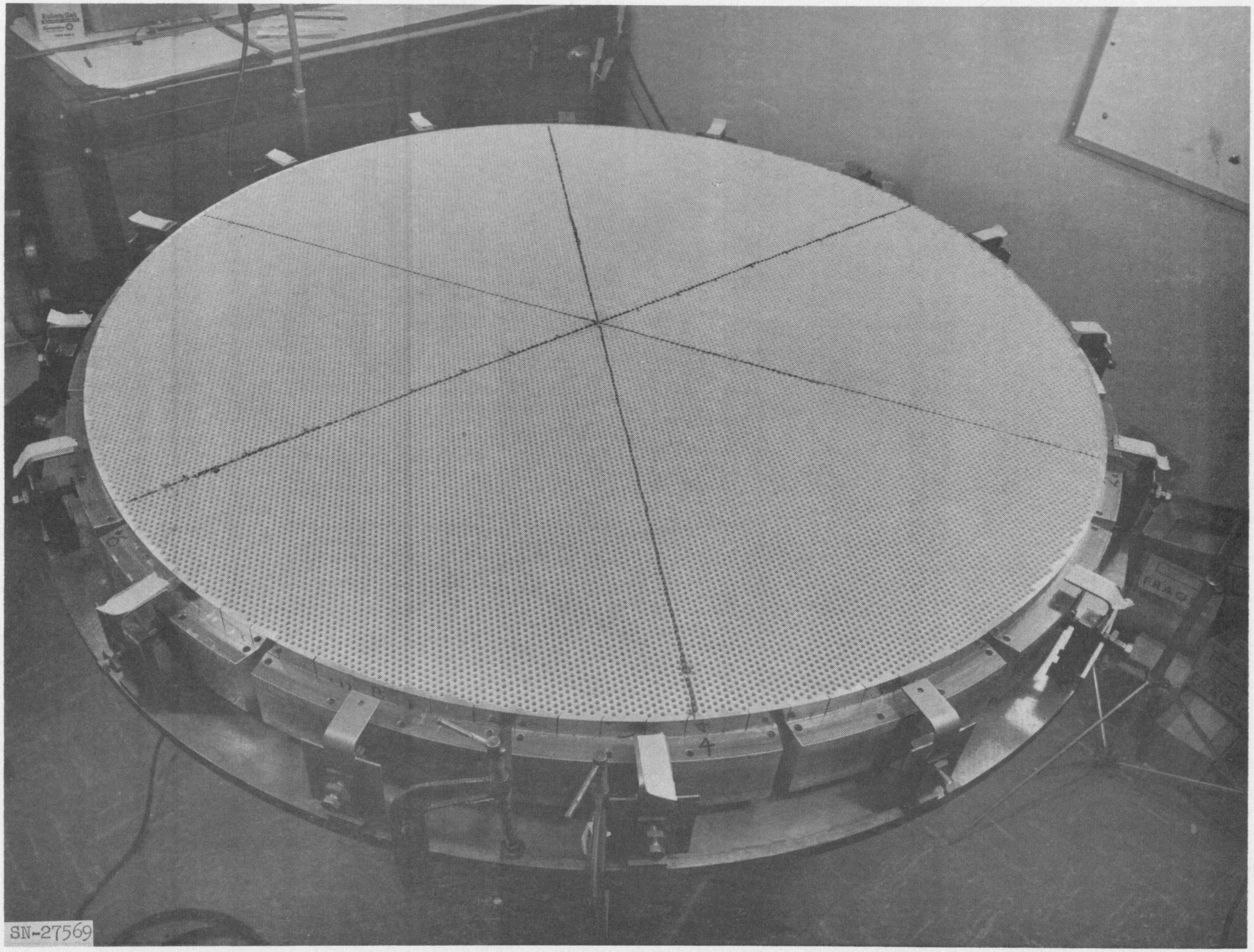

Fig. IV-78. Tory II-C 5-inch full-scale cross section.

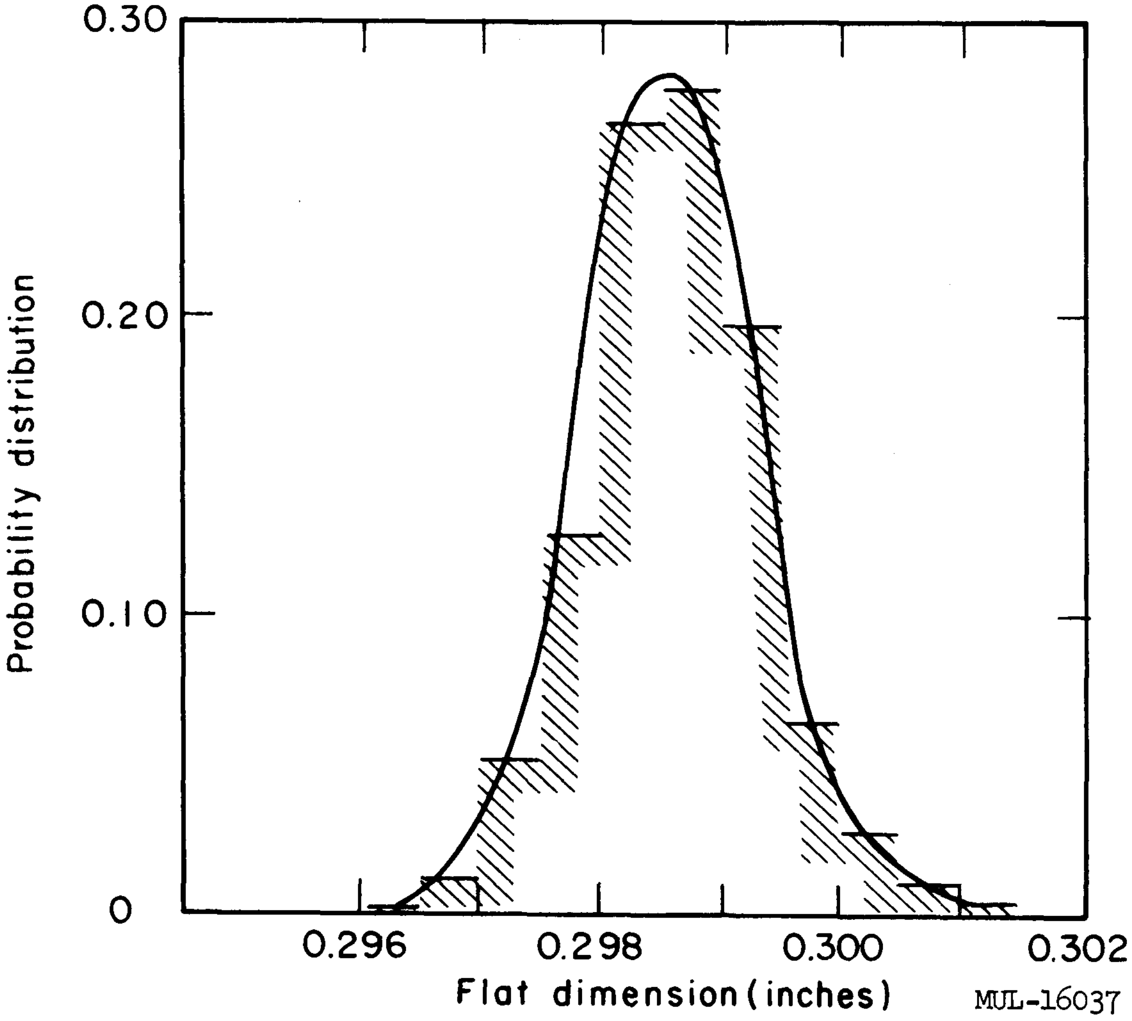

Fig. IV-79. Probability distribution for flat dimension of steatite tubes; 1624 tubes measured.

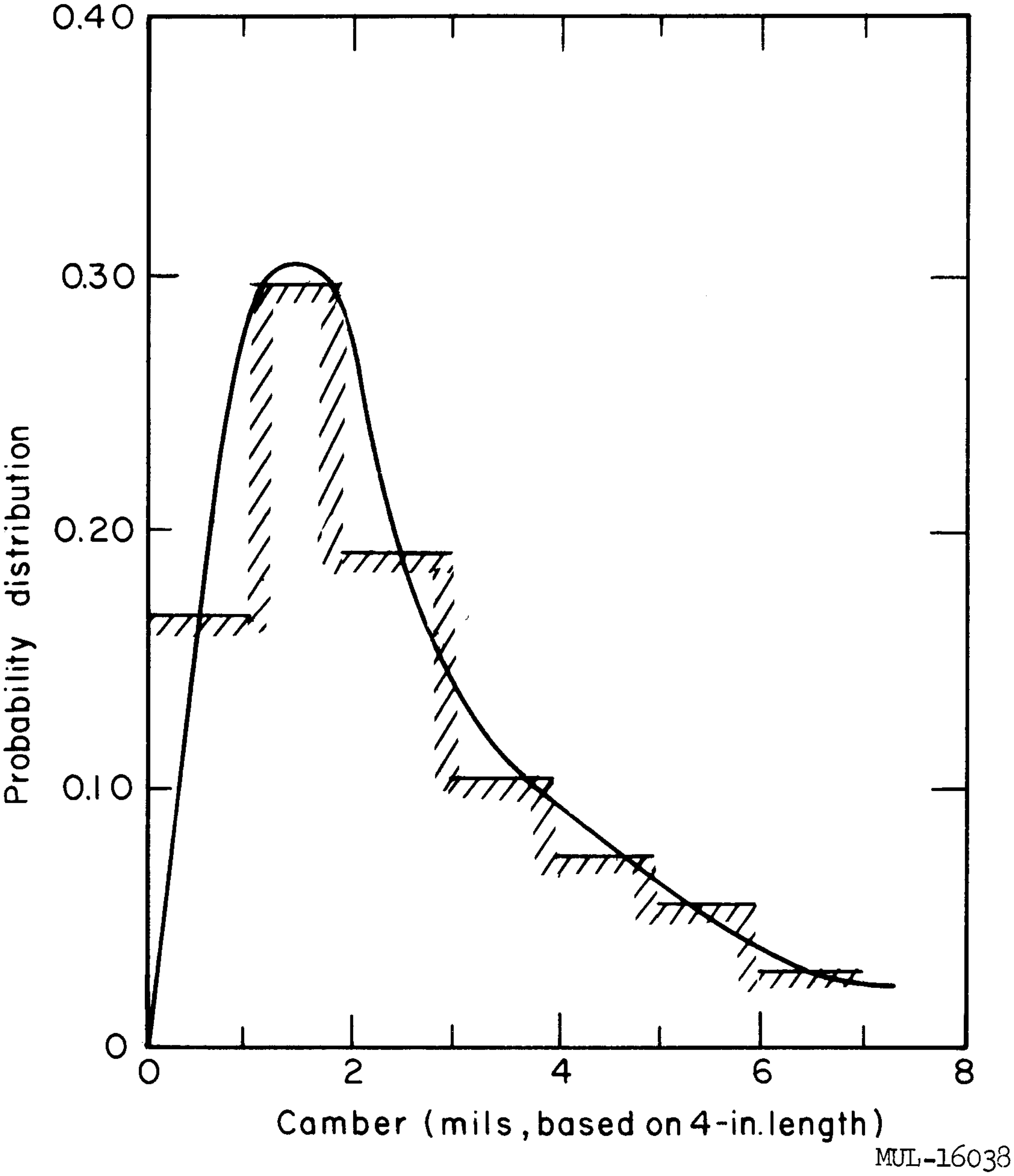

Fig. IV-80. Probability distribution for camber of steatite tubes; 1624 tubes measured.

corners was measured. The various fixtures for these experiments are shown in Figs. IV-81 through IV-84.

The tensile stresses induced in the case of opposite-flat loading are estimated from photoelastic results. In Fig. IV-85, the short-time strength data are presented in terms of load, bearing pressure, and estimated tensile stress. The next figure (IV-86) shows the results of testing specimens at various fractions of the short-time fracture load for a period of 10 hours. From these graphs a rough estimate can be obtained of the maximum allowable load for 10-hour survival at various temperatures. The ordinate in Fig. IV-86 includes the results of all test run up to and including the value of P/P_s for which the point is plotted. Thus, as a rough estimate, 0.3 of the short time ultimate load will cause few or no failures for 10 hours at 1200°F. One might similarly guess at a value of 0.2 for 2250°F.

The tests in 3-flat and 2-corner loadings resulted in very high loads and high fixture mortality. These were also run on 1-in.-long specimens:

Orientation	Temp (°F)	Load (lb)	Result
3-flat	Room	2250	Broken load ram (alumina rod)
"	1400	2325	" " " " "
"	1400	1925	" " " " "
"	1400	1505	Broken specimen
"	1400	1250	Broken specimen
2-corner	1800	395	Broken specimen
"	1800	390	" "
"	1800	384	" "
"	1800	1165 lb	Broken specimen and rod
"	2250	750	Broken ram
"	2280	420	Broken fixture

It is possible that in the 2-corner loading at high temperatures, slight yielding resulted in a horizontal thrust load giving an arch stability to the fuel element and producing failure in the apparatus.

TEST VEHICLE

Considerable progress has been made in the design and fabrication of the test vehicle which will carry the Tory II-C reactor. A photograph of an approximate model is shown in Fig. IV-87.

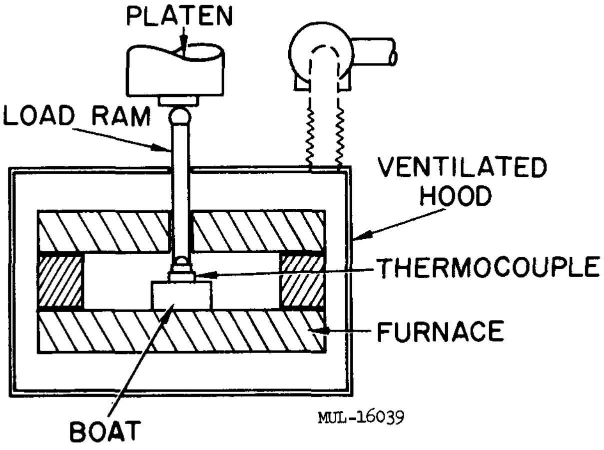

FIG. IV - 81
SCHEMATIC OF TEST EQUIPMENT

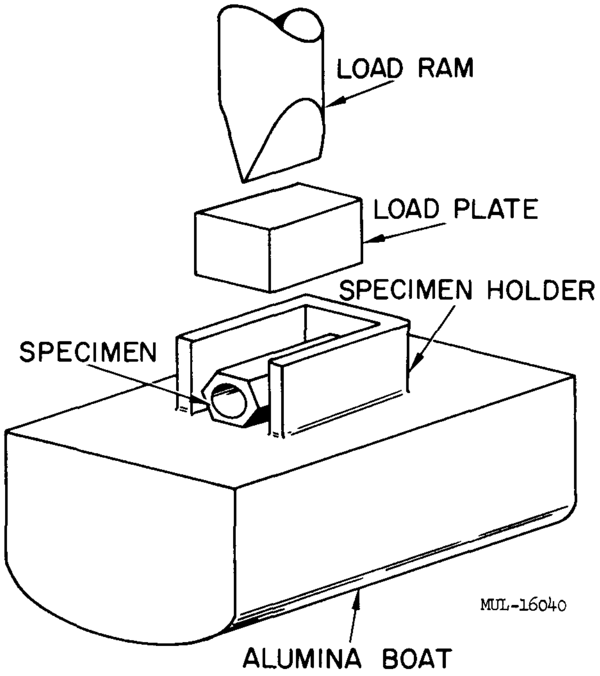

FIG. IV -82
DETAIL OF 2-FLAT LOADING

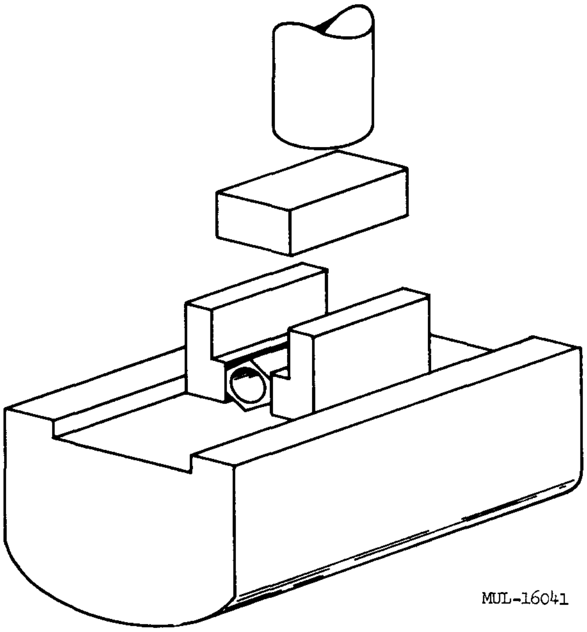

FIG. IV -83
DETAIL OF 2-CORNER LOADING

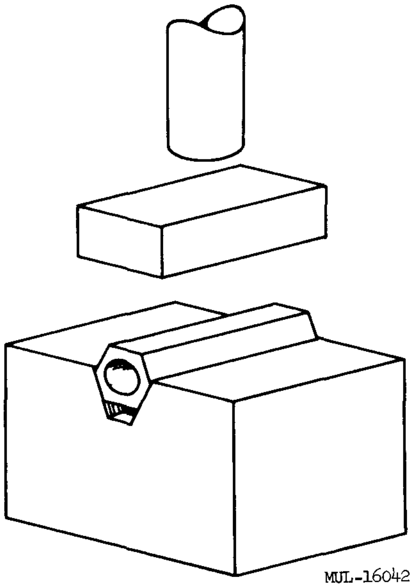

FIG. IV -84
DETAIL OF 3-FLAT LOADING

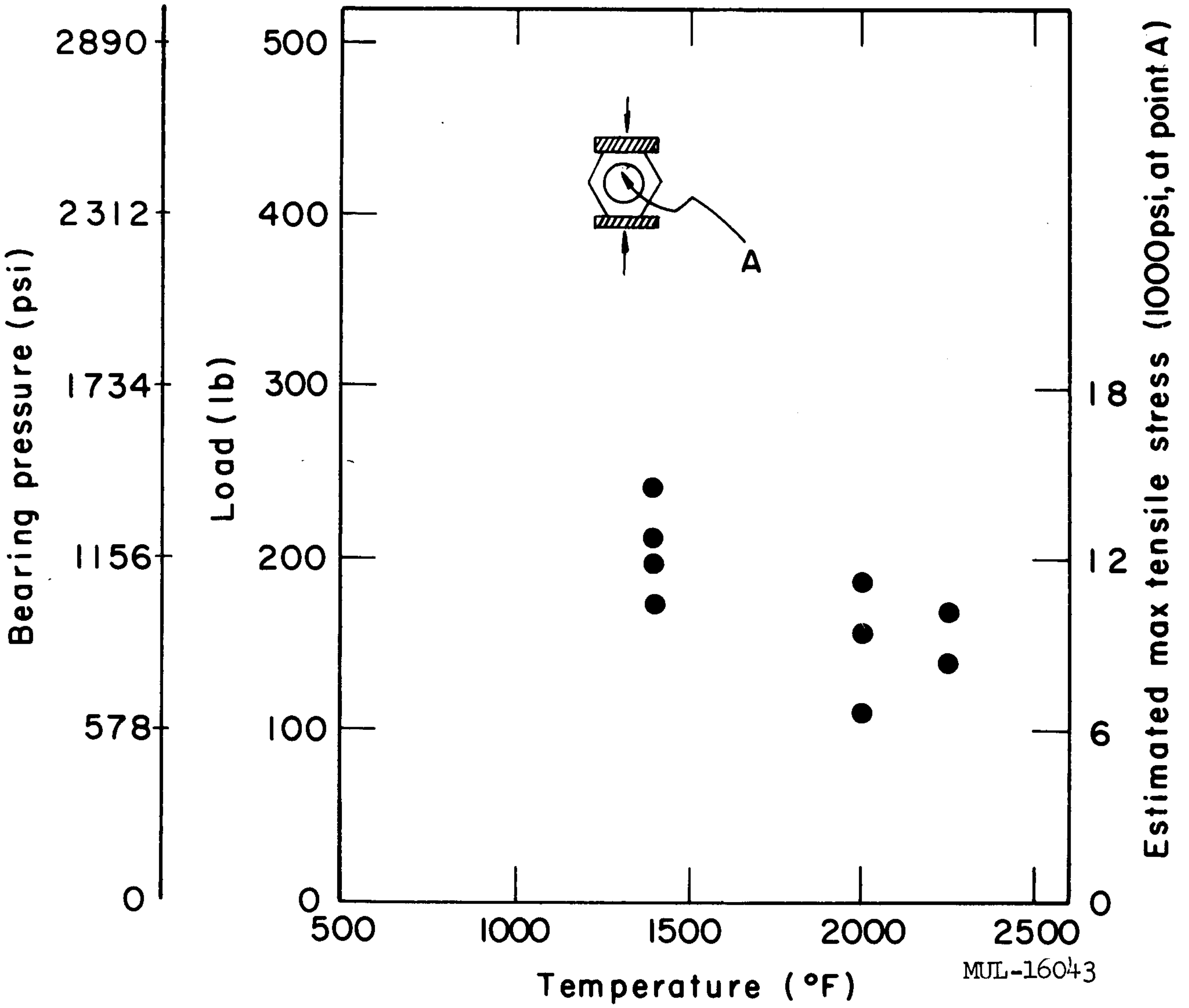

Fig. IV-85. Short-time strength vs temperature for 2-flat loading of fuel element tubes. Specimens 1 in. long, bearing area 0.173 in^2. Mean load values: 1400 °F, 210 lb; 1800 °F, 230 lb; 2000-2250 °F, 150 lb.

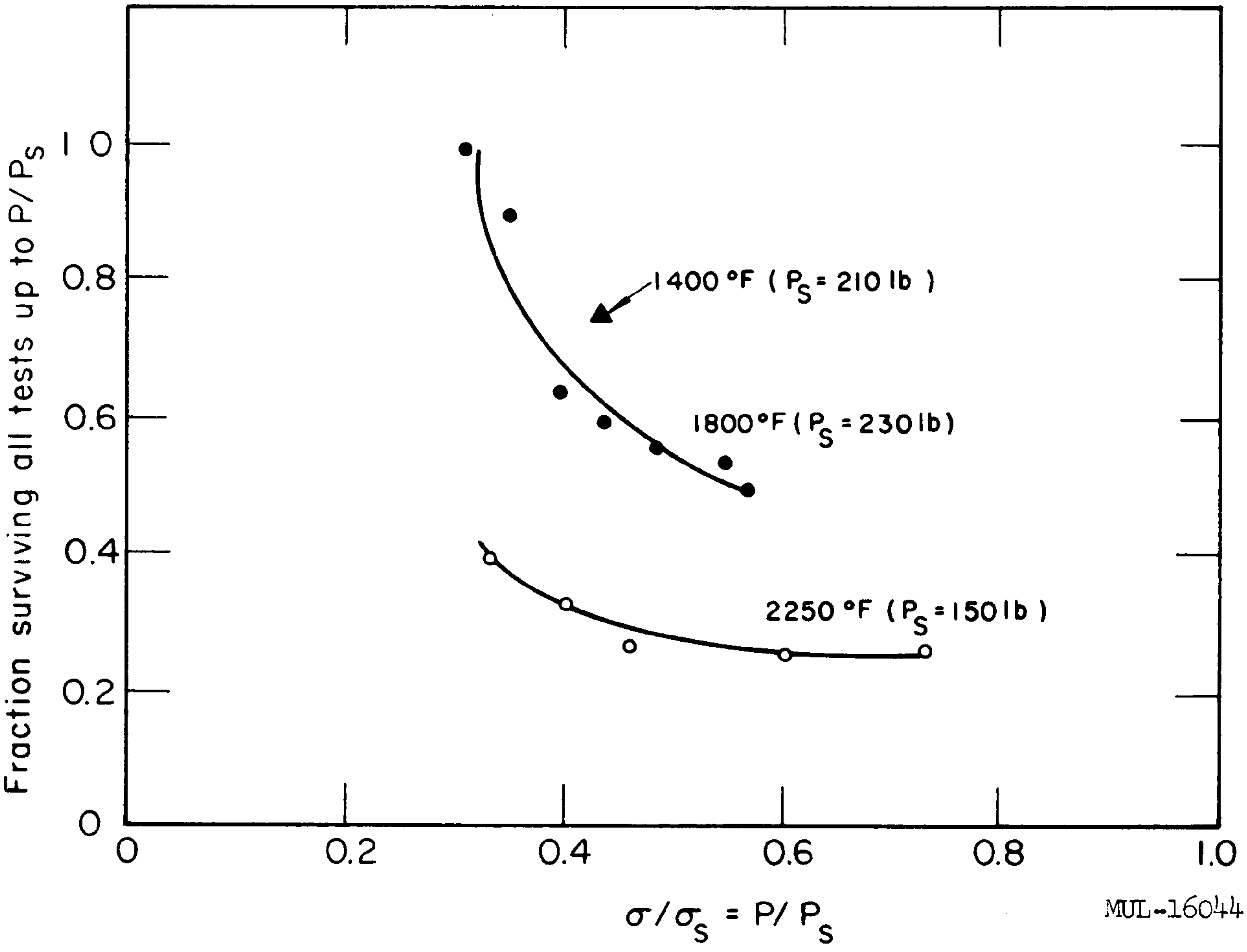

Fig. IV-86. Effect of long-time (10-hr) 2-flat loading of fuel element tubes. Fraction of specimens surviving test is expressed as a function of the ratio of long-time applied load (P) to short-time ultimate load (P_s). Specimens 1 in. long, bearing area 0.173 in^2.

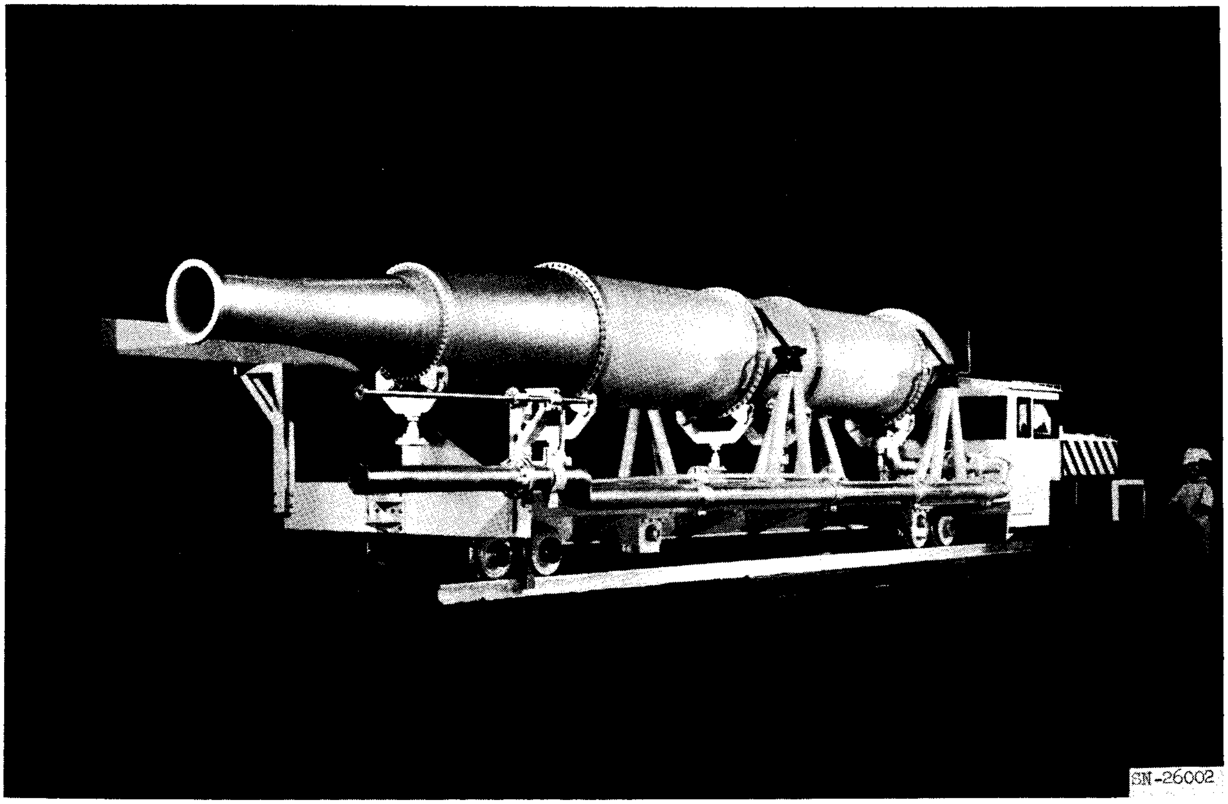

Fig. IV-87. Photograph of model of Tory II-C test vehicle and locomotive. The model is nearly authentic in scale and detail, except for outrigger wheel assemblies. The doll represents a 6-ft man.

The basic flat car is similar to the one used to transport the Tory II-A-1 reactor. The car is of standard railway car design and all-welded construction suitably reinforced to withstand anticipated loads. Overall length is 34 feet. Overall width is 10 feet. It is mounted on two standard-gage four-wheel swivel trucks. Power braking is supplied to all four wheels of the rear truck.

The upper deck and supporting transverse frame members are designed to resist the loads imposed by the duct assembly through the support stands. Four outrigger support wheels located directly under the support stands ride on a pair of outrigger rails. These support wheels provide vertical alignment of the duct assembly with the supply duct in the bunker. Four rollers provide lateral alignment in a similar manner. Adjustable support jacks are located above the deck to assist in assembly of the duct sections. The car is being fabricated at present.

The trucks and brake system have been completed. The brake system consists of spring-loaded brake shoes which are released only upon application of gas pressure from a standard gas cylinder attached to the car. Brake release requires an electrical signal from the locomotive to a 3-way normally-closed solenoid valve. This energizes the valve, admitting compressed air or nitrogen into the brake cylinders. A schematic of the brake system is shown in Fig. IV-88.

TEST VEHICLE WIREWAY

The wireway enclosure is a steel trough divided into three longitudinal compartments. It is covered with a series of separate lids which allow access to cables at any point. The forward portion of the wireway contains terminal connections. Some detail of the wireway can be seen in Fig. IV-87. The wireway is already fabricated.

DUCT SYSTEM

The duct system has been designed. Hastelloy C plate is being inspected and cut to size in preparation for forming the duct sections. Some ring-rolled forgings for flanges have been received.

The evaluation of Hastelloy C has been completed. The welding and heat treat schedules which have developed from this study call for welding by the metal-inert gas (MIG) method followed by solution-annealing of the assembly at 2125°F and water quench.

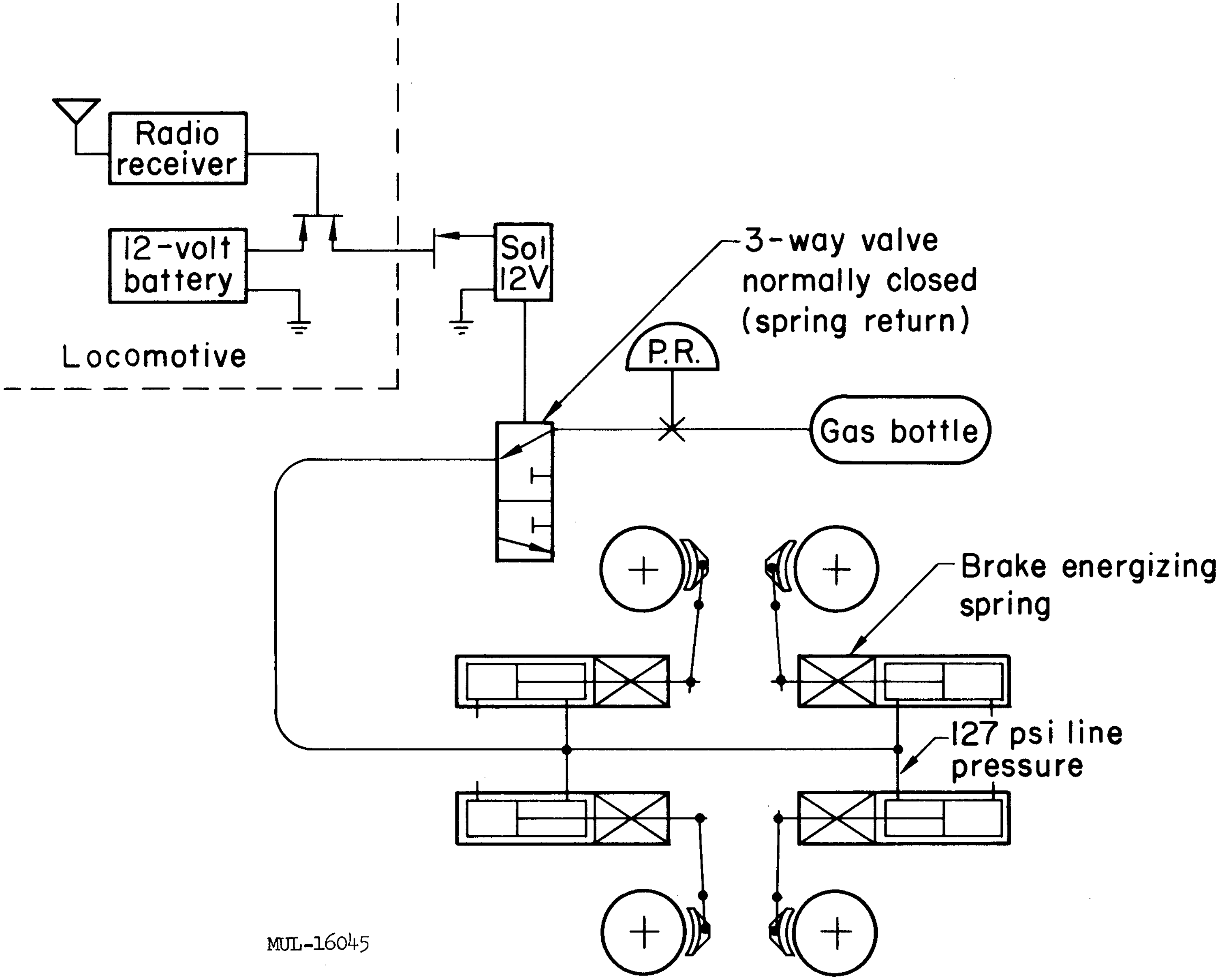

Fig. IV-88. Schematic of fail-safe brake system for Tory II-C test vehicle.

PLASTIC STRAIN FATIGUE TESTING

Bending fatigue tests at elevated temperatures and high (beyond yield) strain levels have been run on specimens of SS 347 and Hastelloy C. The purpose of these tests is to establish a convenient method to gather engineering data for service in a thermal-strain fatigue environment; i.e., the case of constrained members subject to thermal cycling, as in the Nevada blowdown facility and reactor ducting. Evidence is presented in the literature [L. F. Coffin, Jr., Trans. ASME 76, 923 (1954)] to the effect that the lifetime of SS 347 specimens subject to thermal cycling fatigue is effectively the same when mechanical strains are induced at a mean temperature; i.e., the mean of the temperature cycling. The first tests, on SS 347, were to corroborate Coffin's results. Figure IV-89 shows Coffin's curve and three points which have been obtained to date. It is possible that Coffin's specimens had a rougher surface finish which would account, in part, for their shorter lifetimes. It should be noted that Coffin's curve is for axial loading which generally exhibits slightly lower lifetimes than bending fatigue.

Figure IV-90 shows the specimen geometry. This assembly is placed in a furnace and mounted on support shafts. Because of the four-point-flexure loading geometry, the maximum strain level in the cross section is constant over the test section.

Three runs have been made on Hastelloy C specimens subjected to the following double solution heat treatment after machining, as is currently planned for the Tory II-C air ducting:

2125 ± 25°F for 2 hours, rapid air-cool;
2125 ± 25°F for 2 hours, rapid air-cool.

The following results have been obtained with these specimens with a bending strain range of 5000 microinches per inch (±2500):

Temp (°F)	N	Remarks
600	80,000	Specimen undamaged; run was stopped.
1000	214,000	Specimen undamaged; run was stopped.
1200	10,000	Fractured in test section.

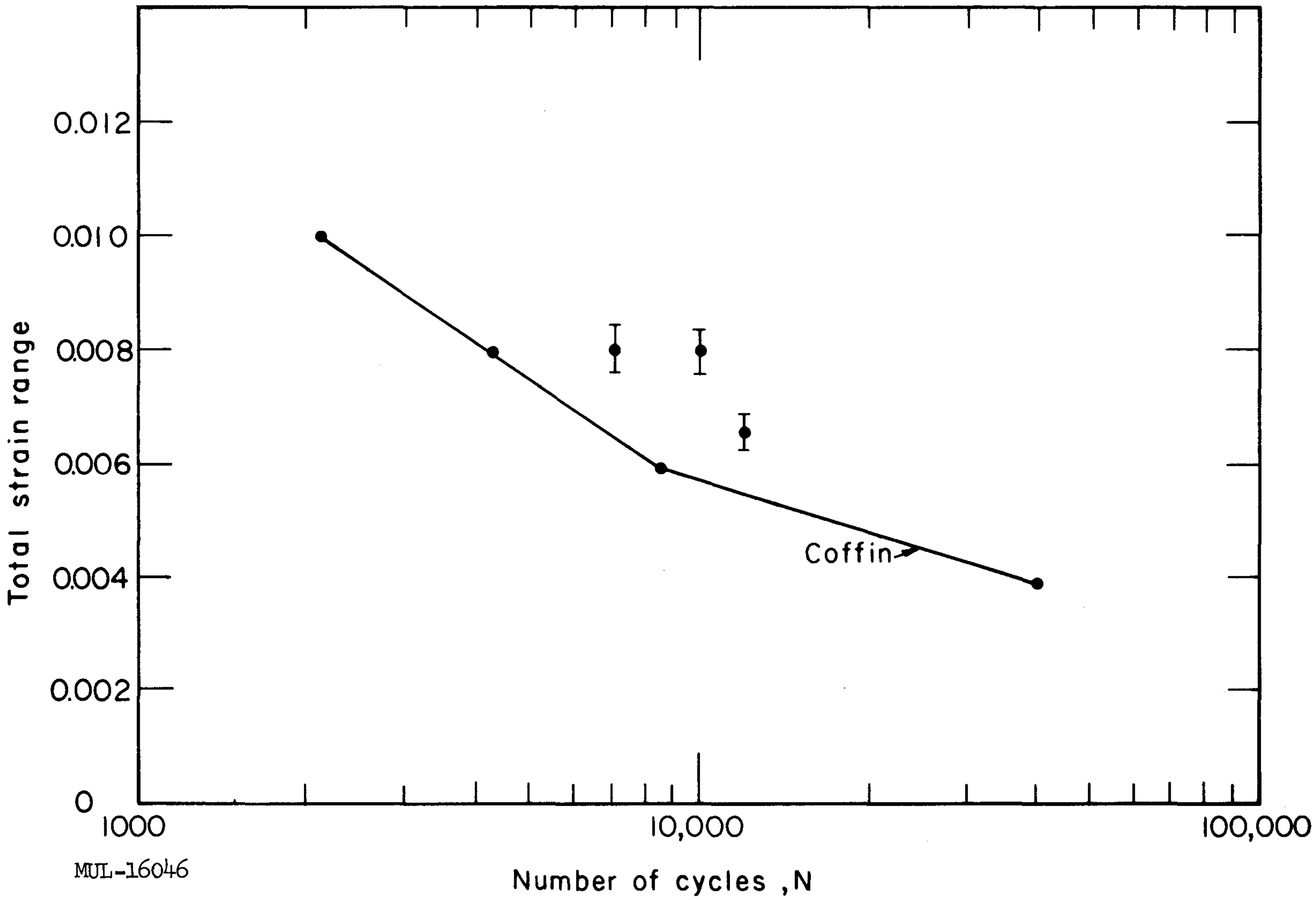

Fig. IV-89. Bending fatigue tests at 660 °F for SS 347. Total strain range is plotted as a function of number of bending cycles, N, which were at the rate of one per second. Coffin's results are shown for comparison. Specimen is detailed in Fig. IV-90; surface finish ~8 rms.

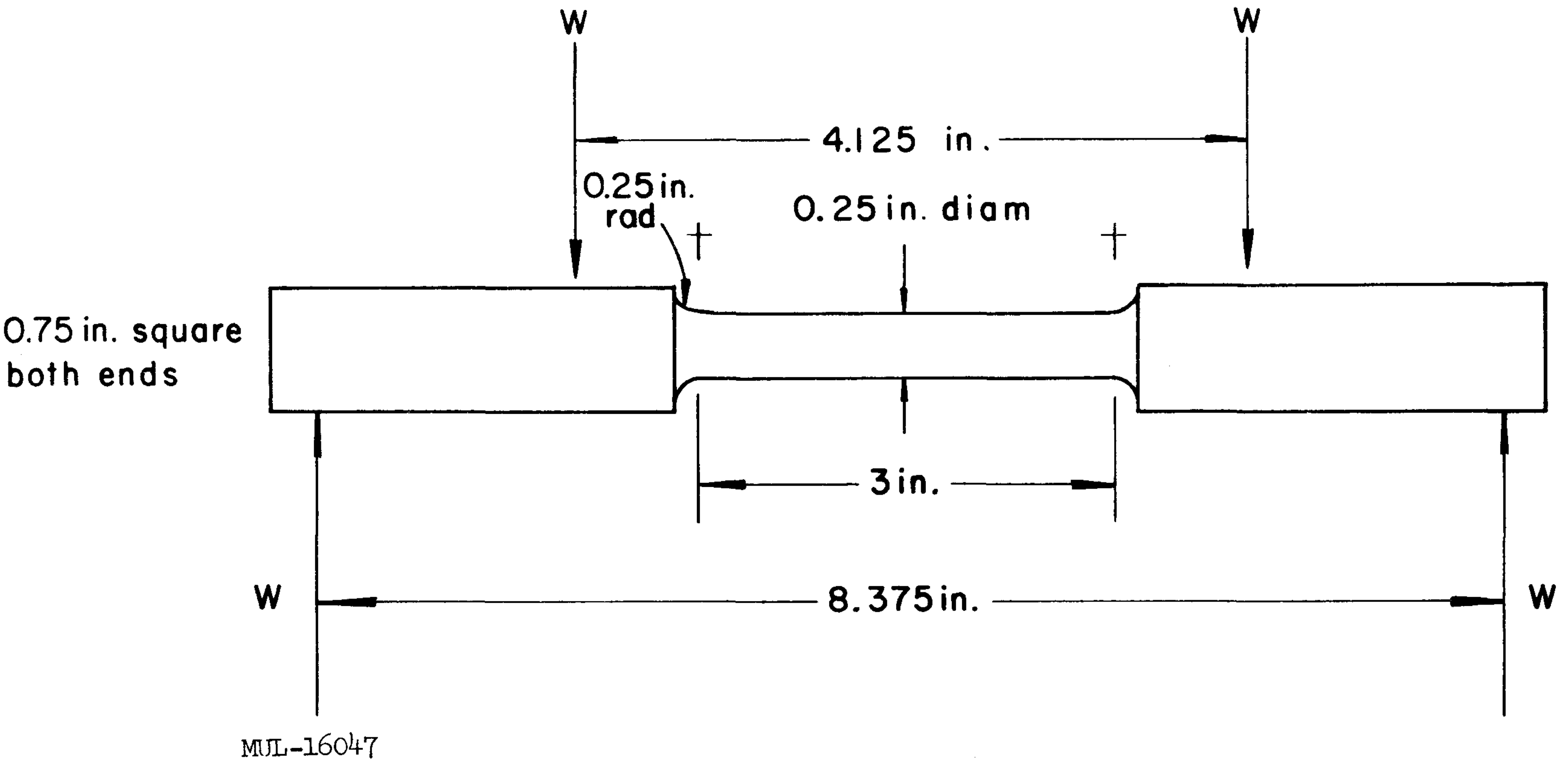

Fig. IV-90. Dimensions of SS 347 specimens used in bending fatigue tests of Fig. IV-89.

CHAPTER V. TORY III.

SECTION I. ENGINEERING

AXIAL SUPPORT STRUCTURE ("DOME") FABRICATION DEVELOPMENT

A 36-in. prototype silicon carbide dome assembly has been completed. It is composed of seven segments of dense fired KT silicon carbide, and is intended for use in elevated-temperature environmental and structural testing. The test conditions to be explored will include loadings of as much as 300,000 lb under both static and dynamic conditions in an oxidizing atmosphere at temperatures up to 2750 °F for a total duration of about 30 hours. Fig. V-1 shows the two segment types. Figures V-2 and V-3 show a partial and a complete dome assembly, respectively.

Fabrication of the component parts was accomplished jointly by LRL and the supplier. Initially, green die-pressed compacts 18 in. in diameter consisting of epoxy-resin-bonded silicon carbide and graphite particles were prepared and cured by the supplier.

These were then shipped to LRL for the primary machining operations. After rough cropping to shape on a diamond edge band saw, the slugs were partially imbedded in a plaster potting fixture and external contours were ground with diamond grinding wheels on a vertical boring mill (Fig. V-4). The contoured parts were then completely potted in plaster-filled split tooling molds and the flow holes were bored on a horizontal boring mill using air-cooled diamond core drills. A tilting head rotary table was used to index the compound angles of the bores. This operation is shown in Fig. V-5. Grinding of the step detail on the upper face of the part was done with diamond routers mounted in a tool post grinding head quill (Fig. V-6), the parts being mounted on a rotary table. Upon completion of the machining operations, the parts were stripped of potting compound, inspected with the aid of fluorescent penetrant (Fig. V-7) and shipped to the supplier for firing and finish-machining.

The green machined parts were first baked at temperatures up to 580 °C to graphitize the epoxy binder and then mounted on porous graphite setters before insertion in the reaction furnace. Reaction sintering of the silicon carbide and graphite particles to a dense self-bonded state takes place in a graphite induction furnace. The furnace atmosphere is silicon vapor and nitrogen at a temperature of about 2100 °C. The resultant fired articles have a density of

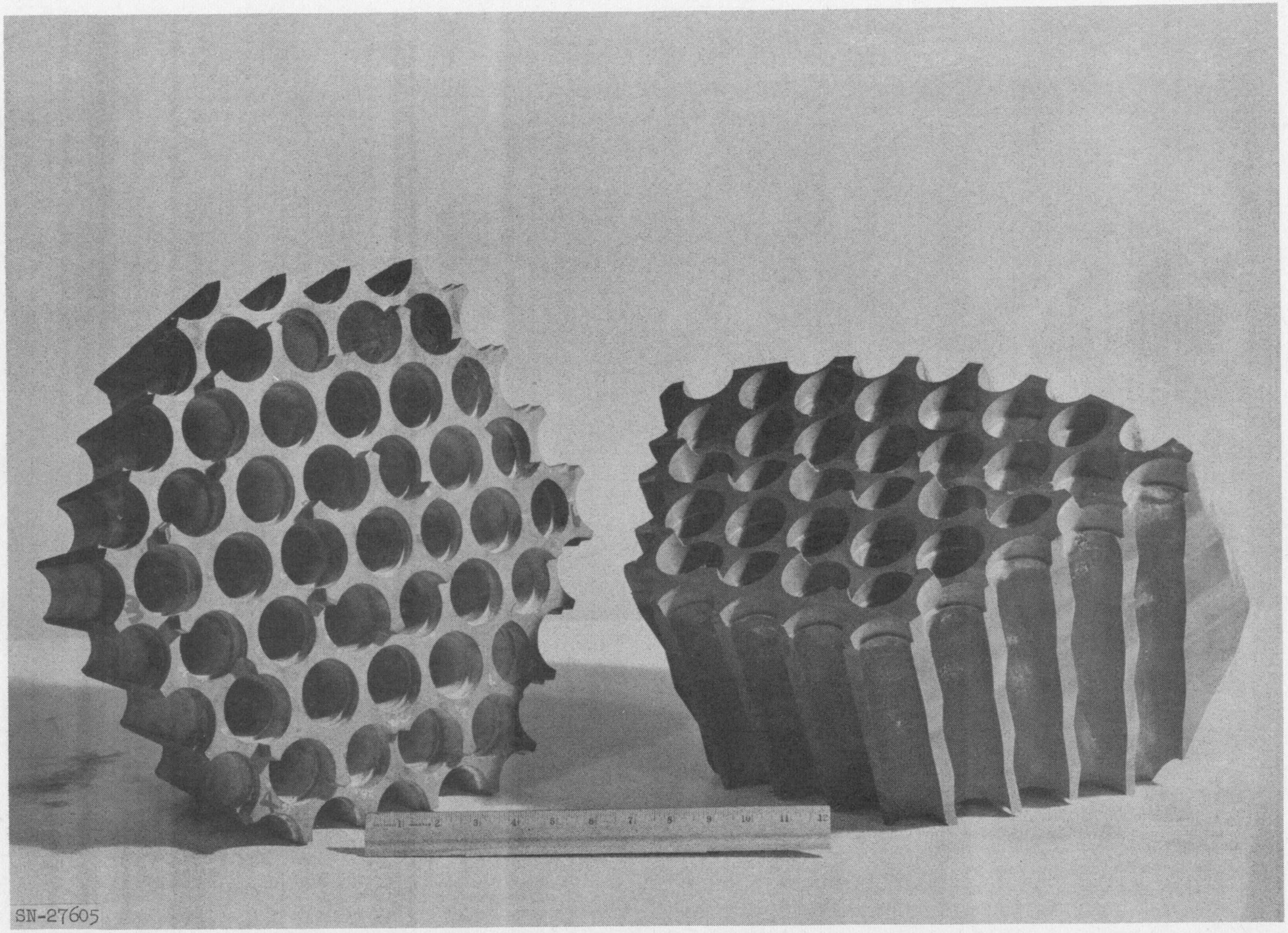

Fig. V-1. Two segment types used in dome assembly.

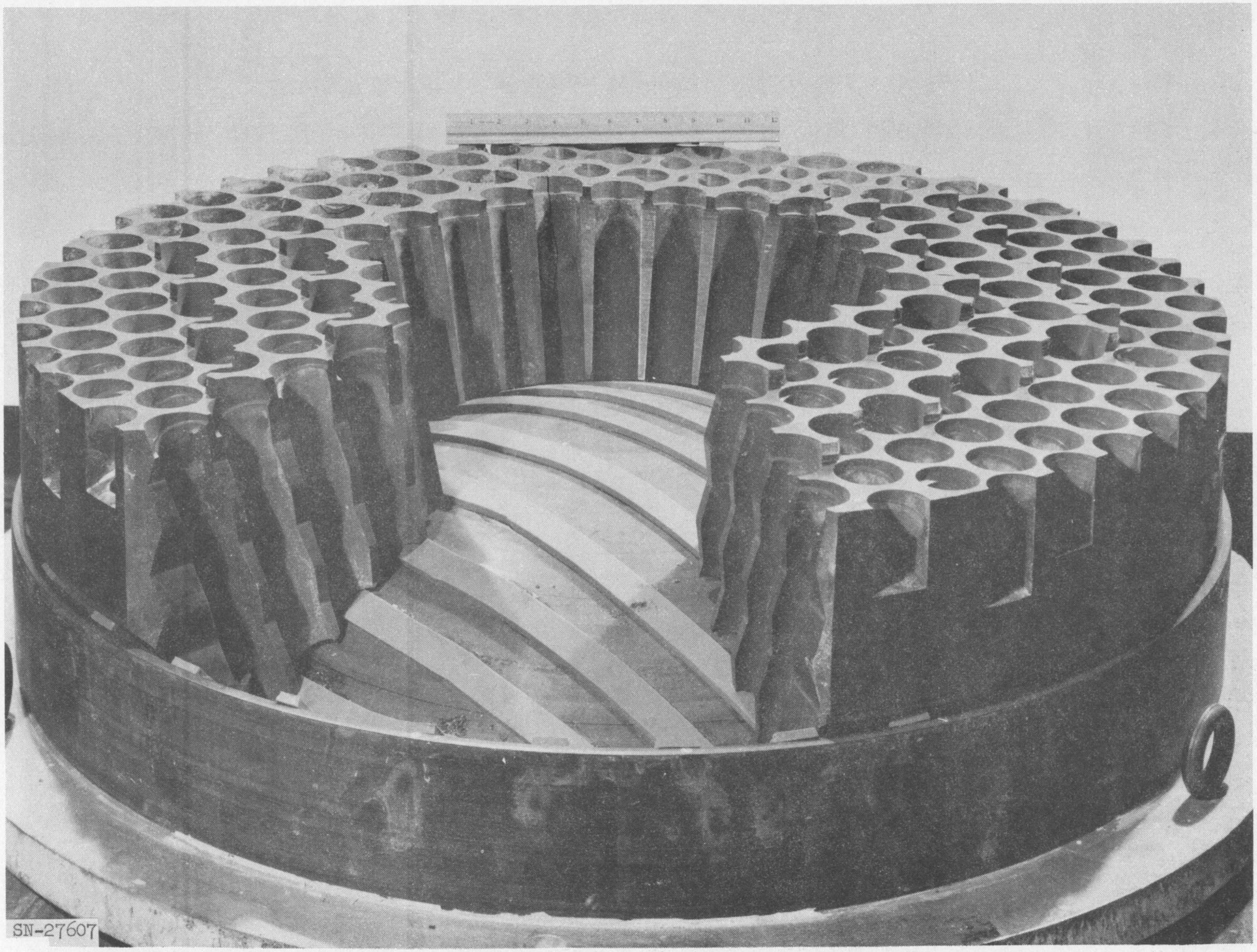

Fig. V-2. Partial dome assembly.

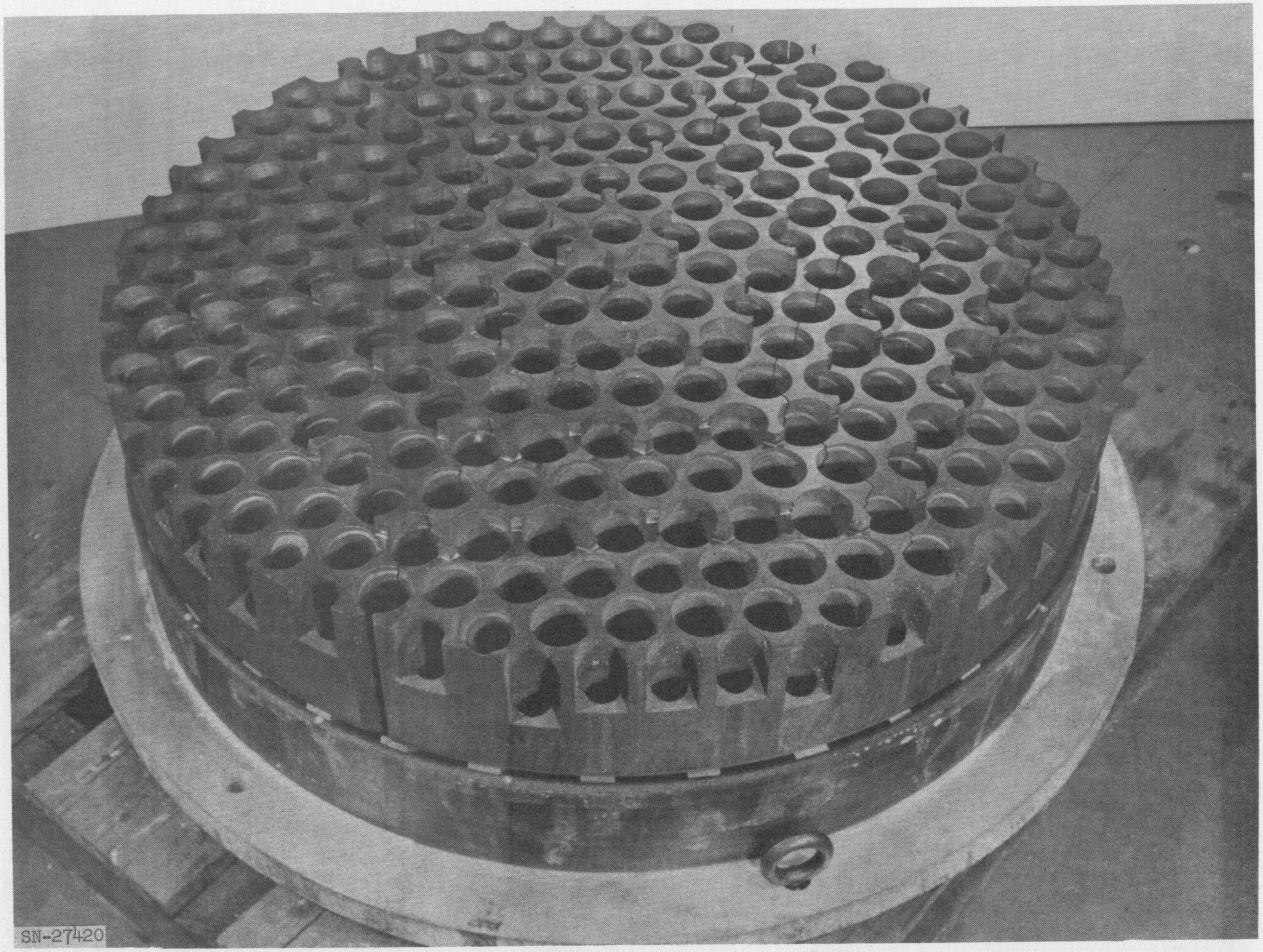

Fig. V-3. Complete dome assembly.

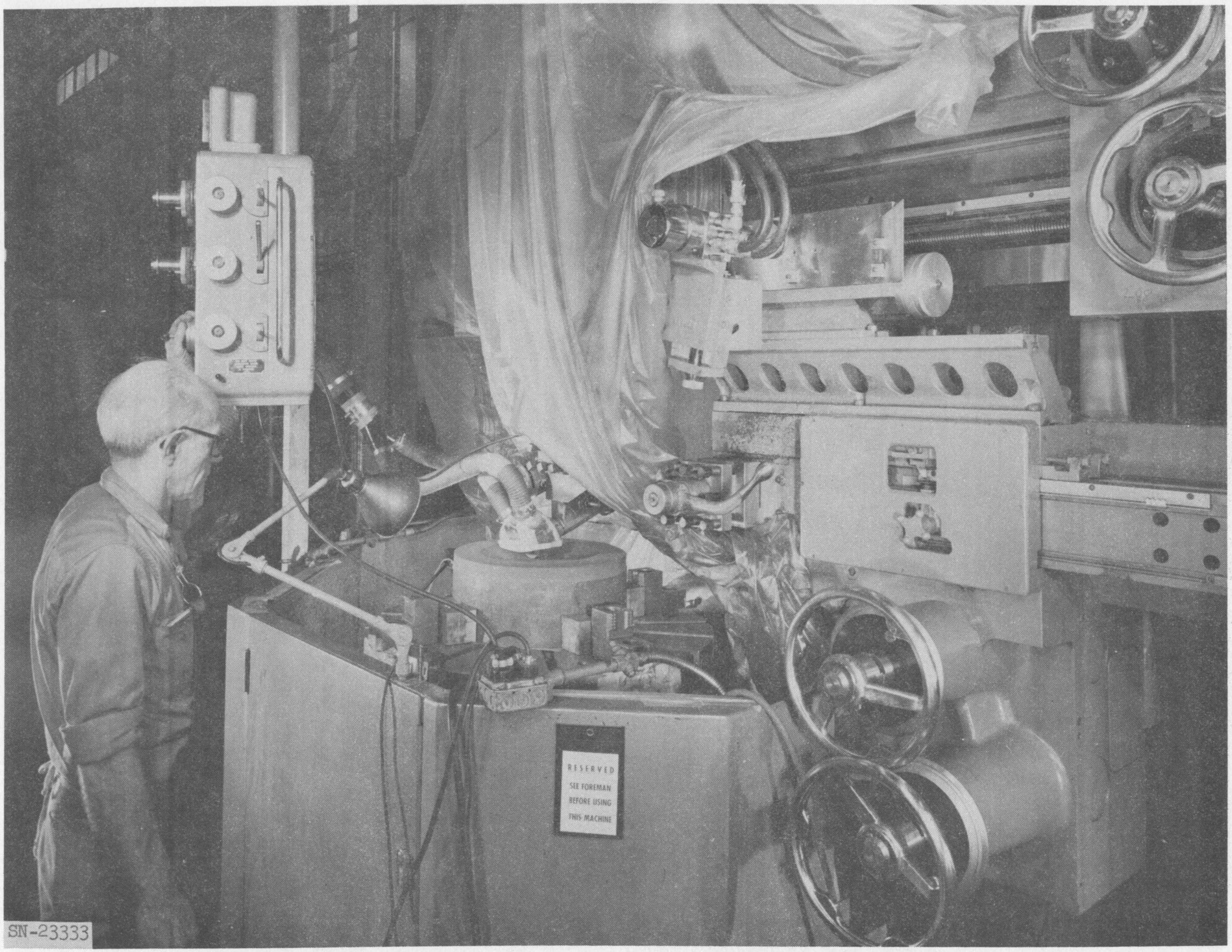

Fig. V-4. Grinding external contours of dome component.

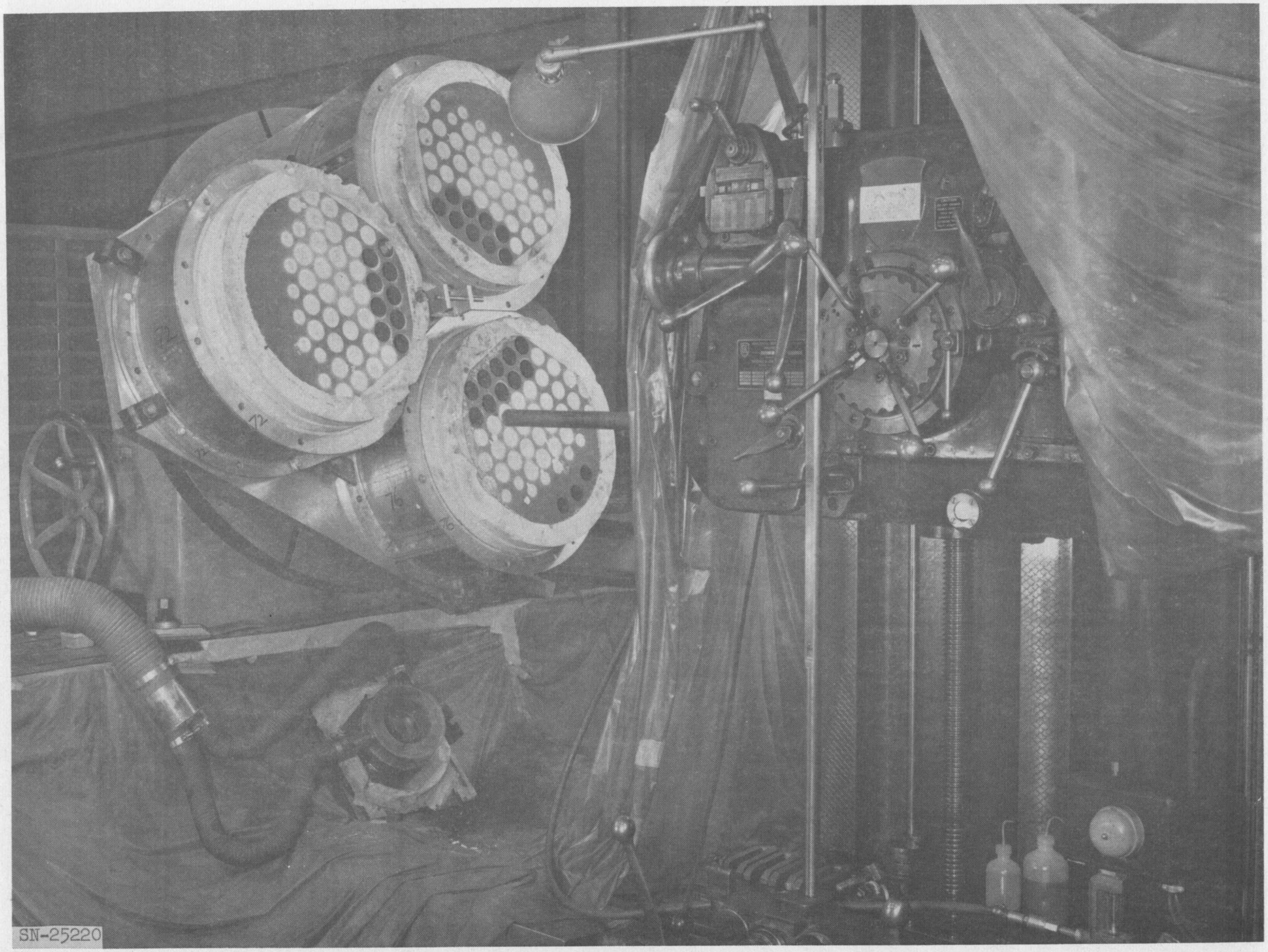

Fig. V-5. Indexing compound bore angles in dome components.

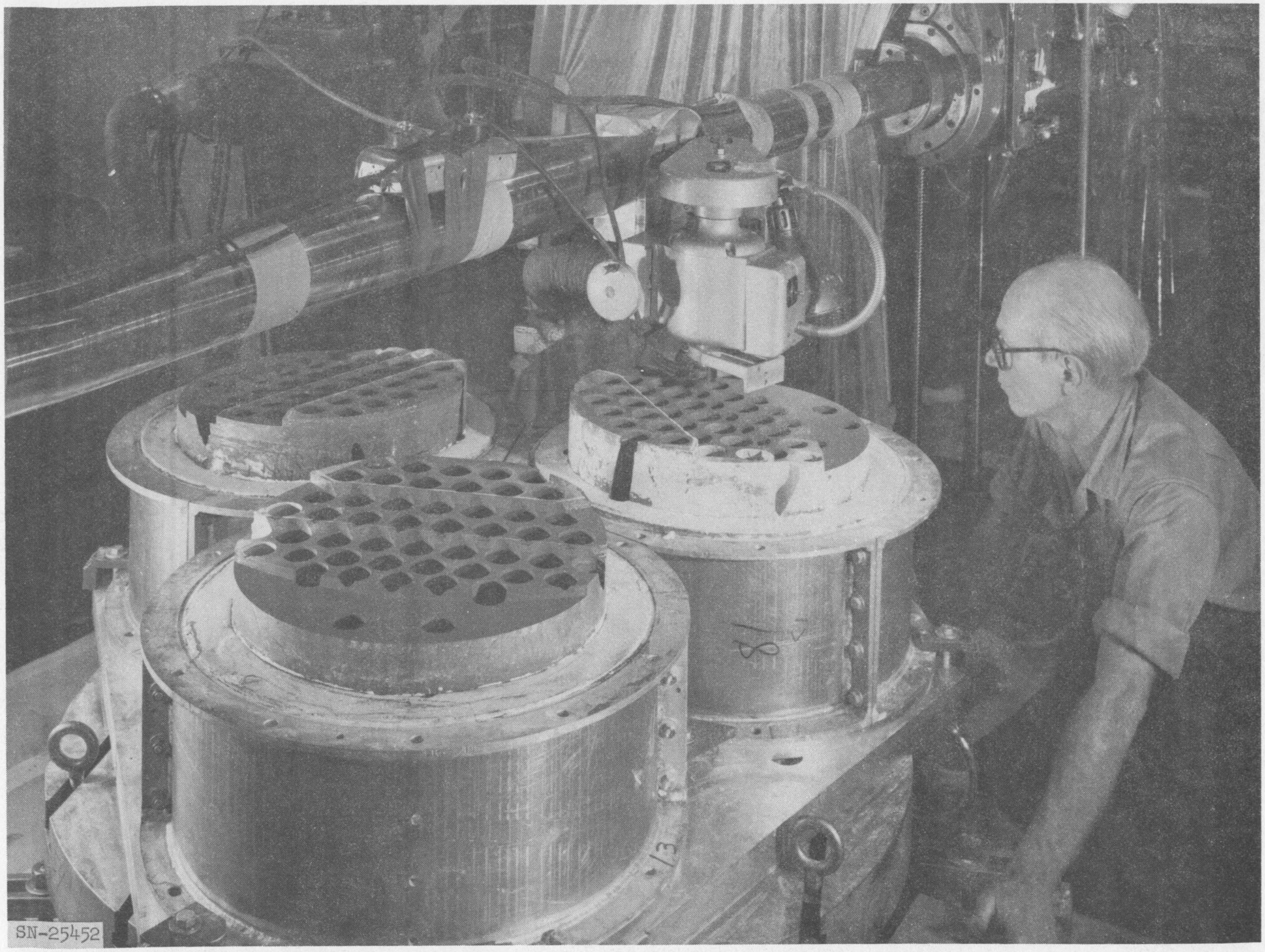

Fig. V-6. Grinding steps on dome components.

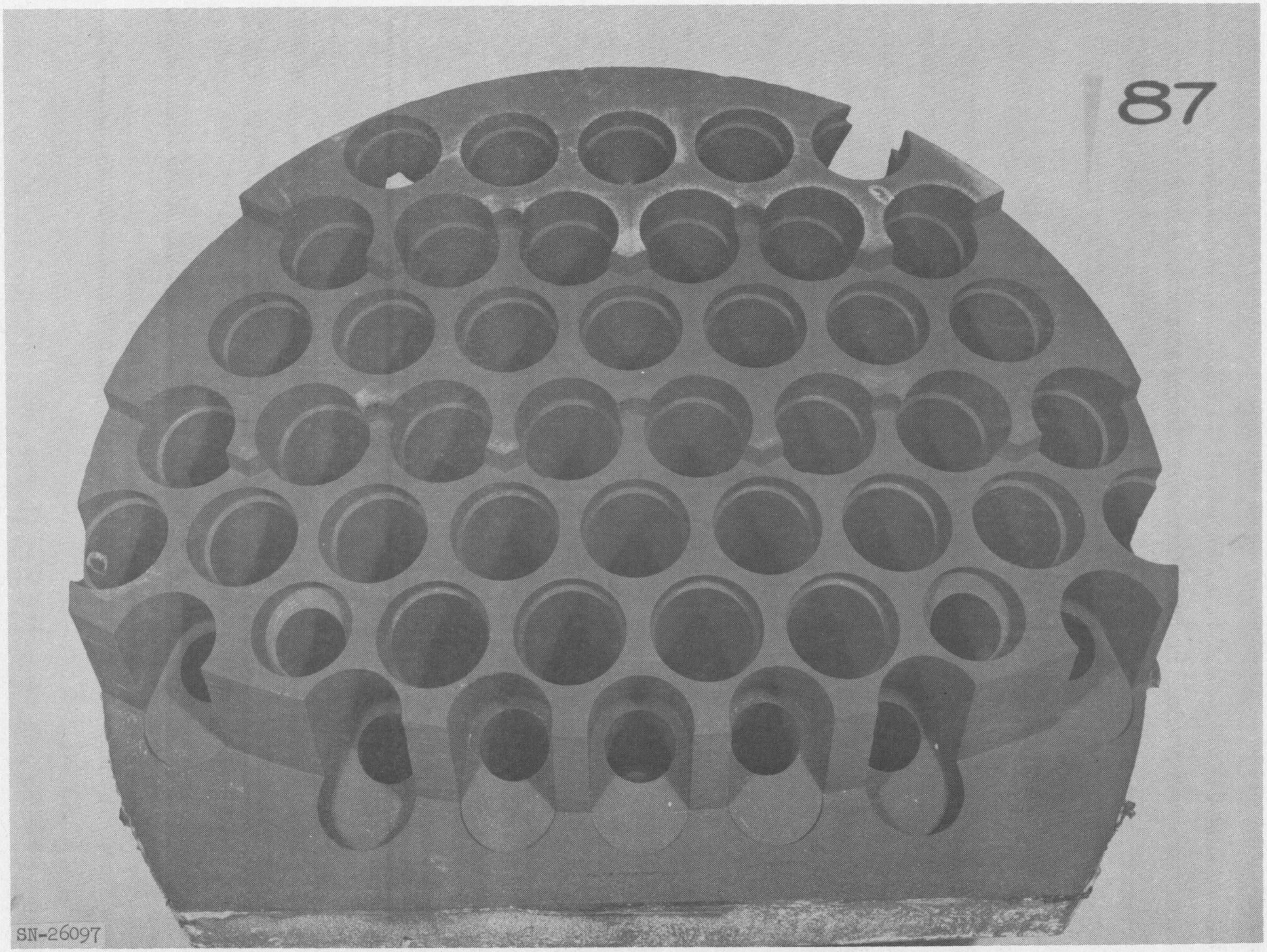

Fig. V-7. Green machined dome segment after treatment with fluorescent penetrant.

about 3.1 g/cc (compared with 2.2 g/cc in the green state). Firing is followed by diamond grinding to finished form and tolerances. Figure V-8 shows the final operation of grinding the conic seat region.

Fabrication development has continued on unclassified shapes similar to segments of a seven-piece, 54-in.-diameter dome at the supplier's plant. In pieces similar to an edge segment (like the right-hand element in Fig. V-1 except larger, with parallel holes, and without the stepped surface), a source of cracking was found which did not occur in the smaller pieces. This cracking occurred during the oven carbonizing process. It was eliminated by relocating the piece in the oven for better convection and providing radiation shields to reduce temperature gradients in the piece. In addition, the epoxy resin content was reduced from 9 wt % to 5 wt % to reduce shrinkage in this carbonizing operation. These steps have resulted in producing three crack-free pieces, one of which has already been fired. The other two have been through the carbonizing process and have been inspected with a penetrant at that stage.

A limited effort to scale up the fabrication process for silicon-carbide bonded graphite is under way at the supplier's plant. The normal phenolic binder did not allow diamond core drilling, so it was successfully replaced with an epoxy binder which did allow drilling of a 9 × 12-in. cylinder. The attempt to fire the piece, however, resulted in extensive cracking.

DOME TEST MATERIALS INVESTIGATION

1. Flow Tests

A supplier's hot flow facility was used to test silicon carbide, silicon nitride, Chrome Cerametalix, Monofrax, and zircon specimens in a high-temperature air flow, in connection with a subsequent dome flow-testing program. Results are summarized in Table V-1. A gas-sampling run was made in addition to these tests and showed the oxygen content to be 23.3 wt %, at a pressure of 200 psia and a stream temperature of 2200 °F. A test at 2500 °F gave the same oxygen percentage.

Sonic flow through an orifice was investigated for Chrome Cerametalix, silicon carbide, and silicon nitride. These orifices will allow the dome test load to be obtained at available facility air flow rates and must hold dimensions during the test or accurate flow control will become quite difficult. The one-hole (0.488-in. diam) specimens listed were for this purpose and pressure and

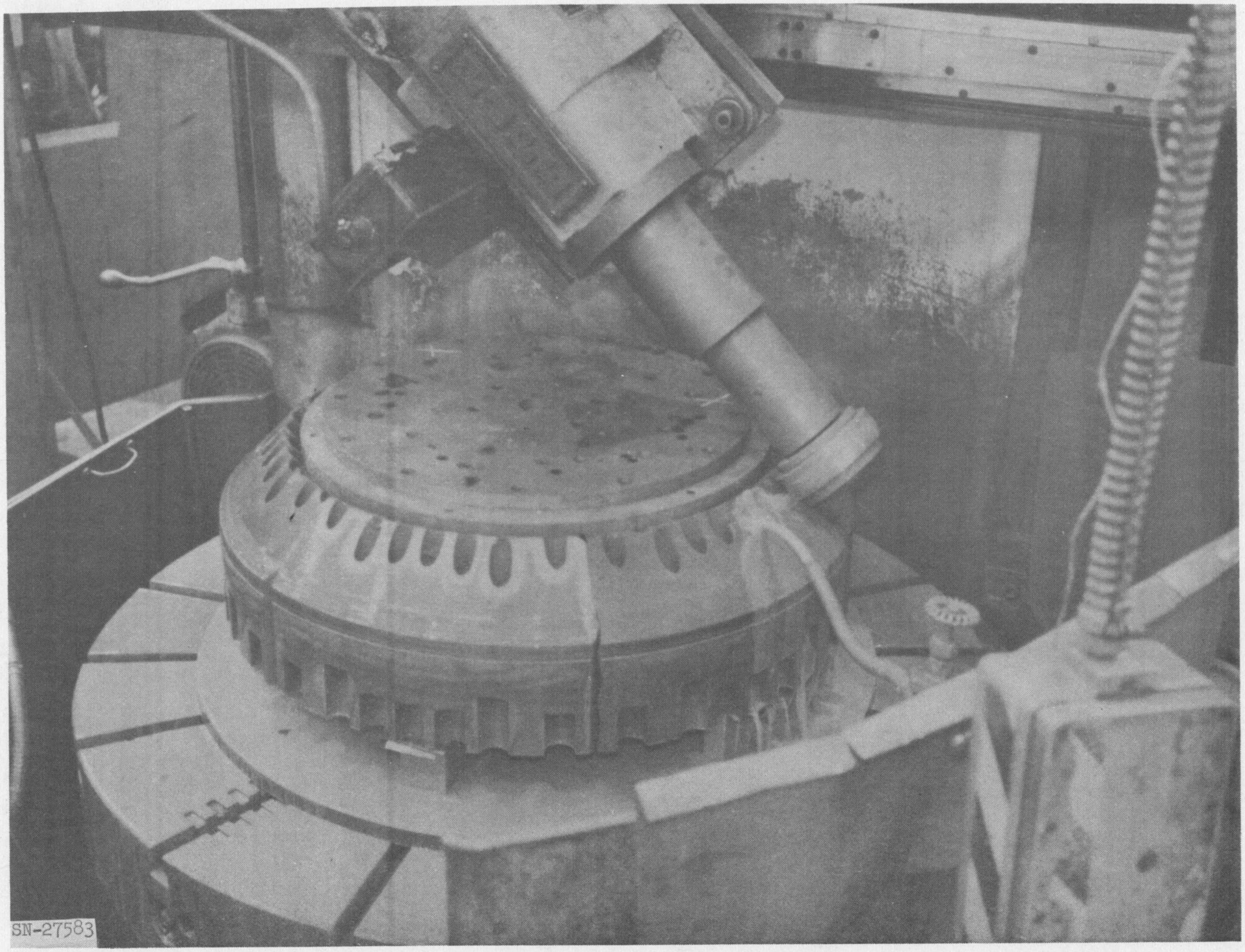

Fig. V-8. Diamond-grinding conic seat region of dome component.

Table V-1. Results of Hot Flow Tests of Materials. All Tests at 200 psia; Oxygen Content 21 ± 1%.

Test No.	Material	Configuration	Number tested	Temp (°F)	Time (hr)+(min)	Flow rate (lb/sec)	Purpose	Weight change (%)	Remarks
1	Chrome Cerametalix	10-hole	2	2500	5 + 00	0.493	Oxidation	-2.1 -2.3	
2	Chrome Cerametalix	10-hole	2	2700	0 + 31	0.385	Oxidation	-0.477 ---	2nd spec. ignited
2	Chrome Cerametalix	1-hole	1	2700	0 + 31	0.385	Erosion	---	Sonic orifice ignited
3	Silicon nitride (Supplier)	7-hole	2	2700	2 + 00	0.488	Oxidation	+0.079 +0.038	
3	Silicon nitride (Supplier)	1-hole	1	2700	2 + 00	0.488	Erosion	+2.7	Sonic orifice
4	Silicon nitride (Supplier)	7-hole	1	2700/1200	0 + 05	0.257	Thermal shock	0	2000°F/sec, cracked[a]
5	Silicon nitride (Supplier)	7-hole	1	2700/1200	0 + 05	0.259	Thermal shock	0	480°F/sec cracked[a]
6	Silicon nitride (LRL)	7-hole	3	2700	2 + 00	0.260	Oxidation	-0.22 -1.37 +1.47	2 specimens cracked
7	Zircon	7-hole	3	2400	1 + 00	0.283	Oxidation	167, 7.87 130, 3.65 175, 0.334	Cracked
8	Zircon	7-hole	2	2500	1 + 00	0.231	Oxidation	130, 3.19 175, 0.493	
7	Monofrax M, S	7-hole	2	2400	1 + 00	0.283	Oxidation	M, 0.21 S, 0.02	
8	Monofrax M, S	7-hole	2	2500	1 + 00	0.231	Oxidation	M, 0.13 S, 0.10	
1	KT silicon carbide	1-hole	1	2500	5 + 00	0.493	Erosion	-0.273	Sonic orifice

[a] See text for discussion of these crack failures.

temperature readings downstream, although erratic, indicated that the flow through all of them was sonic.

KT silicon carbide. A single one-hole specimen was tested for 5 hours at 2500°F and a flow rate of 0.493 lb/sec. No change was observed in the hole dimension and a weight loss of 0.273% took place. Except for the high cost, KT silicon carbide would be a good choice for the orifice discussed above.

Chrome Cerametalix. A supplier produces this Cr-5 MgO material as a high-temperature structural material (David M. Scruggs, "Modified Chromium for Unprotected Structures," Am. Rocket Soc. J. 31, No. 11, November, 1961). Due to its good oxidation resistance and high-temperature ductility, this material shows promise for Pluto applications. However, in this series of tests Chrome Cerametalix ignited at 2700°F and showed unsatisfactory creep properties, making doubtful its usefulness for 10-hour periods at over 2300°F, and then only for stresses below 500 psi. However, the fact that Chrome Cerametalix requires no protective coating makes it very desirable material.

In the flow tests, two specimens were tested for 5 hours at 2500°F with a flow rate of 0.493 lb/sec and showed a weight loss of 2.20% (0.55%/hr) with no other ill effects evident. When tested at 2700°F with two 10-hole specimens and a single 1-hole specimen, the second 10-hole specimen and the one-hole specimen ignited after 31 minutes. The first 10-hole specimen survived and is shown in Fig. V-9. The material evident on the face came from the failure of a thermocouple sheath upstream. Supplier's personnel suspected that a reaction between the alumina holders and the specimen may have caused the ignition reaction. Subsequent supplier's tests indicate that this is not true, and the ignition temperature of 2700°F is probably accurate. In addition, a previous test at another facility ignited a chromium specimen at 2690°F. Flow conditions for that test were: 100 psia, 20% O_2, flow rate of 288,000 lb/ft^2-hr. The material was arc-melted chromium with a 0.010-inch-thick coating of an Fe, Cr, Al, Y mixture. The comparable flow rate for the Cerametalix was 113,100 lb/ft^2-hr. These parameters are obtained by dividing the flow rate by the total free stream area at the specimens. The threshold oxygen quantity and required temperature for chromium ignition are not known at this time. While numerical predictions can be made, greater accuracy is given by actual tests. The uncertainty of oxidation constants for metals is quite high, and these constants heavily influence the prediction of ignition.

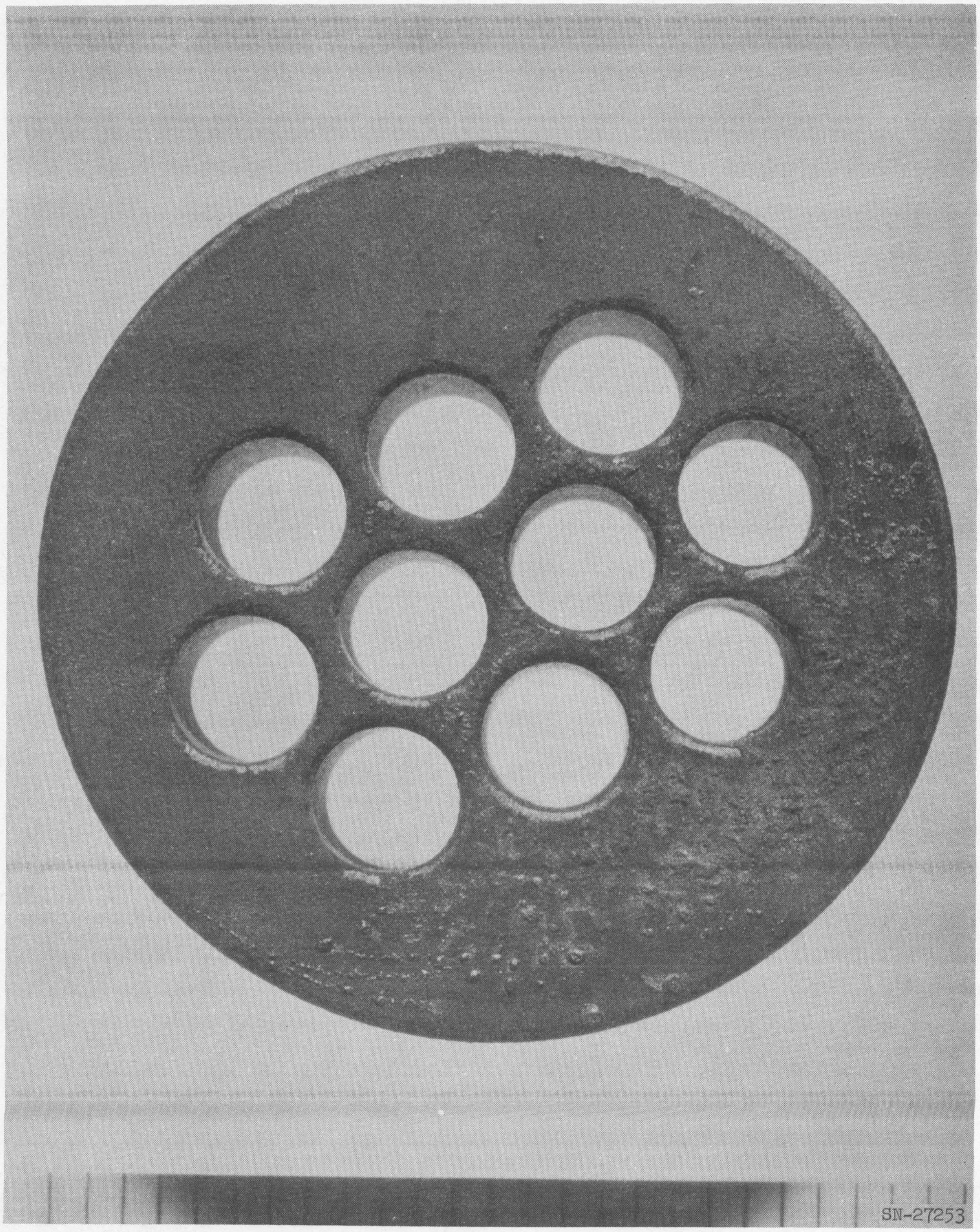

Fig. V-9. Surviving 10-hole specimen after 5-hour flow test at 2500°F with 0.493-lb/sec flow rate.

Creep tests on Chrome Cerametalix are summarized in Fig. V-10. The data were obtained by testing 2-in.-long by 0.75-in.-diam cylinders to 1 and 2% strain. A small tube, shown in Fig. V-11, was tested at 2500°F at a compressive stress of 2200 psi. It failed by plastic buckling in about 8 minutes as can be seen from the photograph. Based on these tests, a design limit for 10-hour structural life at 2300°F would be 500 psi.

Silicon nitride. LRL-produced silicon nitride (described later in this report) as well as supplier-produced silicon nitride have been tested. The latter was tested for 2 hours at 2700°F with a flow rate of 0.488 lb/sec in both the seven-hole and the sonic orifice (one-hole) configurations. The weight gain of less than 0.10% that took place in the seven-hole specimens indicates a very desirable structural material. However, the thermal shock qualities were poor. One of the seven-hole specimens cracked during the oxidation tests and both of the thermal shock tests (Fig. V-12: N-1, 2000°F/sec; N-2, 480°F/sec) resulted in severe cracking.

The KT silicon carbide tested in a similar fashion and reported in the last Pluto quarterly progress report (UCRL-6625) cracked in a similar fashion, but only under more severe conditions (772 to 871°F/sec) of thermal shock. The silicon nitride of both LRL and supplier showed the same crack failure pattern, which was not like the typical patterns caused by thermal stress. Specimen geometry also influences the failures, as none of the single-hole specimens of any material cracked.

The LRL silicon nitride was tested in the seven-hole configuration for 2 hours at 2700°F and a flow rate of 0.260 lb/sec. Two specimens cracked during the test, showing weight losses of 0.22% and 1.37%. The third specimen was intact and showed a weight gain of 1.47%.

Densities of the two materials were: LRL's, 2.4 g/cc; supplier's, 2.1 g/cc.

A 3.45-in.-diameter dome made of LRL silicon nitride of 2.4-g/cc density was tested at room temperature by being hydraulically loaded through a thin diaphragm. Load deflection for the center portion is shown in Fig. V-13. Testing at 2500°F and a pressure of 250 psi was then carried out for 10 hours using the molybdenum test fixture used to test small silicon carbide domes (Pluto quarterly reports 7 and 8). Resulting maximum stress in the dome would be about 3640 psi.

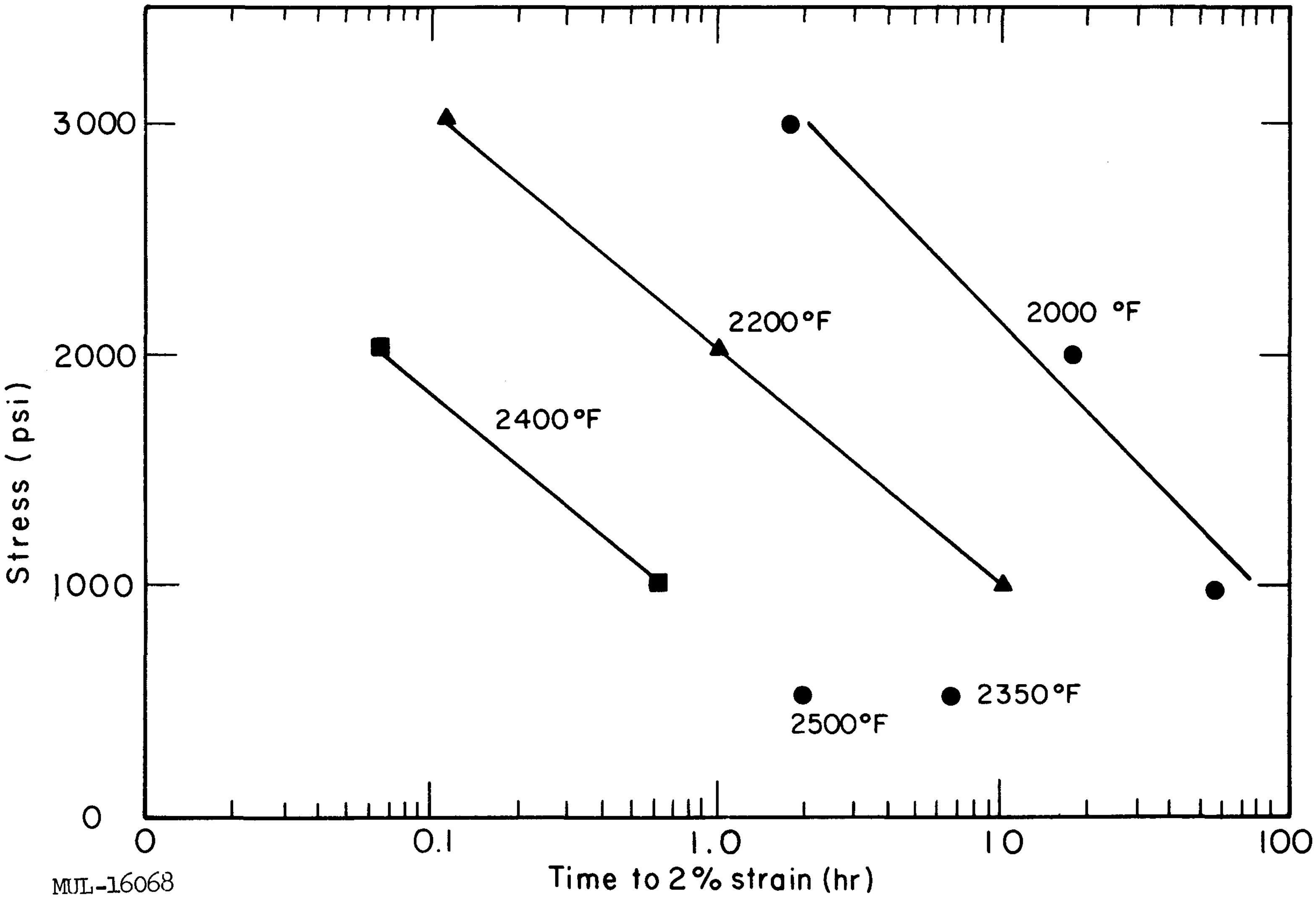

MUL-16068

Fig. V-10. Results of creep tests on Chrome Cerametalix.

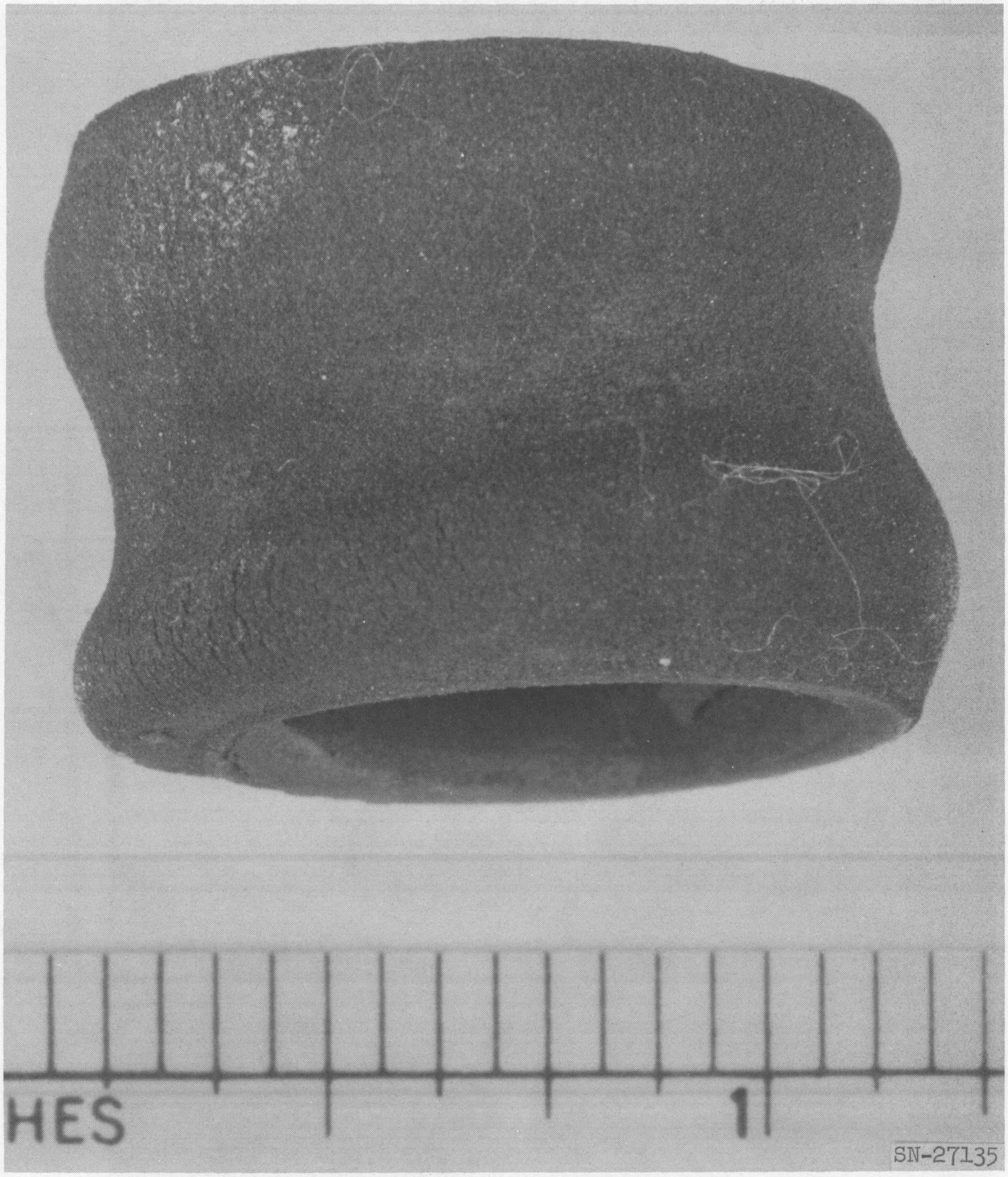

Fig. V-11. Chrome Cerametalix tube after testing at 2500 °F under compressive stress of 2200 psi.

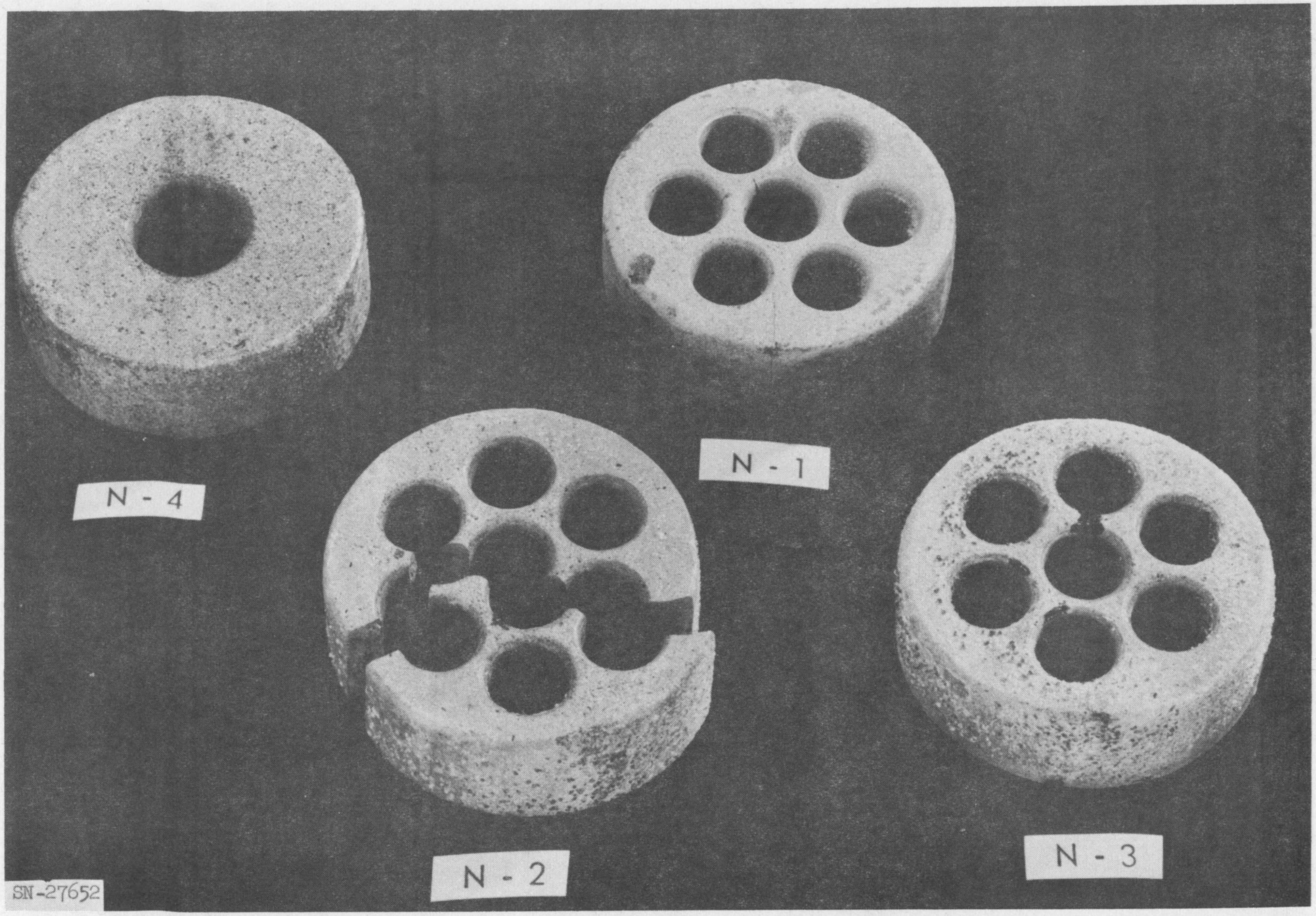

Fig. V-12. Silicon nitride specimens after oxidation and thermal shock tests.

5

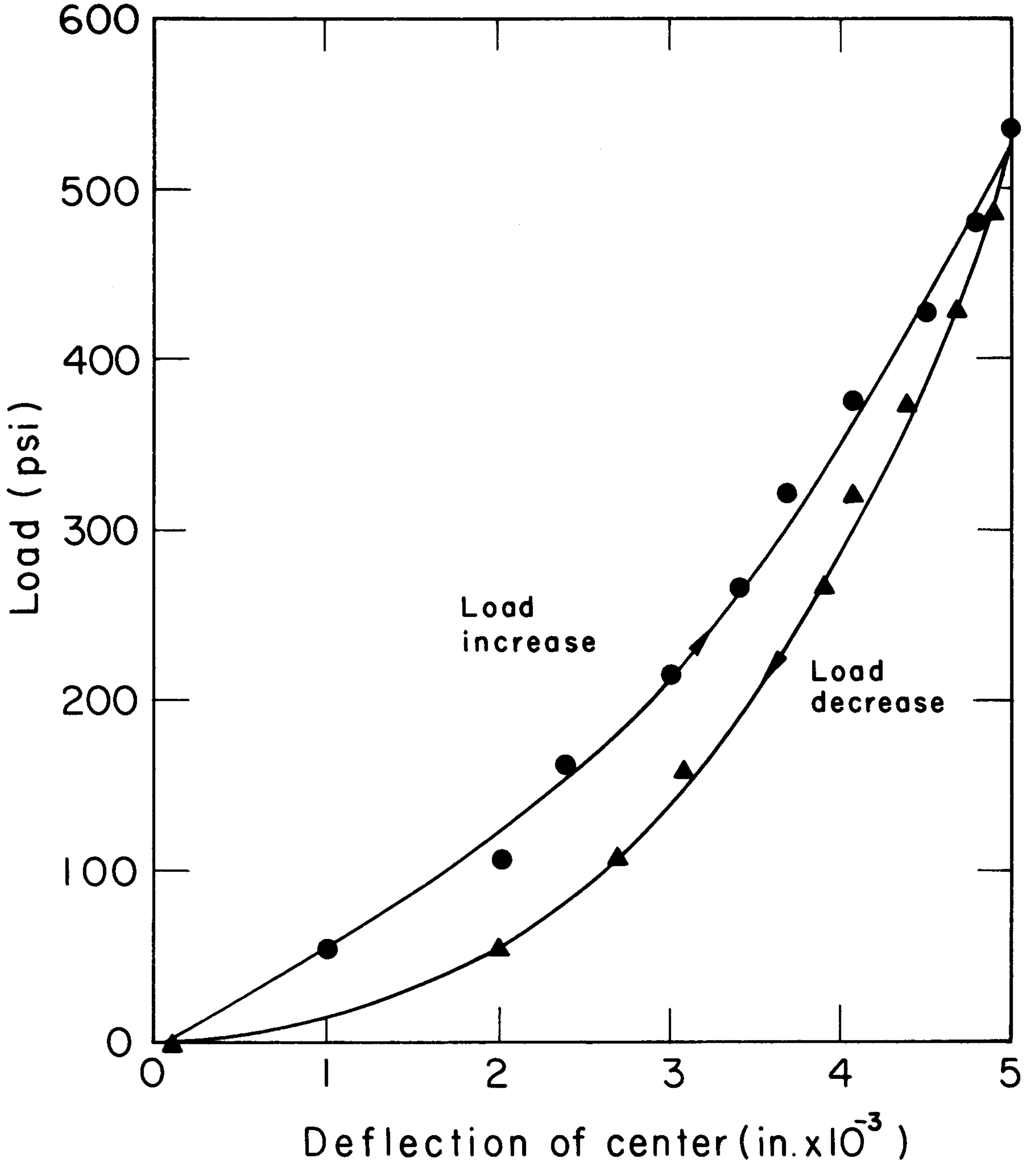

MUL-16069

Fig. V-13. Load deflection for center portion of 3.45-in.-diam dome made of LRL silicon nitride, 2.4-g/cc density.

The dome seat apparently stuck to the test fixture, during heat-up, in the failure area seen in Fig. V-14. The sticking would result in a bending moment being applied when the dome was loaded since the free side could move down the seat. Figure V-15 shows the mechanism surmised. The sticking was probably caused by the reaction $Mo + Si_3N_4 \rightarrow MoSi_2 + N_2\uparrow$. MgO was used as a separating medium on the basis of previous tests, but here it failed to maintain the separation.

Zyglo tests disclosed thin cracks in the 15 holes in the broken-off portion, the cracks extending into the holes axially. The photos do not show these cracks, as they are very small and difficult to detect even by fluorescent penetrants.

Other properties of the supplier's silicon nitride as tested at LRL are listed below. All tests were done on bars of 0.5-inch-square cross section.

Compressive strength (60°F): 47,800 psi (average of three).

Modulus of rupture(room temp): 10,450 psi (deflection 0.003 in. at center of 4.5-in. span).

Modulus of elasticity (by sonic method): 9.58×10^6 psi.

Creep at 2700°F: Negligible when loaded for flexure modulus of 4000 psi. Failure of load apparatus after test resulted in an impact loading of about 44,000 psi (in flexure) which broke the test beam.

Zircon. A supplier has produced three zircon materials consisting primarily of milled zircon with small amounts of other materials. They were tested at 2400°F (0.283 lb/sec) and 2500°F (0.231 lb/sec), with the following results.

	Weight loss (%) after 1 hr	
Material	2400°F	2500°F
130 (cracked on 2500°F test)	3.65	3.19
167 (cracked on 2400°F test)	7.87	--
175	0.334	0.493

Exact production processes of the materials were not known at test time, but superior properties of hot strength, oxidation resistance, and thermal shock resistance were claimed. The weight losses indicated above as well as the cracking of the 167 and 130 specimens indicate that only the 175 specimen is of interest.

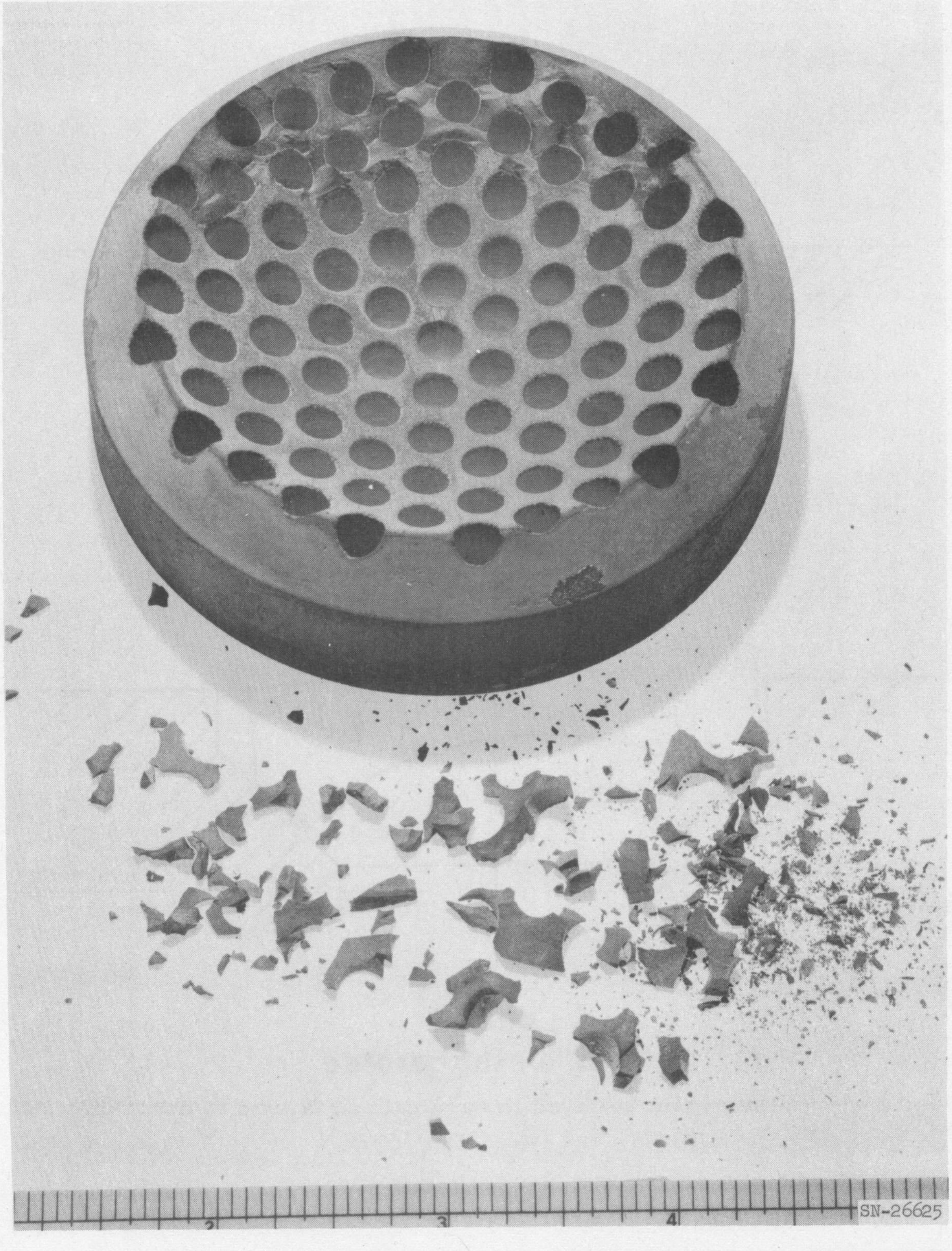

Fig. V-14. Dome of LRL silicon nitride, which failed during 10-hour test at 2500°F with 250-psi loading.

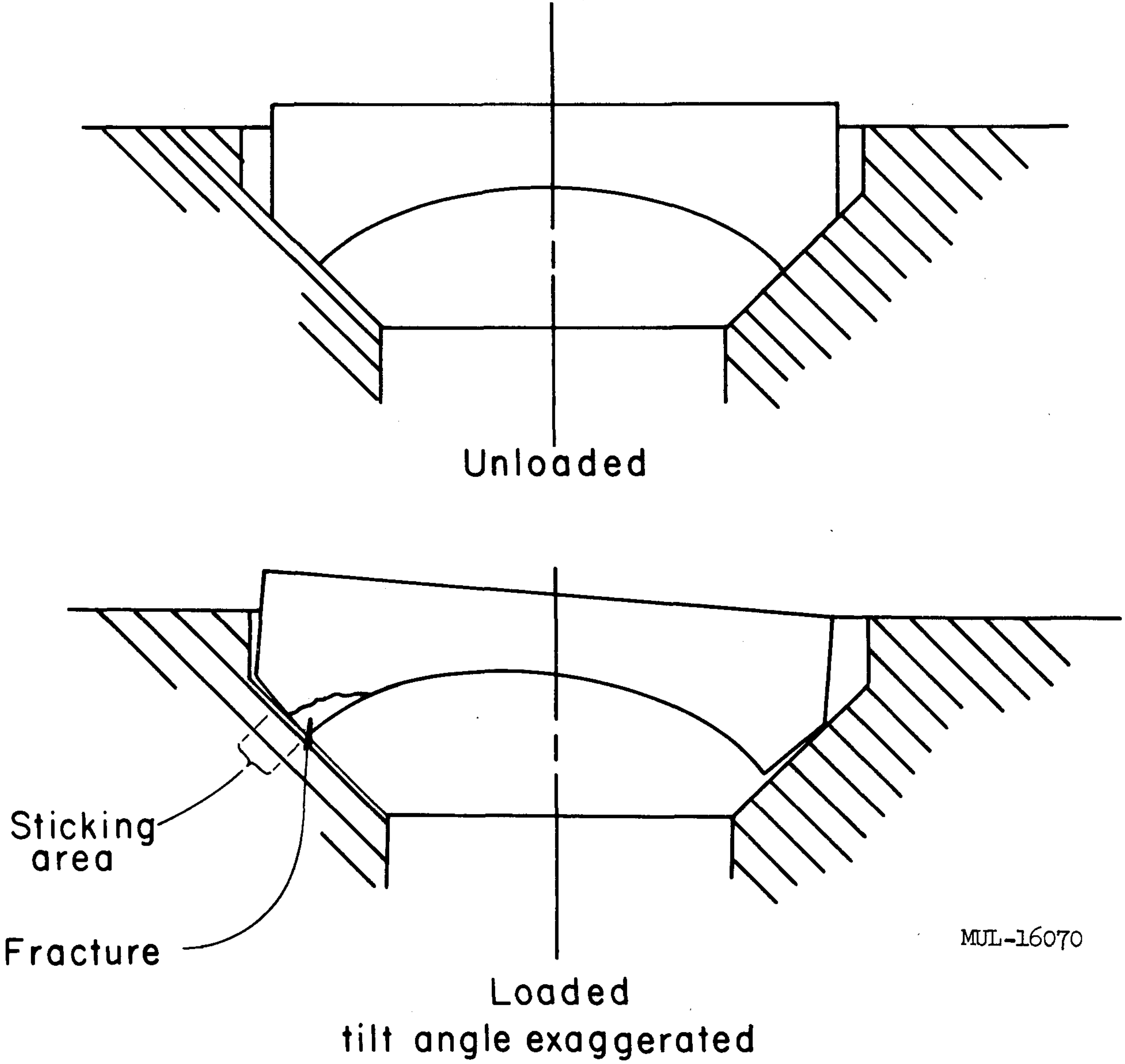

Fig. V-15. Mechanism believed to have caused failure of dome pictured in Fig. V-14.

Monofrax M and S. These refractories are manufactured primarily as liners for glass furnaces. Composition and some advertised properties are listed below.

		Monofrax M	Monofrax S
Chemical comp.	Al_2O_3	94.76%	47.56%
	ZrO_2		36.01
	SiO_2	1.09	14.65
	Na_2O	3.58	1.19
	Other	< 1	<1
Crystal formation		Alpha and beta alumina	Alumina and zirconia
Density (g/cc)		3.18	3.46
Coeff. of thermal expans.		4.58×10^{-6}	2.93×10^{-6}
Melting point		3540°F	3180°F

Because of their availability and low cost compared with silicon carbide, these refractories were investigated as possible structural materials. Both were tested for 1 hour at 2400°F and a flow rate of 0.283 lb/sec and 1 hour at 2500°F with a flow rate of 0.231 lb/sec. The Monofrax S had a weight loss of 0.02% at 2400°F and 0.10% at 2500°F and cracked on the 2500° run. The Monofrax M had a weight loss of 0.21% on the 2400°F run and 0.13% on the 2500°F run and was crack-free.

Monofrax M is composed of a dense structure of interlocked alpha and beta alumina crystals which should result in excellent thermal shock resistance. Since the material is cast, it can be produced in large shapes.

2. Silicon Nitride

Work has continued at LRL on developing and understanding of silicon nitride as a reactor material. The original objective was to show the feasibility of fabricating large silicon nitride bodies. However, it became apparent that detailed understanding of the nitriding process was necessary before acceptable material could be fabricated.

Three large isostatic pressings of silicon powder 14 in. in diameter and 10 in. high have been biscuit-fired in a supplier's furnace. This consisted of heating the pressings in a nitrogen atmosphere for 16 hours at 2080°F. The heating rate of the first two pressings exceeded 500°F/hr and severe cracking was revealed by x ray and sectioning. It was suspected that the powder compact had a low coefficient of thermal conductivity and that a large thermal gradient was developed during heating. Also, it was known that the reaction was exothermic and would develop a reverse thermal gradient after nitriding became appreciable. Therefore, a thermocouple was placed at the center of the pressing in a drilled hole in the third pressing. The pressing was then heated at a rate of 70°F/hr, but this rate still gave a maximum ΔT of 190°F. When the external temperature leveled off at 2080°F the internal temperature was at 2000°F and continued to rise off the recording chart. It was estimated the temperature reached 2250°F giving a ΔT of 170°F. The temperature then returned to 2200°F in 1 hour, and slowly returned to 2080°F in 15 hours. Cracking was greatly reduced by the lower heating rate, but the body contained one serious crack. This would indicate a lower rate of heating and a method of controlling the exothermic reaction would be necessary to fire large crack-free bodies. The first large fired pressing was machined to a hexagonal shape 10.5 in. across flats and 9 in. high with nineteen 1.6-in.-diam holes (see Fig. V-16). The part was then fired for 33 hours at 2450°F and 24 hours at 2650°F (melting point of silicon is 2588°F). During this phase of the nitriding there was some extension of the existing cracks, but no new cracks were detected. Also some bleeding of the silicon occurred at the surface. The final density reached was 2.45 g/cc which compares well with densities reached by other people on small specimens.

Due to the exothermic reaction, the nitriding of silicon powder compacts proceeds more rapidly in larger specimens for a given time at a given temperature. The results shown in Table V-2 are for an average of at least three specimens for each diameter. All specimens were isostatically pressed from -200 mesh powder of 98% purity and were held at 2080°F for 16 hours.

Table V-2. Results of nitriding three sizes of silicon nitride specimens.

Diameter (in.)	Height (in.)	% wt increase
13.75	10	11.0
4.5	2.75	5.3
1.25	0.5	3.5

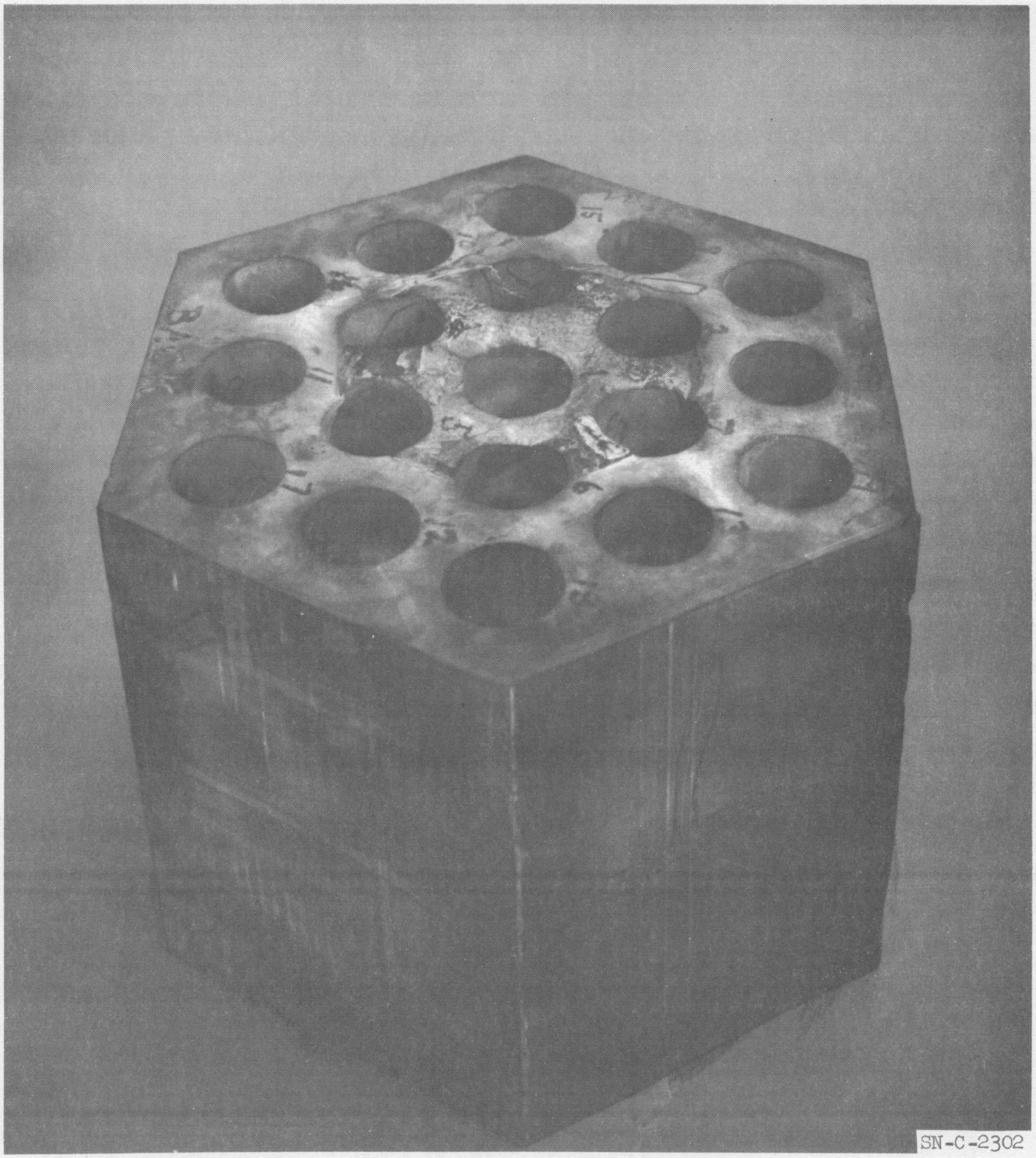
SN-C-2302

Fig. V-16. Part machined from partially fired silicon nitride.

Eight specimens of various powders and densities were used to investigate nitriding rates. All specimens were cylinders 1.25 in. in diameter and approximately 0.5 in. high. Particle size, purity, and density were the three variables used in seven combinations. Specimens UC-3-91 and UC-8-101 were isostatically pressed at 20,000 psi and the remaining six were die-pressed at 8000 psi using 2% Carbowax as a binder. Specimens were fired simultaneously and rotated in the furnace between data points. Firings were carried out in a vacuum-atmosphere furnace with molybdenum and graphite in the hot zone. The procedure was to pump the furnace below 1 micron pressure and raise the temperature to 800°F. Nitrogen was then introduced to 3 psig. The desired temperature was reached in approximately 1 hour and a nitrogen flow of 5 furnace changes per hour was used. Specimens were removed from the furnace and weighed for each datum point. It was felt that the small size of the specimens reduced the effect of the exothermic reaction, which could therefore be ignored. The results are shown in Table V-3 and Fig. V-17. The successive-temperature method used does not give nitriding rates back to zero time for temperatures above 2090°F. However, all curves can be extrapolated to zero for any temperature with reasonable accuracy. The data clearly show the effect of particle size in the rates. To substantiate this, a piece of silicon with a largest dimension of 3.5 cm was nitrided at 2265°F. Results showed that percentage nitriding rates are roughly inversely proportional to the largest dimension of the particles. Density and purity effects did not follow any pattern, and they appear to be small. At the end of the 2420°F run, approximately one-third of the specimen was removed for x-ray diffraction and microstructure studies. These results are not yet available.

It has been suggested that the oxidizing of free silicon in Si_3N_4 could possibly have a detrimental effect on the material. Also, a silicon-free silicon nitride would be more compatible with other materials at high temperatures. Therefore it seemed desirable to determine if free silicon could be removed from silicon nitride containing silicon. A sample of each section removed from specimens in Table V-3 was fired in vacuum at 2750°F for 2 hours. Results are shown in Table V-4. It is interesting to note that samples UC-4-93-A and UM-6-97-A both lost more weight than can be accounted for by free-silicon loss, which would suggest the sublimation of Si_3N_4 at this temperature in vacuum.

Table V-3. Nitriding Rates of Silicon Pressings.

Specimen No.	Green density	Max particle size, microns	Min particle size, microns	% purity	Percent weight increase				
					33 hr at 2090 °F	93 hr at 2265 °F	44 hr at 2420 °F	16 hr at 2500 °F	16 hr at 2640 °F
UC-1-87	1.470	70	1	98.0	3.66	20.9	47.7	58.2	58.4
UC-2-89	1.375	70	44	98.0	2.36	11.7	39.4	55.5	56.1
UC-3-91	1.59	70	1	98.0	4.39	24.1	49.3	56.3	57.2
UC-4-93	1.345	37	1	98.0	6.03	39.2	59.1	59.7	59.6
UM-5-95	1.438	70	44	99.6	5.85	14.7	31.3	36.5	36.7
UM-6-97	1.362	37	1	99.6	11.77	43.0	60.6	60.6	60.5
UM-7-99	1.51	70	1	99.6	2.13	25.4	46.9	56.5	56.8
UC-8-101	1.58	70	1	98.0	4.11	26.7	54.0	59.9	60.2

Table V-4. Effects of High-Temperature Treatment of Silicon Nitride Samples in Vacuum.

Sample No.	Density	% nitridation by weight increase	Free silicon, wt %	% weight loss	% porosity
UC-1-87-A	2.17	71.5	19.3	10.8	28.7
UC-2-89-A	1.92	59.1	29.3	12.3	35.3
UC-3-91-A	2.38	74.0	17.4	9.9	22.2
UC-4-93-A	2.14	88.7	7.1	13.0	31.8
UM-5-95-A	1.89	47.0	40.4	21.1	34.5
UM-6-97-A	2.19	91.0	5.6	17.5	30.5
UM-7-99-A	2.21	70.3	20.4	19.1	28.3
UM-8-101-A	2.43	81.0	12.3	10.2	21.5

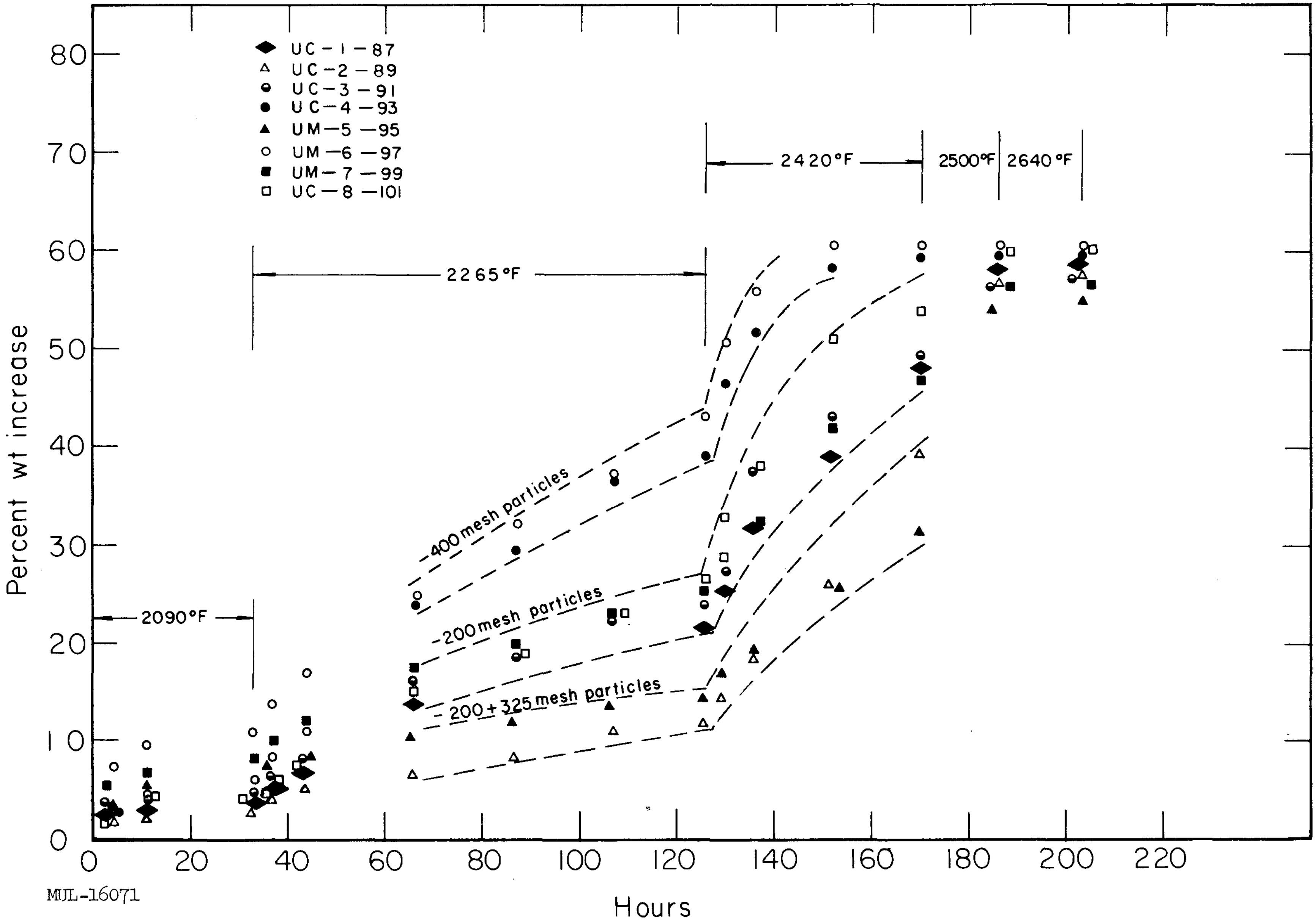

MUL-16071

Fig. V-17. Nitriding rates of silicon.

X-ray diffraction has been able to identify the alpha and beta phases of several different samples, and in most cases the beta phase has been predominant. It is planned to use an x-ray furnace to determine if the alpha phase converts to the beta phase at temperatures from 2650 to 2750 °F. If the conversion does take place, it probably would be desirable to convert to the beta phase before the silicon nitride is used as a structural material.

Popper and Ruddlesden of the British Ceramic Research Association report that their low density material (2.06 g/cc) withstood nearly 30 times the number of thermal shock cycles withstood by the higher density material (2.22-2.52 g/cc), whereas the latter had about 10 times the creep resistance of the low density material, a higher oxidation resistance, and a higher impact strength. Creep and thermal-shock resistance are both desirable in reactor components, and so it is not clear which density would be the more desirable.

/fj